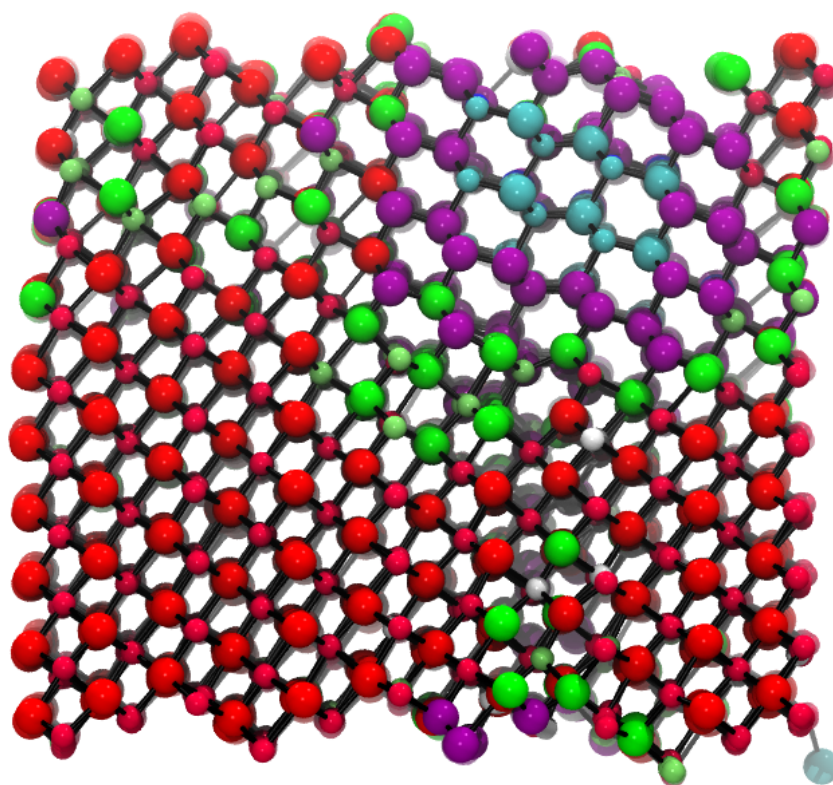


On the Use and Development of  
Advanced Computational Techniques  
to Determine the Properties and  
Behaviour of Metastable Materials



**Samuel Alexander Jobbins**

**Ph.D. Thesis, Cardiff University**

**September 2017**



## **Declaration**

This work has not been submitted in substance for any other degree or award at this or any other university or place of learning, nor is being submitted concurrently in candidature for any other degree or award.

Signed: .....

Date: .....

## **Statement 1**

This thesis is being submitted in partial fulfilment of the requirements for the degree of Ph.D.

Signed: .....

Date: .....

## **Statement 2**

This thesis is the result of my own independent work/investigation, except where otherwise stated, and the thesis has not been edited by a third party beyond what is permitted by Cardiff University's Policy on the Use of Third Party Editors by Research Degree Students. Other sources have been acknowledged by explicit references. The views expressed are my own.

Signed: .....

Date: .....

## **Statement 3**

I hereby give consent for my thesis, if accepted, to be available online in the University's Open Access repository and for inter-library loans **after expiry of a bar of access previously approved by the Academic Standards and Quality Committee.**

Signed: .....

Date: .....



## Table of Contents

<b>Declaration.....</b>	<b>II</b>
<b>Table Of Contents.....</b>	<b>III</b>
<b>Acknowledgements.....</b>	<b>VII</b>
<b>Abstract .....</b>	<b>VIII</b>
<b>Chapter 1: Introduction .....</b>	<b>1</b>
<b>Chapter 2: Theoretical Background .....</b>	<b>5</b>
<b>2.1. Classical Potentials.....</b>	<b>5</b>
2.1.1. Introduction to Forcefields.....	5
2.1.2. Van der Waals Interactions .....	6
2.1.3. Electrostatic Interactions.....	9
<b>2.2. Density Functional Theory .....</b>	<b>13</b>
2.2.1. Beyond Forcefield Methods .....	13
2.2.2. Solving the Schrödinger Equation .....	14
2.2.3. Introduction to Density Functional Theory .....	14
2.2.4. The Basis of Density Functional Theory.....	15
2.2.5. The Hohenberg-Kohn Theorems .....	16
2.2.6. The Kohn-Sham Equations .....	19
2.2.7. Solving the Kohn-Sham Equations.....	22
2.2.8. Exchange-Correlation Functionals.....	24
2.2.9. Pseudopotentials.....	26
References .....	29
<b>Chapter 3: Methodology I .....</b>	<b>30</b>
<b>3.1. Molecular Dynamics .....</b>	<b>30</b>
3.1.1. Introduction to Molecular Dynamics.....	30
3.1.2. Integration of the Equations of Motion .....	31
3.1.3. Calculating Properties in MD Simulations .....	36
3.1.3.1. The <i>Microcanonical Ensemble</i> (NVE) .....	36
3.1.3.2. Non-Natural Ensembles .....	38
3.1.3.3. Thermostats.....	39
3.1.3.4. Barostats .....	41
<b>3.2. Geometry Optimisations .....</b>	<b>43</b>
3.2.1. Introduction to Geometry Optimisation .....	43
3.2.2. Steepest Descent method .....	44
3.2.3. Conjugate Gradient method .....	45
References .....	46

<b>Chapter 4: Methodology II</b>	<b>47</b>
<b>4.1. Introduction to Rare Events</b>	<b>47</b>
<b>4.2. Metadynamics</b>	<b>49</b>
4.2.1. Introduction to Metadynamics	49
4.2.2. The Choice of the Collective Variable	51
4.2.3. Implementations of Metadynamics	54
4.2.3.1. 'Standard' Metadynamics	54
4.2.3.2. Well-Tempered Metadynamics	56
4.2.3.3. Adaptive Gaussian Metadynamics	57
4.2.3.4. Using the Simulation Cell as the Collective Variable	58
<b>4.3. Transition Path Sampling</b>	<b>63</b>
4.3.1. Introduction to Transition Path Sampling	63
4.3.2. Importance Sampling	64
4.3.3. Path Probability	65
4.3.4. Sampling the Transition Path Ensemble	67
4.3.5. The <i>Shooter</i> Algorithm	69
4.3.6. The Order Parameter	74
4.3.7. Summary of the Path Sampling Procedure	75
<b>4.4. Hardware and Software</b>	<b>77</b>
4.4.1. Hardware	77
4.4.2. Software	78
4.2.2.1. <i>cp2k</i>	78
4.2.2.1. <i>SIESTA</i>	78
4.2.2.1. <i>plumed</i>	79
4.2.2.1. Visualisation Packages	79
References	80
 <b>Chapter 5: Phase Transitions of Zinc Oxide</b>	 <b>82</b>
<b>5.1. Introduction</b>	<b>82</b>
<b>5.2. Structure of Zinc Oxide</b>	<b>84</b>
<b>5.3. Formation and Transformations of the Polymorphs of Zinc Oxide</b>	<b>87</b>
5.3.1. The Wurtzite to Rocksalt transformation	87
5.3.2. The Rocksalt to Caesium Chloride transformation	90
5.3.3. Formation of Zincblende ZnO	90
5.3.4. Summary	93
<b>5.4. Determination of the Transition Mechanism</b>	<b>95</b>
5.4.1. Methodology	95
5.4.2. Results and Discussion	96
5.4.2.1. Determination of the Transition Pressure	96
5.4.2.2. The Geometric Trajectory	98
5.4.2.3. Finding a Dynamical Transition State	100
5.4.2.4. Defining the Order Parameter	101
5.4.2.5. Transition Path Sampling Results	103
5.4.2.5.1. Analysis of Data	103
5.4.2.5.2. Overview	105
5.4.2.5.3. The 'High-to-Low Pressure Phase' Transition	106
5.4.2.5.4. The 'Low-to-High Pressure Phase' Transition	115

<b>5.5. Free Energy Calculations .....</b>	<b>118</b>
5.5.1. Introduction to “Metashooting” .....	118
5.5.2. Methodology .....	122
5.5.3. Results and Discussion .....	124
5.5.3.1. Overview .....	124
5.5.3.2. Evolution of the Free Energy Surface .....	124
5.5.3.3. Analysis of the Intermediates and Transition States .....	128
5.5.3.3.1. Overview .....	128
5.5.3.3.2. The Intermediate Basins <i>i-1</i> and <i>i-2</i> .....	129
5.5.3.3.3. The Transition States <i>TS-A</i> , <i>TS-B</i> and <i>TS-C</i> .....	130
5.5.3.4. Energy Barriers .....	132
5.5.3.5. Change in Free Energy .....	136
5.5.3.6. Mapping the Trajectories .....	137
<b>5.5. Conclusions and Future Work .....</b>	<b>139</b>
References.....	142
 <b>Chapter 6: Phases of Water Ice .....</b>	 <b>146</b>
<b>6.1. Introduction to Water and Ice .....</b>	<b>146</b>
6.1.1. Overview .....	146
6.1.2. The Bernal-Fowler Rules .....	150
6.1.3. The Structure of Water Ice .....	151
<b>6.2. Atomistic Water Models .....</b>	<b>155</b>
6.2.1. Introduction .....	155
6.2.2. Transferrable Intermolecular Potential ( <i>TIPnP</i> ) Models .....	158
6.2.3. <i>TIP4P/Ice</i> Model .....	162
<b>6.3. Previous Simulations of Ice Phases.....</b>	<b>163</b>
<b>6.4. Summary .....</b>	<b>166</b>
<b>6.5. Metadynamics to the Cell with “Rotational Shooting” .....</b>	<b>167</b>
6.5.1. Methodology .....	167
6.5.1.1. The Basis of “Rotational Shooting” .....	167
6.5.1.2. Computational Details .....	169
6.5.2. Results and Discussion .....	171
6.5.2.1. Overview .....	171
6.5.2.2. Melting Events.....	171
6.5.2.3. Amorphous Phases .....	173
6.5.2.4. Non-Typical Events .....	177
<b>6.6. Metadynamics using <i>plumed</i> .....</b>	<b>178</b>
6.6.1. Methodology .....	178
6.6.1.1. Introduction .....	178
6.6.1.2. Steinhardt Parameters .....	178
6.6.1.3. Tetrahedral Parameters .....	180
6.5.1.4. Computational Details .....	180
6.6.2. Results and Discussion .....	182
6.6.2.1. Evolution of the Metatrajectory .....	182
6.6.2.2. Evolution of the Collective Variables .....	189
<b>6.7. Conclusions and Future Work .....</b>	<b>192</b>
References.....	195

<b>Chapter 7: Crystal Structure Prediction</b>	<b>200</b>
<b>7.1. Introduction</b>	<b>200</b>
<b>7.2. Crystal Structure Prediction Methodologies</b>	<b>202</b>
7.2.1. Random Sampling Techniques	202
7.2.2. Simulated Annealing Techniques	203
7.2.3. Metadynamics for Structure Prediction	204
7.2.4. Topological Techniques	205
7.2.5. Evolutionary Techniques	206
<b>7.3. This Work: Random Structure Searching using <i>Random Atomic Placement</i></b>	<b>207</b>
<b>7.4. Carbon Structure Prediction at Ambient Pressure</b>	<b>210</b>
7.4.1. Introduction	210
7.4.2. Carbon Allotropes	211
7.4.2.1. The Structures of Graphite and Graphene	211
7.4.2.2. The Structure of Diamond	213
7.2.2.3. Comparison of Graphite and Diamond	215
7.2.2.4. Fullerenes and <i>Glassy Carbon</i>	216
7.2.2.5. Carbon Nanotubes	218
7.2.2.6. Even More Exotic Allotropes	219
7.2.2.7. Summary	222
7.4.3. Methodology	222
7.4.4. Results and Discussion	224
7.4.4.1. Overview and Efficacy of the Random Atomic Placement Method	224
7.4.4.2. The Eight Novel Carbon Structures	229
7.4.4.2.1. Overview	229
7.4.4.2.2. $sp^2$ -layer Carbons – C12 and C36	232
7.4.4.2.3. $sp^2$ -3D molecular Carbons – C14	235
7.4.4.2.4. $sp^2$ - $sp^3$ mixed Carbons – C11, C17 and C30	237
7.4.4.2.5. $sp^3$ -3D molecular Carbons – C33 and C38	241
7.4.5. Conclusions and Future Work	244
<b>7.5. Zinc Oxide Structure Prediction at High Pressure</b>	<b>246</b>
7.5.1. Introduction	246
7.5.2. Previous Work on Bulk ZnO Crystal Structure Prediction	247
7.5.3. Methodology	249
7.5.4. Results and Discussion	250
7.5.4.1. Overview	250
7.5.4.2. The Five Predicted Phases of ZnO	254
7.5.4.2.1. Structure A – NaCl-like with FeSi distortion	254
7.5.4.2.2. Structure B – NaCl-NiAs intergrowth	257
7.5.4.2.3. Structure C – NbAs-like	259
7.5.4.2.4. Structure D – $\alpha$ -WC-like	262
7.5.4.2.5. Structure E – NiAs-like	264
7.5.5. Conclusions and Future Work	266
References	269
<b>Chapter 8: General Conclusions and Closing Statements</b>	<b>273</b>

## Acknowledgements

Firstly, I would like to express considerable gratitude to my project supervisor, Dr. Stefano Leoni, for giving me such a fantastic, exciting and varied Ph.D. project. His guidance, support (and humour!) has been integral to my professional development over the last four years. It has been an absolute privilege to work with him – I truly hope that he has enjoyed it as much as I have. *Diolch yn fawr*, boss!

I must give thanks to Dr. Jamie Platts and Prof. Peter Knowles for their continual support as my internal mentor and examiner, respectively. Their advice has been invaluable and their guidance integral to my development during these past years. Thanks also to Prof. Richard Catlow and Prof. Roman Martonák, for their roles as the final examiners of this Ph.D. work.

Considerable gratitude must go to Advanced Research Computing at Cardiff University (ARCCA), High Performance Computing Wales (HPCW) and the UK national supercomputing service (ARCHER) for their respective allowances of computing time, without which many of the calculations presented here would not have been possible.

Notably, thanks go to Dr. Daniele Selli and Dr. Salah Boulfelfel, whose expertise and continual guidance have been invaluable throughout the course of this project. Significant gratitude must also go to Dr. Igor Baburin, for his generosity and willingness to help with all matter of academic issues! I also thank current members of the Leoni group – Mr. Timothy Flack, Mr. Duncan Hardie, and Mr. Darren Wragg – for their constant support and discussion (academic and otherwise!) during these four years. These three gentlemen have become great friends of mine, and I wish them all the very best for their future endeavours.

Finally, I would like to extend thanks to all of my family, in particular: my grandparents, Mrs Joan Bees, Mr Bryan Bees, Mrs Dawne Jobbins and Mr William “Bill” Jobbins; my sister, Miss Katherine “Kate” Jobbins; and, especially, my parents, Dr Julie Jobbins and Dr Marc Jobbins. Without their unconditional love and support, I would likely not have had the strength, nor the conviction, to be where I am today.

## Abstract

This thesis contains discussions and results pertaining to three distinct pieces of work, all related by an underlying theme: the use and development of computational techniques to discover and characterise novel metastable materials.

Zinc oxide is a cheap and abundant material with many potential uses in the electronics and optics industries. However, its wurtzite ground state structure gives rise to a number of undesirable properties. Thus, knowledge of how to stabilise more useful metastable phases is desirable. To that end, the mechanism of the pressure-induced phase transition between the zincblende and rocksalt polymorphs of the compound was deduced using transition path sampling. Following this, a novel technique combining TPS methods with metadynamics was applied to classify the free-energy landscape relevant to the transition pathway. This provided further information relating to the transition that would have been impossible to determine using path based analyses alone.

Water ice exhibits a wealth of structural polymorphism, with at least eighteen phases known to experiment and many more configurations predicted. However, a true understanding of the transition pathways that link these structures remains elusive. Using both metadynamics techniques and a novel procedure known as *rotational shooting*, attempts to deduce pathways between different phases of ice have been made. The results presented include successful transformations between two crystalline phases of ice and several amorphous phases, as well as the possible elucidation of a novel ice polymorph.

Crystal structure prediction remains a challenge in materials science. Using a random structure search technique, eight novel allotropes of carbon and three novel high-pressure polymorphs of zinc oxide have been found and subsequently characterised using density functional theory. Each of the materials displays its own unique array of properties, demonstrating both the variety exhibited by polymorphs of the same material and the ability of random structure prediction techniques to predict such dissimilar materials.

## Chapter 1

### Introduction

**“Science requires both observation and comprehension. Without observation there are no facts to be comprehended; without comprehension, science is mere documentation”**

- Dennis Rapaport, “The Art of Molecular Dynamics Simulation”

With recent advancements in computer hardware and software, as well as the further understanding of advanced scientific concepts, the study of chemical and physical systems using computational techniques has never before been so accessible nor so fruitful. Nowadays, powerful machines can be purchased or built at little expense, allowing for the complete classification of hypothetical materials using any level of theory, ranging from classical, semi-empirical calculations to advanced, *ab initio* computations. Thus, computational materials science now has the ability to play a key role in the acquisition of knowledge like never before; not only can it be used to emulate and model experimental observations, it can also be used to transcend what is experimentally known in the form of prediction and simulation.

However, the efficacy of simulation and its relationship with experimental studies is often a contentious point of discussion. Whilst it can be easily demonstrated that simulation has no match in probing the essentially-invisible atomistic world in a vibrant and scientifically valuable way, its accuracy and reliance on approximations is sometimes questioned. This perception of simulation is both incorrect and unfair. Of course, simulation significantly relies on theory and its associated approximations, but so too does experiment. Indeed, the very equations utilised in both theoretical and experimental analyses rely on myriad simplifications, in many cases just to allow them to be solvable and/or to give meaningful physical data. As such, simulation and theory cannot be used interchangeably, as both experiments and simulations utilise theory in order to advance knowledge.



In addition, both simulations and experiments must be treated with rigorous levels of statistical analysis in order to establish the integrity of the results and ensure the accurate sampling of the system of interest. Additionally, akin to experimental, simulation requires the prediction and measurement of systems within a rigorous mathematical and scientific framework.

As such, simulation cannot be regarded simply as an extension of *theory* – it must be regarded as a *numerical experiment* within a *virtual laboratory*. Simulation and experiment, therefore, must both be regarded as two equally valid ways of utilising theory and method to extend scientific knowledge. Both methods have their relative advantages and disadvantages, with the primary advantage of simulation being the exquisitely detailed view into the atomistic world it can provide.

Such an atomistic view can give unparalleled information about the underlying properties and behaviour of chemical systems. In particular, there is a constant need for new, high-performance materials made from inexpensive elements and compounds to combat the problems of the modern world – namely, the issues associated with man-made climate change, energy consumption and storage, and the ever-expanding demand for natural resources driven by the global economy.

Accurate and efficient atomistic modelling can provide detailed insight into novel materials prior to their fabrication, at a fraction of the cost and risk of synthesising and testing a new hypothetical material. This kind of efficient, accurate and inexpensive analysis of chemical systems is exactly what is required to face these contemporary problems. With increasing computational power and scientific knowledge, such calculations and predictions will only become more powerful and more accurate.

With this in mind, this thesis represents work from three varied but connected fields, utilising cutting-edge methods to look at well-known materials in a different way, in order to push the boundaries of current knowledge. Using an atomistic approach, this thesis details the incorporation of both existing techniques and the design of new methods in an effort to contribute to the rapidly growing field of computational materials science. Thus, the ultimate

aim of this work is both to investigate the properties and behaviour of a wide range of relevant metastable materials, and to contribute to the ‘tool box’ of techniques available to the computational materials scientist.

In Chapter 2, an introduction to the theory of computer simulations is given. A detailed discussion relating to the two levels of theory used in this work – namely, classical mechanics-based force fields and density functional theory - are presented in detail, within an appropriate historical and mathematical context.

Chapter 3 delivers an introduction to the fundamental techniques of molecular dynamics and geometry optimisations, the two core techniques utilised in this work. This includes a discussion on the important central principles, such as thermodynamic ensembles and numerical integration techniques.

Chapter 4 presents an in-depth discussion of the two advanced methods used to accelerate the sampling of rare events: *metadynamics* and *transition path sampling*. These two techniques are central to the work presented in this thesis, and all appropriate manifestations of the two procedures are presented within this chapter. In addition, a short section detailing the hardware and software utilised in this work is also presented.

Marking the beginning of the presentation of this work, Chapter 5 reports an investigation into the pressure-induced phase transition between the zincblende and rocksalt structures of zinc oxide (ZnO). Zinc oxide is a common, inexpensive material that could find use in future electronics and optics devices, however its potential application is hindered by the lack of knowledge of how to transform this versatile material into its metastable zincblende polymorph. A review of current knowledge is first delivered, followed by an in-depth analysis of the deciphered transition pathways. The transformation mechanism is first explored by using path sampling techniques. To capture all subtleties of the mechanism, a novel combination of transition path sampling and metadynamics, dubbed *metashooting*, was subsequently developed.

Chapter 6 involves an investigation into the polymorphism of water-ice. Despite its ubiquity, the properties and behaviour of water are poorly understood; this work attempts to help to characterise the elusive transitions between the condensed phases of water using both metadynamics and the novel *rotational shooting* technique. A detailed review of water modelling and phase transitions between condensed phases is presented prior to the discussion of the results, which includes a number of possible phase transitions and the elucidation of an unidentified, potentially novel polymorph of water ice. This could have broad ramifications in the fields of biology, geology and medicine, amongst others.

The final results section, Chapter 7, involves a detailed investigation into the generation of novel crystal structures of carbon and zinc oxide using a random structure searching technique. Eight novel carbon allotropes at 0 GPa are presented, as well as three novel ZnO polymorphs at high pressure. Prior to the discussion of the results, once again a detailed investigation into the literature is presented, detailing the various methods of crystal structure prediction and the latest investigations into the fields of carbon and zinc oxide bulk structure elucidation. The polymorphs presented exhibit a range of electrical and mechanical properties, some of which may be suitable for future fabrication and use.

To conclude, Chapter 8 presents a broad overview of the results described in this thesis, before ending with some appropriate closing statements relating to the work delivered and its context within the broader field of computational materials science.

### References – Chapter 1

F. Jensen, *Introduction to Computational Chemistry*, John Wiley & Sons, 2<sup>nd</sup> Edition, 2011.

D. C. Rapaport, *The Art of Molecular Dynamics Simulation*, Cambridge University Press, 2<sup>nd</sup> Edition, 2004

## Chapter 2

### Theoretical Background

***“If in other sciences, we should arrive at certainty without doubt and truth without error, it behoves us to place the foundations of knowledge in mathematics”***

– Roger Bacon (1214-1292), *Opus Majus*, c. 1267

#### 2.1. Classical Potentials

The following references are essential to the content within section 2.1.<sup>[1-4]</sup>

##### 2.1.1. Introduction to Forcefields

Interatomic potentials known as *forcefields* are often employed within computer simulations of materials to calculate the potential energy of a system. In a forcefield, the electronic energies of atoms are supplied as a parametric function of the nuclear coordinates. As such, bonding information is provided explicitly by the parameters, which are usually fitted to experimental, *ab initio* data or both.

The basis of forcefield or *molecular mechanics* methods is that structural units within molecules appear to behave very similarly even when in different environments (indeed, this notion of *functional groups* is central to the discipline of organic chemistry). Molecules are thought of as being “balls” of different sizes attached to “springs” which have different lengths and levels of stiffness, and as such the system is reduced to a purely classical problem. As a result, Newton’s second equation of motion can be used to calculate the dynamics of the system.

The total potential energy calculated from the forcefield can be expressed as the sum of a number of contributions. The primary contributions can be broken down into two categories

– *intramolecular* contributions (including the bond lengths, angles and torsions) and *intermolecular* contributions (i.e. non-bonded interactions such as van der Waals and *electrostatic* (or *Coulombic*) contributions for charged systems). Additional terms, such as out of plane bending, coupling between intramolecular interactions and many-body interactions can also be included. The total potential energy can therefore be generally expressed as:

$$E_{Forcefield} = E_{Bonds} + E_{Angles} + E_{Dihedrals} + E_{VDW} + E_{Elect} + E_{Other} \quad (Eq\ 2.1)$$

where each  $E$  term is the sum of all contributions of that type within the system. The most computationally expensive components of the potential to calculate are the van der Waals ( $E_{VDW}$ ) and electrostatic ( $E_{Elect}$ ) terms, which together form the intermolecular interaction terms. The exact analytical function used to describe each of these contributions varies. For example, the simplest function to describe bonding interactions is a Taylor expansion around an equilibrium bond length. However, this is often insufficient for calculating bond lengths in more complex systems, and such simple polynomial expressions do not encapsulate the correct limiting behaviour of bonding systems. As such, a different analytical function (such as a Morse potential) could be used to closer approximate the correct behaviour of the interaction.

### 2.1.2. Van der Waals Interactions ( $E_{VDW}$ )

The first of the intermolecular interactions terms, the  $E_{VDW}$  term describes the short range attraction and repulsion between atoms that are not bonded.  $E_{VDW}$  becomes extremely large at bond lengths approaching zero as a result of the repulsion between electron clouds of the two atoms. At very long bond lengths,  $E_{VDW}$  tends to zero as the two atoms are not physically close enough to each other to induce a strong interaction. However, at intermediate distances there is an attraction caused by induced dipole-dipole interactions between the electron clouds of the two atoms. This attractive interaction varies as a function of the inverse sixth power of the distance between the two atoms.

The most commonly used function to describe this interaction is the *Lennard-Jones* (L-J) potential,<sup>[5]</sup> sometimes referred to as the *12-6 potential*:

$$E_{VDW(LJ)} = 4\varepsilon \left[ \left( \frac{\sigma}{r} \right)^{12} - \left( \frac{\sigma}{r} \right)^6 \right] = \varepsilon \left[ \left( \frac{r_0}{r} \right)^{12} - 2 \left( \frac{r_0}{r} \right)^6 \right] \quad (Eq\ 2.2)$$

where  $\varepsilon$  is the depth of the potential energy well,  $r$  is the distance between the two atoms,  $\sigma$  is the distance between the two atoms where the interatomic potential energy is equal to zero and  $r_0$  is the distance at which the interatomic potential is at its minimum value  $-\varepsilon$ . The parameters  $\sigma$  and  $r_0$  are related to each other, as  $r_0 = 2^{\frac{1}{6}}\sigma$ .

The  $r^{-6}$  term corresponds to the attractive component of the potential, whereas the  $r^{-12}$  approximates the repulsion of overlapping electronic wave functions. The Lennard-Jones potential finds widespread use in many forcefield calculations, due to its relative simplicity (only two parameters  $\varepsilon$  and  $\sigma$  are required) and fast computation.

Whilst the exponent of the attractive component has physical justification, the exponent of the repulsive component is chosen purely for computational convenience, being the square of  $r^{-6}$ . It is not possible to derive a function for the repulsive interaction. In theory, any exponent can be taken, with the conditions that the function tends towards zero as the distance goes to infinity, and that it approaches zero faster than the attractive ( $r^{-6}$ ) term.

However, despite its computational convenience, the  $r^{-12}$  form of the repulsive component has been shown to be quite a poor description, as the repulsion at low values of  $r$  tends to infinity much too steeply. Quantum mechanics has shown that electron density actually falls off approximately exponentially with distance from the nucleus. As the repulsion between two atoms is caused by the overlap of electron clouds, it is a better approximation to model the repulsive component of the potential as an exponential function. An example of a potential that utilises an exponential function for the repulsive component of the potential is the *Buckingham potential*<sup>[6]</sup> or *exp- $r^6$*  potential:

$$E_{VDW(Buck)} = Ae^{-Br} - \left( \frac{C}{r^6} \right) \quad (Eq\ 2.3)$$

Buckingham-style potentials are therefore sometimes considered to be a more ‘natural’ potential, as the repulsive term is modelled more closely with quantum theory. However, this form of potential has its own drawbacks. A notorious problem with this potential form can lead to the so-called “Buckingham Catastrophe”. As the exponential term converges to a constant as  $r$  tends to zero, the  $r^{-6}$  diverges to  $-\infty$ . This means that, at low values of  $r$ , the Buckingham potential can ‘turn over’ and atoms become unphysically attracted to one another. Precautions must therefore be taken to ensure that atoms (particularly charged systems) defined by the Buckingham potential must not ever come too close to each other during a simulation.

A third type of potential, the *Morse Potential*,<sup>[2]</sup> has been used extensively in the inter-atomic interaction modelling, particularly in diatomic molecules. Few details of the Morse potential are reported here, as it was not used extensively in this work. Such potentials generally take the form:

$$E_{VDW(Morse)} = D_e(e^{-2a(r-r_0)} - 2e^{-a(r-r_0)}) \quad (Eq\ 2.4)$$

where  $r$  and  $r_0$  are once again the instantaneous and equilibrium distances between the two atoms respectively,  $D_e$  is the depth of the potential energy well, and  $a$  corresponds to the width of the potential energy well, which is related to the force constant at the bottom of the potential energy well  $k_0$  by the relationship:

$$a = \sqrt{\frac{k_0}{2D_e}} \quad (Eq\ 2.5)$$

The Morse potential is slightly more accurate than the Buckingham potential, which in turn is slightly more accurate than the Lennard-Jones potential. One reason for this more accurate depiction of the atomic interaction is the use of three parameters in the Morse and Buckingham models, versus the two parameters used in the Lennard-Jones potential. Additionally, much of the discrepancy in these potentials originates from the poor modelling



of the repulsive part of the potential, which is over-estimated in the Buckingham potential and, as mentioned previously, even more-so in the Lennard-Jones model.

Despite the additional accuracy conferred by the Buckingham and Morse models, the Lennard-Jones potential continues to be the most popular potential model used in computer simulations. Despite the use of three parameters in the Buckingham and Morse models leading to a more accurate interaction model, it also means that creating such potentials can be a more difficult procedure. Buckingham and Morse potentials also take around four to five times longer to compute than corresponding Lennard-Jones descriptions due to the presence of exponential functions, making them a less desirable choice in computer simulations. As Lennard Jones functions are comprised of values of  $r$  raised to even powers (and  $r^{-12}$  is simply the square of  $r^{-6}$ ), the computation time for this type of potential is much quicker. In addition, the failures of the repulsive component in the potential models are generally encountered in regions of very small bond lengths or very high energies, which are seldom realised in actual, meaningful calculations. As a result, the Lennard-Jones potential form gives comparable results to the more accurate potential functions in ‘real-world’ calculations, whilst being much quicker to compute.

### 2.1.3. Electrostatic Interactions ( $E_{Elec}$ )

The second intermolecular interaction term  $E_{Elec}$  corresponds to the electrostatic interactions between atoms or molecules in the system described. This is created by the internal distribution of electrons in molecules, including the presence of partial charges and induced dipoles. In its simplest form, the electrostatic interactions between two point charges is given by Coulomb’s Law:

$$E_{Elec(Coulomb)} = k_e \frac{q_i q_j}{r_{ij}} \quad (Eq\ 2.6)$$

where  $q_i$  and  $q_j$  correspond to the atomic charge of species  $i$  and  $j$  respectively,  $r_{ij}$  refers to the distance between species  $i$  and  $j$ , and  $k_e$  is Coulomb's Constant, which is approximately  $8.988 \text{ N m}^2 \text{ C}^{-2}$  and is expressed by the formula:

$$\frac{1}{4\pi\epsilon_0} \quad (\text{Eq 2.7})$$

where  $\epsilon_0$  is the vacuum permittivity, a fundamental constant corresponding to the ability of a vacuum to permit electric field lines, approximately equal to  $8.85 \times 10^{-12} \text{ C}^2 \text{ J}^{-1} \text{ m}^{-1}$ .

Whilst simply summing the Coulomb contributions for each site is appropriate in molecular and non-periodic systems, this method is not appropriate for systems with periodic boundary conditions. This is because summing the Coulombic interactions between neighbouring sites in periodic replicas would converge very slowly and the final solution would be dependent on the order of the summation, potentially requiring an infinite number of summations. As such, periodic systems require a different approach to calculate the electrostatic potential – the most common of which is the *Ewald* summation, which makes two modifications to the simple Coulomb model.

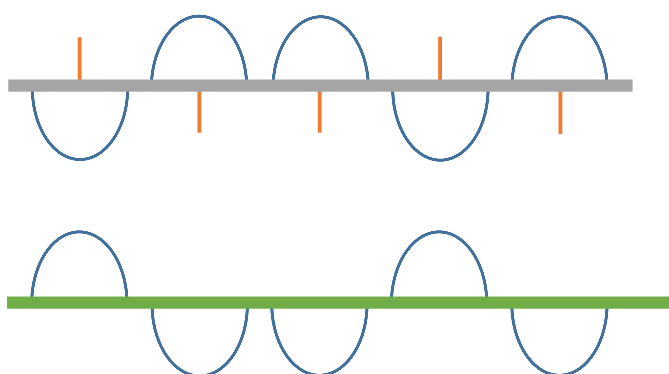


**Figure 2.i:** Diagram illustrating the 'Ewald' method. The top diagram (grey) shows the *short-range* component of the summation, with vertical orange lines illustrating point charges and the opposing blue curves representing the spherical Gaussians of opposite charge. The bottom green diagram shows the 'long range' component, with the compensating charges.

Illustration concept adapted from reference 2.

Firstly, spherical Gaussian functions of opposite charge are centred on each ion, in order to effectively neutralise the charge at long range. This combination of ionic charges and Gaussian clouds is the *short-range* component of the Ewald summation and is solved in real space. The second modification involves another superposition of Gaussian functions with the same charge as the original ion. This second Gaussian cloud is also centred on the original point charges, thereby cancelling out the effect of the first Gaussian cloud of opposite charge. The potential as a result of this second set of Gaussian functions is acquired from the Poisson Equation,<sup>[1]</sup> which is then solved in reciprocal space as a Fourier series. This *long-range* component is transformed to short-range in reciprocal space, and what was a potentially infinite Coulombic summation has been reduced to two finite sums – one in real space and one in reciprocal space. In addition, a self-correction term is also required, as a result of Gaussian clouds acting on their own sites. The Ewald summation can therefore be summarised as:

$$E_{Elec(Ewald)} = E^S + E^L - E^{Self} \quad (Eq\ 2.8)$$

where  $E^S$  corresponds to the short-range component solved in real space,  $E^L$  is the long-range component solved in reciprocal space, and  $E^{Self}$  is the self-energy correction term. Most of the computation involves calculation of the long-term component, as in general the short-term component is summed easily. More completely, the Ewald sum is written in full below, with  $E^S$ ,  $E^L$  and  $E^{Self}$  corresponding to the first, second and third terms respectively:

$$\begin{aligned} E_{Elec(Ewald)} = & \frac{1}{2} k_e \sum_n \sum_{i=1}^N \sum_{j=1}^N, \frac{q_i q_j}{|r_i - r_j + nL|} \operatorname{erfc} \left( \frac{|r_i - r_j + nL|}{\sqrt{2} \sigma} \right) \\ & + \frac{1}{2V\epsilon_0} \sum_{k \neq 0} \frac{e^{-\sigma^2 k^2/2}}{k^2} \left| \sum_{i=1}^N q_i e^{ik \cdot r_i} \right|^2 - k_e \frac{1}{\sqrt{2}\pi\sigma} \sum_{i=1}^N q_i^2 \quad (Eq\ 2.9) \end{aligned}$$

In the above complete expression,  $r_i$  and  $r_j$  correspond to the position of ions  $i$  and  $j$ ,  $L$  represents the length of the supercell utilised,  $\sigma$  is the standard deviation of the Gaussian distribution and  $V$  is the volume of the supercell.  $k$  refers to the vector of the ions in reciprocal

space (i.e. after undergoing Fourier transform). The ' in the  $E^S$  term means that the term  $j = i$  is not included when  $n = 0$ .  $erfc$  is the complementary error function, and is defined as:

$$erfc(x) \equiv 1 - erf(x) = \frac{2}{\sqrt{\pi}} \int_x^{\infty} e^{-t^2} dt \quad (Eq\ 2.10)$$

The Ewald summation is extremely effective at summing the Coulombic interactions between point charges in periodic systems,<sup>[1,4]</sup> as both summations converge quickly in their respective spaces. However, a number of requirements are implicit in the Ewald method. The system must be overall charge neutral, and the systems under scrutiny must have perfect periodic symmetry. In addition, the cut-offs of the short- and long-range components of the summations must be defined carefully, as poorly chosen cut-offs can produce unwanted artefacts in the simulation.

## 2.2. Density Functional Theory

The following references have been essential for the completion of Section 2.2.<sup>[2,3,7-9]</sup>

### 2.2.1. Beyond Forcefield Methods

Forcefield methods involve the treatment of particles in a simulation as solid bodies connected by springs which interact under the influence of an external potential. While this approximation is sufficient for a wide variety of systems, there are intrinsically more involved aspects of atomistic simulation that require a much more rigorous mathematical description. Many important properties and interactions arising from quantum effects are completely absent in forcefield-based calculations unless they have been defined explicitly, which can be a non-trivial and system specific process.

*Ab initio* (from the Latin for ‘*from the beginning*’) methods allow for the complete description of atomic and molecular systems using mathematical models based solely on first principles. Such models aim to provide solutions to the time-independent, non-relativistic Schrödinger equation, which gives a fully quantum description of any physical system.<sup>[10]</sup> The time-independent form of the Schrödinger equation is expressed as the simple eigenequation:

$$\hat{H}\psi(\mathbf{r},t) = E\psi(\mathbf{r},t) \quad (\text{Eq 2.11})$$

$E$  is the total energy of the state under scrutiny and  $\hat{H}$  is the Hamiltonian operator of the system, containing potential and kinetic energy terms.  $\psi(\mathbf{r},t)$  is the wavefunction of the quantum system, which contains complete information about the degrees of freedom available to the system, including spatial and spin coordinates. From the wavefunction, the probability distributions of possible measurements may be derived, from which all physical properties of the system can be determined. This is crucially different to classical methods – properties and interactions are explicitly defined by a forcefield, whereas in *ab initio* methods all physically relevant information can be derived from solutions to the Schrödinger equation.

### 2.2.2. Solving the Schrödinger Equation

Due to the inherent mathematical complexity of Schrödinger equation, a number of physically intuitive approximations must be applied for it to be solvable for chemically relevant systems. An essential simplification is the Born-Oppenheimer approximation, which assumes that the coupled motion between the nuclei and electrons of a system can be neglected and that nuclear and electronic dynamics can be separated. The electronic component of the wavefunction can then be solved independently, with the nuclei fixed in position exerting a constant external potential. However, even under the Born-Oppenheimer approximation the Schrödinger equation can only be solved for hydrogenic systems, such as H,  $\text{He}^+$  and  $\text{Li}^{2+}$  due to the highly complex nature of electron-electron interactions – the so-called *many-body problem*.

A number of techniques have been developed over the years to obtain *approximate* solutions to the Schrödinger equation for systems with many interacting electrons. Many methods, such as Hartree-Fock theory and its later variants known as Post-Hartree methods (such as Coupled Cluster and Møller-Plesset methods)<sup>[11]</sup> involve the expansion of the wavefunction in a series of Slater determinants. However, all of these so-called ‘wavefunction-based’ techniques are computationally expensive and are impractical for systems of more than a few atoms. A wavefunction for a system containing  $N$  electrons contains  $4N$  variables, thus wavefunction-based methods become exponentially more complicated with increasing number of electrons. As such, a technique that did not become increasingly complex in this way was highly desirable.

### 2.2.3. Introduction to Density Functional Theory

Arguably the most successful technique utilised in computational chemistry is Density Functional Theory (DFT), which has enjoyed considerable popularity for decades as a result of its ability to reasonably model a wide range of systems. The basis behind Density Functional Theory is that the ground state electronic energy is directly related to the electron density of

a system. As the electron density is the square of the wavefunction and can be used to obtain the Hamiltonian operator of the system, it can be used to solve the Schrödinger equation of the system under study.

Unlike in wavefunction-based methods, problems in Density Functional Theory do not become exponentially more complex with increasing numbers of electrons - the electron density has the same number of variables regardless of the system size. However, the functional that links the electron density with the energy is not directly known, except for in the case of a free electron gas. As a result, a number of assumptions must be made to create a suitable functional linking these two functions. Despite this deficiency, many of the standard functionals in Density Functional Theory are able to calculate physical properties to a reasonable degree of accuracy, and research is constantly underway to improve the rigour of the exchange-correlation functionals utilised within the technique.

#### 2.2.4. The Basis of Density Functional Theory

Under the Born-Oppenheimer approximation, the Hamiltonian operator utilised in the many-body Schrödinger equation can be broken up into three components:

$$\hat{H}\psi = [\hat{V}_{ext} + \hat{T} + \hat{U}]\psi \quad (Eq\ 2.12)$$

where  $\hat{V}_{ext}$  is the operator corresponding to the static Coulomb potential exerted by the fixed nuclei,  $\hat{T}$  is the kinetic energy operator for the electrons and  $\hat{U}$  is the interaction energy operator acting between the electrons in the many-body system. The general form of these operators is given by:

$$[\hat{V}_{ext} + \hat{T} + \hat{U}]\psi = \left[ \sum_i^N V_{ext}(\mathbf{r}_i) + \sum_i^N \left( -\frac{\hbar^2}{2m_i} \nabla^2 \right) + \sum_{i<j}^N U(\mathbf{r}_i, \mathbf{r}_j) \right] \psi \quad (Eq\ 2.13)$$



where  $V_{ext}$  and  $U$  are the external potential energy and electron-electron interaction functions respectively,  $\nabla$  is the Laplacian operator and  $\hbar$  is the reduced Planck constant. The operators  $\hat{T}$  and  $\hat{U}$  are so-called *universal operators* – i.e. their values are universal for any system with  $N$  electrons. For simplicity, these two operators can be combined into a single operator known as the *electronic operator*  $\hat{F}$ , which clearly is also universal for any system with  $N$  electrons. The Hamiltonian therefore depends only on the external potential  $V_{ext}$  and the number of electrons  $N$ , and can be written as:

$$\hat{H} = \hat{V}_{ext} + \hat{F} \quad (Eq\ 2.14)$$

The crux of Density Functional Theory is that the external potential  $\hat{V}_{ext}$  can be determined solely from the measurable quantity electron density  $\rho$ , and that the electron density integrated over all space gives the number of electrons  $N$ :

$$N = \int \rho(\mathbf{r}) d\mathbf{r} \quad (Eq\ 2.15)$$

If  $N$  and  $V_{ext}$  are known for a system, the Hamiltonian can be constructed and the Schrödinger equation solved. As such, only a single measurable quantity  $\rho$  is needed to determine any physical property of the system under study.

#### 2.2.5. The Hohenberg-Kohn Theorems

In the mid 1960s, Pierre Hohenberg and Walter Kohn<sup>[12]</sup> proposed two theorems which demonstrated that the many-body wavefunction, containing  $3N$  position variables, could be solved using the electron density functional, which contains only 3 variables. The two theorems were at the time only applicable to non-degenerate ground states but have since been extended to also apply to degenerate systems.

Both of the theorems are proved using the *variational principle* – a mathematical tool used in quantum mechanics invoking the selection of a ‘trial wavefunction’ and fixing one or more

parameters to find an estimate of the ground state energy for the system of interest. Energies computed using the variational principle are always equal to or higher than that of the true solution, and thus any variations to the trial wavefunction which reduce the total energy means that the new approximate energy must be closer to the real solution.

The two theorems devised by Hohenberg and Kohn are as follows:

*i. The external potential  $V_{ext}(\mathbf{r})$  is a unique functional of the electron density  $\rho(\mathbf{r})$ .*

The proof of this theorem proceeds by *reductio ad absurdum*. Consider a hypothetical scenario of two systems  $A$  and  $B$ . Both systems have different external potentials  $V_A$  and  $V_B$ , leading to two different Hamiltonians  $\hat{H}_A$  and  $\hat{H}_B$  and therefore two different ground state wavefunctions  $\psi_A$  and  $\psi_B$ . However, in this fictitious scenario both systems have the same number of electrons  $N$  and the same electron density  $\rho$ . Starting from the time-independent form of the Schrödinger equation for each system, using the variational principle the following inequality for the ground state energy of  $A$  is obtained:

$$E_A^0 < \langle \psi_B | \hat{H}_A | \psi_B \rangle = \langle \psi_B | \hat{H}_B | \psi_B \rangle + \langle \psi_B | \hat{H}_A - \hat{H}_B | \psi_B \rangle \quad (\text{Eq 2.16})$$

As both systems have the same electron density  $\rho = \rho_A = \rho_B$ , the above can be re-written in the following form:

$$E_A^0 < E_B^0 + \int \rho(\mathbf{r})[V_A(\mathbf{r}) - V_B(\mathbf{r})] d\mathbf{r} \quad (\text{Eq 2.17})$$

An analogous inequality for  $E_B^0$  is obtained if the subscripts  $A$  and  $B$  are reversed:

$$E_B^0 < E_A^0 + \int \rho(\mathbf{r})[V_B(\mathbf{r}) - V_A(\mathbf{r})] d\mathbf{r} \quad (\text{Eq 2.18})$$

Adding the two inequalities gives the obviously unreasonable result:

$$E_A^0 + E_B^0 < E_B^0 + E_A^0 \quad (\text{Eq 2.19})$$

This is clearly a contradiction and indicates that it is not possible for two systems with two different external potentials to have the same electron density. Thus, the external potential is determined *uniquely* by the ground state electron density. With this proof, Hohenberg and Kohn showed that the energy functional  $E$  linking the external potential  $V_{ext}$  and the electron density  $\rho$  is expressed as:

$$E[\rho(\mathbf{r})] = \langle \psi | \hat{H} | \psi \rangle = \int \rho(\mathbf{r}) V_{ext}(\mathbf{r}) d\mathbf{r} + F[\rho(\mathbf{r})] \quad (\text{Eq 2.20})$$

The functional  $F[\rho(\mathbf{r})]$  is known as the *universal functional* whose analytical form is unknown but is equal to the expectation value of the electronic operator  $\hat{F}$ .

$$F[\rho(\mathbf{r})] = \langle \psi | \hat{F} | \psi \rangle \quad (\text{Eq 2.21})$$

The value of  $\hat{F}$  and therefore  $F[\rho(\mathbf{r})]$  is universal for any system with  $N$  electrons. As stated previously, this shows that the Hamiltonian of this system relies only on the external potential energy and number of electrons. Thus both the external potential  $V_{ext}$  and the wavefunction of the system  $\psi$  are unique functionals of  $\rho$  and any property of the system can be determined solely knowledge of the electron density.

*ii. The electron density that minimises the total energy corresponds to the ground state density*

Consider a system in which the energy functional  $E[\rho_A(\mathbf{r})]$  is defined using an external potential  $V_{ext}$  in terms of a second, unrelated electron density  $\rho_B$ .

$$E[\rho_A(\mathbf{r})] = \int \rho_B(\mathbf{r}) V_{ext}(\mathbf{r}) d\mathbf{r} + F[\rho_B(\mathbf{r})] \quad (\text{Eq 2.22})$$

Once again from the variational principle, it can be stated that:

$$\langle \psi_B | \hat{F} | \psi_B \rangle + \langle \psi_B | \hat{V}_{ext} | \psi_B \rangle > \langle \psi_A | \hat{F} | \psi_A \rangle + \langle \psi_A | \hat{V}_{ext} | \psi_A \rangle \quad (Eq\ 2.23)$$

In this scenario,  $\psi_A$  is the correct wavefunction which corresponds to the ground state electron density  $\rho_A$ . This can then be rewritten as the integrals:

$$\int \rho_B(\mathbf{r}) V_{ext}(\mathbf{r}) d\mathbf{r} + F[\rho_B(\mathbf{r})] > \int \rho_A(\mathbf{r}) V_{ext}(\mathbf{r}) d\mathbf{r} + F[\rho_A(\mathbf{r})] \quad (Eq\ 2.24)$$

This can then clearly be written in terms of the energy functional:

$$E[\rho_B(\mathbf{r})] > E[\rho_A(\mathbf{r})] \quad (Eq\ 2.25)$$

Thus, Hohenberg and Kohn showed that not only does the electron density uniquely determine the external potential and the wavefunction, but that the minimised electron density corresponds directly to the ground state energy of the system. To put it another way, for every value of  $\rho$  the functional  $F[\rho(\mathbf{r})]$  enforces that the energy functional  $E[\rho(\mathbf{r})]$  is at its minimum for the ground state electron density of  $N$  electrons under the influence of external potential  $V_{ext}$ .

#### 2.2.6. The Kohn-Sham Equations

Despite the obvious power and simplicity of Hohenberg and Kohn's proofs, the two theorems alone did not provide a practical way of computing the ground state electron density. The complexity of the universal functional  $F$ , containing the terms for the interacting electrons' kinetic energies and the electron-electron interactions, still hindered the ability to practically utilise density functional theory. However, one year later in 1965 Walter Kohn and Lu Jeu Sham developed a method which made such calculations both accurate and tractable.<sup>[13]</sup> Their idea was to reduce the problem of many-electrons interacting under the influence of a

static external potential to a much simpler problem of non-interacting electrons affected by an effective potential. There are numerous advantages to such a simplified scheme:

- As the particles are non-interacting, the electron density can be treated as a series of single-particle orbitals. The wavefunction for the system can therefore be easily solved exactly using Slater determinants;
- The kinetic energy for a single-particle system is directly known; thus, the kinetic term in the universal functional is significantly simplified;
- The electron-electron interactions  $U$  need not be directly computed, again significantly simplifying the universal functional  $F$ .

Thus, the Kohn-Sham equations well used in density functional theory today were conceived. Consider the energy functional derived from Hohenberg and Kohn's theorems:

$$E[\rho(\mathbf{r})] = \int \rho(\mathbf{r})V_{ext}(\mathbf{r})d\mathbf{r} + F[\rho(\mathbf{r})] \quad (Eq\ 2.26)$$

Kohn and Sham defined the universal functional as the sum of three terms:

$$F[\rho(\mathbf{r})] = T_{1e}[\rho(\mathbf{r})] + E_{Hart}[\rho(\mathbf{r})] + E_{XC}[\rho(\mathbf{r})] \quad (Eq\ 2.27)$$

$T_{1e}$  is the kinetic energy functional for non-interacting electron, whilst  $E_{Hart}$  corresponds to the classical electrostatic, or Hartree energy, of the electrons. These two terms are known precisely and constitute the majority of the energy. The third term  $E_{XC}$ , known as the exchange-correlation functional, is thus the only unknown quantity within the universal functional, and only constitutes a very small part of the energy. It is defined as:

$$E_{XC}[\rho(\mathbf{r})] = T[\rho(\mathbf{r})] - T_{1e}[\rho(\mathbf{r})] + U[\rho(\mathbf{r})] - E_{Hart}[\rho(\mathbf{r})] \quad (Eq\ 2.28)$$

where  $T[\rho(\mathbf{r})]$  is the real kinetic energy functional for a many-electron system, and  $U[\rho(\mathbf{r})]$  contains all of the non-classical electron-electron interaction terms, including exchange and correlation effects. Thus, the exchange-correlation function contains all of the ‘corrections’ to the other classical and approximate components of the universal functional. The complete expression for the energy functional is thus:

$$E[\rho(\mathbf{r})] = \left[ \int \rho(\mathbf{r}) V_{ext}(\mathbf{r}) d\mathbf{r} + T_{1e}[\rho(\mathbf{r})] + E_{Hart}[\rho(\mathbf{r})] + E_{xc}[\rho(\mathbf{r})] \right] \quad (Eq\ 2.29)$$

Applying the variational principle once more to the energy expression gives:

$$\delta E[\rho(\mathbf{r})] = \left[ V_{ext}(\mathbf{r}) + \frac{\delta T_{1e}[\rho(\mathbf{r})]}{\delta \rho(\mathbf{r})} + \frac{\delta E_{Hart}[\rho(\mathbf{r})]}{\delta \rho(\mathbf{r})} + \frac{\delta E_{xc}[\rho(\mathbf{r})]}{\delta \rho(\mathbf{r})} \right] \delta \rho(\mathbf{r}) = 0 \quad (Eq\ 2.30)$$

These partial derivatives are denoted as potentials corresponding to the original functionals, and so the above expression can be rearranged and simplified to:

$$\delta E[\rho(\mathbf{r})] = \left[ \frac{\delta T_{1e}[\rho(\mathbf{r})]}{\delta \rho(\mathbf{r})} + V_{ext}(\mathbf{r}) + V_{Hart}(\mathbf{r}) + V_{xc}(\mathbf{r}) \right] \delta \rho(\mathbf{r}) = 0 \quad (Eq\ 2.31)$$

These three potential terms are often grouped together into a single potential known as the Kohn-Sham potential  $V_{KS}$ :

$$V_{KS}(\mathbf{r}) = V_{ext}(\mathbf{r}) + V_{Hart}(\mathbf{r}) + V_{xc}(\mathbf{r}) \quad (Eq\ 2.32)$$

The Kohn-Sham potential is therefore an effective potential which takes into account the ‘true’ many-electron behaviour of the system as a result of the exchange-correlation potential  $V_{xc}$ . As alluded to previously, the functional for the kinetic energy of non-interacting electrons is known precisely and is defined as a series of Slater determinants for each orbital  $\varphi_i$ :

$$T_{1e}[\rho(\mathbf{r})] = \sum_{i=1}^N \left\langle \varphi_i \left| -\frac{1}{2} \nabla^2 \right| \varphi_i \right\rangle \quad (Eq\ 2.33)$$

As a result, it is now possible to construct a Schrödinger-type equation in terms of each single-electron non-interacting orbital  $\varphi_i$  of the density within a local potential field:

$$\left(-\frac{1}{2}\nabla^2 + V_{KS}(\mathbf{r})\right)\varphi_i(\mathbf{r}) = \varepsilon_i\varphi_i(\mathbf{r}) \quad (Eq\ 2.34)$$

Within this framework, the electron density is given by the sum of the square of the individual orbital wavefunctions:

$$\rho(\mathbf{r}) = \sum_{i=1}^N \sum_{spin} |\varphi_i(\mathbf{r}, spin)|^2 \quad (Eq\ 2.35)$$

### 2.2.7. Solving the Kohn-Sham Equations

In Density Functional Theory based calculations the potential  $V$  depends on the electron density  $\rho$  which depends on the wavefunction  $\psi$ , which in turn depends on the potential  $V$ . As such, the Kohn-Sham equations must be solved iteratively using the so-called *Self-Consistent Field* method, in a very similar way to Hartree-Fock and post-Hartree-Fock methods.

To begin, a set of trial functions are defined based on the atomic coordinates of the system. These basis functions are then combined to form a linear combination of atomic orbitals, which act as the *initial guess* for the calculation. It is interesting to note at this point that the Kohn-Sham orbitals are not mathematically the same as Hartree-Fock or natural orbitals, however they still appear to accurately describe the system. From this initial guess wavefunction  $\psi_a$ , a guess electron density  $\rho_a$  is generated, which gives a potential  $V_a$  and a Kohn-Sham Hamiltonian  $\hat{H}_a$  for the system. The Kohn-Sham equations can then be solved, which give as an output new set of orbitals  $\psi_b$  and thus a new electron density  $\rho_b$  and new



potential  $V_b$ . The process is repeated until the input and output electron densities are equal, or equal to within a tolerance.

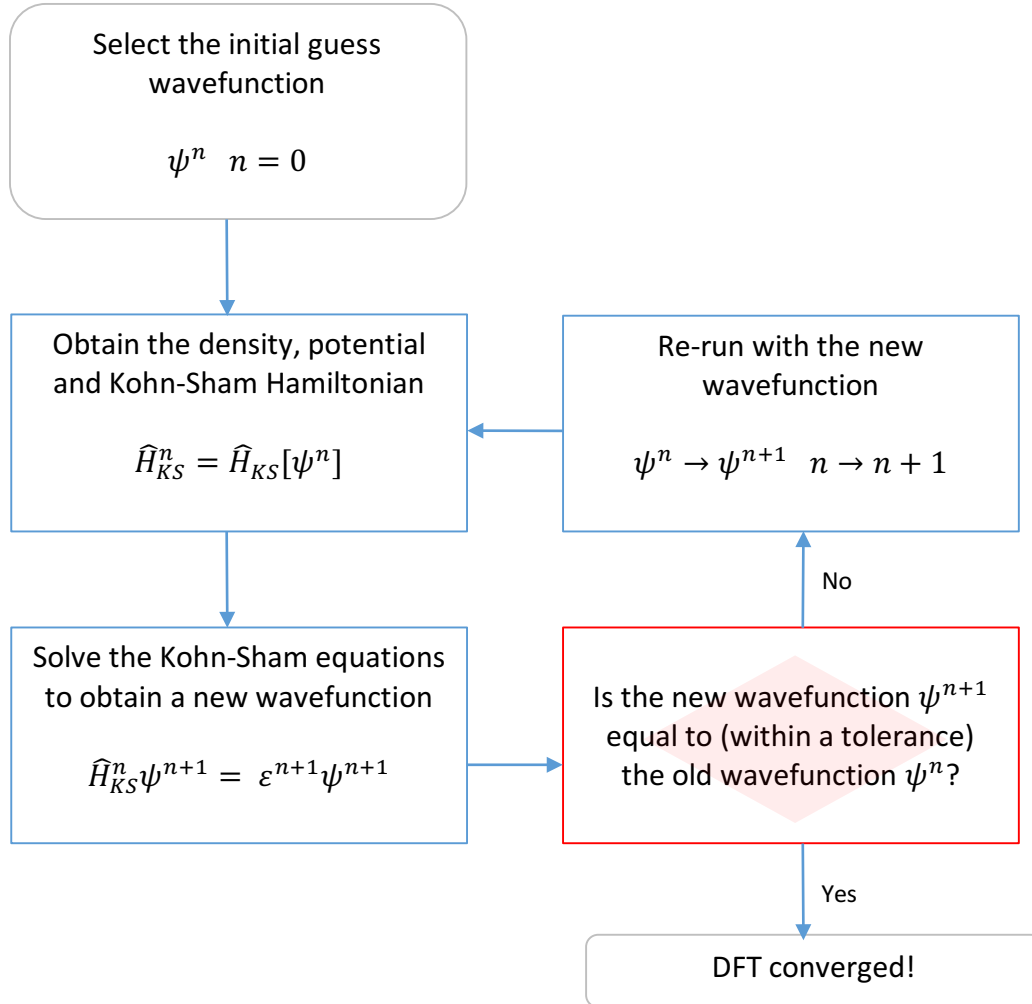


**Figure 2.ii:** A flow chart showing the general procedure of a Self-Consistent Field (SCF) Density Functional Theory calculation. The procedure iterates until the input and output wavefunctions and electron densities are equal to within some tolerance.

2.2.8. Exchange-Correlation Functionals

The Kohn-Sham equations give exact solutions to compute the energies for a given density if and only if the exact form of the exchange-correlation functional is known. Unfortunately, the precise form of the functional is not known, save for in a very select few model systems such as the free electron gas. Although it constitutes only a very small constituent of the energy, the exchange-correlation functional is still a very important component and without an accurate description chemical systems cannot be suitably described. Fortunately, even very simple approximations for the exchange-correlation term give very good results for a wide range of systems.

One of the simplest and most commonly employed methodologies in density functional theory to estimate the exchange-correlation functional is the *Local Density Approximation (LDA)*. In the Local Density Approximation, the portion of exchange-correlation energy from an infinitesimal volume in space  $d\mathbf{r}$  is considered to be equal to the value it would have if the whole space was filled with a homogenous electron gas with the same density:

$$E_{XC}^{LDA}[\rho(\mathbf{r})] = \int \rho(\mathbf{r}) \epsilon_{xc}[\rho(\mathbf{r})] d\mathbf{r} \quad (Eq\ 2.36)$$

where  $\epsilon_{xc}$  is the exchange-correlation functional in an homogenous electron gas with density  $\rho(\mathbf{r})$ , which is one of the few scenarios for which the exchange-correlation is known numerically. As such, the exchange-correlation potential within the Local Density Approximation is now defined as:

$$V_{XC}^{LDA}[\rho(\mathbf{r})] = \frac{\delta E_{XC}^{LDA}[\rho(\mathbf{r})]}{d\rho(\mathbf{r})} = \epsilon_{xc}[\rho(\mathbf{r})] + \rho(\mathbf{r}) \frac{d\epsilon_{xc}[\rho(\mathbf{r})]}{d\rho(\mathbf{r})} \quad (Eq\ 2.37)$$

The Local Density Approximation provides exact solutions for systems with very slowly varying electron densities. However, in real systems local density seldom exists and electron density fluctuates greatly. Because of this, Local Density Approximation has a tendency to

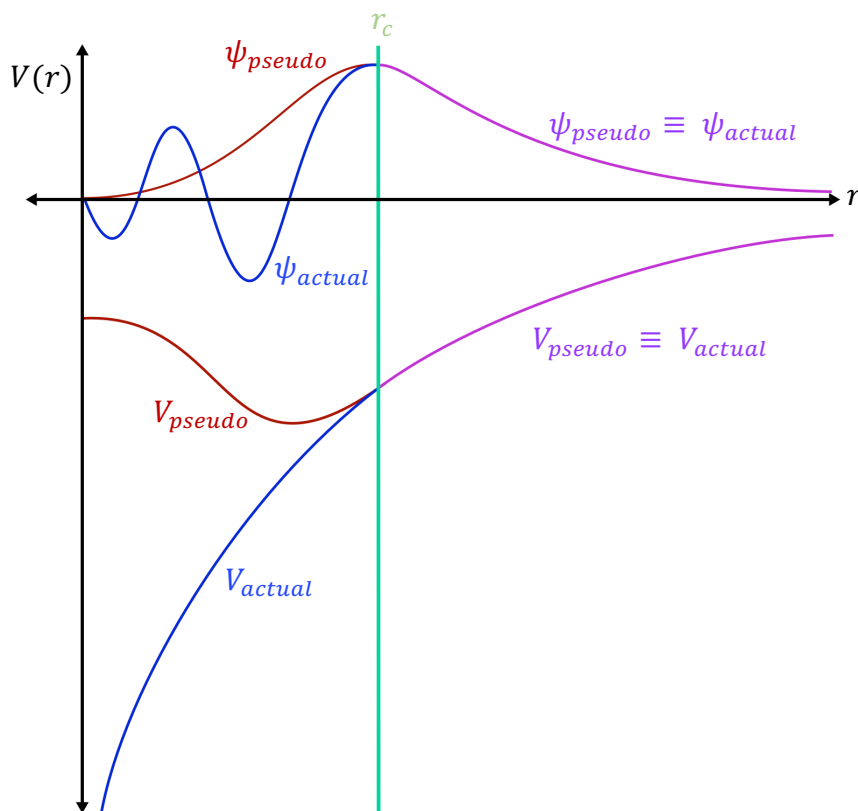
overestimate the exchange-correlation energy. Despite this, the method proves surprisingly effective at predicting the properties of real systems.

There are numerous ways in which the Local Density Approximation can be improved upon. One such improvement is to include the first derivative of the electron density as an additional term within the functional. This gives a more accurate picture of the varying nature of the electron density. Such a scheme is called the *Generalised Gradient Approximation (GGA)* or *non-local* methods. The exchange functional within the Generalised Gradient Approximation is therefore:

$$E_{xc}^{GGA}[\rho(\mathbf{r})] = \int \rho(\mathbf{r}) \epsilon_{xc}[\rho(\mathbf{r})] F_{xc}[\rho(\mathbf{r}), \nabla \rho(\mathbf{r})] d\mathbf{r} \quad (Eq\ 2.38)$$

where  $F_{xc}$  is called the *enhancement factor* and is the term that accounts for the non-homogeneity of the electron density. Unlike in the Local Density Approximation, numerous forms of Generalised Gradient Approximation methods exist, each employing a different enhancement factor. Such methods include those of Perdew and Wang (PW91)<sup>[14]</sup> and Perdew, Burke and Ernzerhof (PBE).<sup>[15]</sup> Generalised Gradient Methods have been shown to reduce the energy overestimation experienced in Local Density Approximation calculations, and as such are considered a more reliable method for Density Functional Theory calculations.

Despite the marked improvement obtained by utilising Generalised Gradient Approximation methods, overestimation of the exchange-correlation energy is still problematic, particularly in systems with highly localised and correlated electrons. Methods such as meta-GGA<sup>[16]</sup> partially solve this by utilising higher derivatives of the electron density to further account for variations in the density thus increasing the accuracy of the exchange-correlation energy. In addition, advanced methods also exist to further refine the energy calculation, including the introduction of a penalty to the energy term in the form of a Hubbard parameter (DFT+U), or the introduction of dispersion corrections to account for Van der Waal effects (DFT-VdW).

2.2.9. Pseudopotentials

**Figure 2.iii:** Consider the above hypothetical system. At distances close to the nucleus, the electronic wavefunction oscillates rapidly as a result of Coulombic interactions with the positive atomic core. The pseudopotential approximation ‘freezes’ the core electrons by assigning a modified effective potential described by a much smoother wavefunction with far fewer nodes. After the core cut-off  $r_c$ , the pseudo-wavefunction has the same form as the real wavefunction. As only the valence electrons are involved in most chemical processes, such an approximation significantly reduces the computational cost of a Density Functional Theory based calculation without compromising the fidelity of the results.

The electrostatic force attracting protons and electrons to each other varies greatly with distance. Correspondingly, the form of the electronic wavefunction changes with distance from the atomic nucleus - in particular, at close proximity to the nucleus the wavefunction

oscillates considerably. As such, it is often very difficult to define an analytical function for the wavefunction which describes the behaviour of the system for all distances from the nucleus. In addition, complex functions with multiple nodes and turning points rapidly incur computational expense.

Fortunately, it is possible to simplify the problem as it is feasible to make a distinction between the *core* electrons and the *valence* electrons. Almost all chemical bonding phenomena, especially in metals and semiconductors, are completely determined by the configuration of the valence electrons. On the contrary, the strongly bound core electrons seldom play a role in chemical bonding, but are involved in the screening of the positive nucleus. As a result, it is reasonable in most cases to approximate the coupled nucleus and inner electrons as an ionic core interacting with the only the valence electrons. Such an interaction is deemed an *effective core potential* or *pseudopotential* and has found widespread use in Density Functional Theory calculations. The concept was first described by Hans Hellman in 1934,<sup>[17]</sup> however pseudopotentials were largely ignored for a number of decades, despite their obvious capabilities.

Pseudopotentials are generated in a four step process:

1. Generate an accurate ‘true’ wavefunction for the system corresponding to the all-electron system. This can be achieved using Density Functional Theory or a different method, such as Hartree-Fock;
2. Replace valence orbitals with a set of pseudo-orbitals which have no nodes. The orbitals must be designed such that they behave correctly in the valence region;
3. Remove core orbitals and replace with an effective potential characterised using simple expressions such as Gaussian or polynomial functions;
4. Ensure that the parameters of the potential are fitted such that solutions to the Schrödinger equation produce pseudo-orbitals which match the original ‘true’ wavefunction outside of a cut-off radius  $r_c$ . “Hard” pseudopotentials with very

small values of  $r_c$  give more accurate results but are more computationally demanding, as they require a much larger set of basis functions. “Softer” pseudopotentials with larger values of  $r_c$  are cheaper to compute with, at the cost of accuracy and transferability.

One method of generating pseudopotentials is to construct both the valence and effective core potential regions from Gaussian functions. The quality of such an effective potential depends strongly on both the number of electrons approximated and those treated explicitly. A second method of generating pseudopotentials is to use a plane-wave basis set for the valence component of the potential, and a simple polynomial or spherical Bessel function for the core component. The quality of such pseudopotentials depends strongly on the position of the core radius, i.e. the distance from the nucleus at which the core-valence boundary (and hence change in mathematical description) occurs.

Arguably the most widely used type of pseudopotential is the so called *norm-conserving pseudopotential*.<sup>[18]</sup> In such an effective potential, the pseudo-wavefunction must have the same integral as the original wavefunction between zero and the core cut-off  $r_c$ :

$$\int_0^{r_c} \psi_{pseudo}^*(r) \psi_{pseudo}(r) dr = \int_0^{r_c} \psi_{actual}^*(r) \psi_{actual}(r) dr \quad \text{if } r < r_c \quad (\text{Eq 2.39})$$

At values of distance from the nucleus greater than the core cut-off, the pseudo-wavefunction is forced to coincide with the real wavefunction:

$$\psi_{pseudo}(r) = \psi_{actual}(r) \quad \text{if } r \geq r_c \quad (\text{Eq 2.40})$$

Another type of effective potential used is the *ultra-soft* pseudopotential,<sup>[19]</sup> where the first norm-conserving requirement is relaxed. Both norm-conserving and ultra-soft pseudopotential allow for an even smaller basis set of functions to be used, thereby reducing the computational expense of the calculation involved. Another method used to produce pseudopotentials is the *Projector Augmented Wave* method.<sup>[20]</sup>

References – Chapter 2

1. D. Frenkel and B. Smit, *Understanding Molecular Simulation: From Algorithms to Applications*, Academic Press, 2<sup>nd</sup> Edition, 2001.
2. F. Jensen, *Introduction to Computational Chemistry*, John Wiley & Sons, 2<sup>nd</sup> Edition, 2011.
3. D. Young, *Computational Chemistry: A Practical Guide for Applying Techniques to Real World Problems*, John Wiley & Sons, 1<sup>st</sup> Edition, 2001.
4. H. Lee and W. Cai, *Lect. Notes. Stanf. Univ.*, 2009, **3**, 1-12
5. J. E. Jones, *Proc. R. Soc. Lond. Math. Phys. Eng. Sci.*, 1924, **106**, 463-477
6. R. A. Buckingham, *Proc. R. Soc. Lond. Math. Phys. Eng. Sci.*, 1938, **168**, 264-283
7. [http://cmt.dur.ac.uk/sjc/thesis\\_ppr/node11.html](http://cmt.dur.ac.uk/sjc/thesis_ppr/node11.html) "Density Functional Theory" - Last Accessed 27/09/2017
8. <https://www.tcm.phy.cam.ac.uk/~pdh1001/thesis/node17.html> "Density-functional Theory" - Last Accessed 27/09/2017
9. C. J. Cramer, *Essentials of Computational Chemistry*, Wiley-Blackwell, 2<sup>nd</sup> Edition, 2004
10. E. Schrödinger, *Phys. Rev.*, 1926, **28**, 1049-1070
11. A. Szabo, N. S. Ostlund, *Modern Quantum Chemistry: Introduction to Advanced Electronic Structure Theory*, Dover Publications, New Edition, 1996
12. P. Hohenberg and W. Kohn, *Phys. Rev.*, 1964, **126**, B864-B871
13. W. Kohn and L. J. Sham, *Phys. Rev.*, 1965, **140**, A1133-A1138
14. J. P. Perdew and Y. Wang, *Phys. Rev. B.*, 1992, **45**, 13244-13249
15. J. P. Perdew, K. Burke and M. Ernzerhof, *Phys. Rev. Lett.*, 1996, **77**, 3865-3868
16. J. Tao, J. P. Perdew, V. N. Staroverov, G. E. Scuseria, *Phys. Rev. Lett.*, 2003, **91**, 146401
17. P. Schwerdtfeger, *ChemPhysChem*, 2011, **12**, 3143-3155
18. D. R. Hamann, M. Schlüter and C. Chiang, *Phys. Rev. Lett.*, 1979, **43**, 1494-1497
19. D. Vanderbilt, *Phys. Rev. B.*, 1990, **41**, 7892-7895
20. P. E. Blöchl, *Phys. Rev. B.*, 1994, **50**, 17953-17979
21. J. M. Soler, E. Artacho, J. D. Gale, A. García, J. Junquera, P. Ordejón and D. Sánchez-Portal, *J. Phys. Condens. Matter*, 2002, **14**, 2745

Chapter 3Methodology I

***“I can calculate the motion of heavenly bodies, but not the madness of people”***

– Sir Isaac Newton (1643 – 1727)

Discussions in this Chapter are largely derived from the following sources.<sup>[1-7]</sup>

### 3.1. Molecular Dynamics

#### 3.1.1. Introduction to Molecular Dynamics

Following the success of the Monte Carlo (MC) method utilised by physicists since the final years of World War II, the notion of Molecular Dynamics (MD) was formulated by Berni Alder and Thomas Wainwright in the late 1950s,<sup>[8]</sup> and independently developed by Aneesur Rahman during the mid 1960s.<sup>[9]</sup> The technique involves the computer simulation of the physical movements of objects (usually atoms, molecules or fragments) within a multiple-body system. These simulated particles are deemed heavy enough such that they can be approximated to behave as classical particles. As such, their movements are computed numerically using Newton’s second equation of motion (EOM), which is integrated over time for each interacting object:

$$m_n \frac{\delta^2 \mathbf{r}_n}{\delta t^2} = \mathbf{F}_n \quad n = 1, 2 \dots N \quad (Eq\ 3.1)$$

where  $m_n$  and  $\mathbf{r}_n$  are the mass and position of body  $n$  respectively. The forces between the objects of the system are given by the negative derivative of a potential function  $U$ :

$$-\frac{\delta U}{\delta \mathbf{r}_n} = \mathbf{F}_n \quad (Eq\ 3.2)$$



The potential function  $U$  can be expressed using a wide range of levels of theory, from classical interatomic potentials to high-level *ab initio* calculations. Under most circumstances, the level of theory utilised to define the potential function is dictated by considering both the size of the system of interest and the computational power available. This helps to establish a reasonable compromise between accuracy and tractability.

As a result of the large number of particles and the complexity of the systems scrutinised in a molecular dynamics calculation, it is impossible to solve the equations of motion and hence deduce future states of the system analytically. Once the potential function has been described and the forces derived, the EOMs are derived over discrete time intervals using numerical techniques. A large number of iterative numerical procedures have been designed for this process, such as the *Leapfrog* algorithm, the *Verlet* algorithm, and the principally used *Velocity Verlet* algorithm.<sup>[4]</sup>

In a typical Molecular Dynamics simulation, the conditions of the system under scrutiny are set by defining a specific thermodynamic ensemble. Commonly utilised ensembles include the *Microcanonical* ensemble (*NVE*), the *Canonical* ensemble (*NVT*) and the *Isothermal-Isobaric* ensemble (*NpT*). For any of these statistical ensembles, the average of a conserved variable at equilibrium over infinite time is equal to the average over the statistical ensemble. As such, the progression of a single MD calculation over sufficient time may be used to calculate the macroscopic thermodynamics properties of a system. This concept, known as the *ergodic* principle, is central to molecular dynamics, as it allows computation of macroscopic properties from time averages of microscopic configurations within a simulation.

### 3.1.2. Integration of the Equations of Motion

As mentioned previously, the basis of molecular dynamics is that the nuclei of atoms are approximated as classical particles, and as such their dynamics can be simulated using Newton's Second Equation of Motion. However, as the particles in a molecular dynamics simulation are under the influence of a continuous potential and their motions are inherently coupled together (i.e. it is a many-body problem), the equations cannot be solved analytically.

As such, the equations of motion must be solved numerically and a number of algorithms have been developed to perform this task, all based on the concept of *discretising* the integration into small time steps. Consider a set of particles, which are found at positions  $\mathbf{r}_0$  at time  $t$  (for the remainder of this section, subscripts on labels corresponding to positions, velocities etc. (e.g.  $\mathbf{r}_n$ ) denotes this property after  $n$  time steps). Their positions  $\mathbf{r}_1$  after a small time step  $\Delta t$  can be determined by the following Taylor expansion:

$$\mathbf{r}_1 = \mathbf{r}_0 + \frac{\partial \mathbf{r}_0}{\partial t}(\Delta t) + \frac{1}{2} \frac{\partial^2 \mathbf{r}_0}{\partial t^2}(\Delta t)^2 + \frac{1}{6} \frac{\partial^3 \mathbf{r}_0}{\partial t^3}(\Delta t)^3 + \dots \quad (\text{Eq 3.3})$$

The velocities  $\mathbf{v}_0$ , accelerations  $\mathbf{a}_0$  and hyper-accelerations  $\mathbf{b}_0$  (also known as the jerk) of the particles are expressed here as, respectively, the first, second and third derivatives of the position with respect to time. In addition, higher derivatives of the position (the affectionately and somewhat facetiously named jounce (or snap), crackle and pop for the fourth, fifth and sixth derivatives of position respectively) are also present in higher terms of the expansion. However, these can almost always be ignored and so the expansion is usually truncated at this point. The expansion can therefore be simplified to:

$$\mathbf{r}_1 = \mathbf{r}_0 + \mathbf{v}_0(\Delta t) + \frac{1}{2} \mathbf{a}_0(\Delta t)^2 + \frac{1}{6} \mathbf{b}_0(\Delta t)^3 + \mathcal{O}(\Delta t)^4 \quad (\text{Eq 3.4})$$

Just as the above expression allows us to calculate the positions of the particles one time step forward in time, the positions of the particles one time step backwards in time can also be calculated simply by multiplying each  $\Delta t$  term by  $-1$ :

$$\mathbf{r}_{-1} = \mathbf{r}_0 - \mathbf{v}_0(\Delta t) + \frac{1}{2} \mathbf{a}_0(\Delta t)^2 - \frac{1}{6} \mathbf{b}_0(\Delta t)^3 + \mathcal{O}(\Delta t)^4 \quad (\text{Eq 3.5})$$

All of the integration algorithms used in molecular dynamics codes assume that the positions, velocities and accelerations of the particles in a simulation can be estimated in this way. In general, the smaller the value of  $\Delta t$ , the more ‘realistic’ the trajectory (up until the limit of precision in the calculation of the forces). However, a smaller time step means that more iterations of the molecular dynamics integration algorithm must be calculated in order to

simulate the time scale over which a meaningful chemical or physical process takes place. Generally, the time step is chosen to be shorter than the fastest dynamic process of interest in the simulation (for example, the vibrations of particular chemical bonds).

There are three commonly used integration algorithms implemented within molecular dynamics codes, each with its own sets of advantages and disadvantages. The first such algorithm is the *Verlet* algorithm, which gives a framework in which the positions and accelerations (but not the velocities) of the simulated atoms after a time step  $\Delta t$  can be computed. The Verlet algorithm is obtained simply by adding the two above equations together to obtain the expression:

$$\mathbf{r}_1 = 2\mathbf{r}_0 - \mathbf{r}_{-1} + \mathbf{a}_0(\Delta t)^2 + \mathcal{O}(\Delta t)^4 \quad (Eq\ 3.6)$$

All of the terms with  $\Delta t$  raised to an odd power are therefore cancelled out, meaning that although the  $\mathbf{v}_0$  and  $\mathbf{b}_0$  terms have disappeared from the expression it is still correct to third-order in  $\Delta t$ . The acceleration of the particles can be calculated from the forces (i.e. the negative of the potential function):

$$\mathbf{a}_i = \frac{\mathbf{F}_i}{m} = -\frac{1}{m} \frac{dV}{d\mathbf{r}_i} \quad (Eq\ 3.7)$$

The accelerations must be computed at each time step, which allows the positions of the particles to be propagated to generate a trajectory. The Verlet algorithm is very easy to implement, is computationally inexpensive and is quite accurate, meaning that it has been very popular in molecular dynamics codes. In addition, it allows for time-reversibility. However, it has a number of disadvantages, the principal of which is that the velocities are not explicitly calculated, which are needed for calculating the kinetic energy of the particles (and therefore the checking of the conservation of total energy during a simulation). Velocities can be estimated using the position terms within the mean value theorem:

$$\mathbf{v}_0 = \frac{\mathbf{r}_1 - \mathbf{r}_{-1}}{2\Delta t} + \mathcal{O}(\Delta t)^2 \quad (Eq\ 3.8)$$

However, the local error in this expression is of order  $\mathcal{O}(\Delta t)^2$ , as opposed to  $\mathcal{O}(\Delta t)^4$  for the integration algorithm itself. In addition, the above estimation only gives the velocities at time  $t$  and not at time  $t + \Delta t$ , meaning the velocities are constantly one step out of sync with the positions. The velocities at time  $t + \Delta t$  can however be approximated, at further cost to the accuracy of the propagation.

As a result, a number of different variants have been created to overcome the issues of the Verlet algorithm. One of the most commonly used algorithms used in lieu of the Verlet method is the *Leapfrog* algorithm. In the Leapfrog method, the Taylor expansions forward and backwards in time are performed with half-time steps rather than full-time steps, and the expressions are subtracted from each other instead of added. Velocities can also be obtained by an analogous expansion of the Taylor series. This gives the expressions:

$$\mathbf{r}_1 = \mathbf{r}_0 + \mathbf{v}_{\frac{1}{2}}\Delta t \quad (Eq\ 3.8)$$

$$\mathbf{v}_{\frac{1}{2}} = \mathbf{v}_{-\frac{1}{2}} + \mathbf{a}_0\Delta t \quad (Eq\ 3.9)$$

This algorithm is also correct to third order, and this time the velocities are calculated explicitly within the algorithm, which is useful for defining specific thermodynamic ensembles. However, the positions and velocities are not known at the same time - they are out-of-sync by half a time step.

A third algorithm allows for explicit computation of the positions, velocities and acceleration. This algorithm, known as the *Velocity Verlet* algorithm, is a modified Verlet algorithm and is arguably the most popular used in molecular dynamics calculations. The Velocity Verlet algorithm is computed as a series of steps:

1. Calculate the positions at time  $t + \Delta t$  using the same expression as for the standard Verlet algorithm:

$$\mathbf{r}_1 = \mathbf{r}_0 + \mathbf{v}_0(\Delta t) + \frac{1}{2}\mathbf{a}_0(\Delta t)^2 \quad (Eq\ 3.10)$$

2. Calculate the velocities at time  $t + \frac{1}{2}\Delta t$ :

$$\mathbf{v}_{\frac{1}{2}} = \mathbf{v}_0 + \frac{1}{2}\mathbf{a}_0\Delta t \quad (Eq\ 3.11)$$

3. Derive the forces and accelerations from the expression, again in an analogous way to the initial Verlet algorithm:

$$\mathbf{a}_1 = \frac{\mathbf{F}_1}{m} = -\frac{1}{m} \frac{dV}{d\mathbf{r}_1} \quad (Eq\ 3.12)$$

4. Finally, the velocities are computed at one full time step, and the system is ready to advance to the next time step of the procedure:

$$\mathbf{v}_1 = \mathbf{v}_{\frac{1}{2}} + \frac{1}{2}\mathbf{a}_1\Delta t \quad (Eq\ 3.13)$$

Using the Velocity Verlet algorithm, we now have a scheme in which the positions, velocities and accelerations at  $t + \Delta t$  can be calculated. The algorithm itself is as accurate as the initial Verlet algorithm, but the velocities are known explicitly, which makes calculating properties such as kinetic energy and defining thermodynamic ensembles much more straight forward. In addition, as the algorithm is balanced, its form remains the same when reversing the sign of the time coordinate  $t$  - thus simulations performed with the velocity Verlet scheme are, in theory, completely reversible.

### 3.1.3. Calculating properties in MD Simulations

#### 3.1.3.1. The Microcanonical Ensemble (NVE)

A ‘natural’ MD simulation will generate a *microcanonical ensemble* of states, in which the number of particles  $N$ , the volume of the simulation box  $V$  and the energy of the system  $E$  remain constant. As a result, such an ensemble is often referred to as the *NVE* ensemble. In this scenario, the temperature and pressure will fluctuate over the course of the simulation.

The total energy of an  $N$  particle simulation is simply the sum of the kinetic and potential energies:

$$E_{total} = E_{kinetic} + E_{potential} = \sum_{i=1}^N \frac{1}{2} m_i v_i^2 + V(\mathbf{r}_i) \quad (Eq\ 3.14)$$

As previously discussed, the potential can be evaluated at varying levels of theory, from forcefield techniques to highly accurate and expensive *ab initio* methods. It should be noted that as the atomic forces can only be calculated with finite precision and the MD integration is discretised into small time-steps, the total energy is not exactly constant even in an *NVE* simulation. However, this numerical error can be kept under control by using a small integration time step, and monitoring the drift in the total energy over the course of the simulation.

The absolute temperature  $T$  of the system under scrutiny is proportional to the average of the kinetic energy  $\langle E_{kinetic} \rangle$ :

$$T = 2 \frac{\langle E_{kinetic} \rangle}{n_{df} k_B} \quad (Eq\ 3.15)$$

where  $k_B$  is the Boltzmann’s constant and  $n_{df}$  corresponds to the number of degrees of freedom.  $n_{df}$  is computed from the expression:

$$n_{df} = 3N - n_{con} \quad (Eq\ 3.16)$$

In the above expression,  $n_{con}$  is the number of constraints imposed upon the system. In a standard molecular dynamics simulation,  $n_{con} = 3$  corresponding to the conservation of linear momentum. However, additional constraints (such as those on bond lengths, angles etc.) that limit the total number of degrees of freedom must also be included in this term. The pressure of the system can also be calculated using the expression:

$$p = \frac{Nk_B T}{V} + \frac{1}{DV} \left\langle \sum_{i=1}^N \mathbf{r}_i \cdot \mathbf{F}_i \right\rangle \quad (Eq\ 3.17)$$

where  $V$  is the volume of the computational box and  $D$  corresponds to the dimensionality of the system under scrutiny (usually equal to 3). This second part of this is known as the *pressure virial*. It is worth noting here that the virial cancels to the simple equation of state for a *perfect gas* if the simulated particles are non-interacting.

3.1.3.2. Non-Natural Ensembles

Name	Symbol	Equilibrium	N	P	V	T	E	$\mu$
<i>Micro-Canonical</i>	$NVE$	S maximum	X		X		X	
<i>Canonical</i>	$NVT$	A minimum	X		X	X		
<i>Isothermal-Isobaric</i>	$NpT$	G minimum	X	X		X		
<i>Grand-Canonical</i>	$\mu VT$	pV maximum			X	X		X

Figure 3.i: Table summarising the various conserved quantities for four different ensembles

Despite  $NVE$  being the natural ensemble generated by a molecular dynamics simulation, it is possible to produce other statistical ensembles, such as the *canonical* ( $NVT$ ), the *isothermal-isobaric* ( $NpT$ ) and the *grand-canonical* ( $\mu VT$ ) ensembles, by modifications to the particles at each time step. This is extremely beneficial, as true chemical and physical processes often rely on constant temperature and pressure regimes and very rarely feature constant energy over the course of a dynamic process.

The first method utilised to control temperature and pressure in molecular dynamics simulations was to simply apply instantaneous corrections to these variables by simply rescaling until a target equilibrium value was reached. However, such techniques detrimentally perturb the dynamics of the simulation and do not generate a true canonical ensemble. The best way to control the macroscopic properties during a simulation is to couple the system it to a *heat-bath* (to control temperature) and a *pressure-bath* (to control pressure). These algorithms, known as *thermostats* and *barostats*, allow both the regulation of the temperature and pressure of the system and the generation of the correct thermodynamic ensemble.



3.1.3.3. Thermostats

Numerous thermostats have been developed over the years. The first such algorithm, the *Andersen thermostat*, involved rescaling the velocities of a set of particles by a Maxwell distribution at random time intervals.<sup>[10]</sup> This allowed the generation of a true *NVT* ensemble in a molecular dynamics simulation for the first time, allowing real chemical processes to be scrutinised using the technique. However, it could only be used to scrutinise time independent processes, and as such most interesting chemical processes could not be analysed in this way. In addition, the algorithm suffered from very poor efficiency and it did not have an associated conserved quantity which could be monitored over the course of the simulation.

Since the formulation of the Anderson thermostat, numerous other algorithms have been developed to allow the generation of true canonical ensembles for time dependent processes which are efficient and reliable. For example, one of the simplest and widely used is the *Berendsen thermostat*,<sup>[11]</sup> which rescales the velocities of the system by a scaling factor  $\lambda$  after every time step  $\Delta t$ :

$$\lambda = \left[ 1 + \frac{\Delta t}{\tau} \left( \frac{T_0}{T} - 1 \right) \right]^{\frac{1}{2}} \quad (Eq\ 3.18)$$

where  $T$  is the instantaneous temperature,  $T_0$  is the desired temperature, and  $\tau$  is a relaxation constant. This simple scheme has found widespread use, however it fails to produce a canonical ensemble, especially in very small systems.

Arguably the most widely used (and indeed the algorithm used predominantly in this work) is the Nosé-Hoover method.<sup>[12,13]</sup> In this method, the Equations of Motion are modified slightly:

$$\frac{d\mathbf{v}_t}{dt} = \frac{\mathbf{F}_t}{m} - \zeta_t \mathbf{v}_t \quad (Eq\ 3.19)$$

where  $\zeta_t$  is a frictional coefficient given by the differential equation:

$$\frac{d\zeta_t}{dt} = \frac{1}{Q} n_{df} k_B (T_t - T_{ext}) \quad (Eq\ 3.20)$$

In this expression,  $T_t$  is the instantaneous temperature of the system at time  $t$ ,  $T_{ext}$  is the requested temperature of the system and  $n_{df}$  is once again the number of degrees of freedom in the system. The term  $Q$  is the ‘effective mass’ of the thermostat, and is given by the expression:

$$Q = n_{df} k_B T_{ext} \tau_t^2 \quad (Eq\ 3.21)$$

where  $\tau_t$  is a constant used to determine the time-scale of the temperature fluctuation in the thermostat. The value of  $\tau_t$  normally falls between 0.5 and 2.0 ps – too high a value leads to very ineffective temperature control, whereas too low a value will cause the system to simply oscillate about its equilibrium value.

This formalism produces canonical ensembles for most systems, however in certain small systems (an often quoted example is a chain of harmonic oscillators), Nosé-Hoover dynamics be *non-ergodic* and therefore not generate a correct *NVT* ensemble. A modification to the original formalism involving coupling the thermostat to another, or a chain of other Nosé-Hoover thermostats, allows for the generation of a true canonical ensemble even in these small systems. Each thermostat is regulated by its own thermostat, which in turn is regulated by another thermostat, and in the limit of an infinite chain of thermostats produces entirely ergodic dynamics. Although many argue that this ‘spoils’ the mathematical simplicity of the Nosé-Hoover method, even small chains of such thermostats can produce almost perfectly ergodic dynamics in any system.<sup>[14]</sup>

Another type of thermostat used in this work is the recently developed *Canonical Sampling through Velocity Scaling (CSVR)* thermostat.<sup>[15]</sup> This method involves multiplying all of the velocities of the particles by a factor  $\alpha$  which is calculated by enforcing the total kinetic energy be equal to a selected value of kinetic energy.

$$\alpha = \sqrt{\frac{E_{kin}^{TARGET}}{E_{kin}^{ACTUAL}}} \quad (Eq\ 3.22)$$

This is different to simple velocity scaling as rather than using the average value of the kinetic energy, instead a target value  $E_{kin}^{TARGET}$  is selected using a stochastic procedure with the aim of producing a true canonical ensemble. Between the rescaling steps, the system is evolved normally and, assuming that the corresponding evolution is ergodic within the microcanonical ensemble, produces an overall scheme of ergodic dynamics within the canonical ensemble.

#### 3.1.3.4. Barostats

Just as the temperature of the system may be regulated with a thermostat, so too can the pressure be controlled with a barostat. This is carried out in a very similar manner to that of the thermostat, only this time a modification is made to the equations of motion allowing the pressure of the simulation to be maintained over its duration. There are two approaches for this – one allowing only for isotropic box changes, and another for anisotropic box changes.

The former approach is employed by using scaling methods very similar to the thermostats previously described. For example, in the *Berendsen barostat*, the atomic coordinates and box vectors are simply rescaled at every step of a calculation.<sup>[11]</sup> This works in a very similar fashion to the Berendsen thermostat, in that a scaling factor is applied to the simulation cell at each time step:

$$\mu = \left[ 1 + \frac{\beta \Delta t}{\tau} (P_0 - P) \right]^{\frac{1}{3}} \quad (Eq\ 3.23)$$

where  $P$  is the instantaneous pressure,  $P_0$  is the desired pressure,  $\tau$  is a relaxation constant and  $\beta$  is the isothermal compressibility. An anisotropic extension to the Berendsen thermostat does exist, however much like the Berendsen thermostat, such schemes do not

generate the correct ensemble and more involved schemes are required to produce the correct dynamics.

Another widely used implementation of pressure control is the *Andersen barostat*,<sup>[10]</sup> which unlike the Berendsen thermostat is not at all similar to its thermostat namesake. The Andersen thermostat is better compared to the Nosé-Hoover thermostat, in that it evokes the use of an extra degree of freedom in the form of a fictitious ‘mass’ parameter. In the Andersen barostat, the simulation cell is coupled to a ‘pressure-bath’, which replicates the action of a mechanical piston applying pressure to the system of interest. The volume of the cell  $V$  is regarded as the coordinate of the piston and so too is treated as a free parameter. The piston has a mass value  $Q$ , which dictates the rapidity of simulation cell fluctuations. Small values of the piston mass lead to very rapid changes in the box size, whereas a large mass leads to only small adjustments to the volume. The Nosé-Hoover<sup>[16]</sup> and Martyna-Tuckerman-Klein<sup>[17]</sup> barostats are widely used modifications to the Andersen barostat.

In order for shape and size changes to the box not to be isotropic, the Parrinello-Rahman modification to the Andersen barostat is required.<sup>[18,19]</sup> When studying solid systems, anisotropic changes are generally required in order to observe phase changes, study transitions and to simulate the formation of defects and internal surfaces. In the Parrinello-Rahman scheme, the simulated system is once again coupled to an external pressure-bath and controlled by a fictitious mass parameter, however in this scheme the cell may adopt an arbitrary shape which can be described by the independent cell parameters  $a$ ,  $b$  and  $c$ . This allows for the simulation of directional pressure or strain, as well as for anisotropic shape changes to the simulation cell.

Both the Andersen barostat and the Parrinello-Rahman modification produce isoenthalpic-isobaric ensembles ( $NpH$ ). Combining these barostats with a numerical thermostat allows for the generation of a true isothermal-isobaric ( $NpT$ ) ensemble.

## 3.2. Geometry Optimisations

### 3.2.1. Introduction to Geometry Optimisation

*Geometry optimisation*, also called *energy minimisation* or *structural relaxation*, is the process of determining an arrangement of atoms within a chemical system which corresponds to a minimum on its associated potential energy surface, according to the level of theory used to describe the simulated material. Such configurations define the (meta)stable states of a system, and are physically meaningful as they correspond to atomic arrangements for a particular composition of atoms that can possibly, or already do exist, in the natural world.<sup>[2]</sup>

Geometry optimisation procedures can be applied to a wide range of simulated systems, ranging from the geometry of a single molecule or ion to the arrangement of atoms in a periodic condensed phase. The work presented within this thesis deals exclusively with the latter problem, although the basis behind the methods described is exactly the same for all types of simulated chemical system.

The crucial idea behind geometry optimisation is that, given a set of vectors corresponding to the positions of the atoms  $\mathbf{r}$ , one can define the energy as a function of the atomic coordinates  $E(\mathbf{r})$ . The problem then becomes purely mathematical, in that one must now find the values of  $\mathbf{r}$  which minimise the function  $E(\mathbf{r})$ . When located at an energy minimum, the first derivative of the energy is equal to zero, and the matrix of the second derivative (the *Hessian* matrix) is *positive definite* – i.e. all of its eigenvalues are positive.

An array of methods has been developed to tackle such problems, two of which are briefly discussed in the below section – the *Steepest Descent* method, and the more advanced *Conjugate Gradient* method. The latter is the method principally used in this work for structural relaxations. It is worth mentioning here that various other methods of geometry optimisation exist, many of which are much more sophisticated. A number of these methods utilise higher derivatives of the function to be optimised, for example the Newton-Raphson method, which expands the function to second order.

### 3.2.2. Steepest Descent method

*Steepest descent* methods involve moving the system in the direction of the negative gradient vector  $\mathbf{g}$ , which points towards the direction in which the function is most rapidly increasing. Using this negative gradient, one can compute a new position based on the old configuration:

$$\mathbf{r}_{n+1} = \mathbf{r}_n - \alpha \mathbf{g}_n \quad (\text{Eq 3.24})$$

where  $\alpha$  is a parameter that can be adjusted accordingly. If  $\alpha$  is chosen to be small enough, the gradient  $\mathbf{g}_n$  will always be larger than or equal to  $\mathbf{g}_{n+1}$ , meaning that the system has moved against the gradient of the function. If the gradient vector starts to increase again, the process restarts and a new negative gradient is computed from this new position, perpendicular to the original path. This process iterates until the nearest local minimum is reached.

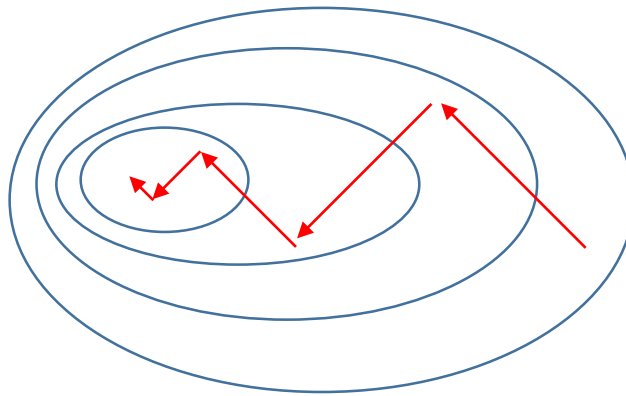


**Figure 3.ii:** Schematic of the *steepest descent* method, showing the movement of the system along the negative of the gradient vectors, changing paths to perpendicular vectors five times over the procedure before finding the associated minimum. Image inspired by figure in reference 2.

This is a very simple and effective technique to reach the minimum values of certain functions. However, the steepest descent method does have a number of limitations. Firstly, the true

position of the minimum is never actually reached, as the rate of convergence decelerates as the algorithm converges upon the minimum of the function. Secondly, the zig-zagging nature of the optimisation path is highly inefficient, and can cause problems in systems with complex energy landscapes, particularly those featuring long and narrow ‘valleys’.

### 3.2.3. Conjugate Gradient method

*The conjugate gradient* method can be thought of as an improvement to the steepest descent method. The very first step is identical to the steepest descent method, in that the system moves along the negative gradient vector. However, subsequent searches are based along lines that contain some component of previous searches, i.e. they are ‘conjugate’ to previous directions.

$$\mathbf{d}_n = -\mathbf{g}_n + \beta_n \mathbf{d}_{n-1} \quad (Eq\ 3.25)$$

$\mathbf{d}_n$  corresponds to the direction of travel in the current path, whereas  $\mathbf{d}_{n-1}$  denotes the search direction in the previous step.  $\beta$  is a value which can be defined in a number of ways, including using the Fletcher-Reeves method, the Polak-Ribiere method and the Hestenes-Stiefel method. For practical reasons, the Polak-Ribiere parameterisation is the method that is most often used.<sup>[2]</sup> Regardless of the method of its parameterisation, the  $\beta$  parameter removes the mandatory requirement that the next search direction must be orthogonal to the previous one, significantly increasing the efficiency of the algorithm. As with the steepest descent method, the algorithm must iterate until the local minimum is reached.

The conjugate gradient method is not without its problems, however. Most significantly, the conjugate property only holds true for purely quadratic systems, and so occasionally the procedure must be restarted by periodically setting  $\beta$  to 0. However, convergence time is significantly decreased by using the conjugate gradient method, and as such is much more prominently used than the steepest descent method in computational materials science.

References – Chapter 3

1. D. C. Rapaport, *The Art of Molecular Dynamics Simulation*, Cambridge University Press, 2<sup>nd</sup> Edition, 2004
2. F. Jensen, *Introduction to Computational Chemistry*, John Wiley & Sons, 2<sup>nd</sup> Edition, 2011
3. D. Young, *Computational Chemistry: A Practical Guide for Applying Techniques to Real World Problems*, John Wiley & Sons, 2<sup>nd</sup> Edition, 2001
4. D. Frenkel and B. Smit, *Understanding Molecular Simulation: From Algorithms to Applications*, Academic Press, 2<sup>nd</sup> Edition, 2001
5. E. de Miguel and G. Jackson, *J. Chem. Phys.*, 2006, **125**, 164109
6. [http://www.grs-sim.de/cms/upload/Carloni/Tutorials/FMCP/Thermostats\\_and\\_Barostats.pdf](http://www.grs-sim.de/cms/upload/Carloni/Tutorials/FMCP/Thermostats_and_Barostats.pdf)  
 “Molecular Dynamics meets the Physical World: Thermostats and Barostats” - Last Accessed 28/09/2017
7. M. P. Allen, D. J. Tildesley, *Computer Simulation of Liquids*, Clarendon Press, 1989
8. B. J. Alder and T. E. Wainwright, *J. Chem. Phys.*, 1959, **31**, 459-466
9. A. Rahman, *Phys. Rev.*, 1964, **136**, A405-A411
10. H. C. Andersen, *J. Chem. Phys.*, 1980, **72**, 2384-2393
11. H. J. C. Berendsen, J. P. M. Postma, W. F. van Gunsteren, A. DiNola and J. R. Haak, *J. Chem. Phys.*, 1984, **81**, 3684-3690
12. S. Nosé, *Mol. Phys.*, 1984, **52**, 255-268
13. S. Nosé, *J. Chem. Phys.*, 1984, **81**, 511-519
14. G. J. Martyna, M. L. Klein and M. Tuckerman, *J. Chem. Phys.*, 1992, **97**, 2635-2643
15. G. Bussi, D. Donadio and M. Parrinello, *J. Chem. Phys.*, 2007, **126**, 14101
16. W. G. Hoover, *Phys. Rev. A.*, 1986, **34**, 2499-2500
17. G. J. Martyna, D. J. Tobias and M. L. Klein, *J. Chem. Phys.*, 1994, **101**, 4177-4189
18. M. Parrinello and A. Rahman, *Phys. Rev. Lett.*, 1980, **45**, 1196-1199
19. M. Parrinello and A. Rahman, *J. Appl. Phys.*, 1981, **52**, 7182-7190



## Chapter 4

### Methodology II

***“One should always be a little improbable”***

– Oscar Wilde (1854-1900), *Phrases and Philosophies for the Use of the Young*, 1894

#### 4.1. Introduction to Rare Events

Despite major advancements in both computational techniques and the development of computer hardware and software, there still exists a huge number of intrinsic problems resulting from the difficulties of carrying out computer simulations of physical systems.

One of the primary reasons for this results from the time-scales employed in molecular dynamics simulations. Integration time-steps must be commensurate to the time-scales of the fastest events of interest in a simulation. This is generally of the order of femtoseconds, and as such molecular dynamics simulations must be run for thousands or millions of steps to simulate a meaningful time period for most dynamic processes. Given current hardware and methods, simulations can be run in the order of nanoseconds using classical potentials, and in the order of picoseconds for advanced *ab initio* methods. Events that occur over time-scales longer than this (of which there are very many) are therefore impossible to observe in this way.

Secondly, systems studied with simulation techniques such as molecular dynamics often feature very complex energy landscapes with multiple activation barriers, local energy minima and saddle points. Overcoming such barriers generally have an extremely low probability and as such systems tend to linger within local energy minima for long periods of time. A standard molecular dynamics simulation will therefore fail to simulate much of the phase space of a given system over a plausible simulation time scale. This is known as the *rare event problem* and most dynamic physical and chemical processes (reactions, phase transitions, protein folding, molecular docking etc.) are rare (i.e. non-equilibrium) events.

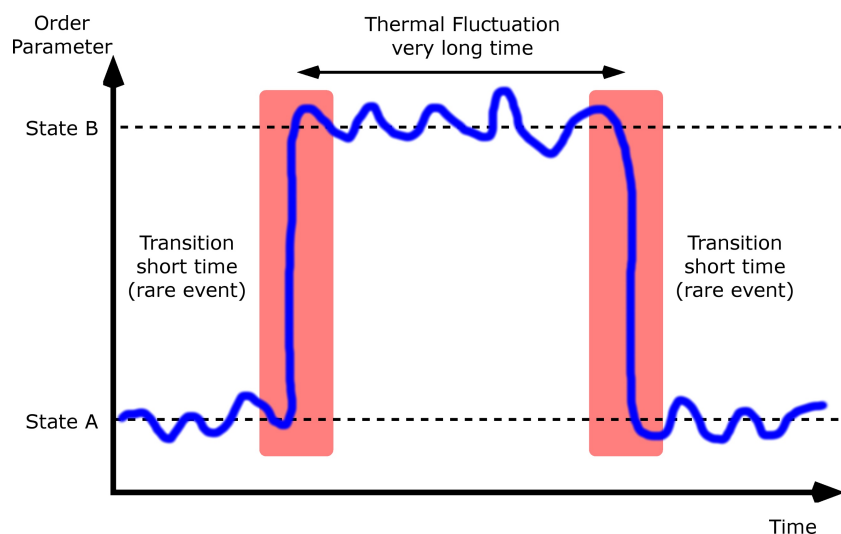


**Figure 4.i:** Schematic showing the concept of a ‘rare event’ – in this case, a transition between two states A and B. The system spends most of its time in basins A and B, fluctuating due to thermal energy, and transitions between basins A and B are infrequent and very rapid. Almost all interesting processes in chemistry and physics are rare events, however they are notoriously difficult to simulate.<sup>[1]</sup>

An example of a rare event postulated by Dellago *et al.* considers a single water molecule, which has an approximate life time of ten hours before dissociating into a hydronium cation and a hydroxide anion.<sup>[2]</sup> To observe the ionisation of this single water molecule in an MD simulation with each time step equating to 1 fs, one would have to simulate to the order of  $10^{18}$  steps in order to witness just ONE dissociation event. If each simulation step were to take 1 s to compute, the transition would not be seen for  $3 \times 10^{10}$  years – about twice as long as the current estimated age of the universe.

Clearly, this is impossible for current computational systems, and extrapolating this to larger systems would require even longer preposterous time scales to observe any events of interest. As such, some acceleration is required to observe *rare events* in the simulations of physical systems. Simply increasing the temperature or time-step utilised in the simulation

works to some extent, however this often spoils the true dynamics of the system. To combat this, numerous enhanced sampling techniques have been developed, which aim to allow efficient sampling of the phase space and/or the collection of ‘true’ dynamics. Two of the more recent techniques are used in this work: *metadynamics*, which can be used to quickly sample the phase space of a physical system, and *transition path sampling*, which can be used to accurately simulate rare events in exquisite detail.

## 4.2. Metadynamics

The discussion in section 4.2 relies on the following references.<sup>[3-6]</sup>

### 4.2.1. Introduction to Metadynamics

Metadynamics is a technique used to rapidly explore potential energy surfaces in the space of a number of reaction coordinates, known as *collective variables* (CVs). The technique was first described in 2002 by Laio and Parrinello as an extension to standard molecular dynamics and is designed to enable a simulation to quickly escape from free energy minima.<sup>[3]</sup>

In a metadynamics simulation, the dynamics in the space of the chosen collective variable(s) are biased by a ‘history-dependent’ potential. This potential is constructed as a sum of Gaussian functions along the trajectory in the collective variable space. As the system evolves, more Gaussian functions cumulatively fill the local energy minimum, discouraging the system from returning to its previous state. Filling the potential energy minima with Gaussians in this way has been described as analogous to filling holes with sand or water. Eventually, the system is forced into a new basin of attraction by overcoming the much reduced activation barrier separating the two energy wells. As such, the underlying potential energy surface can be quickly explored and the system is prohibited from returning to an already visited state in the collective variable space.

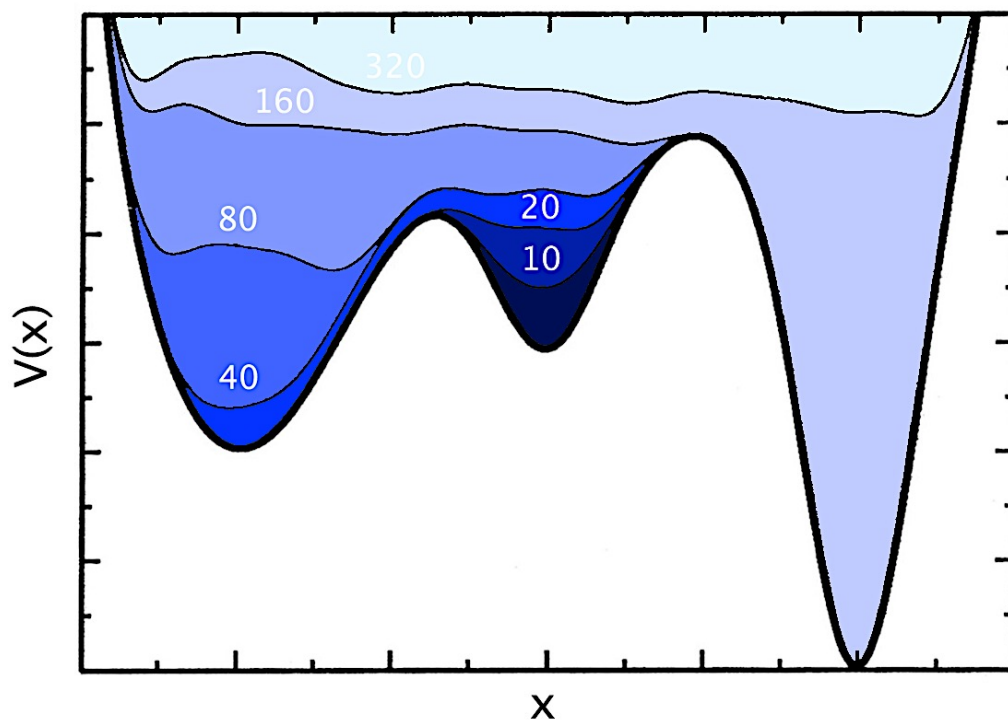


**Figure 4.ii:** An example of a one-dimensional free energy surface showing the progression of a metadynamics simulation. This hypothetical simulation begins at the metastable basin in the centre of the plot. The lines correspond to the time evolution of the sum of the Gaussian functions used to construct the bias potential. Eventually, the system is forced out of the initial basin and explores other free energy minima in the space of the collective variable  $x$ .<sup>[3]</sup>

In order for metadynamics to successfully sample the phase space of a system, it is imperative that the choice of collective variable used be appropriate. The collective variable must be able to distinguish between the initial, final and intermediate states of the system, and it must be able to describe the events of importance that occur in a system appropriately. The choice of the collective variable also affects the efficiency and quality of the calculation. In addition, tuning the shape of the Gaussian functions deposited on the potential energy surface is also important. For example, the width of the Gaussian must be larger than the thermal fluctuations in the system, but small enough to acquire good resolution and avoid overfilling of the energy minima. The Gaussian height can then be chosen depending on the width of the Gaussian, and the magnitude of the energy barriers of interest in the system.

In addition to ‘standard’ metadynamics, a number of modified techniques have been developed. In *well-tempered metadynamics*, the height of the Gaussian function is periodically rescaled to ensure that the bias converges more smoothly.<sup>[7]</sup> In *adaptive-Gaussian metadynamics*, the widths of the Gaussian functions are allowed to vary in order to more efficiently sample basins of attraction of different breadths.<sup>[8]</sup> In this work, the standard form of metadynamics and the *well-tempered* and *adaptive-Gaussian* modifications have been extensively utilised. In addition, one particular scheme of metadynamics developed by Martonák *et al* involves using the simulation cell as the collective variable.<sup>[9-11,13]</sup> This scheme too has found extensive use in this work.

#### 4.2.2. The Choice of the Collective Variable

Arguably the most involved step in a metadynamics calculation is determining a suitable reaction coordinate to distinguish between the states of interest in a calculation. An appropriate choice of reaction coordinates, known as *collective variables*, has a huge effect on the efficiency of the calculation, and the accessibility of transition and intermediate states. The aim is to identify a set of collective variables of interest that correctly describe the system which are intrinsically difficult to sample, as they are separated by energy barriers that are unlikely to be surmounted within normal molecular dynamics. Failure to determine a set of collective variables that does not fully describe the system of interest can lead to poor sampling of the phase space of the system, as well as incorrect characterisation of energy barriers and pathways of interest.

Occasionally, choosing an appropriate collective variable can be straight forward – for example, in a simulation of bond formation and breaking, an obvious choice of collective variable would be the distance between the two atomic sites of interest. However, in most calculations, the choice of collective variables is far from trivial and there is no *a priori* recipe for their deduction. Collective variables must therefore be determined using chemical intuition, as well as trial and error. As a guideline, collective variables should satisfy the following three properties:

- i. The collective variable should be able to distinguish between initial and final states of the calculation and, if appropriate, all of the necessary transition and intermediate states;
- ii. The choice of the collective variable must be able to describe all of the events of importance that are relevant in a transformation pathway, particularly those that are 'slow';
- iii. The number of collective variables should not be too large – otherwise, the calculation will become prohibitively expensive and will take a very long time to characterise the underlying free energy surface.

It is, however, immediately apparent that points ii. and iii. can often be mutually exclusive, as characterising all of the necessary reaction coordinates to accurately describe a system may indeed invoke a large number of collective variables. Efforts are made, therefore, to find collective variables that are indeed truly 'collective' and can characterise the process under scrutiny using the smallest number of variables possible.

Missing a relevant component of a collective variable within a simulation can lead of significant over-estimation of the energy barriers or even complete failure to sample the relevant pathways. One way to visualise this is to consider a Z shaped two dimensional free energy profile. If metadynamics is applied only to one of the collective variables, then a transition will be observed when the height of the Gaussians is much greater than the barrier height, thereby significantly overestimating the activation energy. This behaviour means that the true underlying free energy surface will never be accurately ascertained.

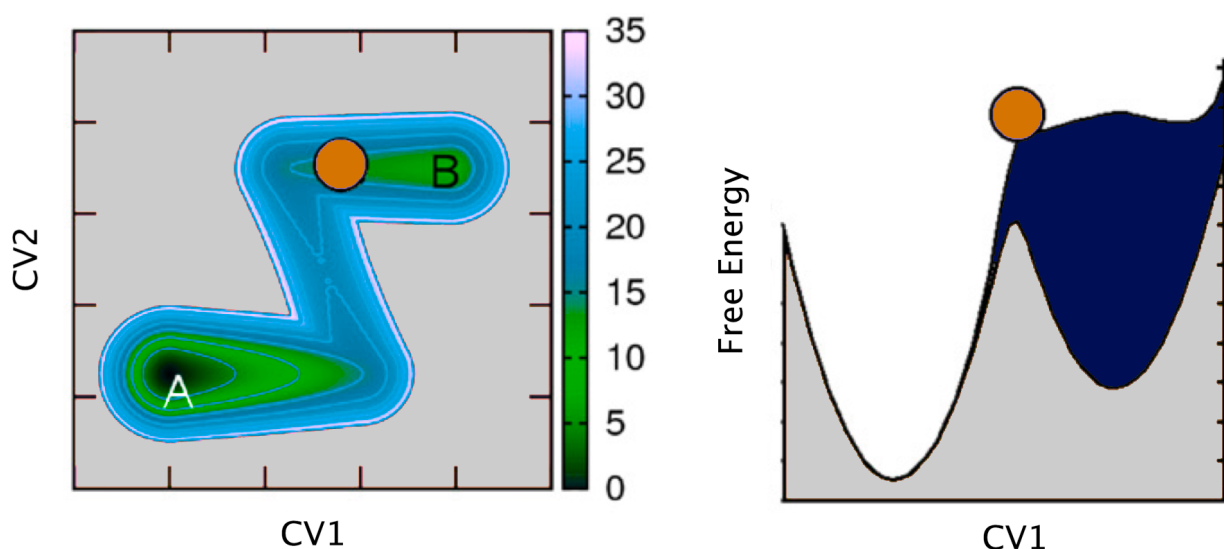


**Figure 4.iii:** A hypothetical Z-shaped potential in the space of two collective variables (left). Imagine a scenario where metadynamics is applied to this system, however only one of the collective variable are biased (“CV1”) while the second (“CV2”) is neglected. A strong hysteresis will have to be induced before observing a transformation. This leads to significant overfilling of the initial minimum and overestimation of the energy barrier (right).<sup>[4]</sup>

As mentioned previously, *a priori* identification of collective variables is often not possible, however the choice of collective variables can often be checked *a posteriori*. Analysing the deposition of Gaussian functions during a calculation can identify lacking relevant reaction coordinates, as simulations with poorly described collective variables tend to show highly hysteretic behaviour when reconstructing the underlying free energy surface. If all of the relevant collective variables are accounted for, the free energy should grow ‘smoothly’ and converge when all of the different basins have been fully explored.

Quantities used as collective variables include, but are not limited to:

- **Geometric variables**, such as bond distances, angles and torsions between atoms or groups of atoms;

- **Coordination numbers**, including distance cut-offs, or more advanced switching functions, as well as Steinhardt parameters;<sup>[12]</sup>
- The **shape and dimensions of the simulation cell** itself;
- The **potential energy** of the system;
- **Path specific parameters**, such as using the root mean squared displacement (RMSD) or construction of periodic minimal surfaces to distinguish between complex states of interest in a one-dimensional way;
- **Normal modes**, by preferentially sampling in the direction of ‘slow’ or ‘soft’ modes within a system.

Within this work, a number of different collective variables have been used for metadynamics calculations, including coordination number, simulation box parameters, distances between atomic sites and Steinhardt parameters. Whilst the implementation of the calculations varies depending on the system and the collective variable utilised, a very general description of the method is given below.

#### 4.2.3. Implementations of Metadynamics

##### 4.2.3.1. ‘Standard’ Metadynamics

During a metadynamics simulation, a history dependent bias potential composed of Gaussian functions is constructed within the space of the chosen collective variable(s)  $S(x)$ . The sum of these Gaussian functions, which are added at every  $\tau$  molecular dynamics steps in the space of  $d$  collective variables, gives the *external* or *metadynamics potential*  $V$  acting on the set of collective variables at time  $t$ :



$$V(S(x), t) = \sum_{k\tau < t} \omega(k\tau) \exp\left(-\sum_{i=1}^d \frac{[S(x) - S(x(k\tau))]^2}{2\sigma_i^2}\right) \quad [Eq 4.1]$$

where  $\omega$  is the height of the Gaussian function and  $\sigma$  is the width of the Gaussian function. A suitable Gaussian width  $\sigma$  must be chosen for each collective variable. Once again, there is no *a priori* recipe for determining the ‘correct’ values to use for a particular system. As eluded to previously, the choice of these parameters (as well as the frequency of Gaussian deposition) greatly affects the efficiency and accuracy of the reconstruction of the free energy surface. Large Gaussians mean that the free energy landscape will be explored rapidly but contain significant errors, whereas smaller Gaussians will create a more accurate landscape at the cost of a significantly more expensive calculation. The relationship between these two parameters is also relevant and so they must be chosen carefully. Some consider it a good approximation to make  $\omega \sim \sigma^2$ , whilst others follow the relationship  $\omega \sim n\sigma$  with  $n$  usually equal to 2, 3 or 4, however there is no hard-and-fast rule about this. It is also beneficial to fix  $\sigma$  to correspond approximately to the variation seen in the collective variable during an *unbiased* simulation. It is also considered good practice to ensure that  $\sigma$  is much larger than the thermal variations in the system  $k_B T$ .

As the time evolution of the metadynamics calculation proceeds, the history dependent potential forces the system to escape from its initial energy well and towards a new basin of attraction. The system eventually leaves the initial basin before relaxing into a second energy well corresponding to a different (meta)stable state. This process can be continued until the entire phase space is sampled, or until the desired intermediate, transition state or product has been found.<sup>[3]</sup>

The key assumption of metadynamics is that, in the long time limit,  $V(S(x), t)$  converges to the negative of the free energy of the system as a function of the collective variables:

$$\lim_{t \rightarrow \infty} V(S, t) = -F(S) + c \quad [Eq 4.2]$$

The above equation shows that the free energy can be estimated using non-equilibrium dynamics, and is in no way derived from any standard formulations of the free energy, as is the case in other techniques of free energy surface reconstruction.

#### 4.2.3.2. Well-Tempered Metadynamics

Within standard metadynamics, the Gaussian functions deposited to form the bias potential are of uniform height over the course of the simulation. It is often difficult to ascertain when a standard metadynamics simulation has concluded, as the bias potential does not converge exactly to the value of the free energy, but oscillates around the real value with an average error proportional to the square root of the rate of Gaussian deposition  $\tau$ . Accuracy can be gained by reducing the value of  $\tau$ , with the consequence of much longer simulation times to quantify the underlying free energy surface.

One of the modifications to the original method designed to alleviate these issues allows the height of the Gaussians to be decreased over the course of the simulation. This is known as *well-tempered metadynamics*.<sup>[7]</sup> The height of the Gaussian is decreased over the simulation according to the equation:

$$\omega(k\tau) = \omega_0 \exp\left(-\frac{V(S(x(k\tau)), k\tau)}{k_B \Delta T}\right) \quad [Eq\ 4.3]$$

where  $\omega_0$  is the Gaussian height at the start of the calculation. The term  $\Delta T$  is a temperature term and can be used to regulate the extent of the free energy exploration. With such a rescaling of the Gaussian height, the metadynamics bias converges more smoothly in the long time limit to the exact solution, rather than oscillate about the true value. However, in this case the bias potential does not completely compensate the free energy in the collective variable space. In a well-tempered metadynamics simulation, the free energy is estimated as:

$$\lim_{t \rightarrow \infty} V(S, t) = -\frac{\Delta T}{T + \Delta T} F(S) + c \quad [Eq\ 4.4]$$

In this case,  $T$  is the temperature of the system. It is interesting to note the two limiting cases, where  $\Delta T = 0$  and  $\Delta T = \infty$ . For  $\Delta T = 0$ , the bias is equal to zero, which corresponds to a standard molecular dynamics calculation. At  $\Delta T = \infty$ , the deposition rate is constant and the original metadynamics relationships are found. In the array of intermediate cases found in well-tempered metadynamics, the simulation samples an ensemble at the higher temperature of  $T + \Delta T$ , but the calculated free energy surface corresponds to the target temperature  $T$ .

#### 4.2.3.3. Adaptive Gaussian Metadynamics

There also exists a scheme of metadynamics in which the width of the Gaussian  $\sigma$  can be changed over the course of the simulation. This is incredibly useful in system where the local properties of the free energy surface vary greatly in different regions of the collective variable space.<sup>[8]</sup> There are two prescriptions for adaptive Gaussian metadynamics: The first confers changes to the width of the Gaussian functions according to the mean square displacement of the collective variables within a particular time interval. The second involves altering the Gaussian width based on the change in mean square displacement of the collective variables as a result of a geometric change in the microscopic coordinates. The two methods are known as *dynamically adapted* and *geometry adapted* Gaussians, respectively.

Once again, the free energy estimator must be modified when using this technique. The equation corresponding to the free energy when using Adaptive Gaussian metadynamics is:

$$\lim_{t \rightarrow \infty} V(S, t) = -F(S) - T \ln N(S, t) + c \quad [Eq\ 4.5]$$

In this case,  $N(S, t)$  corresponds to the accumulated histogram detailing the variance of the collective variables up to time  $t$ . This estimator works regardless of the changes to the size of the Gaussians and can be utilised to estimate the free energy using either dynamically adapted or geometry adapted Gaussian functions.

4.2.3.4. Using the Simulation Cell as the Collective Variable

The metadynamics procedures designed by Martonák, Laio and Parrinello have shown to be excellent candidates for modelling structural phase transitions and deserve extra discussion as their methodologies have been used extensively in this work.<sup>[9-11]</sup> In the Martonák *et al* schemes of metadynamics, the three edges of the cell  $a$ ,  $b$  and  $c$  are used as the collective variables, arranged as a 3 x 3 matrix:

$$h = (a, b, c) \quad [Eq\ 4.6]$$

In small simulation cells,  $h$  is simply an integer value of the unit cell  $u$ , meaning that this quantity is excellent at distinguishing between different shapes and sizes of the cell. In addition, this quantity can be simplified further as only six variables are required to describe it properly - the parameters  $h_{21}$ ,  $h_{31}$  and  $h_{32}$  determine the global orientation of the box and can thus be eliminated by the correct rotation to the system.

Applying metadynamics to the simulation cell is a very effective method of inducing structural change. First-order phase transitions are usually accompanied by sensible changes to the simulation cell, and thus such a method is very appropriate to instigate such a rare event within the system.

In the original Martonák *et al* scheme, the simulation starts from an equilibrated box  $h$  containing the system of interest at temperature  $T$  and pressure  $p$ . These conditions are usually chosen to correspond to the temperature and pressure at a phase boundary within the system being studied. The system is then propagated using molecular dynamics and the pressure tensor  $\vec{p}$  is evaluated for the relaxed system. The pressure tensor can be used to calculate the first derivative of the free energy of the system:

$$-\frac{\delta G}{\delta h_{ij}} = V \left( \frac{(\vec{p} - p)}{h} \right)_{ij} \quad [Eq\ 4.7]$$

where  $V$  is the volume of the system and is calculated as the determinant of  $h$ . The value of collective variable  $h^t$  is then perturbed to  $h^{t'}$  by the expression:

$$h^t = h^{t'} + \frac{\phi^t}{|\phi^t|} \quad [Eq\ 4.8]$$

where  $\phi^t$  is the ‘driving force’ and contains the history dependent Gibbs potential  $-\delta G^t/\delta h$  with a Gaussian added to the potential  $G(h)$  at every previous value of  $h'$  to forbid the system from returning to its previous state. With this new value of  $h'$ , the coordinates of the system are rescaled in order to fit into the new box, and the process is repeated.

The overall metadynamics potential builds up over multiple iterations of the procedure and its analytical form is very similar to that discussed previously. Eventually, substantial changes to the shape and size of the box will lead to the current atomic configuration becoming unfavourable and the positions of the atoms in the system will be forced to radically alter. At this point, a phase transition to a different allotrope or polymorph of the material under scrutiny will be observed.

However, Martonák *et al* have since modified this metadynamics procedure.<sup>[13]</sup> This improvement takes the Gibbs free energy up to its second term and invokes the use of the Hessian matrix  $A$ :

$$G(h) = G(h^0) + \frac{1}{2}(h - h^0)^T A (h - h^0) \quad [Eq\ 4.9]$$

where  $h^0$  is the value of the matrix  $h$  at time = 0. The Hessian  $A$  is given by:

$$A_{ij} = \left. \frac{\delta^2 G(h)}{\delta h_i \delta h_j} \right|_{h^0} \quad [Eq\ 4.10]$$

This quantity is calculated from variations to the matrix  $h$  during a constant pressure simulation. If the configuration is stable, at equilibrium the eigenvalues  $\lambda^i$  of matrix  $h$  will be

positive and real. The equilibrium matrix can also be diagonalised by an orthonormal matrix, denoted  $O$ . Within this new methodology, a new set of coordinates is defined according to the equation:

$$S_i = \sqrt{\lambda^i} \sum_j O_{ij} (h_j - h_j^0) \quad [Eq\ 4.11]$$

By constructing the new collective variable in this way, the energy well becomes spherical in nature...

$$G(h) = G(h^0) + \frac{1}{2} \sum_i S_i^2 \quad [Eq\ 4.12]$$

... and the first derivative of the Gibbs potential with respect to the new coordinates is given as:

$$\frac{\delta G}{\delta S_i} = \sum_j \frac{\delta G}{\delta h_j} O_{ij} \frac{1}{(\sqrt{\lambda^i})} \quad [Eq\ 4.13]$$

The metadynamics procedure in the space of the new  $S$  coordinates may now proceed in the same fashion as the original scheme.

The advantage of this modified scheme is that the new collective variables  $S$  bring all of the degrees of freedom of the six-dimensional  $h$  quantity into the same energy scale and thus symmetrises the underlying shape of the energy basin. This is advantageous as one can easily imagine a situation in the initial scheme where certain modes of deformation of the matrix  $h$  are favoured over others – for example, the energy required to squeeze the box and reduce its volume is significantly greater than the energy required to squeeze the box in one direction and elongate in another. This arises from the fact that in the original scheme the underlying basins are highly anisotropic in shape and sampling of the underlying energy landscape would be far from optimal using a symmetrical Gaussian. Using the modified scheme, the underlying

energy basins are spherical in nature and the the degrees of freedom in the collective variable are now equalised in energy, meaning far more configurations can be visited without over or under filling the energy landscape.

The general procedure, therefore, for the modified Martonák metadynamics scheme, is shown overleaf.

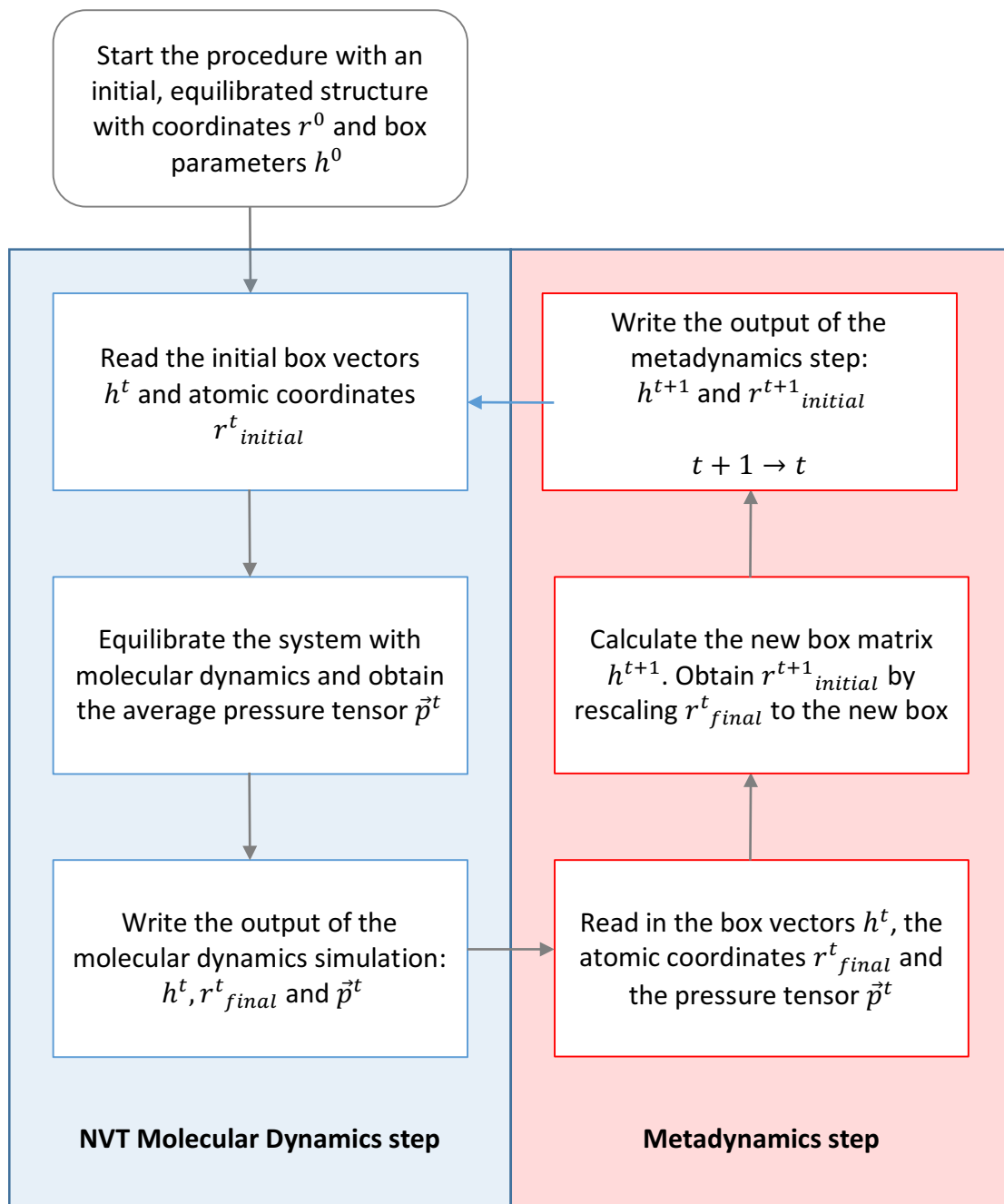


**Figure 4.iv:** Flowchart showing the procedure followed by the Martonák metadynamics driver. The procedure continues indefinitely and may be stopped at any time. Eventually, the system moves away from the original configuration towards a new one. The driving force is the modification to the size and shape of the simulation cell during the metadynamics step – the coordinates move in response to this during the molecular dynamics step.



### 4.3. Transition Path Sampling

Information in this section, relating to the transition path sampling methodology and the underlying theoretical principles, are obtained from the following references.<sup>[2,14,15]</sup>

#### 4.3.1. Introduction to Transition Path Sampling

In complex systems, with high correlation between various degrees of freedom, the underlying energy landscape becomes very complex. Such landscapes are topologically ‘rough’ with countless features of the order of  $k_B T$  and therefore innumerable saddle points and transition states. As such, it is not possible to systematically calculate the landscape for such a system and determination of a relevant set of points for a dynamic trajectory is essentially impossible. The approach one must take is to determine an ensemble of transition paths which link the two basins of attraction. From this ensemble of potential trajectories, we can then characterise their relative probabilities and hence deduce the most plausible pathways for a given physical transformation. This is achieved by *transition path sampling (TPS)*.<sup>[2]</sup>

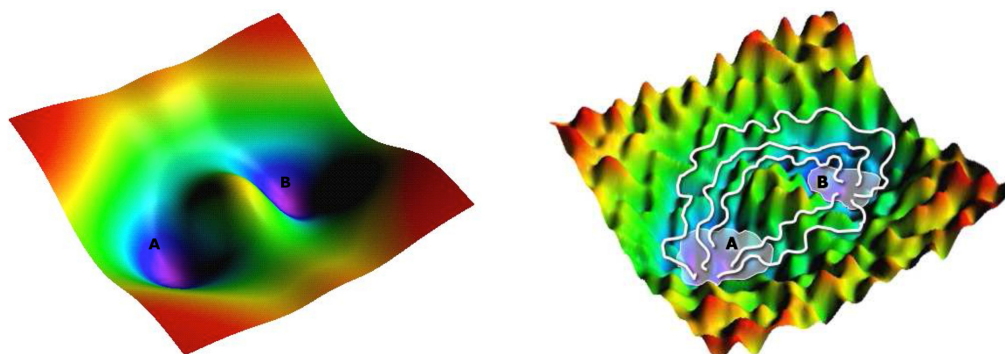


**Figure 4.v:** A schematic of a simple energy landscape corresponding to a system with only a small number of atoms (left) compared to a coarser and more complex surface corresponding to a more realistic system (right). The system on the left has only one pathway linking basins A and B, whereas the system on the right displays numerous feasible pathways between A and B. A single transition pathway for the system on the right is therefore characteristic, and instead an ensemble of pathways must be generated.<sup>[2]</sup>

Consider an ensemble of all the trajectories of a system corresponding to a particular length of time. Nearly all of these trajectories will sample microstates in or around one of the basins of interest. However, a very small number of these trajectories will cross from one basin to another. Transition path sampling provides a means to sample such rare events by the systematic generation and statistical analysis of trajectories within the intermediate region. This set of trajectories is known as the *transition path ensemble*. Because the trajectories accumulated from transition path sampling are truly dynamic, it is also possible to extract kinetic data from transition path sampling simulations as well as the reaction mechanism and relevant intermediates and transition states.

Transition path sampling can be thought of as a modified Monte Carlo procedure acting in trajectory space. The rationalisation for the methods used in the technique deserve some consideration, and are discussed in the following section.

#### 4.3.2. Importance Sampling

In a standard Metropolis Monte Carlo procedure, a random walk in configuration space is biased to ensure that the procedure visits configurations and pathways based on their probability.<sup>[14]</sup> The probability distribution  $p(x)$  is given by the relationship:

$$p(x) \propto e^{\frac{-V(x)}{k_B T}} \quad [Eq\ 4.14]$$

In the canonical ensemble,  $V(x)$  corresponds to the potential energy for the configuration  $x$ . Configurations with lower energies are therefore given a larger weighting, whereas those with prohibitively high energies are assigned less importance. During the random walk, the configuration  $x$  is displaced by a randomly chosen step to generate a new configuration  $y$ . The new configuration  $y$  is then accepted or rejected, depending on its energy relative to  $x$ . Configurations that are lower in energy than  $x$  are automatically accepted, whereas those higher in energy are accepted or rejected according to a probability distribution. Using this procedure, the system is quickly driven to sample only relevant regions of the configuration

space. The walk can be initiated from any starting configuration, including those with very low probabilities, but the procedure will still quickly move towards relevant regions of the configuration space. This important feature of Monte Carlo procedures is known as *importance sampling*.

This technique can also be generalised to trajectory space – this is the crux of the transition path sampling methods. In any ergodic system, any pathway that links two basins A and B within a specific time is characterised by a certain probability. The Monte Carlo walk can be applied in trajectory space to force the system to visit only relevant regions of the trajectory space – i.e. those corresponding to the rare event of a phase transition. The process can then sample the transition path ensemble and ultimately determine those pathways with the highest probability. From this, statistical analysis of the transition can be undertaken, and structural and mechanistic details of the most plausible transition pathways can be characterised.

#### 4.3.3. Path Probability

Consider a trajectory of length  $T$  denoted by  $x(T)$ . For the purposes of molecular dynamics and hence transition path sampling, it is convenient to envisage the trajectory as a discretised sequence of states:

$$x(T) \equiv \{x_0, x_{\Delta t}, x_{2\Delta t}, x_{3\Delta t} \dots x_T\} \quad [Eq\ 4.15]$$

where  $\Delta t$  corresponds to the time increment separating each of the states. Each of these states  $x$  contains a complete set of variables which describe the system. For a Markovian process – a process whose future depends solely on the conditions of the present state – the state  $x_t$  will evolve into the state  $x_{t+\Delta t}$  with probability  $p(x_t \rightarrow x_{t+\Delta t})$ . It then follows that the probability of the whole dynamical trajectory can be expressed as the product of the probability of the discretised time-slices:

$$P[x(T)] = \rho(x_0) \prod_{i=0}^N p(x_{i\Delta t} \rightarrow x_{(i+1)\Delta t}) \quad [Eq\ 4.16]$$

where  $N$  is the total number of discretised states, given by the relationship:

$$N = \frac{T}{\Delta t} - 1 \quad [Eq\ 4.17]$$

The first term  $\rho(x_0)$  corresponds to the distribution of states at the starting points for the trajectories. This distribution is determined by the ensemble of the system under scrutiny.

In transition path sampling, only the reactive trajectories corresponding to the rare event (the transition between the two basins A and B) are of interest. As such, the path ensemble can be restricted to contain only trajectories beginning in region A at  $t = 0$  and ending in region B and  $t = T$ :

$$P_{AB}[x(T)] \equiv h_A(x_0) P[x(T)] h_B(x_T) \quad [Eq\ 4.18]$$

$$P_{AB}[x(T)] = \rho(x_0) h_A(x_0) \prod_{i=0}^N p(x_{i\Delta t} \rightarrow x_{(i+1)\Delta t}) h_B(x_T) \quad [Eq\ 4.19]$$

where  $h_A$  and  $h_B$  are population functions of basins A and B respectively.  $h_A$  and  $h_B$  are equal to 1 if the system within basin A or B respectively, and equal to 0 otherwise. Whether or not a state resides within a basin is determined by the *order parameter*, which is discussed later. As a result, non-reactive pathways that do not link basins A and B are given a statistical weighting of zero and paths connecting the two basins have a non-zero probability which is dependent on the probability of the dynamic pathway  $P_{AB}[x(T)]$ . The transition path ensemble is therefore the weighted selection of reactive trajectories linking basins A and B of a particular length from the ensemble of all possible pathways.

#### 4.3.4. Sampling the Transition Path Ensemble

As described above, transition path sampling corresponds to importance sampling of trajectories, analogous to the importance sampling of configurations seen in standard Monte Carlo techniques. Whereas a standard Monte Carlo procedure takes place in configuration space, transition path sampling takes place in *trajectory* space. This random walk in trajectory space is then biased such that the weight of a particular pathway in the transition path ensemble dictates how often this path is visited. In addition, paths that are not-reactive (i.e. that do not visit the two basins of interest) have a zero-weighting and are therefore excluded).

The random walk in the space of the trajectories is achieved following a two-step procedure:

1. From an initial trajectory  $x^{old}(T)$  with a weight  $P_{AB}[x^{old}(T)] \neq 0$ , i.e. the trajectory is reactive, generate a new trajectory  $x^{new}(T)$ . This first step is called the *trial move*, as at this time it is unknown whether or not the new trajectory  $x^{new}(T)$  will be accepted or rejected;
2. Accept or reject the new path  $x^{new}(T)$  depending on an acceptance probability balanced by the frequency of the reverse move. This second stage is known as the *detailed balance* step, and implies that the following condition must be true:

$$P_{AB}[x^{old}(T)]\pi[x^{old}(T) \rightarrow x^{new}(T)] = P_{AB}[x^{new}(T)]\pi[x^{new}(T) \rightarrow x^{old}(T)] \quad [Eq\ 4.20]$$

Here, the term  $\pi[x^{old}(T) \rightarrow x^{new}(T)]$  corresponds to the probability of moving from the initial path to the newly generated path. This in turn is given as the product of two quantities:

$$\begin{aligned} \pi[x^{old}(T) \rightarrow x^{new}(T)] \\ = P_{gen}[x^{old}(T) \rightarrow x^{new}(T)] \times P_{acc}[x^{old}(T) \rightarrow x^{new}(T)] \quad [Eq\ 4.21] \end{aligned}$$

where  $P_{gen}$  corresponds to the probability of generating the new path and  $P_{acc}$  refers to the probability of the path being accepted. Substituting this into the previous equation and rearranging gives the expression:

$$\frac{P_{acc}[x^{old}(T) \rightarrow x^{new}(T)]}{P_{acc}[x^{new}(T) \rightarrow x^{old}(T)]} = \frac{P_{AB}[x^{new}(T)]P_{gen}[x^{new}(T) \rightarrow x^{old}(T)]}{P_{AB}[x^{old}(T)]P_{gen}[x^{old}(T) \rightarrow x^{new}(T)]} \quad [Eq\ 4.22]$$

We know that  $P_{acc}[x^{old}(T) \rightarrow x^1(T)]$  cannot exceed 1. Therefore, we use the *Metropolis rule* to satisfy the above expression:

$$P_{acc}[x^{old}(T) \rightarrow x^{new}(T)] = \min \left[ 1, \frac{P_{AB}[x^{new}(T)]P_{gen}[x^{new}(T) \rightarrow x^{old}(T)]}{P_{AB}[x^{old}(T)]P_{gen}[x^{old}(T) \rightarrow x^{new}(T)]} \right] \quad [Eq\ 4.23]$$

However, as we know that the initial trajectory is reactive, we also know that the population functions of basins  $h_A(x_0^{old})$  and  $h_B(x_T^{old})$  are equal to one. Therefore, we can re-write the above expression to include the population terms for the new trajectory  $x^{new}(T)$ :

$$\begin{aligned} P_{acc}[x^{old}(T) \rightarrow x^{new}(T)] \\ = h_A(x_0^{new})h_B(x_T^{new}) \times \min \left[ 1, \frac{P[x^{new}(T)]P_{gen}[x^{new}(T) \rightarrow x^{old}(T)]}{P[x^{old}(T)]P_{gen}[x^{old}(T) \rightarrow x^{new}(T)]} \right] \end{aligned} \quad [Eq\ 4.24]$$

Now it is evident that only reactive trajectories are accepted, as any trajectories that do not start and end in basins A and B respectively will receive a value of 0 for their population functions, rendering the entire probability weighting equal to zero for that trajectory.

4.3.5. The Shooter Algorithm

As shown previously, transition path sampling is the realisation of two processes: the first is the dynamics of the system, which takes place in the phase space of the system  $x$ . The second is the path sampling step, taking place in the space of the trajectories  $x(T)$ . However, one requires a method of how to realise this procedure in practice.

There are many ways in which one can generate new trajectories from existing ones, but perhaps the most effective method is the *shooter* algorithm. In a *shooting* move, a single phase space point  $x_\tau^{old}$  is selected from somewhere along the course of the initial trajectory  $x^{old}(T)$ . The momenta of the atoms within this frame  $x_\tau^{old}$  are modified and from this novel state  $x_\tau^{new}$  the new trajectory  $x^{new}(T)$  can be generated by propagating forwards to time  $t = T$  and backwards to time  $t = 0$  using molecular dynamics. By redistributing the atomic momenta at time  $\tau$  and integrating forwards and backwards in time, a new trajectory has been generated.

The generation probability for the forward trajectory  $P_{gen}^{t \rightarrow}$  beginning at time  $\tau$  and ending at time  $T$  is given by the following expression:

$$P_{gen}^{t \rightarrow}[x^{old}(T) \rightarrow x^{new}(T)] = \prod_{i=\tau/\Delta t}^{T/\Delta t-1} p(x_{i\Delta t}^{new} \rightarrow x_{(i+1)\Delta t}^{new}) \quad [Eq\ 4.25]$$

This generation probability is the same as the dynamical path weight for this segment of the new trajectory. The generation probability for the reverse segment of the trajectory  $P_{gen}^{t \leftarrow}$  from time  $\tau$  to time 0 is obtained from the inverted small time step probability:

$$P_{gen}^{t \leftarrow}[x^{old}(T) \rightarrow x^{new}(T)] = \prod_{i=1}^{\tau/\Delta t} \bar{p}(x_{i\Delta t}^{new} \rightarrow x_{(i+1)\Delta t}^{new}) \quad [Eq\ 4.26]$$

Thus, the total generation probability is a combination of the probability of obtaining the state  $x_\tau^{new}$ , and the two generation probabilities for the forward and backward segments of the new trajectory. This can be combined to give:

$$\begin{aligned}
 P_{gen}^{t \rightarrow} [x^{old}(T) \rightarrow x^{new}(T)] \\
 &= p_{gen} [x_\tau^{old} \rightarrow x_\tau^{new}] \times \prod_{i=\tau/\Delta t}^{T/\Delta t - 1} p(x_{i\Delta t}^{new} \rightarrow x_{(i+1)\Delta t}^{new}) \\
 &\times \prod_{i=1}^{\tau/\Delta t} \bar{p}(x_{i\Delta t}^{new} \rightarrow x_{(i+1)\Delta t}^{new}) \quad [Eq\ 4.27]
 \end{aligned}$$

This is the general expression for the *shooting* algorithm. This generation probability can now be used to determine the acceptance probability of any shooting move.

However, in practice a number of simplifications are made to greatly streamline the shooting algorithm. If the modification to the dynamics carried out by the shooting moves conserves a stationary distribution (i.e. conserved quantities, such as total momentum and angular momentum remain unchanged), two assumptions can be made. Firstly, the quantities  $p$  and  $\bar{p}$  are related by *microscopic reversibility*. Secondly, we assume that the generation probabilities from the old to the new trajectory, and vice versa, are equal to one another. This simplifies the acceptance expression to the following:

$$P_{acc} [x^{old}(T) \rightarrow x^{new}(T)] = h_A(x_0^{new}) h_B(x_T^{new}) \times \min \left[ 1, \frac{p(x_\tau^{new})}{p(x_\tau^{old})} \right] \quad [Eq\ 4.28]$$

Thus, in order to evaluate the acceptance probability  $P_{acc}$ , one only needs to know the relative weights of the phase space points  $x_\tau^{old}$  and  $x_\tau^{new}$ , and whether or not the path begins and ends in regions A and B respectively, giving unity values to the population functions  $h_A$  and  $h_B$ . As such, an algorithm which generates a symmetrical modification to the selected point in phase space  $x_\tau^{old}$ , as well as preserving conserved quantities needs to be considered. Thus, the procedure of the shooting algorithm is as follows:



- i. Select a phase-space point  $x_{\tau}^{old}$  from the old trajectory  $x^{old}(T)$ ;
- ii. Modify the momenta of the atoms within this configuration. This is achieved by adding a random displacement  $\delta\rho$  from a one-dimensional Gaussian distribution. This displacement must be symmetrical with respect to the backward move;
- iii. Enforce constraints on the system to ensure there is no change to the total linear and angular momentum. This is often achieved by ensuring these quantities are equal to zero;
- iv. Assess the probability of the modification as  $\min \left[ 1, \frac{p(x_{\tau}^{new})}{p(x_{\tau}^{old})} \right]$ ;
- v. Accept or reject the new configuration. Should the move be rejected, restart the procedure from step 2. If the move is accepted, rescale the atomic momenta in order to conserve the total energy of the system;
- vi. Propagate the system forwards and backwards in time;
- vii. Assess the reactivity of the new trajectory.
- viii. Should the path not start in basin A and end in basin B, reject the trajectory and restart the procedure from step 1 using the original configuration. If the path is successful, accept the new trajectory and restart from step 1 using the new configuration.

There are evidently numerous checkpoints at which it is determined whether or not a shooting move has been successful. Firstly, the ratio of the two weight functions  $\frac{p(x_{\tau}^{new})}{p(x_{\tau}^{old})}$ , before any molecular dynamics propagation has taken place, must be evaluated. Whether or not the new configuration  $x_{\tau}^{new}$  is accepted depends the ratio of the two weight functions:

- If the value of  $\frac{p(x_{\tau}^{new})}{p(x_{\tau}^{old})} > 1$ , the configuration is automatically accepted
- If the value of  $\frac{p(x_{\tau}^{new})}{p(x_{\tau}^{old})} < 1$ , a random number  $\zeta$  is selected between 0 and 1. If the ratio of the probability weights is greater than  $\zeta$ , the configuration is accepted.

If the value of the weight ratios is less than  $\zeta$ , the shooting move is aborted and attempted again. If the procedure is successful at this stage, the system is propagated forwards and backwards in time. Should the forward and reverse trajectories not reach the two basins of interest, the trial move is rejected and, once again, the procedure is restarted from the old path. However, should the two trajectory segments reach basins A and B, the trajectory is accepted and any further shooting moves are initiated from the new trajectory. By doing this iteratively, one can sample the trajectory space in an iterative fashion, until the subset of trajectories with the highest probabilities have been found.

The shooting algorithm works so efficiently because of the vast variety of paths in trajectory space, allowing subsequent trajectories to be quite different to preceding ones. However, one must ensure that the shooting algorithm modifies the momenta of the atoms appropriately, as (for deterministic dynamics) the degree of divergence from the old path to the new path is dependent on the magnitude of modification to  $x_{\tau}^{old}$ . Very small modifications to momenta will leave the path relatively unchanged, whereas very large modifications will completely alter the trajectory and its path may no longer lead to basins A and B. As such, an appropriate momentum modification is required, which is often dependent on the size and nature of the system. As a rule of thumb, it is advisable for 40-60% of trajectories to be accepted, and the rest rejected. This ensures an optimal sampling of the trajectory space.

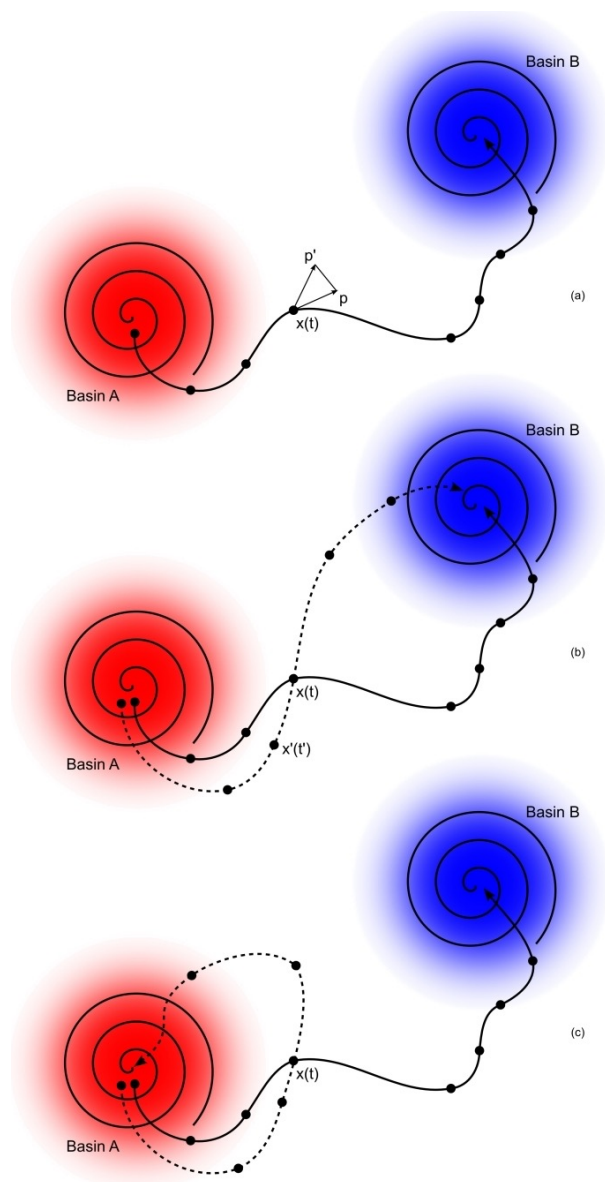


**Figure 4.vi:** Schematics showing possible outcomes of a shooting move. A random time-slice

$x_{\tau}^{old}$  is chosen along an initial reactive trajectory (solid black line), and its momentum distribution modified from  $\rho$  to  $\rho'$  according to the *shooting* algorithm (a). This generates a new trajectory (dashed black line) from the old configuration. Should the new configuration pass the probability tolerance and the new trajectory visit basins A and B, the move is accepted and this new path becomes the starting trajectory (b). If, however, the momentum modification causes the trajectory to diverge away from one or both of the basins of interest, the path is rejected (c). Both the forward and the reverse trajectories end in basin A, leaving basin B unvisited by the path.<sup>[16]</sup>

#### 4.3.6. The Order Parameter

Now that the procedure for generating new pathways and assessing their probabilities is known, all that remains is a procedure to distinguish between the basins of attraction A and B. This final point is discussed below.

Transition path sampling does not require any *a priori* knowledge of the transition mechanism. As such, it is not necessary to define a reaction coordinate, unlike in metadynamics where a set of collective variables must be defined prior to the start of the calculation. However, it is mandatory that the two basins of interest in a transition path sampling calculation be distinguishable. Otherwise, there would be no way of determining whether or not a path had been successful (i.e. whether or not the population functions  $h_A(x_0^{new})$  and  $h_B(x_T^{new})$  are equal to 1).

One way to do this is to define an *order parameter* which can be used to differentiate between the initial and final states of interest. Unlike a collective variable, the order parameter need not represent some physical process along the transformation – instead, it must simply discriminate between the different basins of attraction on the pathway.

However, akin to finding a good collective variable in metadynamics, finding a suitable order parameter for transition path sampling is not always a trivial pursuit. A suitable order parameter generally has the following characteristics:

- i. The order parameter must uniquely distinguish between the initial and final states of a system, and there can be no overlap of its value between basins A and B. If certain values of the order parameter correspond to both basins A and B, the transition path sampling procedure would wrongly collect ‘successful’ trajectories when the pathway is not reactive;
- ii. The order parameter must be able to tolerate equilibrium fluctuations of the order of  $k_B T$  within the basins of attraction, in order to correctly characterise the transition

path ensemble. The regions of the two basins A and B defined by the order parameter must therefore be large enough to accommodate such fluctuations.

Examples of order parameters used in transition path sampling calculations include, but are not limited to, coordination spheres and geometric parameters.

#### 4.3.7. Summary of the Path Sampling Procedure

With the knowledge of how to generate new trajectories and how to assess their probability, and the ability to distinguish between the two configurations of interest using the order parameter, transition path sampling allows for the generation and scrutiny of hundreds of different trajectories from a single (or multiple) initial configurations. This procedure is carried out iteratively until convergence upon the most probable sub-set of trajectories linking two basins of attraction. With this information, one can analyse these most probable pathways and make intuitive analyses about the structure, mechanism and energetics of a phase transition. The entire procedure can be summarised in the flow chart below:

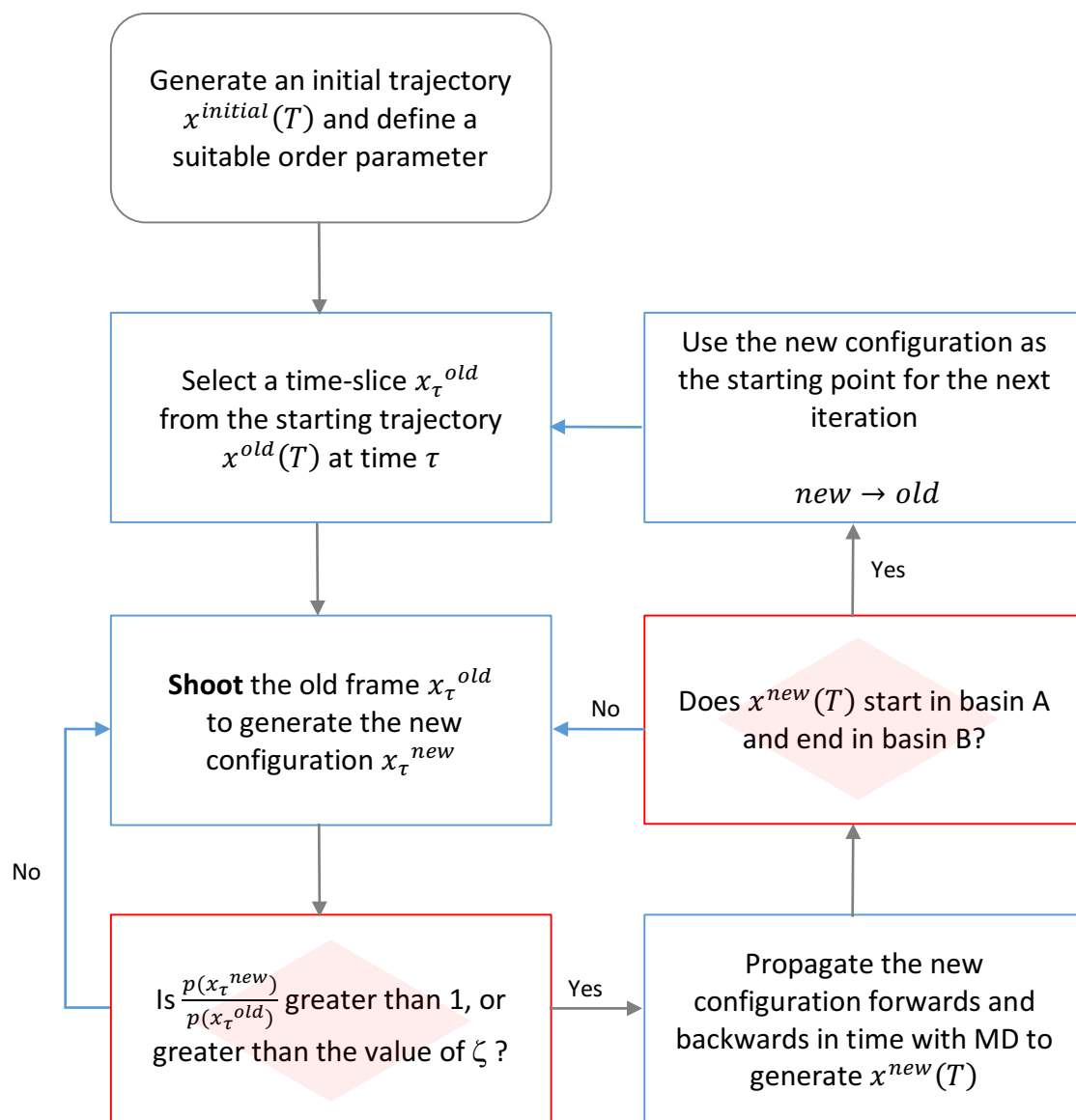


**Figure 4.vii:** Flowchart showing the transition path sampling procedure using the *shooting* algorithm. The procedure is generally iterated until the algorithm converges upon the most probable subset of trajectories linking basins A and B. The procedure can be stopped at any time and in general is repeated until enough mechanistic data has been obtained from the de-correlated trajectories produced by the method.

When one has obtained the most probable subset of transition pathways from the transition path ensemble, a detailed analysis of the relevant transition states and intermediates along the pathway can be made.

#### 4.4. Hardware and Software

##### 4.4.1. Hardware

The work contained within this thesis was completed using a wide variety of computer systems, ranging from personal laptops to high performance supercomputing centres. This section briefly describes the machines used to carry out the work.

A considerable portion of the work was completed on local machines within the Leoni group. The group owns a number of high-end desktop computers, each equipped with 8 to 32 Intel CPUs. All of the machines operate under either the OpenSUSE or Ubuntu operating systems. Local machines tended to be used for background jobs or tasks that required constant supervision.

A great deal of the work contained within this thesis was computed using Cardiff University's *Raven* service, operated by Advanced Research Computing at Cardiff (ARCCA). Within its primary MPI parallel partition, *Raven* consists of 2048 cores Intel Sandy Bridge processors (2.6 GHz, with 4 GB per core and 8 cores per processor). In addition to this, *Raven* also boasts 864 cores Intel Westmere processors (2.8 GHz, with 3 GB per core and 6 cores per processor) for serial or high throughput jobs. The entire cluster contains 8 TB of memory, with over 150 TB of file storage. *Raven* operates under a Linux operating system. Tasks carried out on *Raven* tended to be jobs of intermediate expense, running on 32-64 cores each with a wall time of up to 72 hours.<sup>[17]</sup>

In addition to *Raven*, this project has also made use of High Performance Computing (HPC) Wales' infrastructure. HPC Wales was a service dedicated to providing parallel computing to researchers within Welsh universities and industries, with a number of distributed clusters across Wales. However, the HPC Wales project is no longer active, and has been largely superseded by the Supercomputing Wales initiative.<sup>[18,19]</sup>

Finally, the project described within this thesis made extensive use of the UK national supercomputing service ARCHER. The ARCHER machine consists of the Cray XC30 MPP supercomputer, with external login and post processing nodes, as well as the associated file systems. ARCHER boasts 4920 computer nodes, with each node containing two 12-core Intel Ivy Bridge processors, giving a total of 118,080 cores. Each of the computing nodes has either 64 GB or 128 GB of memory, and its /work file system has 4.4 PB of storage available to users.<sup>[20]</sup> ARCHER was utilised to carry out the most expensive calculations, with up to 512 cores being utilised for some jobs, with a maximum wall time of 24 hours. ARCHER is funded by the Office of Science and Technology through the EPSRC's High End Computing Scheme.

#### 4.4.2. Software

Numerous programs and scripts were utilised throughout this work. However, three programs deserve explicit recognition in this work, as well as the tools used for visualisation.

##### 4.4.2.1. cp2k

*cp2k* is a software package that can be used to 'perform atomistic simulations of solid, liquid, molecular, periodic, material, crystal and biological systems'. *cp2k* provides a framework for modelling chemical and physical systems within an impressive list of methods, ranging from classical forcefields and semi-empirical methods, to density functional tight binding (DFTB), up to density functional theory (DFT).<sup>[21]</sup> The program has been used extensively in this work to carry out molecular dynamics and geometry optimisations, however it can also be used for Monte Carlo calculations, as well as for vibrational analysis and transition state optimisations. *cp2k* is used in Chapters 5 and 6 of this work.

##### 4.4.2.2. SIESTA

The developers of the *Spanish Initiative for Electronic Simulations with Thousands of Atoms* (*SIESTA*) describe it as both a 'method and its computer program implementation to perform



efficient electronic structure calculations and *ab initio* molecular dynamics simulations of molecules and solids'. The *SIESTA* method utilises density functional theory with localised basis sets and norm-conserving pseudopotentials. The tool can carry out electronic structure calculations either by the standard *diagonalisation* methods, or by using linear-scaling algorithms in order to efficiently carry out  $\mathcal{O}(N)$  calculations.<sup>[22,23]</sup> *SIESTA* is utilised for the calculation of the optimised structures, electronic band structures, projected density of states and phonon spectra in Chapter 7 of this work. The majority of the calculations in this work have been completed using the standard *diagonalisation* methods.

#### 4.4.2.3. *plumed*

*plumed* is a plugin that implements a large number of enhanced sampling techniques and collective variables (CVs). *plumed* can be used for umbrella sampling and numerous implementations of metadynamics. The plugin interfaces with a number of molecular dynamics codes, including *cp2k*. *plumed* also provides a number of scripts to reconstruct the free energy profile from the bias potential deposited during a simulation.<sup>[24,25]</sup> *plumed* has been used extensively in this work, and features heavily in both Chapters 5 and 6 of this thesis.

#### 4.4.2.4. Visualisation Packages

A number of excellent tools exist for the visualisation of structures. The two used in this work are the *Visual Molecular Dynamics (VMD)*<sup>[26,27]</sup> and *Visualisation for Electronic and Structural Analysis (VESTA)*<sup>[28]</sup> suites. *VMD* has been used throughout this work to visualise and render the large periodic structures seen in Chapters 5 and 6. *VESTA* has been used to manipulate and visualise the unit cells of structures, and has been used to render the images of resultant structures seen in Chapter 7.

References – Chapter 4

1. D. Selli, “Structure and Property Prediction of Novel Materials using Advanced Molecular Dynamics Techniques: Novel Carbons, Germaniums and High Performance Thermoelectrics”, Ph.D. Thesis, Dresden, TUD, 2013
2. C. Dellago, P. G. Bolhuis and P. L. Geissler, *Advances in Chemical Physics*, edited by I. Prigogine and S. A. Rice, John Wiley & Sons, 2002, 1-78
3. A. Laio and M. Parrinello, *Proc. Natl. Acad. Sci.*, 2002, **99**, 12562-12566
4. A. Laio and F. L. Gervasio, *Rep. Prog. Phys.*, 2008, **71**, 126601
5. A. Barducci, M. Bonomi and M. Parrinello, *Wiley Interdiscip. Rev. Comput. Mol. Sci.*, 2011, **1**, 826-843
6. <https://plumed.github.io/doc-v2.3/user-doc/html/belfast-6.html> “Belfast tutorial: Metadynamics” - Last Accessed 28/09/2017
7. A. Barducci, G. Bussi and M. Parrinello, *Phys. Rev. Lett.*, 2008, **100**, 020603
8. D. Branduardi, G. Bussi and M. Parrinello, *J. Chem. Theory Comput.*, 2012, **8**, 2247-2254
9. R. Martonák, A. Laio, M. Bernasconi, C. Ceriani, P. Raiteri and M. Parrinello, *Crystalline Materials*, 2005, **220**, 489-498
10. R. Martonák, A. R. Oganov and C. W. Glass, *Phase Transit.*, 2007, **80**, 277-298
11. R. Martonák, A. Laio and M. Parrinello, *Phys. Rev. Lett.*, 2003, **90**, 075503
12. P. J. Steinhardt, D. R. Nelson and M. Ronchetti, *Phys. Rev. B.*, 1983, **28**, 784-805
13. R. Martonák, D. Donadio, A. R. Oganov, M. Parrinello, *Nat. Mat.*, 2006, **5**, 623
14. P. G. Bolhuis, D. Chandler, C. Dellago and P. L. Geissler, *Annu. Rev. Phys. Chem.*, 2002, **53**, 291-318
15. C. Dellago, P. G. Bolhuis, F. S. Csajka and D. Chandler, *J. Chem. Phys.*, 1998, **108**, 1964-1977
16. S. E. Boulfelfel, “Atomic Scale Investigation of Pressure Induced Phase Transitions in the Solid State”, Ph.D. Thesis, Dresden, MPI CPfS, 2009
17. <http://www.cardiff.ac.uk/advanced-research-computing/about-us/our-supercomputer> “Raven information” - Last Accessed 10/04/2018
18. <http://portal.hpcwales.co.uk/docs/userguide/introduction.html> “HPCW User Guide” - Last Accessed 10/04/2018

19. <https://www.supercomputing.wales> "Supercomputing Wales homepage" - Last Accessed 10/04/2018
20. <http://www.archer.ac.uk/about-archer/hardware/> "ARCHER hardware" - Last Accessed 10/04/2018
21. <https://www.cp2k.org/about> "cp2k homepage" - Last Accessed 10/04/2018
22. J.M. Soler, E. Artacho, J. D. Gale, A. García, J. Junquera, P. Ordejón and D. Sánchez-Portal, *J. Phys. Condens. Matter*, 2002, **14**, 2745
23. <https://departments.icmab.es/leem/siesta/> "SIESTA homepage" - Last Accessed 10/04/2018
24. G.A. Tribello, M. Bonomi, D. Branduardi, C. Camilloni and G. Bussi, *Comput. Phys. Commun.*, 2014, **185**, 604-613
25. <http://www.plumed.org/home> "plumed homepage" - Last Accessed 10/04/2018
26. W. Humphrey, A. Dalke and K. Schulten, *J. Molec. Graphics.*, 1996, **14**, 33-38
27. <http://www.ks.uiuc.edu/Research/vmd/> "VMD homepage" - Last Accessed 10/04/2018
28. <http://jp-minerals.org/vesta/en/doc.html> "VESTA homepage" - Last Accessed 10/04/2018

## Chapter 5

### Phase Transitions of Zinc Oxide

***“Change is always and everywhere at work. It strikes through cause and effect, and leaves nothing fixed and permanent.”***

– Marcus Aurelius (121-180), *Meditations*

#### 5.1. Introduction

Zinc Oxide ( $\text{ZnO}$ ) is an extremely versatile and useful compound, which exhibits an extraordinary array of practical properties. A naturally occurring compound, zinc oxide is found in nature as the mineral *zincite*, which ordinarily takes on a red-yellow hue resulting from presence of first row-transition metal ion impurities within its structure. However, the overwhelming majority of zinc oxide utilised by industry today is synthesised via three processes, which are responsible for the production of over 100,000 tons of the material per annum.<sup>[1]</sup> The synthesised product finds use in the production of rubbers,<sup>[2,3]</sup> plastics,<sup>[4]</sup> pigments,<sup>[5]</sup> cements,<sup>[6]</sup> ointments (especially sun lotion)<sup>[7]</sup> and lubricants,<sup>[8]</sup> amongst other applications.<sup>[9]</sup>



**Figure 5.i:** A photograph of a sample of powdered zinc oxide.<sup>[10]</sup> Despite its mundane appearance, this innocuous material boasts a wealth of fascinating physical properties.

Zinc oxide is a type II-VI semiconductor, and exhibits a wide, direct band gap of approximately 3.37 eV (corresponding to a near-UV frequency). This makes pure zinc oxide a colourless, clear compound. In addition to its optical transparency and wide band gap, it also features high electron mobility and strong room-temperature luminescence, giving it very desirable characteristics for use in contemporary electronic and optics applications.<sup>[9]</sup> Some potential emerging applications of zinc oxide include use in the production of light emitting diodes,<sup>[11]</sup> transistors,<sup>[12]</sup> piezoelectrics,<sup>[13]</sup> liquid crystal displays,<sup>[14]</sup> chemical sensors,<sup>[15]</sup> and spintronics.<sup>[16]</sup>

Research into zinc oxide began in earnest during the 1930s, with investigation into the material peaking during the 1970s and 1980s. The majority of this research was centred on bulk zinc oxide, which led to extensive characterisation of the properties and curiosities of the material.<sup>[17]</sup> However, interest in the compound waned when structures of reduced dimensionality became fashionable, with a great deal of interest shifted away from zinc oxide and onto pure and aluminium-doped derivatives of gallium arsenide (GaAs).

Since the turn of the twenty-first century, however, zinc oxide has once again come into focus, with the emphasis now on the application of the material in contemporary applications. This renaissance in zinc oxide research has opened the door to many new possible uses for the material, and now considerable work is being undertaken to unlock the full potential of this familiar compound. Some contemporary research avenues into zinc oxide include investigating epitaxial growth of the material,<sup>[18]</sup> the various nanostructures it can form,<sup>[19]</sup> and the formation of zinc oxide quantum dots<sup>[20]</sup> and wells.<sup>[11]</sup>

This work aims to help to further understand the phase behaviour of the material, in order to gain a greater fundamental understanding of zinc oxide, with the ultimate goal of helping to tap into its lucrative potential as a material for use in the electronics and optics industries. Prior to this, a brief introduction to the structure of zinc oxide is given, followed by a review of literature describing the phase behaviour exhibited by the compound.

## 5.2. Structure of Zinc Oxide

Under ambient conditions, zinc oxide crystallises in the hexagonal *wurtzite* structure (B4 type, Hermann-Mauguin space group  $P6_3mc$ ).<sup>[21]</sup> First elucidated by Bragg in 1920<sup>[22]</sup> shortly after the discovery of X-ray diffraction, the wurtzite structure consists of two hexagonal close packed sub-lattices of  $Zn^{2+}$  and  $O^{2-}$  ions, with each  $Zn^{2+}$  tetrahedrally coordinated to four  $O^{2-}$  anions and vice versa. Wurtzite zinc oxide exhibits lattice constants of  $a = 3.250 \text{ \AA}$  and  $c = 5.207 \text{ \AA}$ , giving a  $c/a$  ratio of  $\sim 1.60$  (compared to the ideal value for a hexagonal crystal of 1.633).<sup>[9,17,23,24]</sup>

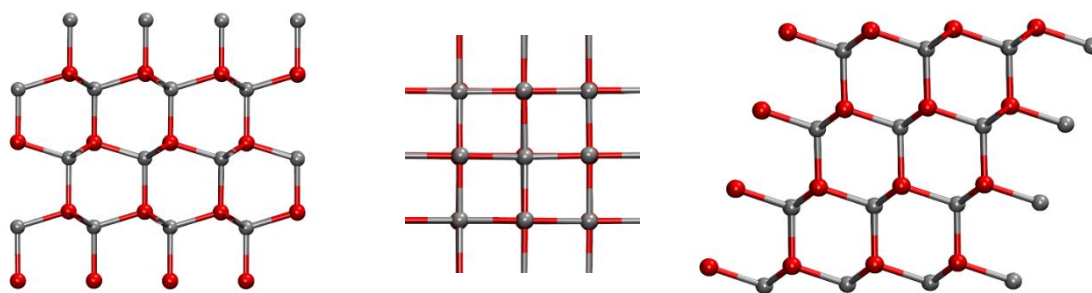


**Figure 5.ii:** Schematics of three experimentally known crystal structures of zinc oxide: the stable wurtzite (B4,  $P6_3mc$ , left); the metastable zincblende (B3,  $F\bar{4}3m$ , right); and the high-pressure rocksalt (B1,  $Fm\bar{3}m$ , centre) phases.<sup>[25-27]</sup>

The  $P6_3mc$  space group exhibited by wurtzite results in the structure having no centre of inversion, which gives rise to the piezoelectric effect (the ability to accumulate an electric charge in response to mechanical strain or pressure) exhibited by ambient zinc oxide. In addition, the experimental bond lengths of wurtzite ZnO show an asymmetry along the [001] axis, exhibiting a shorter bond length. This  $c$ -axis orientated stacking leads to the induction of a macroscopic polarisation, producing an internal electric field. This is one of the central reasons as to why zinc oxide has not yet found widespread use in industry – such internal fields are highly disruptive and undesirable in electronics and optics devices.<sup>[9,24]</sup>

Unlike many other type II-VI semi-conductors, zinc oxide preferentially crystallises in the wurtzite configuration, likely as a result of the highly ionic nature of the  $\text{Zn}^{2+} - \text{O}^{2-}$  interaction. However, zinc oxide is also expected to be able to adopt a second polymorphic phase, which is very close in energy to the ground state: the cubic *zincblende* or *sphalerite* form (B3 type, Hermann-Mauguin space group  $F\bar{4}3m$ ). Unlike in zinc sulphide or zinc selenide, the zincblende form of zinc oxide is *metastable* under ambient conditions, having a higher energy than the more ionic, hexagonal wurtzite structure. However, the Zn-O interaction in the zincblende form of zinc oxide is more covalent in nature, immediately making it a more practical contender for use in semiconducting devices.<sup>[9]</sup>

	O	S	Se	Te
Mg	RS	RS	RS	WZ
Zn	WZ	ZB	ZB	ZB
Cd	RS	WZ	ZB	ZB
Be	WZ	ZB	ZB	ZB

**Table 5.iii:** The thermodynamically stable phase of type II-VI semiconductors, with ZnO highlighted. Here, WZ corresponds to wurtzite, ZB to zincblende and RS to rocksalt. Note that most of the sulphides, selenides and tellurides are stabilised by zincblende structures, however the magnesium compounds and all of the oxides form either wurtzite or rocksalt configurations as a result of their much higher degree of ionicity.<sup>[24]</sup>

Like wurtzite, the zincblende polymorph features tetrahedral coordination and no centre of inversion. However, the zincblende form could be superior for use in electronics applications, as it does not exhibit spontaneous polarisation.<sup>[28]</sup> In addition, the cubic variety features

higher electron drift velocities and lower carrier scattering, as a result of its higher crystallographic symmetry. Zincblende has also been shown to exhibit much higher doping efficiencies, adding to its attraction as a material for use in electronics and optical devices. Moreover, cubic zinc oxide has the potential to be integrated into existing zincblende semiconductor infrastructure (such as *3C-SiC* technology), further increasing the attractiveness of the prospect of using zinc oxide in such devices.<sup>[29]</sup>

The third experimentally known configuration of zinc oxide crystallises in the NaCl-like *rock-salt* structure at high pressures of approximately 10 GPa.<sup>[27,30]</sup> Whilst this phase has been known for over half a century, it has not found any widespread use as a result of the conditions required for it to exist. Despite this, the rocksalt analogue could too find a number of potential uses. Ambient ZnO tends to exhibit *n*-type character, likely due to interstitials and oxygen-vacancies within the wurtzite crystal structure giving an uneven distribution of charges.<sup>[9,31]</sup> However, with a wide, indirect band gap of 2.45 eV, the rocksalt phase would be very suitable for *p*-type doping. As such, trapping the rocksalt form at ambient conditions is of great interest.<sup>[32]</sup>

In addition, a second very high-pressure polymorph which adopts the caesium chloride (CsCl, B2 type) structure has been predicted but not yet experimentally observed.<sup>[9]</sup>

It is plausible that the main reason that zinc oxide has not found extensive use in electronics and optics is due to the inherent difficulty of the synthesis and stabilisation of its more useful zincblende and rocksalt forms, as well as the lack of knowledge about how any transformation to sphalerite occurs. Zincblende can be grown in an epitaxial fashion on cubic substrates, however this process is non-trivial and poorly understood. The external conditions required to drive the transition between the two low pressure regimes are very ambiguous, and it is not even conclusively known whether or not a direct wurtzite-zincblende transformation exists.<sup>[29]</sup>

Thus, full comprehension of the transformations linking the different polymorphs would be desirable, with the motivation that it may be possible to transform ambient wurtzite to a more useful form.



### 5.3. Formation and Transformations of the Polymorphs of Zinc Oxide

#### 5.3.1. The Wurtzite to Rocksalt transformation

The phase transitions undertaken by zinc oxide have been under scrutiny for a very long time. In particular, a great amount of attention has been paid to determining the conversion mechanism between the ambient wurtzite phase, and the high-pressure rocksalt phase.

The first indication of a zinc oxide phase transition was first reported by Bates *et al* in 1962.<sup>[27]</sup> Bates *et al* reported that the new high-pressure polymorph existed with a ‘sodium-chloride form in the 100-kilobar pressure range’, and estimated that the new high pressure rocksalt phase had a lattice parameter of 4.280 Å and a theoretical density of 6.912. This considerable drop in volume (approximately 17%) favoured a greater ionic interaction between the zinc and oxygen ions, explaining the formation of the rocksalt phase at relatively modest external pressure.

It was not until 2000 that subsequent work indicated that the pressure of transition was actually considerably lower (at around 6 GPa).<sup>[33]</sup> The confusion arose perhaps because of the notable hysteresis present in the transition, which has since been extensively characterized: Energy-Dispersive X-ray diffraction (EDXD) experiments have shown that the transition occurs from wurtzite to rocksalt at  $9.1 \pm 0.2$  GPa with complete transformation at 9.6 GPa, with the two phases coexisting in the interim. For the decreasing pressure transformation, rocksalt begins to transform to wurtzite at pressures as low as  $1.9 \pm 0.2$  GPa.<sup>[34]</sup> Other *situ* X-ray diffraction and Mössbauer spectroscopy observations have also demonstrated this large hysteresis in the phase transition.<sup>[35]</sup> Additionally, experiments have repeatedly demonstrated the metastable nature of the B1 phase, with large fractions of the rocksalt phase being retained when pressure is released.<sup>[30,36]</sup>

Considerable mechanistic analysis of the rocksalt to wurtzite transition has been previously studied. Boulfelfel *et al* used transition path sampling to deduce a mechanistic pathway for the transition, and showed that the mechanism proceeds via a rich series of transition states and intermediates.<sup>[32]</sup> Additionally, two five-coordinate intermediate structures can be visited

– a tetragonal and a hexagonal structure – which were shown to compete with one another in the mechanism.

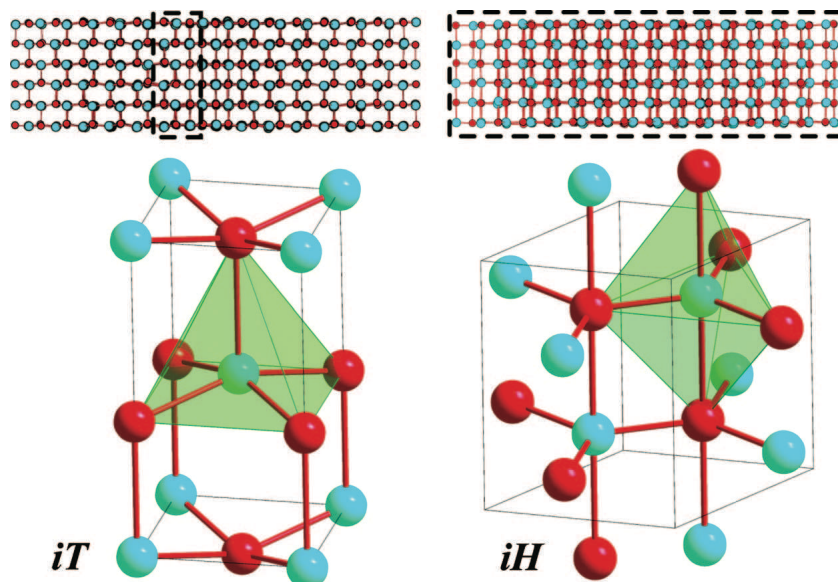


**Figure 5.iv:** The two five-coordinate intermediates elucidated by Boulfelfel *et al.* The tetragonal *iT* ( $I4mm$ , left) and the hexagonal *iH* ( $P6_3/mmc$ , right) were shown to compete against one another in the transformation. Whereas the *iT* was only found at the interface between wurtzite and rocksalt, the *iH* structure sometimes dominated the entire system under study. Despite this, this complete *iH* phase was shown not to be crucial to the transformation.<sup>[32]</sup>

The work of Boulfelfel and Leoni explained on the atomistic level a number of puzzling facets to this transformation, including the presence of numerous coexisting phases and modes of deformation. It also showed that the competition between the two five-coordinate phases directly resulted in the presence of persistent rocksalt defects at low pressure, long after the transition had taken place. This may explain why large regions of the rocksalt structure remain after the high-to-low pressure phase transition has taken place.

Although the level of detail shown in the work of Boulfelfel *et al* was groundbreaking and

aply demonstrated the worth of transition path sampling methods, the presence of the two possible pathways had been speculated for many years before this; however, prior to this atomistic analysis, their competitive nature and pressure dependence was unclear.

For example, in 2004, Saitta and Decremps first discussed the competitive nature of the ‘tetragonal’ and ‘hexagonal’ routes, and their work concluded that semiconductors involving *d*-electrons, such as ZnO, preferred the ‘tetragonal’ path.<sup>[37]</sup> However, other work seemed to contradict this – notably the experimental work of Liu *et al*, which utilised high resolution angular dispersive X-ray diffraction, seemed to indicate that the ‘hexagonal’ pathway was the more favoured for zinc oxide at lower pressures.<sup>[38]</sup>

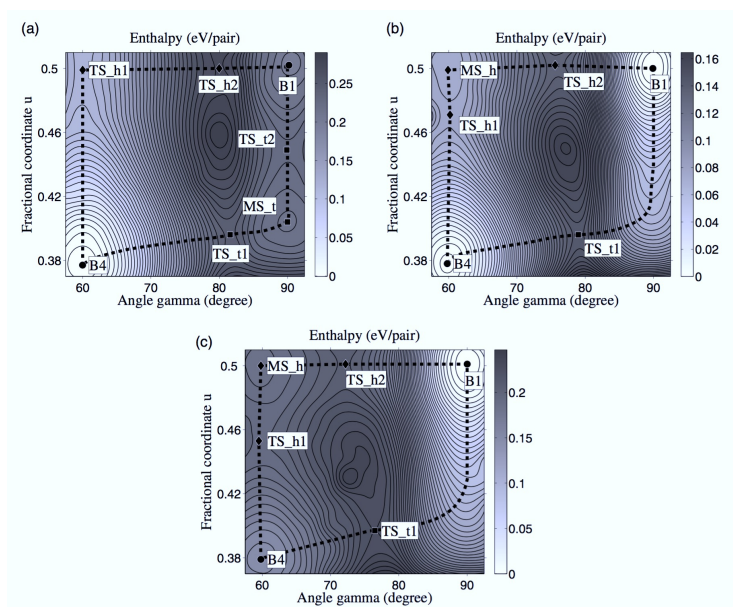


**Figure 5.v:** Potential Energy Surfaces (PES) for the wurtzite to rocksalt transition, from the work of Cai and Chen at ambient pressure (a, top left), the transition pressure (b, top right) and 15 GPa (c, bottom). The dashed lines correspond to the two possible pathways – the ‘tetragonal’ and the ‘hexagonal’ paths, which compete in the transition pressure regime.<sup>[39]</sup>

Subsequent work showed that the true nature of the intermediate phases was far more complex by showing that the two mechanisms were actually competing with each other, and that the formation of either the tetragonal or hexagonal intermediate depended greatly on external pressure, temperature, and local coordination features. A notable example is the

2007 *ab initio* work of Jin Cai and Nanxian Chen, which further added weight to the arguments of directly competing pathways between the two intermediates. Cai and Chen's work seemed to show that the pathways were not system dependent but condition dependent - the so-called 'tetragonal' path was favoured at low pressures, whereas higher pressures appeared to favour the 'hexagonal' path. At the transition pressure, however, the two mechanisms were in direct competition with one another.<sup>[39]</sup>

It is therefore immediately apparent that the phase transition is very non-trivial. Indeed, much debate still rages about its precise nature, and work is still being published to attempt to unravel the minutia of this elusive mechanism.

### 5.3.2. The Rocksalt to Caesium Chloride transformation

As alluded to previously, the caesium chloride type (B2) geometry has been postulated. However, this is yet to be experimentally verified and it is suggested that very high hydrostatic pressures are required to access this phase. Density Functional Theory has predicted that this phase transition should occur at 260 GPa (LDA) or 256 GPa (GGA),<sup>[40]</sup> however classical calculations have placed the transition much higher at 352 GPa.<sup>[41]</sup> In addition, X-ray diffraction studies have shown that the rocksalt phase is stable even at 200 GPa,<sup>[42]</sup> indicating that it is extremely stable over a wide range of pressures and that the caesium chloride phase is unlikely to find any practical use in the near future.

### 5.3.3. Formation of Zincblende ZnO

Most efforts to form sphalerite zinc oxide have been devoted to studying its epitaxial growth on other cubic substrates. Thin layers of metastable zincblende can be grown on cubic substrates, but growth of a single crystal zincblende is a very complex process. One of the main reasons for this is the lack of other zincblende materials with a similar lattice constant to zinc oxide. Lattice constant discrepancies cause the formation of defects that propagate

along the direction of growth, causing complex formation behaviour and hindering the capability of single crystal epitaxial development.<sup>[29]</sup>

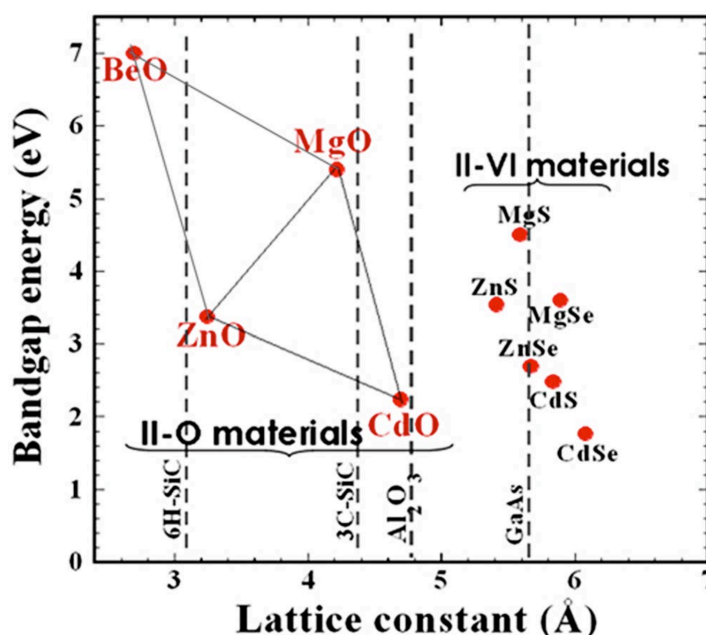


**Figure 5.vi:** Lattice constant vs. band gap energies, plotted for a selection of II-O and II-VI compounds. Note that zinc sulphide and selenide, along with most other II-VI semiconductors, have very similar lattice constants to GaAs. Conversely, ZnO has a much smaller lattice constant, similar to that of 6H-SiC, which is hexagonal. This lack of compatible cubic growth substrates makes zincblende ZnO epitaxy a difficult process.<sup>[29]</sup>

To counter this, most growth techniques utilise zinc sulphide thin layers, which act as interlayers or nucleation layers. The presence of ZnS reduces the mismatch between lattice constants, and acts as a nucleation site for the deposited ZnO. For example, Ashrafi *et al* produced epilayer ZnO utilising metal-organic molecular beam epitaxy, where zincblende ZnO was grown on ZnS-GaAs using plasmas of diethyl zinc and molecular oxygen.<sup>[43]</sup>

Kim *et al* produced cubic zinc oxide using a sol-gel deposition process on a number of different substrates. Kim *et al* also indicated that the presence of hexagonal impurities could be removed by high-temperature annealing, giving a pure zincblende crystal.<sup>[44]</sup> Lee *et al* successfully grew a mixture of hexagonal and cubic zinc oxide on an Al<sub>2</sub>O<sub>3</sub> substrate by the

direct oxidation of thin layers of ZnS.<sup>[45]</sup> However, others have tried this method (such as Yoo *et al*, using a silicon base substrate) without success.<sup>[46]</sup> In the case of Yoo *et al*, it is believed that the oxygen diffuses into the ZnS matrix via interstitial sites, bonding with the ZnO and changing the underlying cubic framework, ultimately to that of the stable wurtzite.

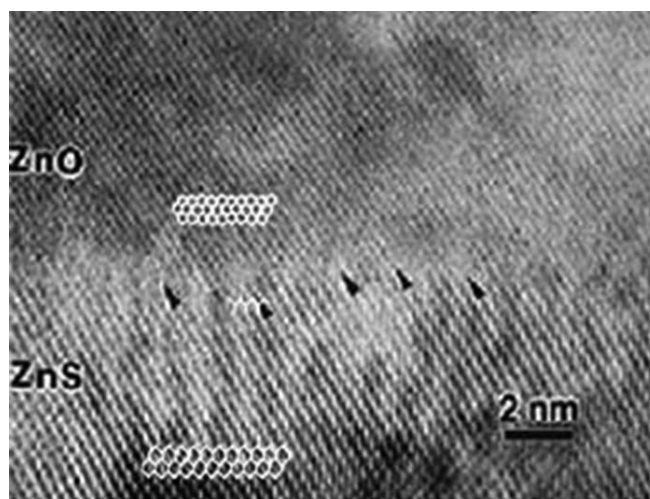


**Figure 5.vii:** Atomic resolution transmission Electron Micrograph (TEM) image of cubic ZnO and ZnS deposited on top of GaAs substrate. The phase boundary between the two zinc compounds is evident, as well as the considerably smaller lattice constant for the ZnO material. Defects are indicated by the arrows; however, they are much fewer in number than would be present without the ZnS interlayer. The lattice constant for the ZnO was shown to be 4.47 Å, as a result of tetragonal distortion caused by strain in the ZnO/ZnS/GaAs system.<sup>[43]</sup>

However, all of these growth processes are still very poorly understood. As such, knowledge of a direct phase transition to the zincblende form of ZnO would be highly desirable.

Unfortunately, hypothetical phase transitions between the wurtzite and zincblende phases have also proven to be much more elusive than transitions from the ground state to the high pressure rock salt phase. The reason for this is likely due to the extremely small energy difference per atom between wurtzite and zincblende ZnO, which is of the order of ~50 meV per atom according to *ab initio* calculations.<sup>[29]</sup> Thus, it is difficult to find conditions where the

zincblende phase is substantially more favoured than the ground state. This would significantly benefit from knowledge of phase nucleation and growth, and how this affects polymorphic selection.

A notable example came in 2008 when Wu *et al* presented evidence of a pressure induced phase transition between wurtzite and zincblende ZnO, based on the calculation of Gibb's free energy with increasing temperature and pressure.<sup>[47]</sup> Wu *et al* showed that a hypothetical phase transition between the two phases should occur at a pressure lower than 30 GPa at 300K, with an activation barrier of 0.386 eV / atom. The group also postulate that the transition path may involve the formation of a transient orthorhombic structure in order to overcome the energy barrier. Sadly, no such transformation has yet been proven by experiment.

#### 5.3.4. Summary

It is apparent from reviewing the literature that, although a great deal of progress has been made to classify the phase transition linking the hexagonal ground state and the high pressure rocksalt forms,<sup>[32-38]</sup> very little is conclusively known about other transformations to and from different polymorphs of zinc oxide. In particular, there is still a considerable lack of knowledge about the formation and stabilisation of the cubic zincblende polymorph, which would be an extremely useful material for use in future electronics and optics devices.<sup>[29,43-46]</sup>

The ultimate goal of this work is to contribute to the knowledge of how to transform zinc oxide into a more useful form. The wurtzite to rocksalt transformation has been extensively studied, and continues to be a competitive area of scrutiny. The direct transformation between the wurtzite and zincblende forms has proven to be very complex, as a result of the two phases' proximity in energy to one another. The remaining pathway, and the one that is virtually unexplored, is that between the cubic zincblende and the high-pressure rocksalt phase. Whilst the merit of such a transformation may not be directly obvious, it is quite apparent that if one could easily transform from the ground state to rocksalt, and then from rocksalt to zincblende, a prescribed route between the ambient and more desirable cubic

forms of zinc oxide could be established. The elucidation of such a procedure could have clear implications for the future use of cubic zinc oxide in electronic devices.

Thus, the work contained within this chapter is an attempt to elucidate the pressure-induced phase transition between zincblende and rocksalt zinc oxide using transition path sampling methodologies. In order to achieve this, the following order of work was undertaken and will be discussed:

1. The deduction of the transition pressure for this transformation;
2. The creation of a suitable transition model, and elucidation of an appropriate dynamical intermediate;
3. Discussion of the order parameter, and justification of its use;
4. Analysis of transition path sampling<sup>[48,49]</sup> results, including full characterisation of the reaction pathway.

In addition, a novel combination of the path sampling *shooting* algorithm and metadynamics<sup>[50]</sup> algorithms will be discussed, which has been developed to quantitatively analyse the transition pathway, as well as accurately describe the transition states and intermediates. This method of '*metashooting*' will be discussed in detail in the second part of this results section, and will be central to the analysis of the transition pathway.



## 5.4. Determination of the Transition Mechanism

### 5.4.1. Methodology

Presented below are computational details relating specifically to the application of TPS methods in this work.

The mechanism deduced by transition path sampling methods critically depends on the number of atoms used in the simulation box. Simulation cells with a very small number of atoms are unlikely to demonstrate any meaningful instances of growth and nucleation (due to the artificial enhancement of such events by periodic images), whereas very large systems would be prohibitively expensive to calculate. Thus, it was decided that the work would be carried out using 2,400 atom systems, corresponding to 1,200 Zn-O pairs. System sizes of this order are widely used in the literature<sup>[32]</sup> and are a good compromise between mechanistic fidelity and computational efficiency. In addition, using simulation cells of a similar size to past work allows for direct comparison with the literature.

$$E_{VDW(Buck)} = Ae^{-Br} - \left(\frac{C}{r^6}\right) \quad [Eq\ 5.1]$$

		$A / \text{eV}$	$B / \text{\AA}^{-1}$	$C / \text{eV \AA}^6$
$\text{Zn}^{2+}$	$\text{Zn}^{2+}$	0.0	0.0	0.0
$\text{Zn}^{2+}$	$\text{O}^{2-}$	529.70	0.3581	0.0
$\text{O}^{2-}$	$\text{O}^{2-}$	9547.96	0.21916	32.0

**Table 5.viii:** The parameters utilised from the work of Binks *et al* in this work.<sup>[51]</sup> The form of the Buckingham potential is shown above.<sup>[52]</sup> Note that the charges of the zinc and oxygen utilised in the work were +2 and -2 respectively.

All calculations were carried out using the *cp2k* package within the isothermal-isobaric ensemble, with a flexible simulation cell (*NpT*) and periodic boundary conditions in the *x*, *y*

and  $z$  directions. Molecular dynamics integration was performed using a *velocity Verlet* scheme with a time-step of 0.2 fs to ensure good time-reversibility. Inter-atomic interactions between the zinc and oxygen atoms were described using a Buckingham-style potential from the work of Binks *et al*, whose parameters have been widely used to model zinc oxide and have been shown to accurately represent a number of critical parameters.<sup>[51]</sup>

Long range electrostatic effects were accounted for using an Ewald summation. Temperature and pressure were controlled by using Nosé-Hoover chains.<sup>[53-56]</sup> Time constants for the thermostat and barostat algorithms were chosen such that temperature and pressure was efficiently regulated, but that the trajectories proceeded reversibly.

#### 5.4.2. Results and Discussion

##### 5.4.2.1. Determination of the Transition Pressure

In order to determine a mechanism for the pressure-induced phased transition between two polymorphs by transition path sampling, one must first ascertain the pressure at which that transition will occur – i.e. the pressure at which both polymorphs A and B can coexist with equal probability. This is done by simply generating an enthalpy vs. pressure plot for the phases of interest.

Using the potential of Binks *et al*, a series of short molecular dynamics calculations on the 2400 atom systems were run using *CP2K* within the isothermal-isobaric ensemble with a flexible cell ( $NpT$ ). The systems were equilibrated, and post-equilibration mean values of external pressure, volume, potential energy and kinetic energy were recorded. The total energy of the system  $U$  is simply the sum of the potential energy  $V$  and the kinetic energy  $T$ :

$$U = V + T \quad [Eq\ 5.2]$$

The enthalpy  $H$  can then be calculated using the equation:

$$H = U + pV \quad [Eq\ 5.3]$$

where  $pV$  is the pressure multiplied by the volume for a particular calculation.

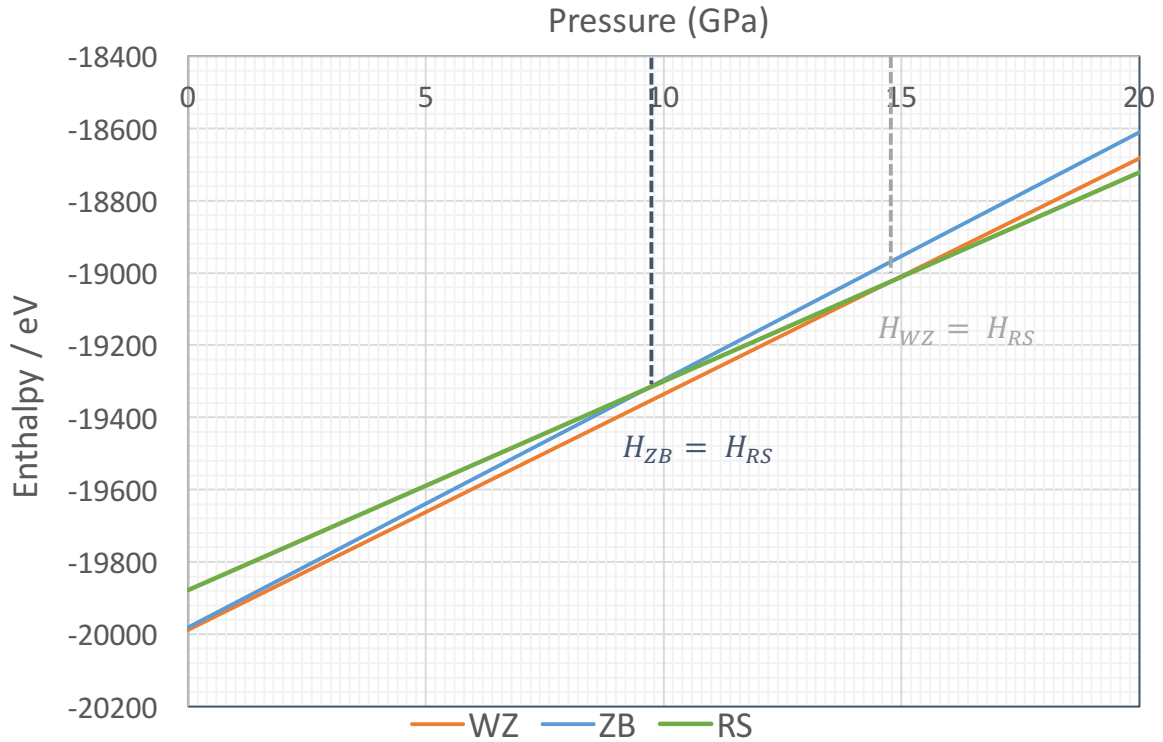


**Figure 5.ix:** Enthalpy vs. Pressure plot for the wurtzite (WZ, orange), zincblende (ZB, blue) and rocksalt (RS, green) phases of zinc oxide. The zincblende-rocksalt crossover occurs at around 9.8 GPa, which was thus taken to the transition pressure for the phase transition. Note how close in enthalpy the wurtzite and zincblende structures are, especially at low pressures. No direct wurtzite-zincblende crossover occurs at any positive value of pressure.

Obtaining this quantity over a range of pressure gives a straight line plot for each system, and the crossover point between two sets of data corresponds to the transition pressure. In this work, the transition pressure for the zincblende-rocksalt transformation was determined to be at around 9.8 GPa.

5.4.2.2. The Geometric Trajectory

It is imperative to have an *initial trajectory* linking the two basins of interest (in this case, the zincblende and the wurtzite configurations of zinc oxide), upon which one can derive the starting configuration for the iterative path sampling procedure.

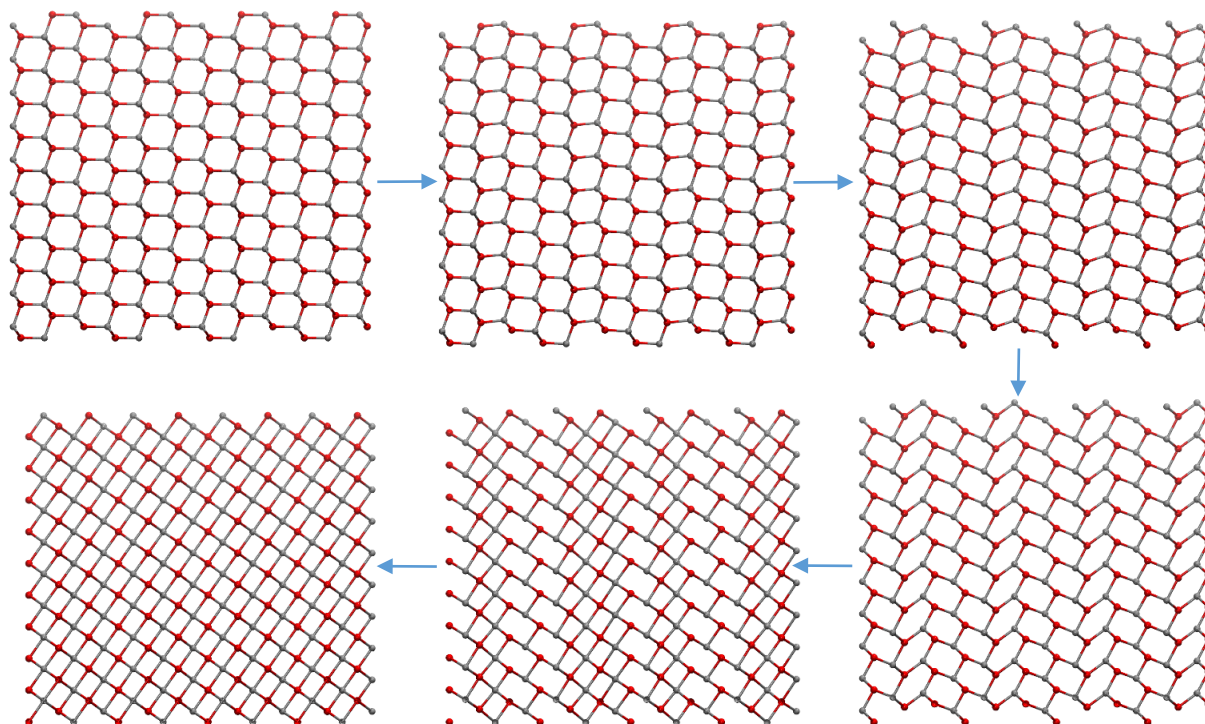


**Figure 5.x:** Snapshots of the two defined starting configurations, zincblende (top far left) and rocksalt (bottom far left), as well as a number of intermediates generated from the geometric trajectory. The intermediate configurations are generated by interpolation, giving a continuum of possible configurations between the two defined structures used in the model.

There are a number of ways in which one can generate an initial trajectory, which need not be representative of a plausible mechanistic pathway in any way – its only requirement is that it links the initial and final configurations of the transition event. However, it is extremely desirable for a first trajectory to proceed via a plausible, albeit geometric/collective transformation mechanism, as such an initial pathway is likely to require far fewer path

sampling iterations before decorrelation from the initial, disfavoured regime towards relevant mechanistic details.

The initial trajectory used in this work was generated using a geometric-topological approach, based on the transformation of *periodic nodal surfaces* (PNS). The atomic coordinates are mapped non-linearly from zincblende and rocksalt configurations, according to a set of particular modes of deformation defined within the model, to derive a dense set of interpolated intermediates. This is achieved by calculating a periodic nodal surface wrapped around the two limiting structures, with one species placed on the ‘positive’ side of the surface, and the other on the ‘negative’ side. The surface is chosen such that it develops in a way corresponding to the encoded transformation and deformation modes. This means that the entire transformation, as well as any intermediate configurations, can be defined by a single parametric expression. Thus, any point along this modelled trajectory may be extracted and used as a starting structure. Full details of the method can be found in the literature.<sup>[32,57,58]</sup>

Such a method gives a respectable initial trajectory, with a great deal of intermediates residing along the transition pathway. This is beneficial for a number of reasons:

- Starting configurations with very high energies, levels of strain, or other undesirable properties can be easily avoided, thus significantly reducing the number of iterations required by the path sampling procedure before initial trajectory decoherence;
- Independent transition path sampling calculations may, if desired, be started from very different initial pathways, or from a number of different starting configurations along the same pathway;
- The transformation and deformation modes encoded into the model can be modified at will. This means that specific features may be deliberately encoded (or avoided) into the initial pathway. This can have a number of advantages - for example, if a particular process is known to occur within the transformation mechanism, it can be encoded in to the initial path in order to greatly reduce the number of transition path

sampling iterations required. Additionally, a direct appreciation of the favourability of a particular model can be ascertained, by monitoring the conservation or disappearance of its overall transition motifs whilst the path sampling procedure is being performed.

#### 5.4.2.3. Finding a Dynamical Transition State

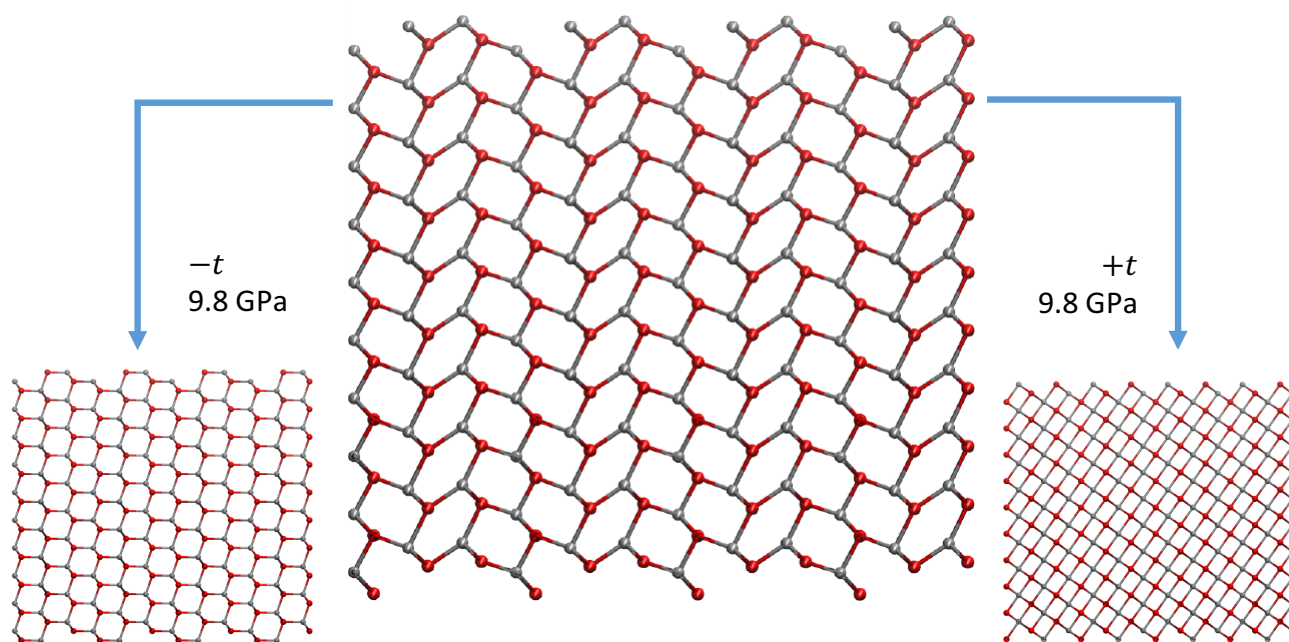


**Figure 5.xi:** Snapshots of dynamical transition state 0.37075 (centre), derived from the geometric model. Using molecular dynamics within the isothermal-isobaric ensemble at the transition pressure, propagation of this intermediate forwards and backwards in time gave the rocksalt (right) and zincblende (left) configurations of zinc oxide, respectively.

Using this initial trajectory, and the single parametric expression required to generate the interpolated intermediates, it was then necessary to find a suitable transition state that linked the two basins of attraction, zincblende and rocksalt. Intermediates were systematically generated and propagated using molecular dynamics within the  $NpT$  ensemble. A true dynamical transition state is one that, upon molecular dynamics propagation, arrives at one

of the basins of attraction when propagated forwards in time, and the other when propagated backwards. This is the point from which the transition part sampling algorithm may be initiated.

From the function used to define the states (with zincblende at 0 and rocksalt at 1), the intermediate 0.37075 yielded a dynamical mid-point which was subsequently used in the path sampling calculations.

#### 5.4.2.4. Defining the Order Parameter

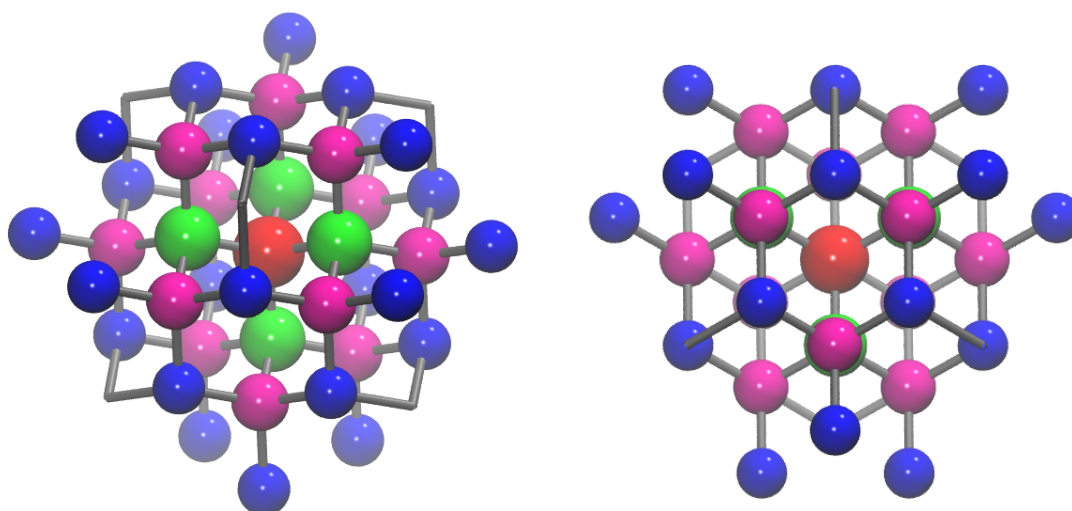


**Figure 5.xii:** Two illustrations of a small section of cubic zinc oxide, based around a central oxygen atom (red) and taken from two different perspectives. The atoms are coloured according to which shell of the coordination sphere they reside within, with respect to the central atom. The first three shells of the coordination sphere of the central are shown – the first (green), the second (magenta) and the third (blue). Zincblende has a first, second and third coordination number of 4, 12 and 24 respectively.

One of the few strict prerequisites of a transition path sampling calculation is that the initial and final configurations of the system must be strictly defined, in order that they may be distinguished from one other with absolutely no confusion (i.e., there is no overlap of their respective basins when projecting onto the order parameter).<sup>[48]</sup> Thus, the path sampling calculations require an *order parameter* to distinctly classify the zincblende and rocksalt phases of zinc oxide, as well as any intermediate configurations that may arise over the iterations of the procedure.

One of the most commonly used order parameters in path sampling calculations (and indeed, one of the most popular collective variables used in metadynamics) in the solid state is the average *coordination number* of the system. The coordination sphere is a set of integers:

$$\{n_1, n_2 \dots n_i \dots\}$$

where each number  $n_i$  corresponds to the number of neighbours separated from the central atom by  $i$  bonds. This quantity can be calculated for all atoms in a system, collated, and the mean value taken to give the average coordination number of the whole system. For example, the first three shells of the coordination spheres of the three phases of zinc oxide are:

zincblende	{4, 12, 24}
wurtzite	{4, 12, 25}
rocksalt	{6, 18, 38}

Thus, the average first coordination number (1<sup>st</sup> CN) of zincblende and rocksalt are 4 and 6, respectively.

In this work, the 1<sup>st</sup> CN of the system was defined as the order parameter, with a nearest neighbour cut-off of 2.7 Å – easily long enough to find all adjacent contacts, but not distant enough to detect centres within higher coordination shells. During the transition path sampling calculations, the coordination spheres of each atom were calculated up to the third shell, but only the 1<sup>st</sup> CN was utilised to dictate the progress of the path sampling calculations.



The 2<sup>nd</sup> and 3<sup>rd</sup> CNs were recorded simply to gain insight into the underlying details of the transition pathways.

The reasons that only the first coordination number was used were twofold:

- Utilising higher coordination spheres increases the likelihood of noise caused by local disorder and defects, which can wrongly lead to the categorisation of a ‘successful’ trajectory as a ‘failure’. It is desirable for the trajectory to evolve in the most ‘natural’ way possible, without any influence from a poorly constructed order parameter being exerted on the calculation;
- Using the first coordination shell only means there is no discrimination between the zincblende and wurtzite phases of zinc oxide. As the system is starting from a pure cubic structure, it was deemed interesting to see whether or not the system would stay within this regime, or move towards one more stabilised by the ground state.

It is important to note here that using the first coordination number as the order parameter exerts absolutely no bias on the calculations. The variation in the order parameter arises simply as a result of the application of the transition pressure to the system. Hence, monitoring the first coordination sphere does not force the system to evolve in any particular way over the course of the path sampling iterations. This is one of the details that distinguishes the *order parameter* used in path sampling calculations from the *collective variables* utilised in metadynamics.

#### 5.4.2.5. Transition Path Sampling Results

##### 5.4.2.5.1. Analysis of Data

For the mechanistic analysis, snapshots of the structures have been colour coded depending on their local coordination sphere, whereas in others have been coloured simply according to

species type. These analysis schemes are referred to as the *Coordination-Coloured* and *Species-Coloured* schemes, respectively. In the *Coordination-Coloured scheme*, zinc cations have been drawn as large spheres, whereas oxygen anions are displayed as the smaller globes. Species have been coloured according to their local coordination number.

Colour	Corresponding Species / Bond
Red	6 coordinate (RS)
Green	5 coordinate (iT / iH)
Dark Blue	4 coordinate (WZ)
Light Blue	4 coordinate (ZB)
Purple	4 coordinate (neither pure WZ nor ZB)
White	Not 4, 5 or 6 coordinate (defect)
Black	Zn-O Bond

**Table 5.xiii:** The colour code used to depict both the zinc and oxygen atoms in different coordination environments within the *Coordination-Coloured scheme*.  $\text{Zn}^{2+}$  and  $\text{O}^{2-}$  are depicted by large and small spheres respectively.

Coordination analysis was calculated by measurement of the number of nearest neighbour sites within the 1<sup>st</sup>, 2<sup>nd</sup> and 3<sup>rd</sup> coordination spheres of every zinc and oxygen atom, using 2.6 Å as the cut-off for nearest neighbour searching (taking periodic boundary conditions into account). It is noted here that, as only a small amount of 5-coordinate is usually found at the interface between other phases, distinguishing between *iT* and *iH* using this method is essentially impossible. Where necessary, discrimination between the two different five-coordinate phases has been carried out by analysing the angles between the five-bonded neighbours to the central atomic site.

In the *Species-Coloured scheme*, atoms are simply labelled according to their type with appropriate van der Waals radii – zinc atoms are labelled grey, whereas oxygens are labelled red. Bonds linking the two species are shown as red-grey lines.

#### 5.4.2.5.2. Overview

Once the dynamical trajectory and an order parameter had been defined, the path sampling procedure was initiated in order to generate the transition path ensemble. The following data are a statistical analysis of the converged subset of trajectories, corresponding to the likely pathways of transformation between the two configurations of interest.

One of the advantages of initiating the process from a reasonable starting trajectory is that it takes very few TPS iterations for the system to move away from the initial, unfavourable regime to a more probable one. This process is known as *trajectory decorrelation*. In fewer than 50 path sampling iterations, the procedure steered the trajectory away from the collective motion encoded by the geometric model and towards a regime which features a number of more nucleation events. The trajectories continued to evolve until no further major mechanistic changes were observed - known as *trajectory convergence*, this occurred after several hundred iterations of the path sampling procedure. Subsequently, very many successful trajectories were analysed and described.

The analysis seemed to show two different pathways of transformation:

- The first trajectory type proceeded by an abrupt change in coordination sphere, followed by a gradual transformation to the final product. This route could also be split into two categories – one which proceeded to the four-coordinate product, and another in which the material could enter into (and stay within) an intermediate five-coordinate basin;

- The second type followed a more step-wise route, featuring numerous abrupt changes to the average coordination sphere, including transition through a predominantly 5-coordinate intermediate.

Whilst both the forward and reverse trajectories showed instances of the two trajectory types, it was found that the first category of pathway was favoured for the high-to-low pressure transition, and the second pathway by the low-to-high pressure transition. To put it another way, whilst both directions of the transition could proceed via the two pathways, most of the successful iterations scrutinised tended to follow one particular transition scheme, depending on whether or not it was the 6-to-4 coordinate or 4-to-6 coordinate transformation.

In addition, both the ‘forward’ and ‘backward’ trajectories had a number of intriguing possibilities and derivative paths, depending on local geometry and fluctuations in external conditions. Such competitive behaviour between possible transition routes has been well described previously, and is both supported by and supports the wealth of literature on the nature of phase transitions involving intermediate schemes, nucleation and growth, as described in the literature review.

#### 5.4.2.5.3. The ‘High-to-Low Pressure Phase’ Transition

The first indication of trajectory decorrelation from the initial geometric scheme was the presence of a distinctive shear along (300), preceded by the rapid creation of a ‘seed’ at around 460 fs, which grows orthogonally to the shear. The ZnO motifs that compose the seed are primarily of a cubic geometry. The formation of this seed and shear accompanies a pronounced initial decrease in volume. This is unexpected, as at the same time, numerous local configurations of rocksalt deform into hexagons, which rapidly propagate to form the seed.

The composition of the shear is a mixture of five, six and higher-coordination defects, which certainly contributes to the overall high-density measurements seen here. However, the seed is predominantly four-coordinate in nature, shifting between zincblende, wurtzite and low-coordination defects. The outer edge of the seed is surrounded by the five-coordinate intermediate, corresponding to both the  $iT$  and the  $iH$  structures, depending on the local geometry. This can clearly be seen in image iii) of Figure 5.xiv, presented overleaf.

These seed and shear structures contain an extraordinary wealth of coexisting ZnO structures, including zincblende, wurtzite, rocksalt, tetragonal and trigonal bipyramidal, as well as other localised defects caused by the rapid shearing and initial compression. It is therefore not surprising that the exact nature of the seed plays a significant role in the next stage of the transition.

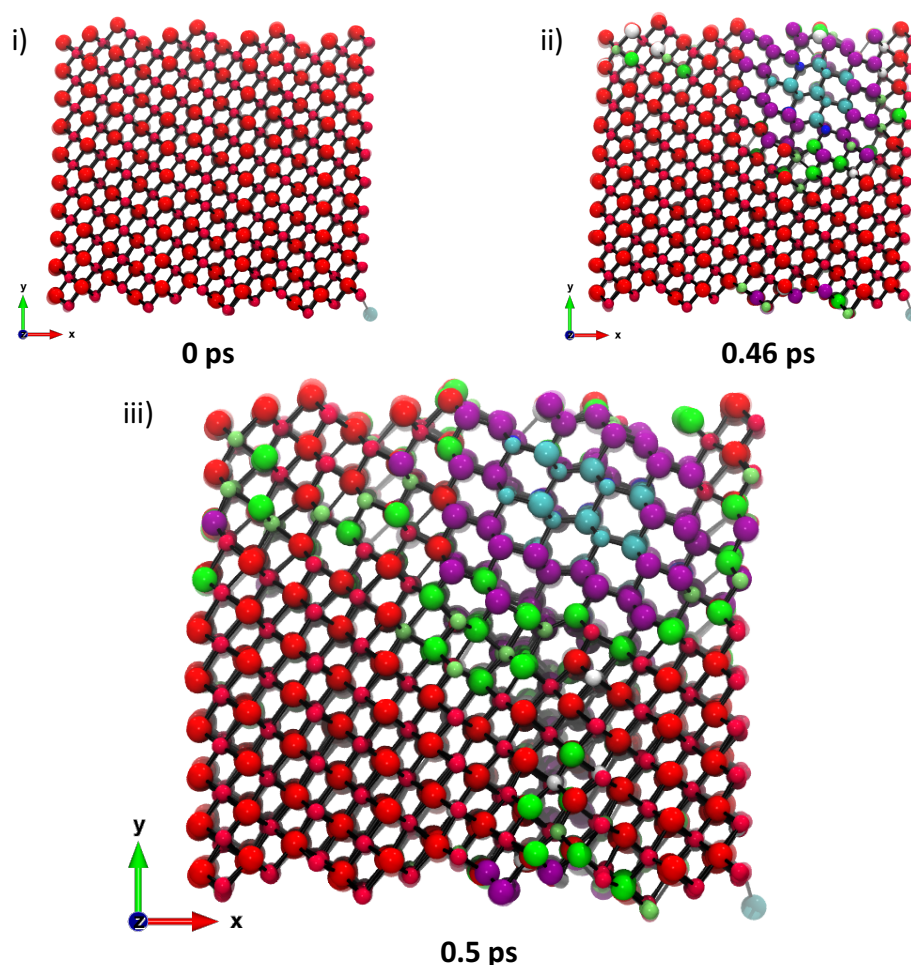


**Figure 5.xiv:** (previous page) *Coordination-Coloured* illustrations showing how the rapid compression forces the pure rocksalt structure (i, top left) to form a small region of four-coordinate ZnO, which is predominantly cubic in nature (ii, top right). The strain caused by the cubic deformation region causes the structure to buckle in the (300) plane, creating a distinctive shear made of distorted four, five and six coordinate ZnO (iii, bottom).

For a time, continued propagation is accompanied by a continued decrease in volume. In a number of trajectories, the cubic seed migrates around the system for some time, moving from the ‘edge’ to the ‘centre’ of the frame and occasionally back again. Whilst in a periodic system such geometric descriptions are largely irrelevant, it does illustrate that oscillation between the two phases can occur at the beginning of the trajectory, and that zinc oxide is able to rapidly convert between four, five and six coordinate material any time after this initial volume compression at the transition pressure.

It is at this point that this trajectory type may proceed in two different ways, depending on the rate of the initial compression – one of which leads to trajectory success, and the other to failure.

Trajectories that are compressed *more rapidly* (see Figure 5.xvi) in the early stages of the transformation tend to form an almost entirely 5-coordinate intermediate, denoted RS-*iH*, within the first picosecond of simulation, with the presence of some regions of rocksalt and high-coordination defects. Such unusual defects presumably arise from an inability of those regions to crystallise in an orderly way, due to the rapid transformation processes that take place once the cubic seed has undergone initial growth. However, such defects (and in particular the rocksalt ‘sandwiching’) may confer stabilisation to this five-coordinate intermediate - this is backed up by the fact that such mixed material persist for a very long time (at least 500 ps!) in subsequent molecular dynamics simulations, indicating the metastability of this mixed phase.

It is worth noting here that the presence of an energy basin which is not vital to the transformation that corresponds to a five-membered intermediate along the transition pathway directly correlates with previous work in the literature, including the previous work

of Boulfelfel *et al* in their studies of the B4 – B1 phase transition of zinc oxide.<sup>[32]</sup> This work does also show conclusively that the nature of this intermediate is the *hexagonal iH* form, and that this metastable intermediate contains no trace of the tetragonal analogue.

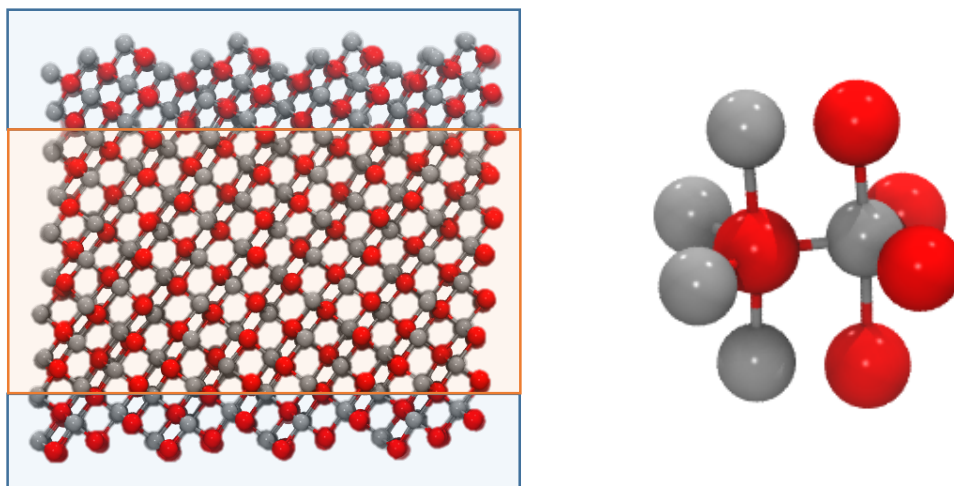


**Figure 5.xv:** *Species-Coloured* illustrations of the almost totally 5-coordinate system RS-*iH* (left), which is occasionally visited when a trajectory undergoes significant volume contraction during the formation of the cubic seed. 5-coordinate regions are highlighted in orange, whereas rocksalt regions at the peripheries are highlighted in blue. The atomic arrangement of the five-coordinate material here consists entirely of the trigonal bipyramidal type (right), giving rise to the hexagonal *iH* structure. No trace of the tetragonal form is found in this type of intermediate, which closely agrees with the previous studies of Boulfelfel *et al* on zinc oxide.

However, it is also hypothesised that the metastability of the *iH* material has been significantly over exaggerated in this work, as a result of the transition path sampling algorithm consistently rejecting such trajectories as they do not start or end in the zincblende basin. It is speculated that the material should eventually fully transform or revert back to the rocksalt structure, and that this represents a transient intermediate. Nonetheless, an investigation into whether or not the transformation could be quenched to retrieve the five-coordinate

structure would be an interesting future pursuit.

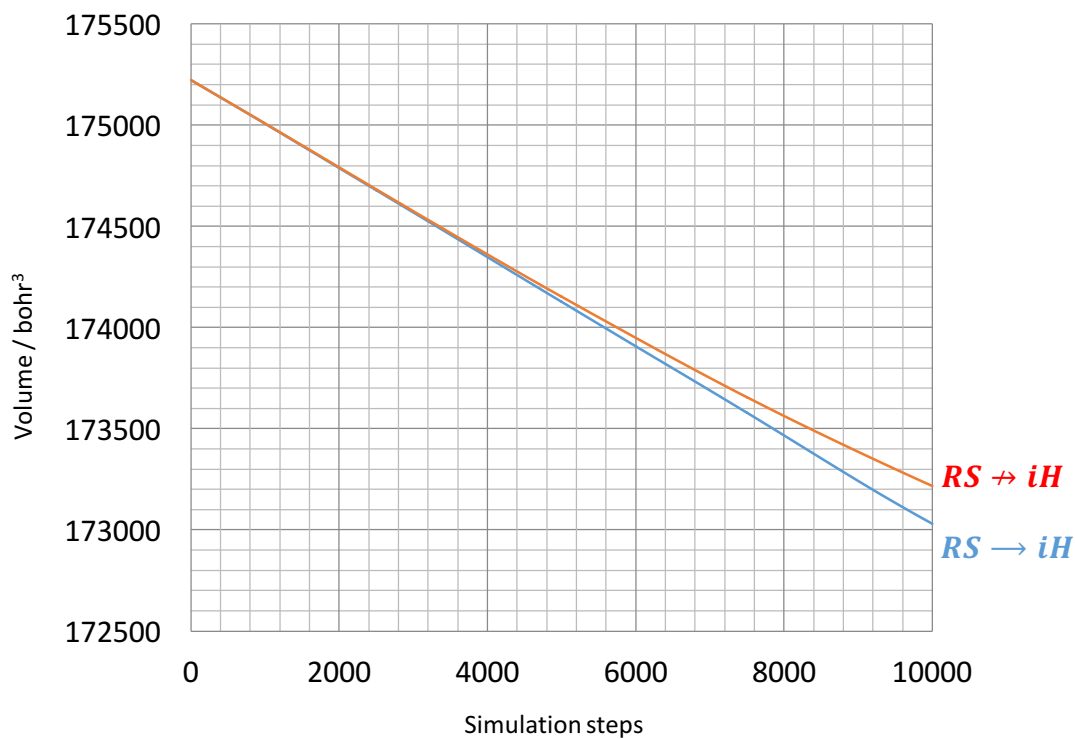


**Figure 5.xvi:** Graph to show the difference in volume over the first 10,000 steps of MD for trajectories that proceed from rocksalt successfully to the four-coordinate ZnO, and those which visit the five-coordinate basin. Trajectories that visit the *iH* structure undergo much greater volume contraction at the formation of the cubic seed motif.

The second possibility, which occurred in trajectories which successfully transformed to four-coordinate zinc oxide, involved systems in which the initial compression was not as extreme as in those that form the *iH* intermediate.

In such regimes, the system containing the cubic seed still underwent a brief decrease in volume, but the compression was not as rapid nor as considerable as in trajectories which proceed to an almost entirely five-coordinate intermediate. Generation of volume profiles over the first steps of representative trajectories shows that the volume decrease is significantly less marked for successful trajectories, compared to those that fall into the



metastable  $iH$  basin. This less-compressed type of configuration allows for the trajectory to proceed via a transition pathway that does not include a complete conversion to the five-membered structure.

In these cases, a very rapid transferal from volume compression to decompression occurs, causing rapid expansion of the cubic seed and deformation of the rocksalt ‘squares’ into four-coordinate ‘hexagons’ at around 700 fs.

Often, this proceeds via configurations that contain significant amounts of isolated 5-coordinate intermediate. This 5-coordinate material tends to be  $iH$  in nature, however  $iT$  has been documented in some of the trajectories and is present in trace amounts. The four-coordinate material seen at this stage has a cubic geometry, but is not a perfect zincblende topology as a result of the manifold defects and distortions present in the structure. This cubic structure grows and relaxes at the expense of the denser rocksalt structure for the remainder of the simulation, causing the volume of the material to steadily expand. There is a pronounced shift at around 4 ps, when the last remaining rocksalt motifs are transformed. Thereafter, the decompression ultimately leads to the formation of an entirely four-coordinate zinc oxide material, after approximately 6 ps of simulation.

Fascinatingly, the final outcome of the procedure is not a pure zincblende structure, but a mixed hexagonal-cubic phase dominated by the wurtzite form. In all successful procedures, the final material consists of only 10-20% zincblende, with the remainder of the structure formed by the more stable hexagonal form. The reason for this is likely to be because only the first coordination number was used as the order parameter, which is identical for the wurtzite and zincblende configurations. Thus, the more stable wurtzite was ultimately preferred by the transition path sampling, leading to a predominantly hexagonal final structure.

Had the third coordination shell also been used, a trajectory forming a completely cubic structure might have been realised. By removing this bias, it is believed that this is a much more plausible transition event for zinc oxide at 9.8 GPa and ambient temperature. Although the aim of this work was to elucidate a phase transition linking the high pressure rocksalt and metastable zincblende polymorphs, this transformation represents a plausible transition at

ambient temperature and the pressure of transition. In addition, such mixed structures are themselves very interesting; for example, materials with internal interfaces between different phases are of great interest in electronics and thermoelectric materials as a result of their ability to conduct electricity but scatter phonons at the inter-layer boundaries.

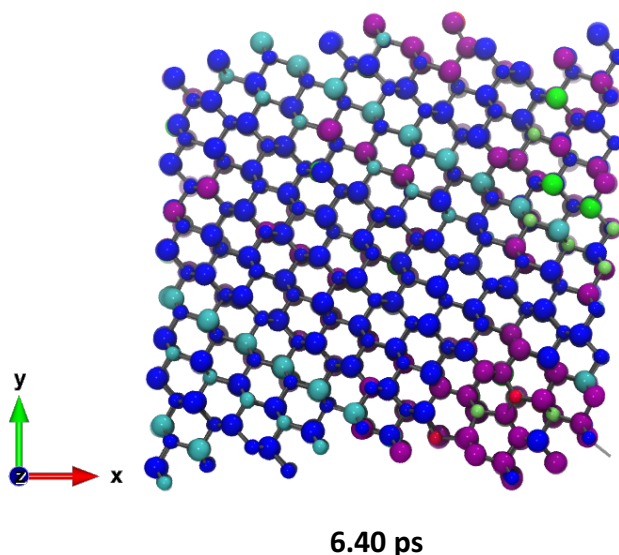


**Figure 5.xvii:** *Coordination-Coloured* illustration showing a frame of the final zinc oxide material formed by the transition. Large regions of hexagonal wurtzite (dark blue) can be seen, with some interpenetrating regions of zincblende (light blue). In addition, some defect regions of uncharacterised four-coordinate (purple) and some 5-coordinate remnants (green) are present, which rapidly oscillate in and out of existence when propagated with molecular dynamics.

Coordination analysis of the entire 6-to-4 trajectory shows an abrupt, step-wise change in coordination sphere at approximately 500 fs, corresponding to the formation of the cubic seed and orthogonal shear. The remainder of the trajectory is characterised by a gradual decrease in coordination number, corresponding to the steady transformation of rocksalt into the four-coordinate form, occasionally via the hexagonal 5-coordinate intermediate.

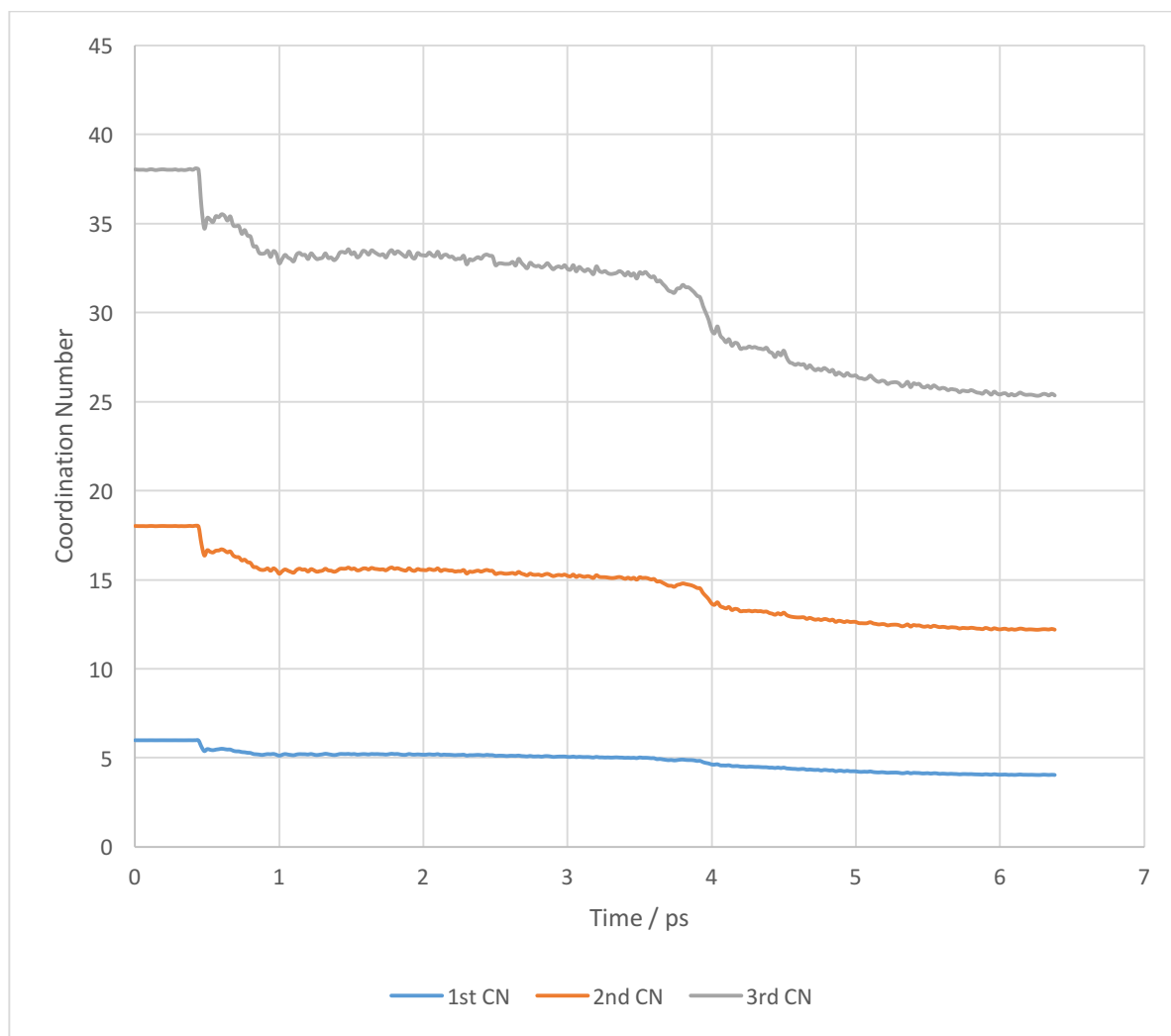


**Figure 5.xviii:** Graph showing the first, second and third coordination spheres over the course of an entire successful transformation from rocksalt to wurtzite-zincblende. The starting rocksalt structure suddenly decreases in coordination upon the formation of the cubic seed at around 500 fs. This leads to the gradual decompression and transformation to four-coordinate ZnO, often via isolated pockets containing the five-coordinate intermediate, with a pronounced shift at around 4 ps when the last rocksalt motifs are transformed. The final structure is a mixed wurtzite-zincblende system after approximately 6.4 ps

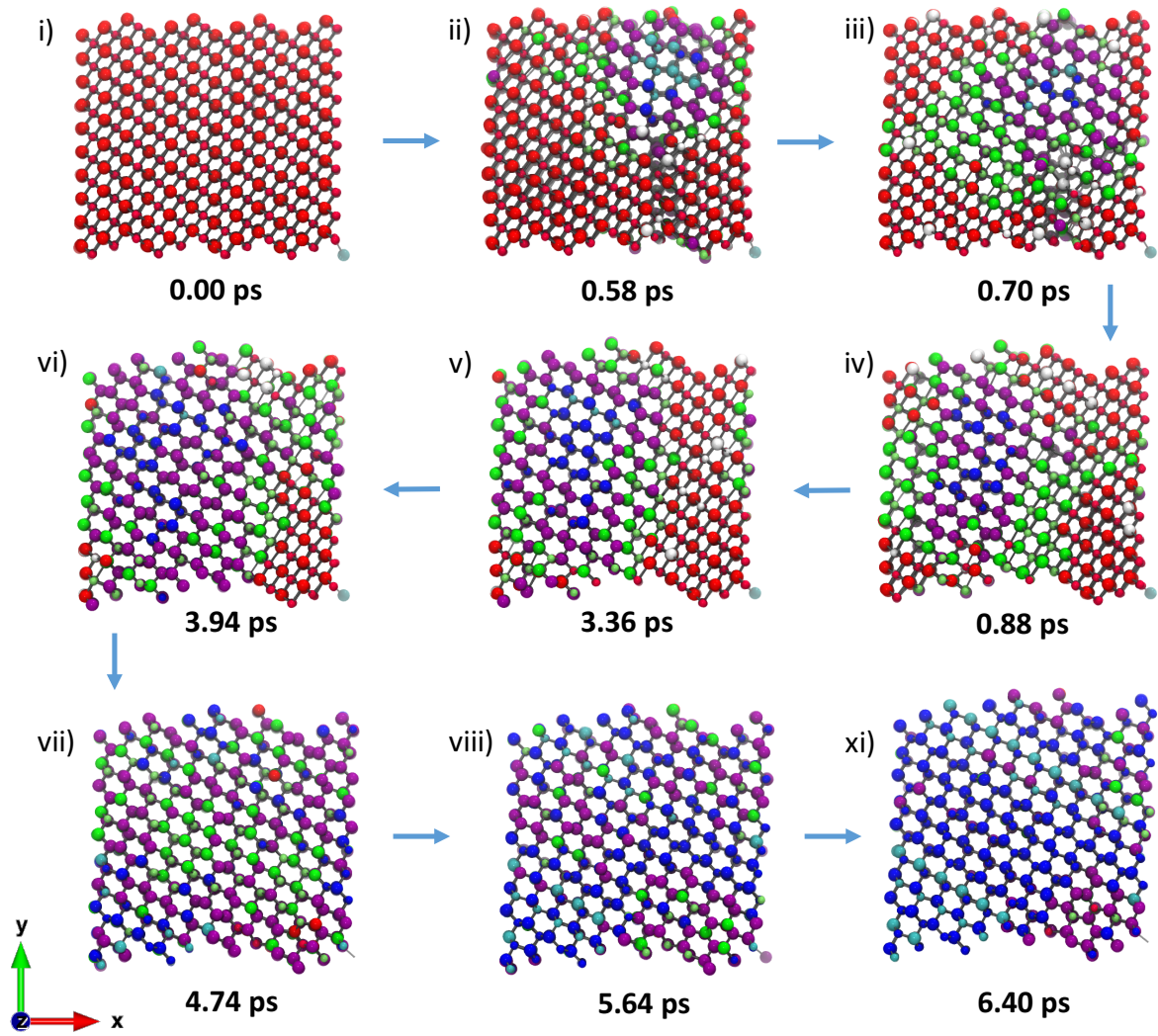


**Figure 5.xix:** *Coordination-Coloured* snapshots, showing the complete sequence from rocksalt to the mixed zincblende-wurtzite phase. The rocksalt system (i) forms the cubic seed within the first 500 fs, with subsequent sheering along the (300) plane (ii). This cubic seed grows orthogonally to the sheer over the next 300 fs (iii and iv) until a large section of the system is occupied by four and five coordinate material (v and vi). Gradually, all of the rocksalt motifs are decompressed to form hexagons (vii and viii) over the next 3 ps, with a pronounced change at around 4 ps when the last rocksalt motifs are eliminated. This eventually results in a complete four-coordinate material (save some defect sites), which is composed primarily of hexagonal wurtzite (ix).

5.4.2.5.4. The ‘Low-to-High Pressure Phase’ Transition

A typical four-coordinate to six-coordinate transition occurred via a slightly different pathway to the high-to-low pressure transformation, featuring (on average) more concerted events along the course of the transition. This could go some way to explaining the notable hysteresis observed in zinc oxide phase transitions and the role of the five-membered intermediate in the phase transition.

In this trajectory type, the entire starting four-coordinate material is first briefly distorted into a pseudo-cubic geometry, until further compression forces most of the Zn-O motifs into the five-coordinate *iH* structure. However, this is a gradual process and varies from trajectory to trajectory, dominating up to the first 4 ps of simulation time. Thus, over half of the time in of this transformation is spent slowly squeezing the system until it can transform into the five-coordinate *iH*, indicating the presence of a deep but fairly gently-sloping energy barrier separating the WZ-ZB basin and the intermediate configurations.

Unlike in the successful trajectories from rocksalt to the four-coordinate ZnO, the *iH* regions in this configuration are relatively long-lived, and it appears that all of the wurtzite-zincblende motifs go through the following sequence en route to the rocksalt product:



This is not the same as the reverse transition, as in this case *iH* regions were formed and quickly eliminated, with the majority of the simulation time instead being dominated by coexisting four- and six- coordinated motifs.

Thus, for this trajectory route, it appears that local conversion to the *iH* intermediate is mandatory and time consuming, and that the system does not remain in this configuration permanently. However, transient *iH* configurations can be seen for approximately 2.5 ps of the simulation. Once again, very small traces of the tetragonal intermediate *iT* are present, but by far the predominant intermediate form is the hexagonal analogue.

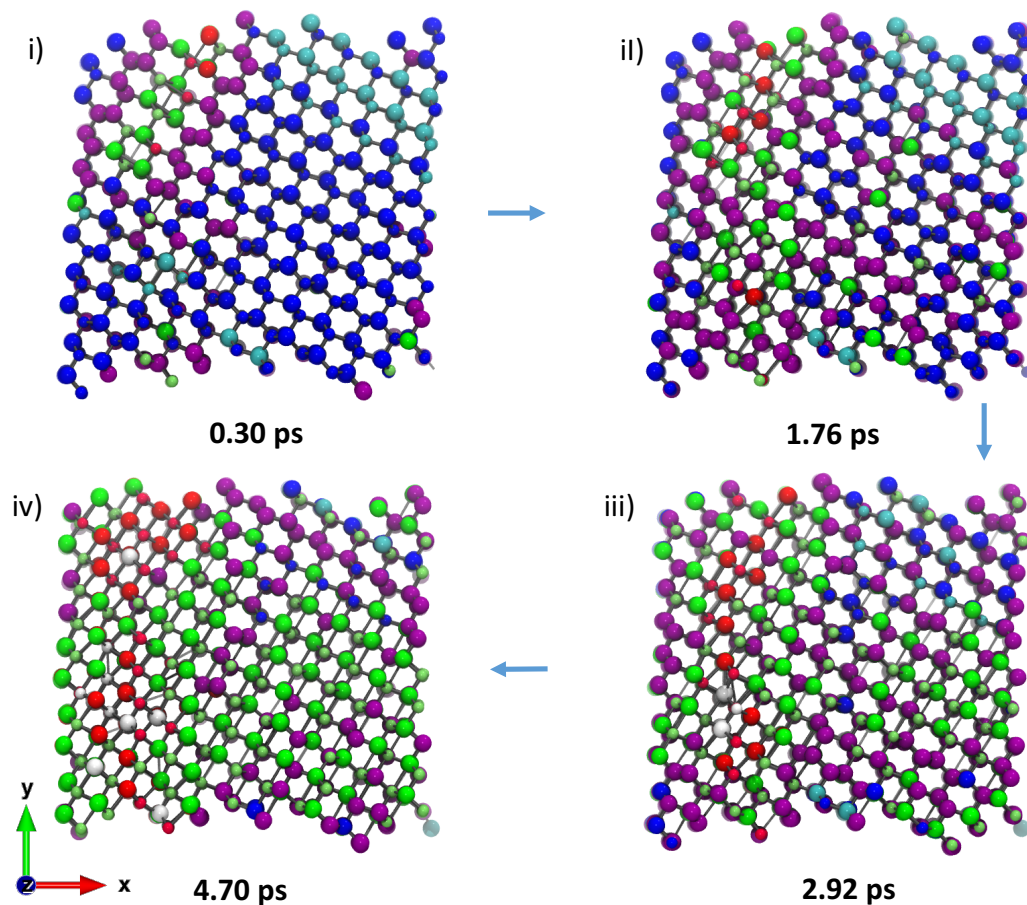


**Figure 5.xx:** *Coordination-Coloured* cartoons showing the transformation from a mixed wurtzite-zincblende system, through the distorted four-coordinate structure into the hexagonal five-coordinate *iH*. Following this, epitaxial growth of rocksalt converts the *iH* 5-coordinate sites into the 6-coordinate NaCl-like structure.

Epitaxial growth of the rocksalt structure then sweeps across the system, growing from the hexagonal *iH* intermediate as a result of the increasing pressure. This appears to proceed in a step-wise fashion, with three distinctive transformation events taken place during the final picosecond of the simulation; the first two steps involve rapid transformation of *iH* motifs to rocksalt, whereas the final event involves the transition of the cubic island, the last region of four- and five- coordinate material, to six-coordinated ZnO. This final step is equal and opposite to the first step in the reverse mechanism, and completes the transformation from the wurtzite-zincblende mixture to the pure rocksalt final product.

It is evident, in terms of the coordination sequence, that this is a much more stepwise process than the rocksalt to wurtzite-zincblende transition. Passage through a predominantly five-coordinate intermediate configuration can clearly be seen. However, unlike the ‘failed’ trajectories seen in the reverse transition, this corresponds to localised regions of metastable *iH* forming before the system transitions to rocksalt through a number of rapid growth events.

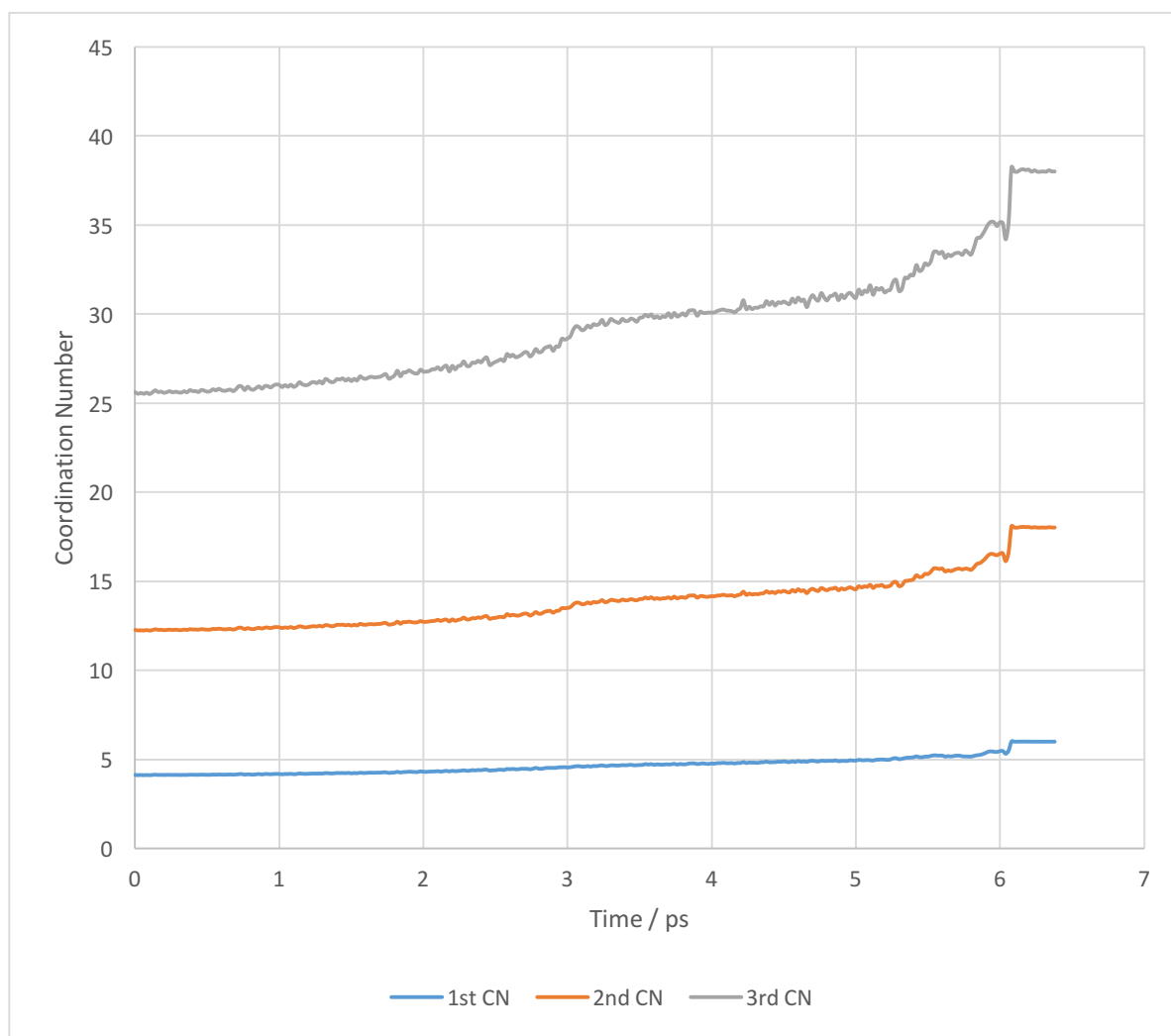


**Figure 5.xxi:** Coordination sequence analysis of the transformation from a mixed wurtzite-zincblende system to the rocksalt phase. Gradual compression of the starting material causes individual motifs to transform to rocksalt via the *iH* intermediate, which can be long lived in this pathway. The final segment (1 ps) is associated with three rapid transformation events, corresponding to quick epitaxial growth of rocksalt at the expense of four-coordinate and *iH* ZnO.

## 5.5. Free Energy Calculations

### 5.5.1. Introduction to “Metashooting”

In order to better understand the competitive nature of different mechanisms on the potential energy surface, the free energy (FE) was evaluated by coarse-graining the potential energy surface onto a suitable set of collective variables. Since free energy calculations are rare in mechanistic investigations of solid-solid transformations, the work presented here is perhaps the most novel aspect of the results discussed within this chapter.

Free energy surfaces are commonly calculated and employed in many computational chemistry and physics calculations. Such calculations have found extensive use for description of biological systems (in particular peptide calculations).<sup>[59,60]</sup> However, to the knowledge of the author, no such calculations have yet been calculated for solid-solid phase transitions. The reasons for this include that:

- The energy barriers associated with a solid-solid phase transition are significantly higher than those that need to be overcome by molecular systems. For example, the energy barrier associated with the rotation of a peptide bond is in the order of  $10^1$  kJ mol<sup>-1</sup>, whereas the barriers associated with a phase transition with a meaningful number of atoms can be many of magnitudes of order higher. This means that methods used to generate free energy profiles of this type are still prohibitively expensive;
- Metadynamics calculations, and their subsequently associated free energy profiles, have found use in structure prediction; however, generated *metatrajectories* frequently contain fewer details compared to path-oriented approaches and seldom show realistic trajectories linking two basins of interest. Thus, categorising a dynamical transition pathway in this way, including all transition states and intermediates, could be prohibitively expensive. In addition, the configuration space



required to be sampled could be very vast, especially for systems with a large number of atoms.

As such, it was deemed desirable to develop a method that efficiently and effectively filled the underlying energy landscape over the course of the trajectory determined by the transition path sampling iterations. This way, computing time would not be expended by filling other regions of the configuration space that had no relevance to the transition, as any attempts to characterise the free energy would only occur in the space of the trajectory. Thus, convergence of the problem could easily be monitored. In addition, mechanistic details acquired from the transition path sampling procedure would remain unspoiled by the metadynamics procedure. As the process is driven by the converged path sampling trajectories, the relevant basins to the transformation will be filled in a *balanced* way – starting from the two known configurations, and finishing with the characterisation of the relevant transition states and intermediates.

To this end, a novel combination of the shooting algorithm from the transition path sampling procedure and metadynamics was developed, tentatively dubbed *metashooting*. The general procedure of the *metashooting* algorithm is as follows:

- i. Starting from a dynamical midpoint along the TPS-converged trajectory, shoot the system such that it transforms to configuration A;
- ii. When residing in basin A, apply a metadynamics scheme for a discrete number of steps, in order to partially fill the as-yet uncharacterised energy well;
- iii. Once the metadynamics iteration has finished, re-shoot from the original dynamical midpoint back to basin A – this time, on top of the biased potential. Thus, the trajectory should be prohibited from returning the points in configuration space in basin A now disfavoured as a result of the applied bias potential. Shooting back to the basin on top of the bias potential ensures that the trajectory still remains on course and stay based on the true dynamics. In addition, this corrects the velocity

distribution such that it corresponds to a *true* TPS trajectory, not one artificially modified by the metadynamics run, allowing for the run to be analysed;

- iv. Steps 4-6 are essentially a mirror repeat of steps 1-3 on the ‘other half’ of the trajectory and with any bias potential accrued from the previous steps carried over. This time, starting from the dynamical midpoint used in step 1, shoot the system such it travels along the trajectory path to basin B.
- v. When residing in basin B, apply a metadynamics scheme for a number of steps to partially fill the second basin of attraction;
- vi. Once again, re-shoot from the dynamical midpoint on top of the bias potential back to configuration B. At this point, shift the dynamical midpoint slightly, such that the starting point of the procedure is not static and is not ‘pinned’ to a false maximum.
- vii. Repeat the above iterations until the underlying free energy profile is fully converged.

Repeated iterations of the *metashooting* algorithm enable the free energy landscape corresponding only to the courses of the transition path sampling derived trajectories to be built up in a step-wise and equally distributed manner, and such that regions around the transition states are considered at the end of the analysis, avoiding any potential bias that may scramble the mechanistic analysis.

The algorithm should first fill up the two starting basins of attraction from the final TPS trajectories (in this case, the wurtzite-zincblende mixture and rocksalt). Eventually, visiting these regions should become discouraged as a result of the bias potential deposited by the metadynamics scheme (steps 2 and 5). Towards the end of the simulations, the free energy should be characterised for the connecting regions of the trajectory, until the ‘forward’ and ‘backward’ steps meet in the central region. The progress of this can be monitored by viewing the history-independent Gaussian deposition, or constructing a histogram of how many Gaussians have been deposited over the CV space over the entire procedure.

Eventually, the *metashooting* algorithm should fully characterise the central and peripheral regions of the CV space over the course of the trajectory. Convergence will be seen in a similar way to a standard metadynamics scheme – that is, the underlying free energy landscape should no longer significantly change with further iterations of the procedure. At this point, meaningful analysis of the intermediates, the transition states, and the energy barriers associated with each process can be carried out.

Measuring the free energy landscape in this way should have a number of advantages to traditional ‘path’ based analyses of phase transitions, as carried out in the previous section. Firstly, it allows for a complete quantitative analysis of the underlying thermodynamics and kinetics of the process; measurement of activation energy and change in free energy between different steps of the procedure, as well as the starting and finishing products, can be trivially taken from the plot. Moreover, intermediates and transition states that are vitally important to the transformation will appear obvious along the reaction scheme. Such insight into trajectories using ‘path’ based analyses of transformations only is not trivial – indeed, it relies heavily on chemical and physical intuition, and it would be facile to miss important mechanistic details or intermediates along the path. Using the free energy analysis on the transition path sampling trajectories allows for quantitative and detailed analysis of almost every aspect of the transition pathway; the free energy landscape can be thought of as the surface upon which trajectories travel, and individual characteristics of the trajectories are determined by which regions of the surface are visited.

Such detail and precision is achieved here using path sampling and metadynamics methods in conjunction, in a non-trivial way. Without the *shooting* element, there would be no new trajectory generation nor any path sampling converged trajectories on which to apply metadynamics. Without metadynamics, there would be no framework for the deposition of Gaussians and the surveying of the underlying energy landscape. As a result, *metashooting* is laying the foundation for future routine investigation of complex processes, and offers an intriguing new paradigm into the elucidation of phase transitions in condensed phases.

5.5.2. Methodology

Details pertaining to the molecular dynamics runs and how the atoms in the system are described are identical to those described in 5.4.1. Information specific to implementation to the *metashooting* algorithm are described in this section.

Metadynamics calculations were carried out using the *plumed* plug-in,<sup>[61]</sup> coupled with the *cp2k* package. As the procedure had not been attempted previously and the metadynamics parameters for a solid-solid transformation between 1,200 pairs of atoms was unknown, a great deal of experimentation was required in order to ascertain the correct variables required for both an efficient and precise calculation. Several metadynamics schemes were tested, including the *well-tempered*<sup>[62]</sup> and *multivariate-Gaussian*<sup>[63]</sup> adaptations to the method, in addition to the standard implementation. Additionally, a great deal of experimentation with both the nature of the collective variables, and the dimensions of the Gaussian functions projected onto their respective spaces, was required. In the end, metadynamics within the *well-tempered* scheme was used without the adaptive Gaussian adaptation.

The collective variables utilised in the metadynamics runs corresponded to the first and third coordination spheres of the zinc oxide systems - similar to the order parameter used in the transition path sampling calculations. The coordination sphere in *plumed* is defined using a switching function, in order for the variable to be differentiable:

$$s(r) = \frac{1 - \left(\frac{r - d_0}{r_0}\right)^n}{1 - \left(\frac{r - d_0}{r_0}\right)^m} \quad [Eq\ 5.4]$$

where  $r$  is simply the distance between a Zn-O contact and  $d_0$ ,  $r_0$ ,  $m$  and  $n$  are adjustable parameters. The switching function returns a value between 0 and 1 for each contact. Once the coordination value between 0 and 1 is calculated for each Zn-O pair, the coordination sphere average for the system is calculated. As both the first and third coordination

sequences involve coordination between a zinc and an oxygen atom, only distances between Zn-O contacts were calculated (i.e. Zn-Zn and O-O distances need not be calculated, as only coordination sequences to the order of even numbers require these quantities). The parameters  $d_0$ ,  $r_0$ ,  $n$  and  $m$  must be ‘tuned’ in order to give the correct distribution of variables – i.e. to give an appropriate first and third coordination sequence for zincblende, wurtzite and rocksalt ZnO.

CN	$d_0$	$r_0$	$n$	$m$
1 <sup>st</sup>	2.6	0.1	6	12
3 <sup>rd</sup>	5.3	0.1	6	12

**Table 5.xxii:** The parameters used to calculate the first and third coordination spheres for the *plumed* metadynamics collective variables.

The values obtained for the third coordination sphere were slightly exaggerated for zincblende and wurtzite ZnO, but correct for rocksalt when using this *plumed* function. However, this had no bearing on the integrity of the final result, and this collective variable will hence be referred to as the *pseudo*-third coordination sphere, in order to distinguish it from the *true*-third coordination sphere based on a purely geometric approach.

Gaussian functions were deposited on the underlying energy landscape every 500 simulation steps. 5 metasteps were calculated on each side of the trajectory during each iteration. This is rapid enough to efficiently fill the basins and escape energy minima, but slow enough for the system to evolve by molecular dynamics. The height of the Gaussians was set at 1000 kJ mol<sup>-1</sup> – arguably very high, but this was necessary due to the extremely deep energy wells associated with a solid-solid system containing 2400 atoms. The Gaussian widths were chosen in accordance with the variance of the CV in an unbiased simulation – as such, these were set to 0.2 and 1.0 for the first coordination number and the pseudo-third coordination number respectively. The well-tempered ‘bias-factor’ was set at 10000, which again is necessary to escape the minima and re-scale the deposited Gaussians within a meaningful time frame.

### 5.5.3. Results and Discussion

#### 5.5.3.1. Overview

Once the transition path sampling trajectory had converged, the free energy profile was constructed using the *metashooting* technique as described in 5.5.1. After 250 iterations of the *metashooting* procedure, the free energy landscape had fully converged, showing details of the mechanistic process including important intermediates, transition states and activation barriers. Running on 32 cores, on average three *metashooting* iterations were completed each day – thus, with the set up used, the entire procedure took around three months to converge upon the final energy profile.

The results of the *metashooting* procedure are given below. The evolution of the free energy landscape according to the *metashooting* algorithm is first discussed, followed by an analysis of the final profile generated by the procedure and its inexorable relationship to the underlying mechanism exhibited by the transition path sampling procedure.

#### 5.5.3.2. Evolution of the Free Energy Surface

The first few iterations of the procedure accumulated Gaussian functions only within the two known basins (zincblende-wurtzite and rocksalt). A small ‘shoulder-peak’ was immediately present in the four-coordinate basin, as a result of the oscillation between different forms of the low coordination material, including zincblende, wurtzite and other forms which were four-coordinate in the first coordination sphere but whose *pseudo*-third coordination sphere did not correspond to zincblende nor wurtzite.

After 50 iterations, a notable ‘shoulder-peak’ was evident adjacent to the rocksalt basin, and by 150 iterations that had resolved into a *bona fide* minimum (labelled on the plot as i-1). By iteration 200, a second minimum centred half-way between the two main basins appeared, which had fully resolved by iteration 225 (labelled i-2). By 250 iterations, the plot was fully

converged – the energy barriers and positions of minima on the plot remained largely unchanged with any further iterations of the metashooting procedure.

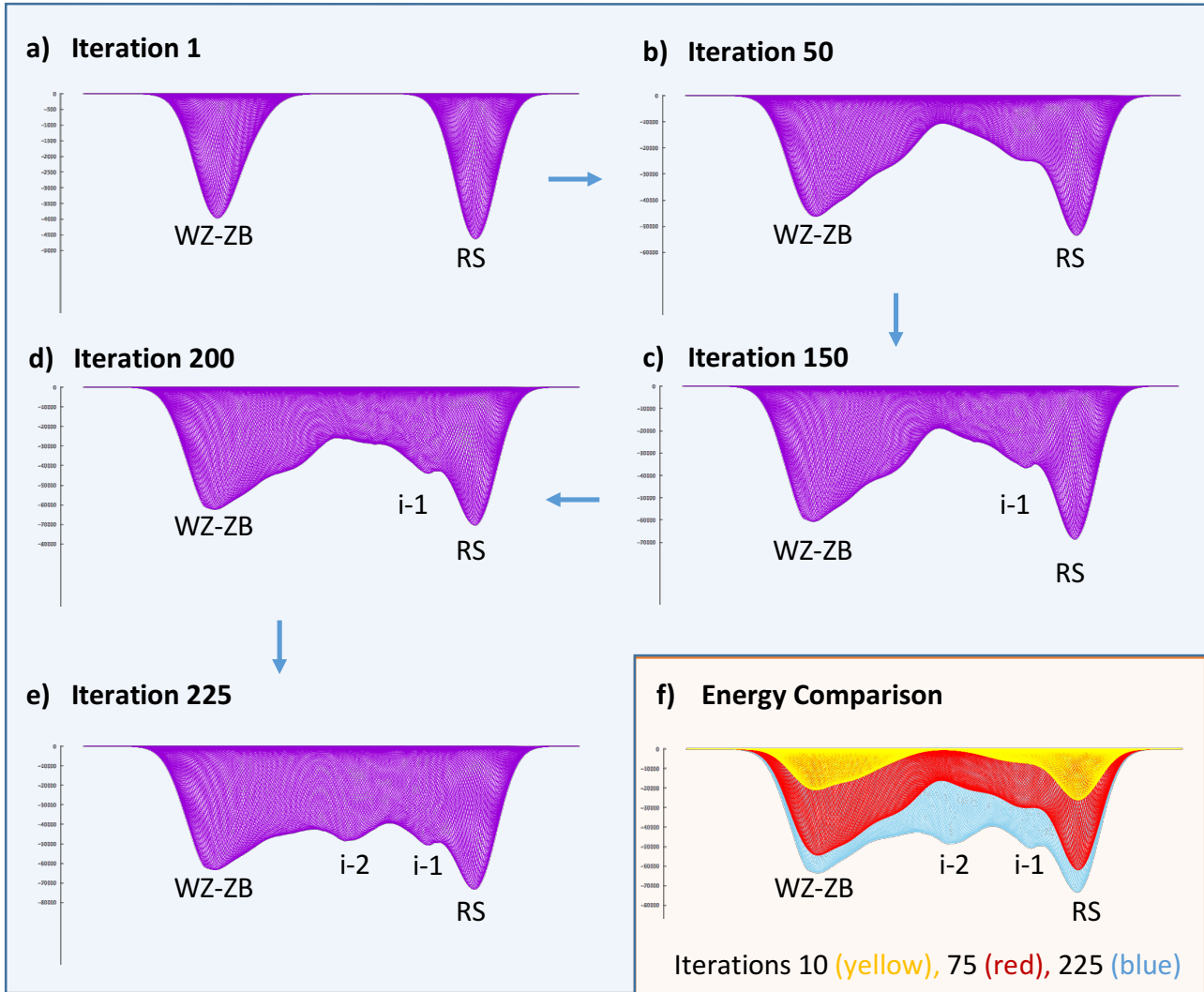


**Figure 5.xxiii:** Sequence of plots showing the free energy at different points during the metashooting procedure. Plots a) to e) demonstrate the development of the free energy surface after a different number of iterations of the *metashooting* algorithm. Note that the  $y$ -axis scale is not the same in each graph and grows larger as the algorithm proceeds, as a result of the free energy landscape deepening from the deposition of Gaussians during the metadynamics steps. For comparison of the energy, three energy plots have been plotted together in f) (bottom right) to highlight how the energy minima and maxima have progressed over the course of the *metashooting* iterations.

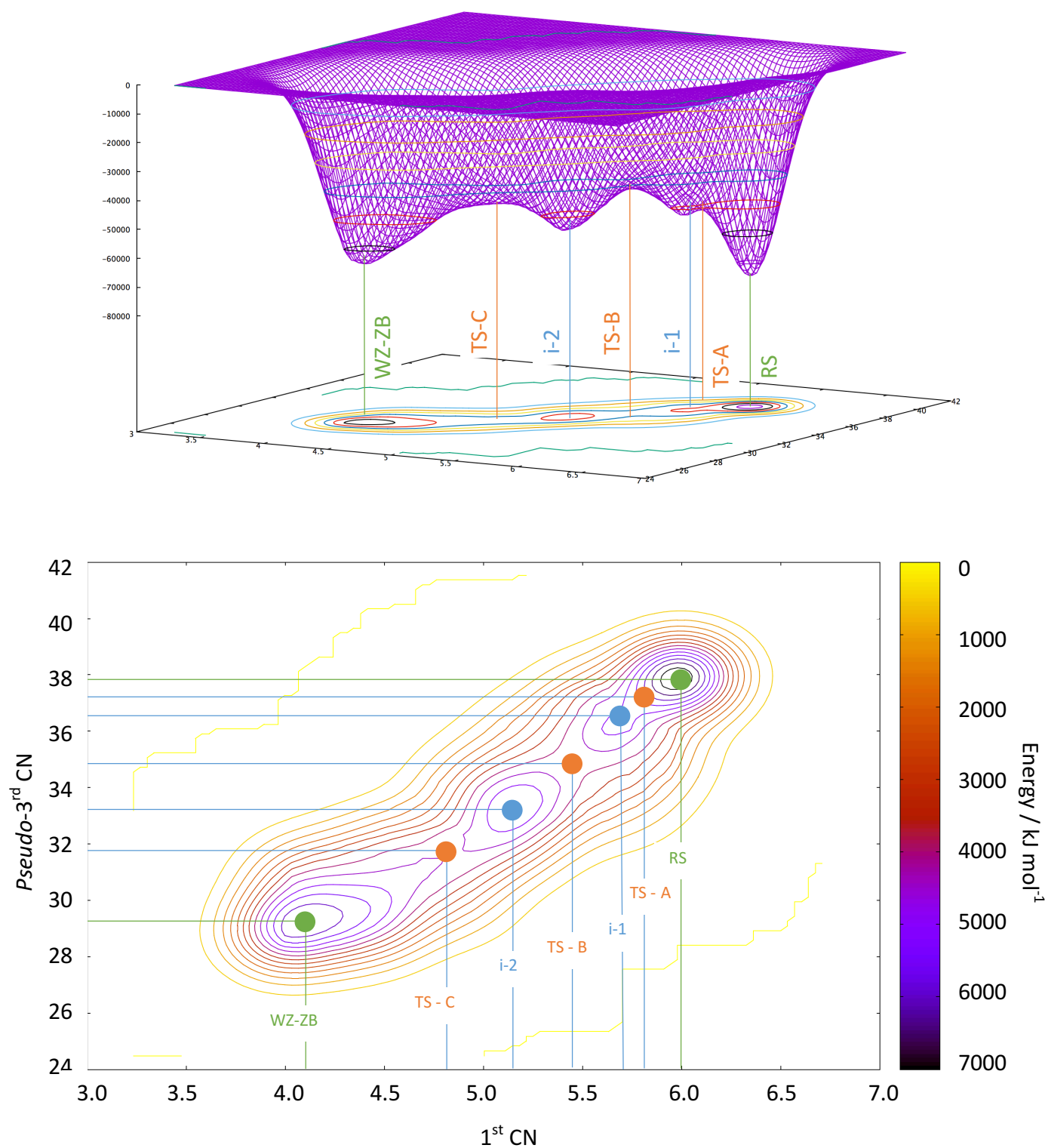


**Figure 5.xxiv:** Three-dimensional plot (above) and two-dimensional contour plot (below) of the converged free-energy surface for the transition after 250 iterations of the metashooting procedure. Note the presence of the two main basins of attraction and the two pronounced intermediate basins, as well as three transition states.



The evolution of the profile can also be analysed using the *metatrajectories* obtained from the metadynamics steps of the procedure. Mapping these trajectories on top of the final free energy surface gives a good indication of the spread of deposited Gaussian functions along the path of the trajectory. These plots also help to show that after 250 iterations, the profile had converged, allowing the process to be ceased.

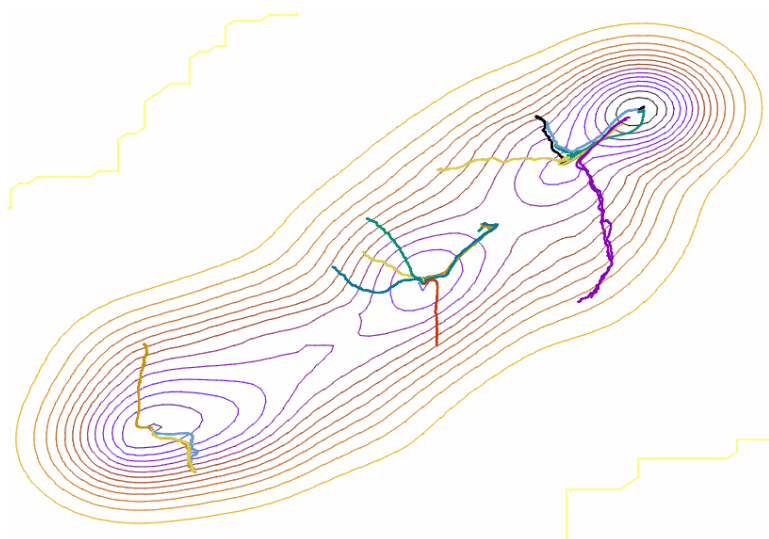


**Figure 5.xxv:** An example of 20 meta-trajectories from *step 5* of Iterations 220-239 of the metashooting procedure. One can see that the extent of landscape exploration by this point is quite advanced, and that the metadynamics runs are exploring large regions of the energy landscape. At the very beginning of the procedure, such trajectories are localised within their starting basins, whereas towards the end of the procedure more and more of the energy landscape should be explored during each metadynamics run. *Only in the final stages of the procedure, close to convergence, are the regions around the transition states affected.*

As with the transition path sampling and standard metadynamics procedures, the *metashooting* procedure iteratively built upon the underlying process, until convergence was achieved. However, unlike if the system was surveyed by standard metadynamics alone, only basins relevant to the transition were filled and convergence could easily be ascertained.

5.5.3.3. Analysis of the Intermediates and Transition States5.5.3.3.1. Overview

Constructing and visualising a free energy surface in this way allows for clear determination of which points along the path correspond to important ‘milestones’ of the trajectory. There are seven points of interest on the free energy surface – the two initial basins of attraction (corresponding to wurtzite-zincblende and rocksalt), two intermediate basins and three maxima, corresponding to transition states.

The structures and roles of these turning points in the transformation can be ascertained by obtaining the first and *pseudo*-third coordination numbers of the turning points on the graph and matching these up to structures along both the hundreds of trajectories from both the ‘plain’ TPS runs and the *metashooting* trajectories. It stands to reason that these regions must play an important role in the transformation mechanism. However, it is also evident that the individual regions are unlikely to correspond to a single configuration only.

Turning point	1 <sup>st</sup> CN of feature CENTRE	<i>Pseudo</i> -3 <sup>rd</sup> CN of feature CENTRE
RS	<b>5.98</b>	<b>37.90</b>
TS-A	<b>5.75</b>	<b>36.66</b>
i-1	<b>5.68</b>	<b>36.21</b>
TS-B	<b>5.43</b>	<b>34.86</b>
i-2	<b>5.15</b>	<b>33.13</b>
TS-C	<b>4.87</b>	<b>31.62</b>
WZ-ZB	<b>4.10</b>	<b>29.22</b>

**Table 5.xxvi:** Table of the first and *pseudo*-third coordination spheres corresponding to the centre of the regions defining the turning points. Note that larger regions may be composed of numerous configurations, many of which do not correspond exactly to these values.

The RS and WZ-ZB basins need not be identified, as the nature of these structures is evident. However, it is curious that the wurtzite-zincblende basin is centred away from its perfect values of 4 and 28/29. This is due to the presence of higher-coordination defects present after the decompression of the trajectory, particularly trace amounts of five-membered ZnO, as seen in the path sampling trajectories.

#### 5.5.3.3.2. The Intermediate Basins $i-1$ and $i-2$

The species forming  $i-1$  correspond to the metastable configurations occupying the ‘shoulder-peak’ adjacent to the rocksalt basin. Every single trajectory, regardless of its prior path, congregates at  $i-1$  before proceeding along a single pathway to or from the rocksalt structure. This is clearly exhibited in Figure 5.xxiv, where every single meta-trajectory which has one end point within the rocksalt basin proceeds through this channel to or from  $i-1$ . Thus, despite the small and shallow dimensions of the basin, it clearly must play a central role in the transformation.

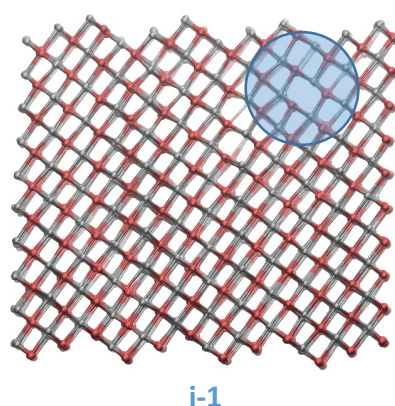


**Figure 5.xxvii:** *Species coloured* representation of a configuration corresponding to the small minimum  $i-1$ , which is just after the very first rocksalt motifs deform into hexagons (highlighted) en route to the ‘small’ cubic seed.

It transpires that i-1 corresponds to small fragments of the ‘cubic seed’ motif. The i-1 structure is composed almost exclusively of rocksalt, however it contains a component of four- and five- coordinated zinc oxide. This small region is extremely short lived but present in every successful trajectory sampled, thus explaining its presence on the free energy profile as the fundamental seed of the transformation.

The second intermediate region, i-2, is a deep energy well placed directly between the two defined basins of attraction. Indeed, it appears large enough to be defined as a metastable phase in its own right. i-2 corresponds to numerous possible states which occupy this basin, including configurations:

- Along *successful* trajectories where there is a coexistence of four, five and six coordinate ZnO, giving an overall average first coordination sphere of five;
- Along *successful* trajectories where the system proceeds through a predominantly five-coordinate intermediate;
- Residing in the RS-*iH* structure (as described in chapter 5.4.2.5.3 of the path sampling analysis).

It seems likely, therefore, that the depth of this basin (and hence the energy barriers associated with it) is slightly exaggerated. This is because it corresponds to numerous possible configurations with very similar *average* values of coordination which have all added weight to the free energy surface at these values of the collective variables, even though not every configuration is realisable in every trajectory.

#### 5.5.3.3.3. The Transition States *TS-A*, *TS-B* and *TS-C*

TS-A corresponds to the region visited during the transformation from rocksalt to the ‘small’ cubic seed, or *vice versa*. The configuration associated with the maximum is an almost entirely

rocksalt structure at the moment of the deformation of the first (or last) rocksalt motifs. This can easily be rationalised – the first few Zn-O sites to transform from six- to four- coordinate must overcome an activation energy. The small minimum subsequently seen (*i-1*) must therefore correspond to a ‘stretching-out’ of the Zn-O bonds to produce a more typical four-coordinate geometry.

TS-B is associated with the formation of the ‘large’ cubic seed and the shear seen in the (300) plane, as seen in both the forward and reverse mechanisms. The system containing the large cubic seed corresponds precisely to the coordination values of TS-B, proving that this configuration is actually an energy maximum. This is again likely due to the strained configurations of Zn-O upon initial formation of the seed, but also due to the formation of the shear and the initial compression of the system.

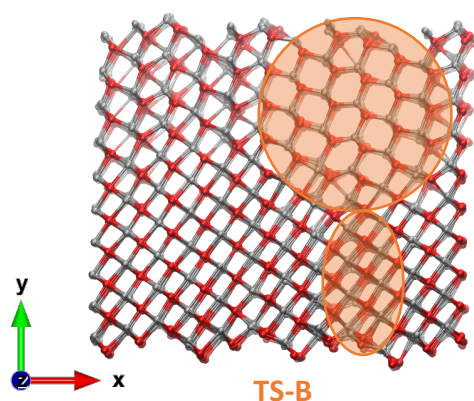


**Figure 5.xxviii:** A representative configuration corresponding to the maximum TS-B, showing the formation of the ‘large’ cubic seed (above) accompanied by the sheering down the [003] direction, which prevailed in every mechanism observed.

Thus, the formation or resorption of the cubic seed, which is integral to every converged transition pathway analysed, is actually composed of two steps; one which forms or destroys the first few motifs of four-coordinate material, and another more substantial step to create the ‘large’ cubic seed. These two processes happen very rapidly in the path sampling trajectories and it is not obvious by inspection that they may correspond to two

different events. When mapped onto the free energy surface, the disconnected nature of these two events appears very clearly.

However, TS-A and TS-B may also be both contributed to by the formation of the five-coordinated *iH* structure sandwiched between rocksalt layers, as discussed in 5.4.2.5.3. Thus, once again it is not possible to assign a single configuration to the maximum observed.

TS-C is an interesting case, as unlike TS-A and TS-B it corresponds to a very ‘gentle’ maximum, with a very shallow gradient either side of it. This again corroborates exactly what was seen in the path sampling investigations – the system spends a great deal of time in a four-coordinate state, or a mixture of four- and five- coordinate, as a result of a slow, steady process corresponding to a gentle energy gradient.

Like its associated intermediate basin *i-2*, the height of TS-C in the observed trajectories is contributed to by a number of configurations, all of which contain some combination of rocksalt, four-coordinate ZnO and occasionally the *iH* intermediate. It appears that this maximum directly corresponds with the significant coordination change seen at approximately 4 ps in Figure 5.xviii and 3 ps in Figure 5.xx.

#### 5.5.3.4. Energy Barriers

One of the greatest advantages of calculating a free energy surface using metadynamics based techniques is the ability to simply measure energy barriers from the final plot, giving fundamental insight into the kinetics of the transformation involved. From the converged free energy surface, it is apparent that there are six distinguishable energy barriers associated with the pathway – three for the WZ-ZB → RS trajectory, and three for the RS → WZ-ZB trajectory.

For the rocksalt to wurtzite-zincblende pathway:

$$E_{\alpha} = \Delta E(RS \rightarrow TS - A) \quad [Eq\ 5.5]$$

$$E_{\beta} = \Delta E(i - 1 \rightarrow TS - B) \quad [Eq\ 5.6]$$

$$E_{\gamma} = \Delta E(i - 2 \rightarrow TS - C) \quad [Eq\ 5.7]$$

For the wurtzite-zincblende to rocksalt trajectories:

$$E_{\chi} = \Delta E(WZ - ZB \rightarrow TS - C) \quad [Eq\ 5.8]$$

$$E_{\psi} = \Delta E(i - 2 \rightarrow TS - B) \quad [Eq\ 5.9]$$

$$E_{\omega} = \Delta E(i - 1 \rightarrow TS - A) \quad [Eq\ 5.10]$$

The total energy barriers that must be overcome by each of the pathways is simply the sum of the three above values for the forward and reverse trajectories. These are not thermodynamically relevant, but illustrate the difference in the two pathways well:

$$E_{tot}(RS \rightarrow WZ - ZB) = E_{\alpha} + E_{\beta} + E_{\gamma} \quad [Eq\ 5.11]$$

$$E_{tot}(WZ - ZB \rightarrow RS) = E_{\chi} + E_{\psi} + E_{\omega} \quad [Eq\ 5.12]$$

A more useful measure is the total overall activation energy for the forward and reverse processes, which corresponds to the amount of energy required to overcome the highest energy barrier from the lowest energy starting configuration. In this case, the activation energies correspond to:

$$E_{act}(RS \rightarrow WZ - ZB) = \Delta E(RS \rightarrow TS - B) \quad [Eq\ 5.13]$$

$$E_{act}(WZ - ZB \rightarrow RS) = \Delta E(WZ - ZB \rightarrow TS - B) \quad [Eq\ 5.14]$$

However, small variations in the trajectories show that the system may proceed along different pathways and thus across different features of the free energy plot. This will lead to different values for the total amount of energy overcome by individual trajectories. The following quantitative analysis of the energy differences assumes measurement to and from the centres of each of the turning points, as described in Table 5.xxv, thereby indicating the energy associated with a transition pathway that visits all maxima and minima. In reality, such pathways are not always seen and each individual pathway will have its own set of energy

values. However, it is stressed that every trajectory must surmount an energy barrier *at least* equivalent to the activation energies presented, as successful trajectories must overcome the highest energy barrier to cross to the other side, irrespective of the path taken.

It is also apparent from inspection that the energy barriers for each stage of the transformation are very different for the forward and reverse trajectories. This may go some way to explaining why there are different pathways associated with the forward and reverse trajectories, and perhaps why there are such notable hystereses present in such transformations.

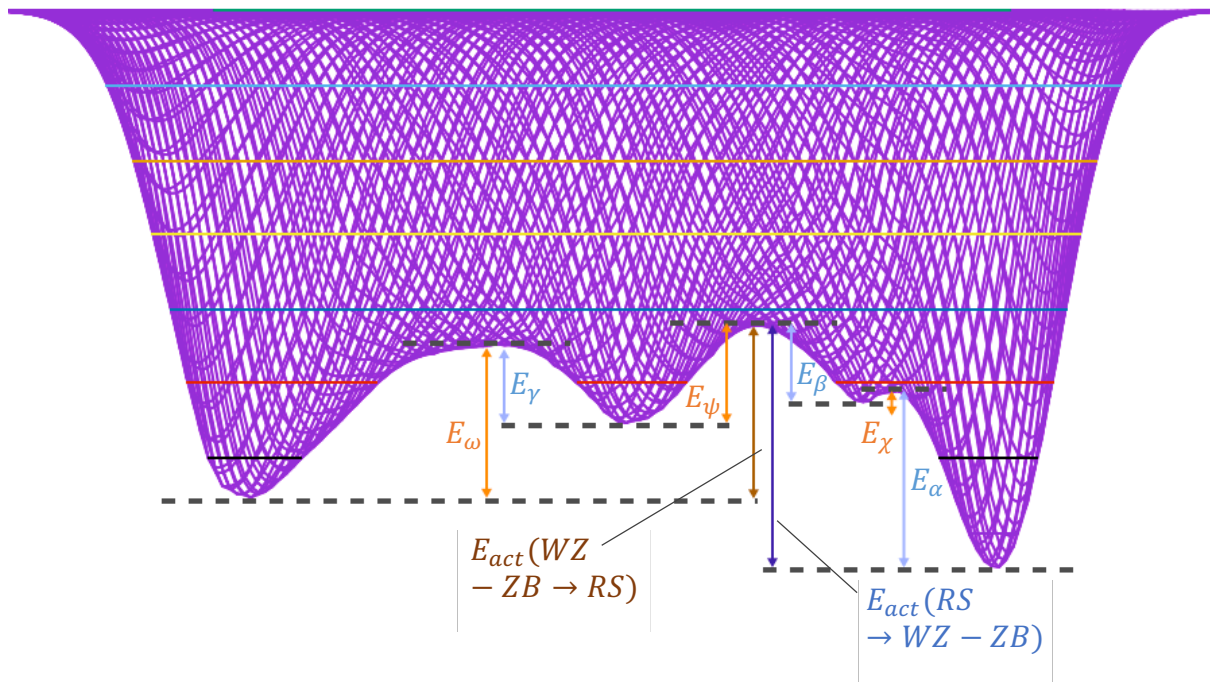


**Figure 5.xxix:** A summary of all the energy barriers associated with the profile. The activation energy for each process is defined as the energy required to surmount the largest barrier from the starting basin. The total energy expenditure (not shown on this diagram) for each transformation is the sum of the energy to surmount each barrier along the course of the trajectory. Note that these barriers correspond to movements from the centres of each of the turning points – there will be considerable variation in the trajectories that move across this energy landscape.



	Energy /kJ mol <sup>-1</sup>	Energy /kJ mol <sup>-1</sup> pair <sup>-1</sup>	Energy /eV pair <sup>-1</sup>	Energy /k <sub>B</sub> T pair <sup>-1</sup>
--	---------------------------------	--	----------------------------------	--

$E_\alpha$	23 726.3	19.8	0.21	7.9
$E_\beta$	10 376.6	8.6	0.09	3.5
$E_\gamma$	10 483.8	8.7	0.09	3.5
$E_{tot}(RS \rightarrow WZ - ZB)$	44 586.7	37.2	0.39	14.9
$E_{act}(RS \rightarrow WZ - ZB)$	32 565.9	27.1	0.28	10.9

RS → WZ-ZB Pathway

$E_\chi$	20 447.0	17.1	0.18	6.8
$E_\psi$	13 085.9	10.9	0.11	4.4
$E_\omega$	1 357.0	1.3	0.01	0.5
$E_{tot}(WZ - ZB \rightarrow RS)$	35 069.9	29.2	0.30	11.6
$E_{act}(WZ - ZB \rightarrow RS)$	23 049.1	19.2	0.20	7.7

WZ-ZB → RS Pathway

**Table 5.xxx:** Energy barriers associated with the forward and reverse trajectories. The total energy spent to overcome all barriers is highlighted in orange, whereas activation energies are coloured blue. Note the discrepancy in the barrier heights between the forward and reverse pathways. The values are measured to and from the centres of the turning points on the energy surface, illustrating a hypothetical trajectory which visits all maxima and minima.

5.5.3.5. Change in Free Energy

The change in free energy is simply the difference between the energy values of the rocksalt and the wurtzite-zincblende basins, or the difference between the activation energies of the forward and reverse trajectories. Ideally, as this trajectory was carried out at the transition pressure of zincblende and rocksalt, this should be very close to zero.

$$\Delta G = G_{RS} - G_{WZ-ZB} \quad [Eq\ 5.15]$$

However, it is evident from inspection of the plot, as well as of the energy barriers, that  $\Delta G \neq 0$  in this case, but rather:

$$\Delta G = 0.08\ eV$$

This difference in the free energy is substantial, corresponding to approximately 3.2  $k_B T$ .

It is speculated that one contribution to this difference is resultant from the change in the four-coordinate starting material caused by the path sampling calculations. The transition pressure of 9.8 GPa corresponded to the conditions at which the enthalpy of *pure zincblende* and rocksalt were equal. This new material, which is a combination of wurtzite and zincblende, will certainly have a different enthalpy vs. pressure plot and hence a different cross-over point with rocksalt. This may explain the disparity between the values in free energy seen, and accordingly a lower transition pressure than the one used can be expected.

However, if this were the only issue to consider, one would have expected the transition pressure to reside between the cross-over values of zincblende-rocksalt (9.8 GPa) and wurtzite-rocksalt (14.8 GPa), depending on the percentage contributions of the two phases in the mixed structure. Thus, the four-coordinate phase would have been lower in free energy at 9.8 GPa, which is not what is seen here. It is possible, however, that this may be a very simplistic view, as the presence of defects within the four-coordinate final structure may contribute to the lowering of the transition pressure. In addition, a significant entropic component may play a role within these mixed phases, which is neglected in the initial enthalpy vs. pressure calculation but can clearly be considered using these free energy

methods. An investigation into these issues, by re-running the *metashooting* procedure at different pressures, specifically the pressure corresponding to the mixed material-rocksalt crossover point, would be useful in the future to address these problems. Hence, the entropic components of the different phases could be fully classified, giving another layer of insight into this phase transition.

#### 5.5.3.6. Mapping the Trajectories

With the collected data, it is possible to map the trajectories on top of the aggregated free energy surface. This is achieved by once again taking the first and *pseudo*-third coordination number for each frame of a trajectory, and plotting this on the underlying landscape generated by the final iteration of the *metashooting* procedure. All of the trajectories produced by the *metashooting* process, as well as those by the original path sampling, are true dynamical trajectories. Hence, any of the collated runs can be plotted on the energy surface to represent a possible path that may cross it.

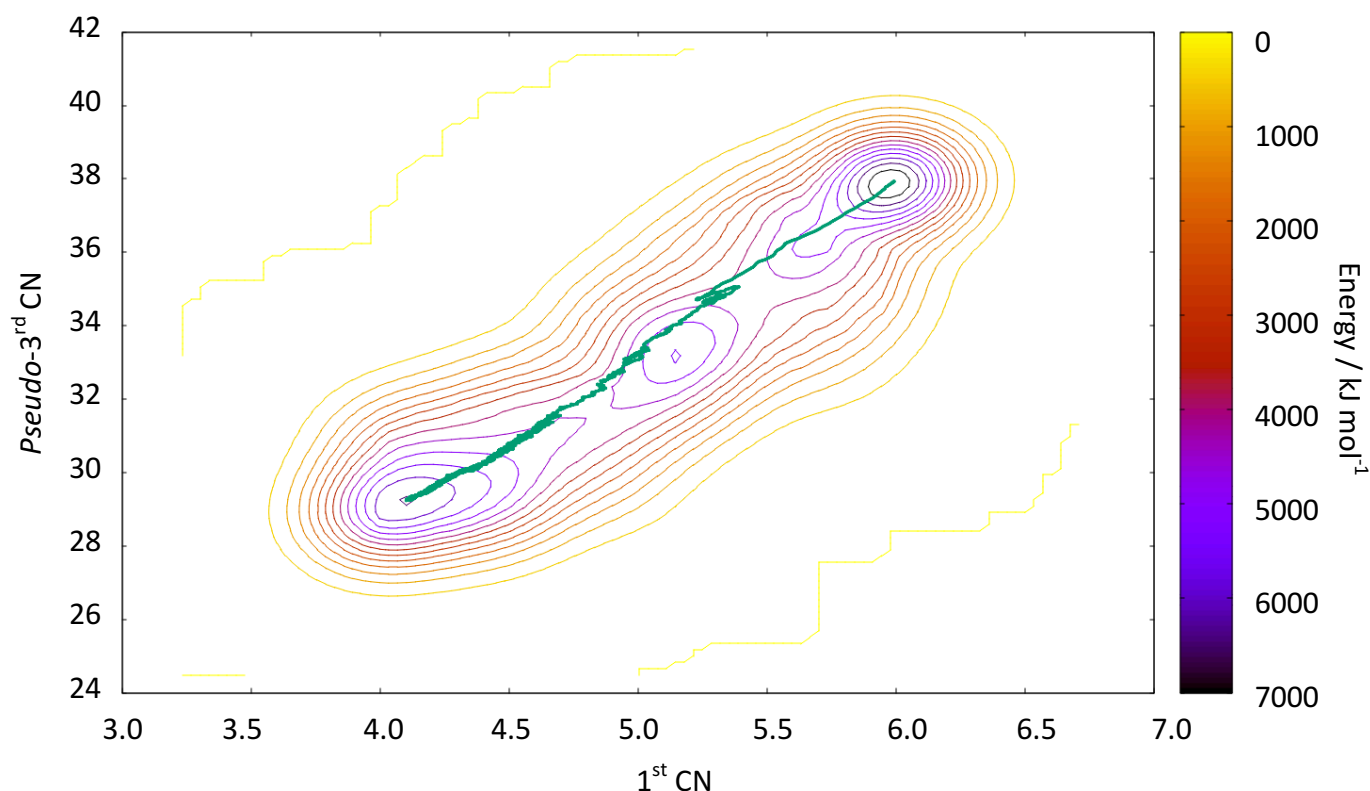


**Figure 5.xxi (previous page):** An example of a successful trajectory prior to any deposition of Gaussians during the *metashooting*, linking the wurtzite-zincblende and the rocksalt basins.

The trajectory avoids the centre of the five-coordinate basin, which corresponds to the *iH* configuration, as seen in the mechanistic analysis in 5.4.2.5.3.

The visualisation of successful trajectories, such as the one seen in Figure 5.xxx, demonstrates that the transformation may not necessarily take the lowest energy pathway, but can take numerous possible routes. This corroborates with exactly what is seen in the variety of trajectories seen in the path sampling. Using such visualisations allows the accurate tracing of the course of each trajectory over the free energy landscape, which in turn permits a detailed structural and energetic analysis of each individual trajectory, if required.

Failed trajectories can also be plotted on the free energy surface, which allows for characterisation of why such pathways were unsuccessful. In addition, such diagrams can give additional insight into the ‘failed’ configurations - for example, the trajectories which fall into the five-coordinate basin prove that there are numerous configurations constituting the *iH* intermediate, corresponding to lower, medium and higher-density structures.

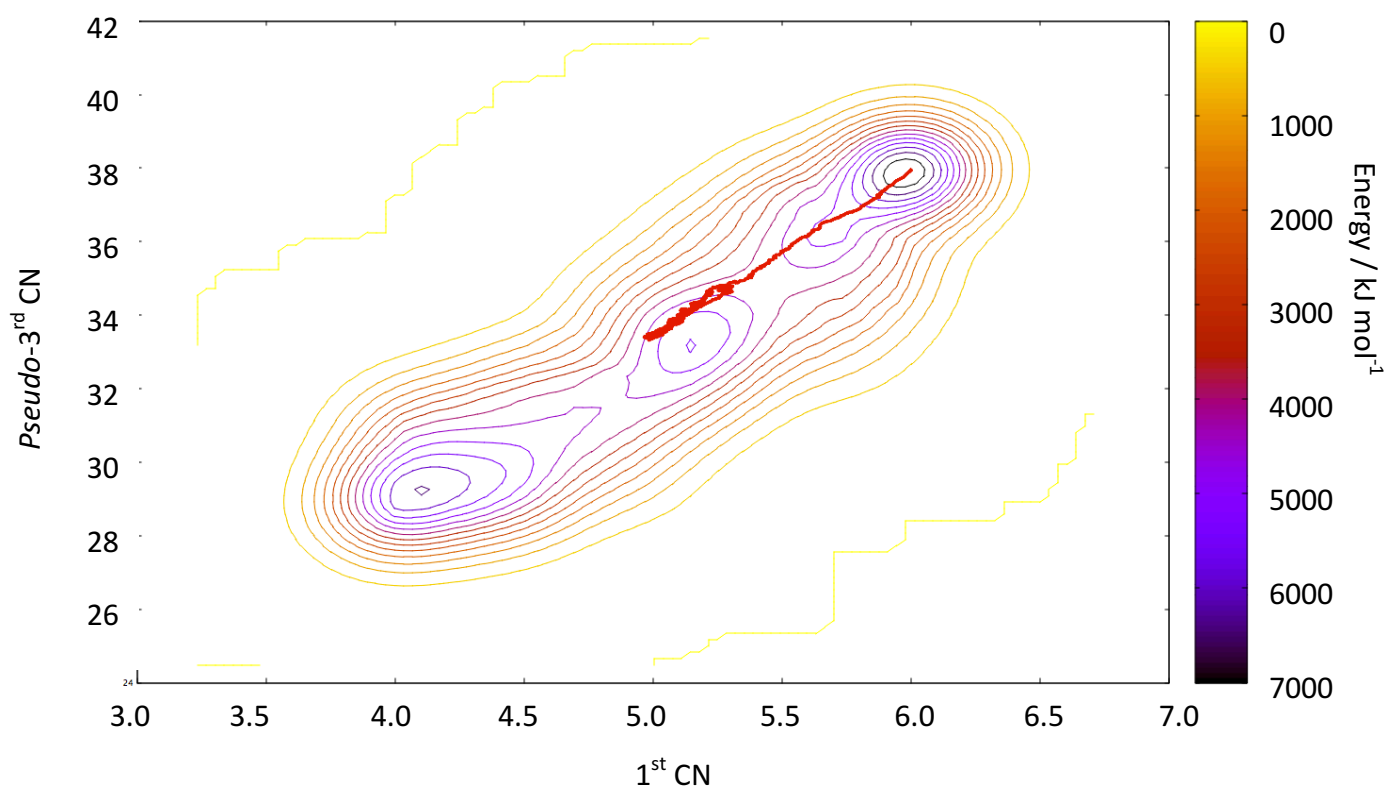


**Figure 5.xxxii (previous page):** An example of a would-be failed trajectory from Iteration 209 of the *metashooting* procedure, showing a failed trajectory in which rocksalt transforms into a high-density *iH* structure and remains stuck in this basin.

## 5.6. Conclusions and Future Work

Using transition path sampling methods, a phase transition characterised by a sequence of nucleation and growth events between a mixed wurtzite-zincblende and rocksalt has been described. The path sampling procedure determined that the forward and reverse trajectories featured different preferred pathways, each with different competing intermediates and concerted events. Whilst both the forward and reverse transformation could proceed by either pathway, there appeared to be a preference for one mechanism over the other for both transformations.

A typical high-to-low pressure trajectory was characterised by the formation of a cubic ‘seed’, followed by gradual transformation to a mixed four-coordinate product via coexisting motifs of rocksalt and wurtzite ZnO. Failed trajectories could also end up becoming trapped in an intermediate five-coordinate basin, corresponding to a mixed rocksalt-5 coordinate hexagonal structure denoted RS-*iH*.

The low-to-high pressure transition was characterised by a more stepwise process, which involved transition to the four-coordinate mixture via local motifs of the hexagonal *iH* before transforming to the final rocksalt product.

Subsequently, the path sampling converged trajectories were analysed using the novel *metashooting* method – a combination of the *shooter* algorithm from transition path sampling and a well-tempered metadynamics scheme using the first and third average coordination spheres as the collective variables. The results presented show that the *metashooting* procedure is able to decipher the underlying free energy landscape of the transformation, and that structural information about the nature of appropriate maxima and

minima can be extracted from the resultant plot. In addition, energy barriers and changes in free energy can be ascertained, and successful and failed trajectories visualised on the final free energy plot, in order to gain a true understanding of the energetics and structural curiosities inherent within each individual trajectory.

There are, however, a number of points here that would be beneficial to address in the future.

Firstly, the nature of the RS-*iH* intermediate, as found in both the path sampling and *metashooting* analysis, is still puzzling and ambiguous. Previous work has suggested that this phase does exist along the reaction coordinate, but is not necessary for the transformation. This work directly corroborates that, however it is unclear as to why the material is so persistent in this work, nor why its associated basin is so deep within the *metashooting* scheme.

This could be a consequence of the parameters used. To consider this, a detailed analysis of the *iH* structure using a different parameterisation or a higher level of theory (such as density functional theory) would be worthwhile to ascertain the mechanical and dynamical stability of this structure.

Alternatively, the phase could be over-stabilised due to repeated path sampling trajectories *rejecting* such a move, when ultimately it may have led to a successful trajectory. Had the path sampling scheme been allowed to propagate for a much longer time period, such a scheme may have correctly gone on to transform successfully. Thus, it would be beneficial to re-initialise the path sampling procedure from the first instance of such an intermediate appearing, with a longer simulation run time to allow for persistent metastable configurations to evolve appropriately.

Despite the *metashooting* procedure being successful, there are a few modifications which could lead to an improvement to the method. For instance, it may be beneficial to use a different set of collective variables, for example higher coordination sequences, in order to better distinguish between the phases. Using the first and third coordination spheres was convenient in this case as it was an identical measurement to the *order parameter* used in

the path sampling calculations. However, it did mean that resolution between different configurations and pathways was often poor.

When visualising multiple trajectories on the free energy plot, the resultant schemes often showed very little difference between the paths of different trajectories, despite those pathways being markedly different when visualised. For example, a scheme which followed the ‘high-to-low’ pressure pathway, with coexisting wurtzite and rocksalt motifs, and a scheme following the ‘low-to-high’ pressure pathway, with large regions of  $iH$ , could barely be differentiated using this method of visualisation. Additionally, instances of  $iT$  had to be distinguished by geometric analysis, rather than from the plot. It is believed that running this scheme with more sensitive collective variables, such as the third and fifth coordination spheres, would give even more detail about the different trajectories, intermediate and transitional configurations along the course of this transformation.

It is believed that the *metashooting* procedure could set a novel paradigm for future investigations into condensed matter phase transitions. Such a scheme could easily be transferred to another system, under any level of theory, to ascertain the underlying thermodynamics and kinetics of a temperature or pressure-induced phase transformation. Such an analysis is only possible by the combined use of path sampling and metadynamics methodologies – neither of which alone would be able to produce the detailed scheme described within this work.

References – Chapter 5

1. C. Klingshirn, *ChemPhysChem*, 2007, **8**, 782-803
2. A. Moezzi, A. M. McDonagh and M. Cortie, *Chem. Eng. J.*, 2012, **185-186**, 1-22
3. H. A. Depew, *Ind. Eng. Chem.*, 1933, **25**, 532-534
4. L. Guedri-Knani, J. L. Gardette, M. Jacquet and A. Rivaton, *Surf. Coat. Technol.*, 2004, **180**, 71-75
5. H. G. Völz, J. Kischkewitz, P. Woditsch, A. Westerhaus, W. D. Griebler, M. de Liedekerke, G. Buxbaum, H. Printzen, M. Mansmann, D. Råde, G. Trenczek, V. Wilhelm, S. Schwarz, H. Wienand, J. Adel, G. Adrian, K. Brandt, W. B. Cork, H. Winkeler, W. Mayer, K. Schnieder, L. Leitner, H. Kathrein, E. Schwab, H. Jakusch, M. Ohlinger, R. Veitch, G. Etzrodt, G. Pfaff, K. D. Franz, R. Emmert, K. Nitta, R. Besold and H. Gaedcke, *Ullman's Encyclopedia of Industrial Chemistry*, Wiley-VCH Verlag GmbH & Co, 2000
6. R. van Noort, *Introduction to Dental Materials*, Mosby, 2002
7. M. A. Mitchnick, D. Fairhurst and S. R. Pinnell, *J. Am. Acad. Dermatol.*, 1999, **40**, 85-90
8. A. Hernández Battez, R. González, J. L. Viesca, J. E. Fernández, J. M. Díaz Fernández, A. Machado, R. Chou and J. Riba, *Wear*, 2008, **265**, 422-428
9. Ü Özgür, Y. I. Alivov, C. Liu, A. Teke, M. A. Reshchikov, S. Dogan, V. Avrutin, S. J. Cho and H. Morkoç, *J. Appl. Phys.*, 2005, **98**, 41301
10. [https://upload.wikimedia.org/wikipedia/commons/1/13/Zinc\\_oxide.jpg](https://upload.wikimedia.org/wikipedia/commons/1/13/Zinc_oxide.jpg) "Zinc Oxide"  
- Last Accessed 28/09/2017
11. A. Bakin, A. El-Shaer, A. C. Mofor, M. Al-Suleiman, E. Schlenker and A. Waag, *Phys. Status. Solidi. C.*, 2007, **4**, 158-161
12. K. Nomura, H. Ohta, K. Ueda, T. Kamiya, M. Hirano and H. Hosono, *Science*, 2003, **300**, 1269-1272
13. Y. Qin, X. Wang and Z. L. Wang, *Nature*, 2008, **451**, 809-813
14. B. Y. Oh, M. C. Jeong, T. H. Moon, W. Lee, J. M. Myoung, J. Y. Hwang and D. S. Seo, *J. Appl. Phys.*, 2006, **99**, 124505
15. L. C. Tien, P. W. Sadik, D. P. Norton, L. F. Voss, S. J. Pearton, H. T. Wang, B. S. Kang, F. Ren, J. Jun and J. Lin, *Appl. Phys. Lett.*, 2005, **87**, 222106



16. A. C. Mofor, A. El-Shaer, A. Bakin, A. Waag, H. Ahlers, U. Siegner, S. Sievers, M. Albrecht, W. Schoch, N. Izyumskaya, V. Avrutin, S. Sorokin, S. Ivanov and J. Stoimenos, *Appl. Phys. Lett.*, 2005, **87**, 62501
17. C. F. Klingshirn, A. Waag, A. Hoffmann and J. Geurts, *Zinc Oxide: From Fundamental Properties Towards Novel Applications*, Springer Science and Business Media, 2010
18. S. A. Kukushkin, A. V. Osipov and A. I. Romanychev, *Phys. Solid. State*, 2016, **58**, 1448-1452
19. Z. L. Wang, *J. Phys. Condens. Matter.*, 2004, **16** R829
20. S. Hsu, Y. Y. Lin, S. Huang, K. W. Lem, D. H. Nguyen and D. S. Lee, *Nanotechnology*, 2013, **24**, 475102
21. J. L. G. Fierro, *Metal Oxides: Chemistry and Applications*, Taylor & Francis, 2005.
22. W. L. Bragg, *Philos. Mag.*, 1920, **39**, 647-651
23. E. H. Kisi and M. M. Elcombe, *Acta. Crystallogr. C.*, 1989, **45**, 1867-1870
24. C. Jagadish and S. J. Pearton, *Zinc Oxide Bulk, Thin Films and Nanostructures: Processing, Properties and Applications*, Elsevier, 2011
25. H. Sowa and H. Ahsbahr, *J. Appl. Cryst.*, 2006, **39**, 169-175
26. W. L. Bragg and J. A. Darbyshire, *Transactions of the Faraday Society*, 1932, **28**, 522-529
27. C. H. Bates, W. B. White and R. Roy, *Science*, 1962, **137**, 993
28. A. Ashrafi, A. Ueta, A. Avramescu, H. Kumano, I. Suemune, Y. W. Ok and T. Y. Seong, *Appl. Phys. Lett.*, 2000, **76**, 550-552
29. A. Ashrafi and C. Jagadish, *J. Appl. Phys.*, 2007, **102**, 71101
30. L. Gerward and J. S. Olsen, *J. Synchrotron Radiat.*, 1995, **2**, 233-235
31. D. C. Look, J. W. Hemsky and J. R. Sizelove, *Phys. Rev. Lett.*, 1999, **82**, 2552-2555
32. S. E. Boulfelfel and S. Leoni, *Phys. Rev. B.*, 2008, **78**, 125204
33. F. Decremps, J. Zhang and R. C. Liebermann, *Europhys. Lett.*, 2000, **51**, 268-274
34. S. Desgreniers, *Phys. Rev. B.*, 1998, **58**, 14102-14105
35. H. Karzel, W. Potzel, M. Köfferlein, W. Schiessl, M. Steiner, U. Hiller, G. M. Kalvius, D. W. Mitchell, T. P. Das, P. Blaha, K. Schwarz and M. P. Pasternak, *Phys. Rev. B.*, 1996, **53**, 11425-11438
36. F. Decremps, J. Pellicer-Porres, F. Datchi, J. P. Itie, A. Polian, F. Baudalet and J. Jiang, *Appl. Phys. Lett.*, 2002, **81**, 4820-4822

37. A.M. Saitta and F. Decremps, *Phys. Rev. B.*, 2004, **70**, 35214
38. H. Liu, Y. Ding, M. Somayazulu, J. Qian, J. Shu, D. Häusermann and H. Mao, *Phys. Rev. B.*, 2005, **71**, 212103
39. J. Cai and N. Chen, *J. Phys. Condens. Matter*, 2007, **19**, 266207
40. J. E. Jaffe, J. A. Snyder, Z. Lin and A. C. Hess, *Phys. Rev. B*, 2000, **62**, 1660-1665
41. A Zaouri and W. Sekkal, *Phys. Rev. B.*, 2002, **66**, 174106
42. Y. Mori, N. Niiya, K. Ukegawa, T. Mizuno, K. Takarabe and A. L. Ruoff, *Phys. Status, Solidi. B.*, 2004, **241**, 3198-3202
43. A. Ashrafi, A. Ueta, H. Kumano and I. Suemune, *J. Cryst. Growth*, 2000, **221**, 435-439
44. S. K. Kim, S. Y. Jeong and C. R. Cho, *Appl. Phys. Lett.*, 2003, **82**, 562-564
45. G. H. Lee, T. Kawazoe and M. Ohtsu, *Appl. Surf. Sci.*, 2005, **239**, 394-397
46. Y. Z. Yoo, Y. Osaka, T. Fukumura, Z. Jin, M. Kawasaki, H. Koinuma, T. Chikyow, P. Ahmet, A. Setoguchi and S. F. Chichibu, *Appl. Phys. Lett.*, 2001, **78**, 616
47. Y. Wu, J. Kang and F. Liu, *J. Mater. Res.*, 2008, **23**, 3347-3352
48. P. G. Bolhuis, D. Chandler, C. Dellago and P. L. Geissler, *Annu. Rev. Phys. Chem.*, 2002, **53**, 291-318
49. C. Dellago, P. G. Bolhuis, F. S. Csajka and D. Chandler, *J. Chem. Phys.*, 1998, **108**, 1964-1977
50. A. Laio and M. Parrinello, *Proc. Natl. Acad. Sci.*, 2002, **99**, 12562-12566
51. D. J. Binks and R. W. Grimes, *J. Am. Ceram. Soc.*, 1993, **76**, 2370-2372
52. R. A. Buckingham, *Proc. R. Soc. Lond. Math. Phys. Eng. Sci.*, 1938, **168**, 264-283
53. S. Nosé, *J. Chem. Phys.*, 1984, **81**, 511-519
54. S. Nosé, *Mol. Phys.*, 1984, **52**, 255-268
55. G. J. Martyna, D. J. Tobias and M. L. Klein, *J. Chem. Phys.*, 1994, **101**, 4177-4189
56. G. J. Martyna, M. L. Klein and M. Tuckerman, *J. Chem. Phys.*, 1992, **97**, 2635-2643
57. H. G. von Schnering, *Angew. Chem. Int. Ed. Engl.*, **26**, 1059-1080
58. H. G. von Schering and R. Nesper, *Z. Für Phys. B. Condens. Matter*, 1991, **83**, 407-412
59. J. Vymetal and J. Vondrásek, *J. Phys. Chem. B*, 2010, **114**, 5632-5642
60. D. Granata, F. Baftizadeh, J. Habchi, C. Galvagnion, A. D. Simone, C. Camilloni, A. Laio and M. Vendruscolo, *Sci. Rep.*, 2015, **5**, 15449
61. G. A. Tribello, M. Bonomi, D. Branduardi, C. Camilloni and G. Bussi, *Comput. Phys. Commun.*, 2014, **185**, 604-613

- 62. A. Barducci, G. Bussi and M. Parrinello, *Phys. Rev. Lett.*, 2008, **100**, 020603
- 63. D. Branduardi, G. Bussi and M. Parrinello, *J. Chem. Theory. Comput.*, 2012, **8**, 2247-2254

## Chapter 6

### Phases of Water Ice

***“Water, water, everywhere...”***

– Samuel Taylor Coleridge (1772-1834), *The Rime of the Ancient Mariner*

#### 6.1. Introduction to Water and Ice

##### 6.1.1. Overview

As the simplest compound of the two most abundant chemically active elements in existence, water is undoubtedly one of the most fascinating and mysterious compounds in the natural world.

An incredibly prevalent molecule, water covers 71% of the Earth’s surface<sup>[1]</sup> and is present in the atmospheres of many moons,<sup>[2,3]</sup> planets<sup>[4]</sup> and stars<sup>[5]</sup> throughout the galaxy. It is able to solvate a huge number of salts and hydrophilic organic compounds, resulting in its famous moniker as the “universal solvent”.<sup>[6]</sup> Water is amphoteric, boasts high melting and boiling points and has a high specific heat capacity, and can also exist on Earth in all three traditional states of matter – solid, liquid and gas.<sup>[7]</sup> Biological systems have exploited its numerous qualities, resulting in the compound being the main constituent of most living organisms on the planet and essential to all life on Earth.

Yet the apparent simplicity of water belies its underlying chemical and physical complexity, as much is still not understood about this fundamental three-atom molecule. This is particularly shocking when taking into consideration that water is one of the most fundamental and (possibly) the most abundant non-elemental molecule in the Universe and arguably the most important compound to humanity and the entire biosphere!

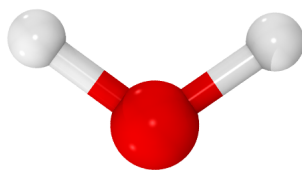


**Figure 6.i:** A familiar cartoon schematic of a water molecule, with the central oxygen atom in red and the two hydrogen atoms in white. The experimental O-H bond length of 0.958 Å and H-O-H angle of 104.45° make it one of the smallest molecules in existence. Despite the evident simplicity of the molecule, it boasts a wealth of fascinating physical and chemical properties – many of which are not fully understood.

In its familiar liquid form, water is a tasteless, odourless, transparent inorganic solvent which appears colourless in small amounts but takes on a distinctive blue-green hue in larger quantities.<sup>[8]</sup> Indeed, its existence as a liquid at ambient pressure and temperature is one of many irregularities exhibited by the compound. All other hydrides of elements in the oxygen group form gases, as do hydrides of all the elements surrounding oxygen in the periodic table.<sup>[7]</sup> Like so many of water's unusual properties, its liquid existence at ambient conditions is largely due to its strong network of hydrogen bonds, formed as a result of the strong dipole moment (approximately 1.855 D)<sup>[9]</sup> induced from the difference in electronegativities between the hydrogen and oxygen atoms. The effects of hydrogen bonding and other inductive effects as a result of water's dipole moment and polarisability mean that explaining the behaviour of the liquid is a complex task.

In the solid form, water exhibits a huge wealth of polymorphs. Current work suggests that there are eighteen experimentally known crystalline forms of ice and several amorphous varieties of different densities accessible at different temperatures and pressures, as well as a number of other predicted crystalline forms (many of which adopt similar polymorphism to silica, such as the formation of cubic clathrate structures).<sup>[10-29]</sup>

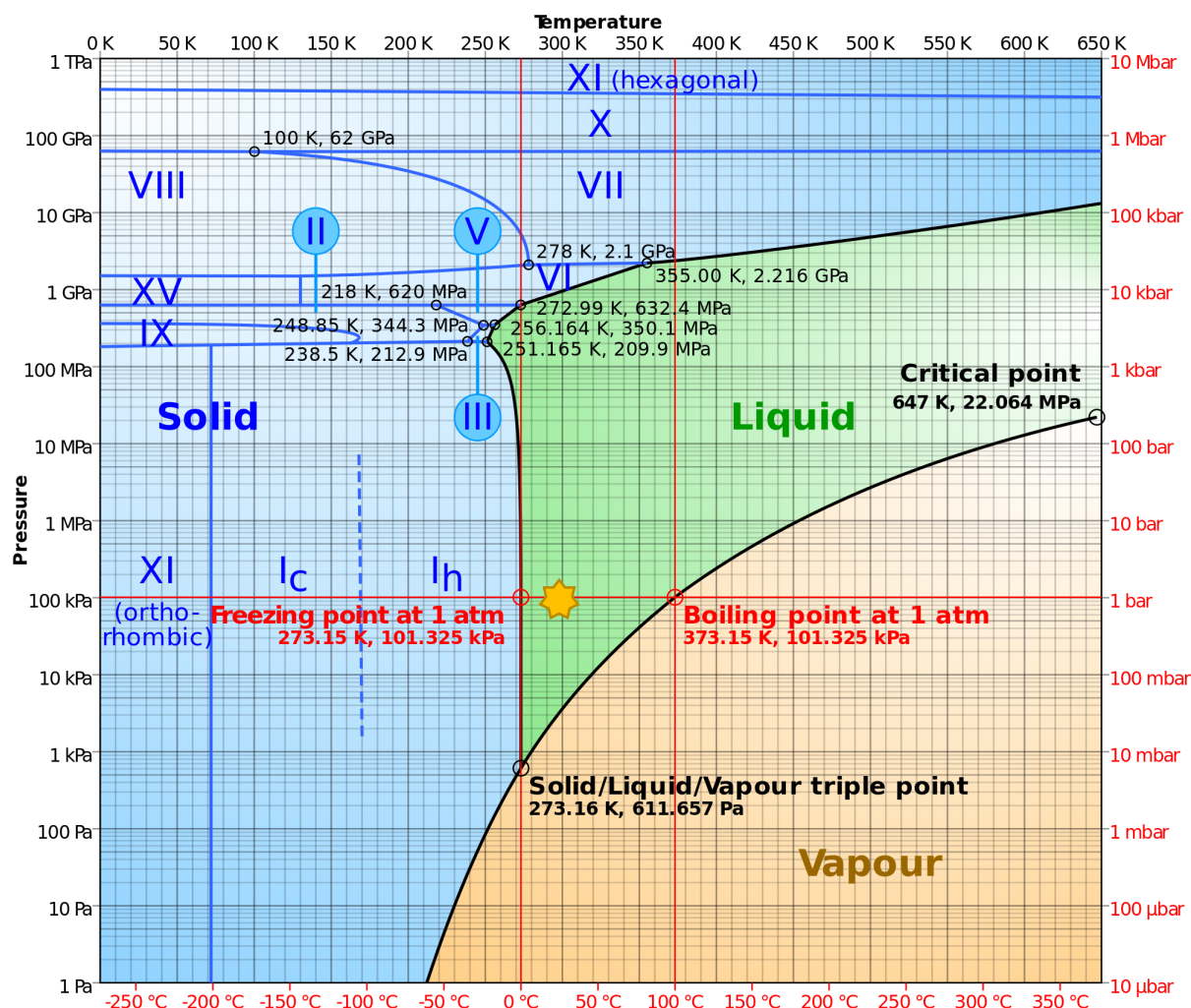


**Figure 6.ii:** The phase diagram of water, showing its rich phase behaviour as functions of temperature and pressure. The golden star indicates the average conditions found on Earth, demonstrating that both i) solid, liquid and gas phases are accessible under ambient conditions, and; b) that the ice on Earth is predominantly of the I<sub>h</sub> type.<sup>[30]</sup>

The eighteen known structures, which all involve water molecules hydrogen bonding with four other neighbours, are classified both by their crystalline structure and their degree of proton ordering. The hydrogen atoms can be either *ordered* or *disordered* within the structure, retaining the correct molecular and crystalline symmetry by obeying the Bernal-Fowler rules (more commonly known as simply the “ice rules”).<sup>[31]</sup> Ice on our planet is comprised almost entirely of the hexagonal Ice I<sub>h</sub> form, with small amounts of cubic Ice I<sub>c</sub> in the high atmosphere.

Ice	Proton Ordering	Crystal ( <i>space group</i> )	Molecular Environments	Density/ g cm <sup>-3</sup> <sup>32</sup>	Note
I <sub>h</sub> <sup>[10]</sup>	Disordered	Hexagonal ( <i>P6<sub>3</sub>/mmc</i> )	1	0.926	<i>a,b</i>
I <sub>c</sub> <sup>[11]</sup>	Disordered	Cubic ( <i>Fd3m</i> )	1	0.933	
II <sup>[12]</sup>	Ordered	Rhombohedral ( <i>R3</i> )	2 (1:1 ratio)	1.195	
III <sup>[13]</sup>	Disordered	Tetragonal ( <i>P4<sub>1</sub>2<sub>1</sub>2</i> )	2 (1:2 ratio)	1.160	<i>c</i>
IV <sup>[14]</sup>	Disordered	Rhombohedral ( <i>R3c</i> )	2 (1:3 ratio)	1.275	<i>d</i>
V <sup>[15]</sup>	Disordered	Monoclinic ( <i>C2/c</i> )	4 (1:2:2:2 ratio)	1.233	<i>e</i>
VI <sup>[16]</sup>	Disordered	Tetragonal ( <i>P4<sub>2</sub>/nmc</i> )	2 (1:4 ratio)	1.314	<i>f</i>
VII <sup>[17]</sup>	Disordered	Cubic ( <i>Pn3m</i> )	1	1.591	<i>g,h</i>
VIII <sup>[18]</sup>	Ordered	Tetragonal ( <i>I4<sub>1</sub>/amd</i> )	1	1.885	
IX <sup>[19]</sup>	Ordered	Tetragonal ( <i>P4<sub>1</sub>2<sub>1</sub>2</i> )	2 (1:2 ratio)	1.160	<i>c</i>
X <sup>[20]</sup>	Symmetric	Cubic ( <i>Pn3m</i> )	1	2.785	<i>h</i>
XI <sup>[21]</sup>	Ordered	Orthorhombic ( <i>Cmc2<sub>1</sub></i> )	1	0.930	<i>b</i>
XII <sup>[22]</sup>	Disordered	Tetragonal ( <i>I42d</i> )	2 (1:2 ratio)	1.301	<i>i,j</i>
XIII <sup>[23]</sup>	Ordered	Monoclinic ( <i>P2<sub>1</sub>/a</i> )	7 (all unique)	1.247	<i>e</i>
XIV <sup>[23]</sup>	Ordered	Orthorhombic ( <i>P2<sub>1</sub>2<sub>1</sub>2<sub>1</sub></i> )	2 (1:2 ratio)	1.294	<i>j</i>
XV <sup>[24]</sup>	Ordered	Triclinic ( <i>P1</i> )	2 (1:4 ratio)	1.328	<i>f</i>
XVI <sup>[25]</sup>	Disordered	Cubic ( <i>Fd3m</i> )	4 (6:6:4:1 ratio)		
XVII <sup>[26]</sup>	Disordered	Hexagonal ( <i>P6<sub>1</sub>22</i> )	1		
XVIII <sup>[27]</sup>	Disordered	Orthorhombic ( <i>PBcm</i> )			
O <sup>[28]</sup>	Disordered	Tetragonal ( <i>P42/ncm</i> )			
Metallic <sup>[29]</sup>	Symmetric	Monoclinic ( <i>C2/m</i> )			

**Table 6.iii:** Miscellaneous data pertaining to experimentally observed polymorphs of ice, as well as a selection of predicted forms (pale grey cells).<sup>[33]</sup> Densities correspond to crystallographic density, where reported. Coloured cells in the ‘Note’ column correspond to structurally similar polymorphs with differing degrees of proton ordering. Data collected from reference 33 using sources from references 10-32.

- a* – This is the predominant form of ice on planet Earth
- b* – Ice XI is the proton ordered form of Ice I<sub>h</sub>
- c* – Ice IX is the proton ordered form of Ice III. Fortunately, this is not the same Ice IX as reported in Kurt Vonnegut’s novel “Cat’s Cradle”!
- d* – Ice IV is not present on the phase diagram as it is metastable within the phase space of Ice V
- e* – Ice XIII is the proton ordered form of Ice V
- f* – Ice XV is the proton ordered form of Ice VI
- g* – Ice VII is formed of two interpenetrating networks of Ice I<sub>c</sub>
- h* – Ice X is the proton symmetric form of Ice VII
- i* – Ice XII is not present on the phase diagram as it is metastable within the phase space of Ice V
- j* – Ice XIV is the proton ordered form of Ice XII

#### 6.1.2. The Bernal-Fowler Rules

The *Bernal-Fowler Rules*, or simply the *Ice Rules*, are a series of rules which dictate the possible arrangements of atoms in the crystal structures of water ice. Named after John Desmond Bernal and Sir Ralph Howard Fowler who first conceived the principles in 1933, the Ice Rules govern which configurations of water molecules are permitted within the structures of water ice.<sup>[31]</sup> The main principles of the Ice Rules are that:

- Each oxygen atom within a water molecule is covalently bound to two hydrogen atoms, thereby maintaining the presence of discrete H<sub>2</sub>O units;
- Every water molecule is arranged such that its two hydrogen atoms are directed towards two of the four neighbouring oxygen atoms, forming a tetrahedron;
- Exactly one hydrogen is located between each O-O link. This hydrogen will be covalently bonded to the one oxygen, and hydrogen-bonded to the other.



These rules mean that every oxygen atom in an ice structure interacts with four hydrogen atoms – two via a strong covalent chemical bond, and two via a weak hydrogen bond – leading to the formation of a periodic lattice. It enforces that two sites of like charge cannot be directly adjacent to each other, for example two protons cannot point at each other. In reality, such defects do occur – so called *Bjerrum defects* occur when an O-O link either contains two protons (a *doppelt-* or *D-defect*), or no protons (a *leer-* or *L-defect*).<sup>[34]</sup> These have been shown to cause numerous anomalous properties within the structure of ice, such as electrical polarization and local structural weaknesses. However, for the purpose of this work, all structures have been prepared such that the ice rules are strictly obeyed and systems exhibiting Bjerrum defects have not been utilised.

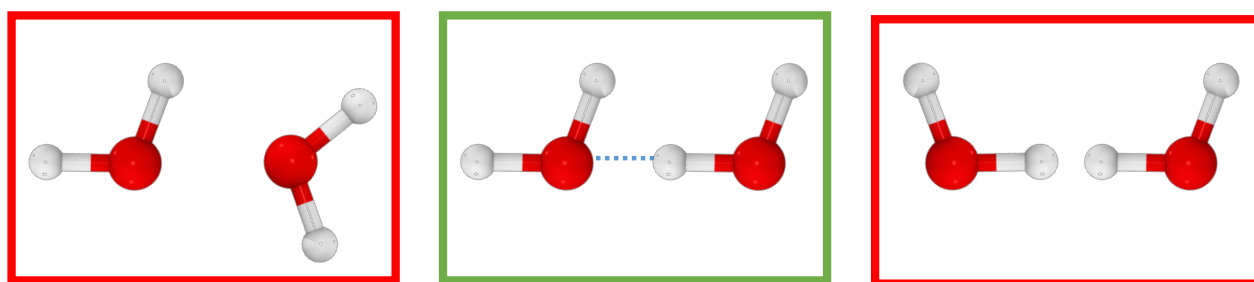


**Figure 6.iv:** Two water molecules with zero protons (*L-defect*, left), one proton (centre) and two protons (*D-defect*, right) between the two oxygens sites. Only the middle configuration is an example of two water molecules that obey the Bernal-Fowler Ice Rules, whereas the other two are disallowed Bjerrum defects.

### 6.1.3. The Structure of Water Ice

Presented below is a brief discussion of the structures of ice exhibited in this work – namely, Ice I<sub>h</sub>, Ice I<sub>c</sub> and Ice III, as well as a short introduction to the amorphous structures.

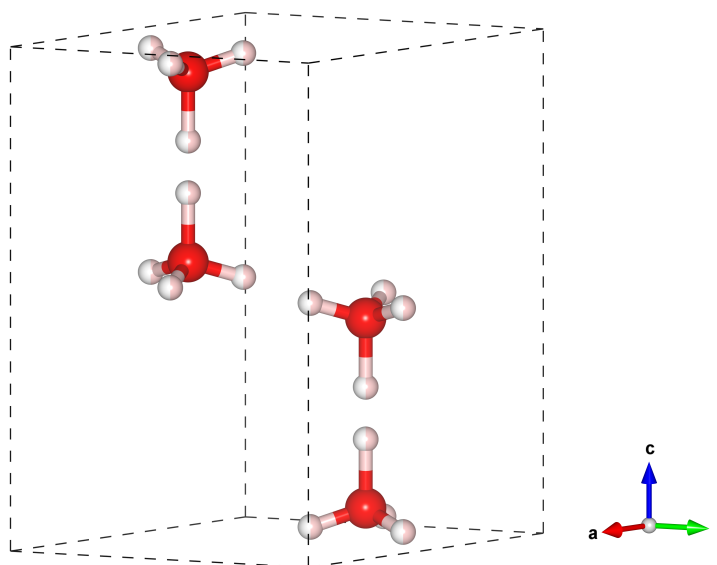


**Figure 6.v:** Illustration of the Ice  $I_h$  unit cell. In this depiction, all of the possible hydrogen positions are shown. In reality, each of the hydrogen atoms has an occupancy of 0.5 to maintain the  $H_2O$  stoichiometry, and their arrangements are determined by the Bernal-Fowler Ice Rules.<sup>[10]</sup>

By far the most common form of ice on Earth, and the form with which we are exclusively familiar in day-to-day life, is Ice  $I_h$  (Hermann-Mauguin space group  $P6_3/mmc$ , analogous to Lonsdaleite or  $\beta$ -tridymite). The structure consists of a hexagonal lattice whose four-molecule unit cell has dimensions  $a = 4.5181 \text{ \AA}$  and  $c = 7.3560 \text{ \AA}$ , giving a  $c/a$  ratio of 1.628 – slightly smaller than the ideal value for a hexagonal cell.<sup>[35]</sup> It forms a low density structure with a very small packing index (approximately  $\sim 1/3$ ). This is very low compared to most other packing arrangements, and much lower than the face-centred cubic structure of solid hydrogen sulphide, the analogous hydride of sulphur. In fact, the packing arrangement is so low that individual water molecules can easily reside within the voids of the structure.<sup>[36]</sup> This is the reason why ‘ice floats on water’ – the liquid form is actually denser ( $1.0 \text{ g cm}^{-3}$ ) than the Ice  $I_h$  structure ( $0.92 \text{ g cm}^{-3}$ ).<sup>[32]</sup> This is a very atypical physical scenario and one which life on Earth has exploited to great advantage.

A cubic arrangement of Ice I also exists as a metastable form under ambient conditions known as Ice I<sub>c</sub> (Hermann-Mauguin space group  $Fd\bar{3}m$ , analogous to  $\beta$ -cristobalite). This polymorph is formed by a face centred cubic lattice with unit cell parameters  $a = 6.358 \text{ \AA}$  with half of the tetrahedral holes filled. As with Ice I<sub>h</sub>, the packing index is very low ( $\sim 1/3$ ) giving it a very low density – like its hexagonal counterpart, Ice I<sub>c</sub> floats on liquid water.<sup>[11]</sup>

Ice I<sub>c</sub> is proposed to be present high in the Earth's atmosphere, and elsewhere in the Universe in low temperature environments. This polymorph of ice forms from water vapour at around  $-80^\circ\text{C}$  at ambient pressure.<sup>[37]</sup> Interestingly, Ice I<sub>h</sub> does not readily transform to Ice I<sub>c</sub> at  $-80^\circ\text{C}$ , but the reverse is true<sup>[38]</sup> – indicating a significant hysteresis in the phase change behaviour.

The third form of Ice scrutinised in this work is the tetragonal Ice III polymorph (Hermann-Mauguin space group  $P4_12_12$ ).<sup>[13]</sup>

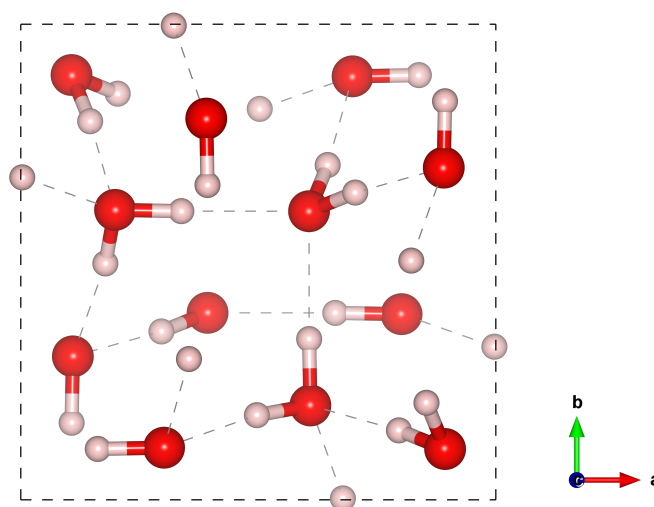


**Figure 6.vi:** Schematic of the Ice III unit cell. In this example, the H<sub>2</sub>O stoichiometry is presented (i.e. not all proton positions are shown) and an acceptable hydrogen distribution according to the Ice Rules is displayed.<sup>[13,39]</sup>

From the phase diagram, Ice III can be formed by cooling liquid water to 250 K at 300 MPa. It is the least dense of the high pressure polymorphs of ice, with a density of only  $1.16 \text{ g cm}^{-3}$ .<sup>[32]</sup> It also occupies only a very small region of the water ice phase diagram, however ice III can

also exist as a metastable polymorph within the ice II phase region if prepared appropriately.<sup>[40]</sup>

Ices I and III have a *triple point* with liquid water at 251.2 K and 209.9 MPa.<sup>[41]</sup> The triple point corresponds to the point on the phase diagram of a system at which the temperature and pressure of the three phases are in equilibrium. Thus, all three phases coexist at the conditions of the triple point.

There also exists a number of amorphous and ‘glassy’-type water structures. Of particular note are the three experimentally known amorphous ices – low density amorphous (LDA), high density amorphous (HDA) and very high density amorphous (VHDA) ices. Their structures are non-crystalline and poorly defined (there likely exists numerous types of each amorphous ice material); however, the three amorphous ices have known densities, corresponding to 0.94, 1.13 and 1.26 g mol<sup>-1</sup> for LDA, HDA and VHDA respectively.<sup>[42]</sup> In addition, their three radial distribution functions are very different, allowing to easily distinguish between the three forms.

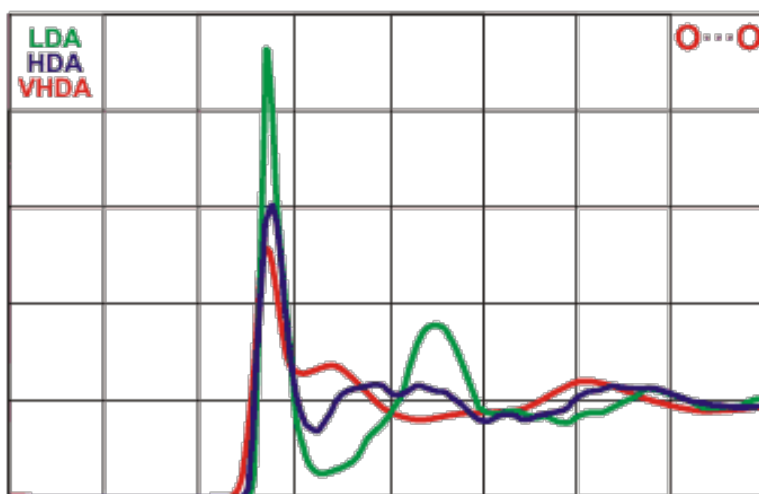


**Figure 6.vii:** Oxygen-oxygen radial distribution plots<sup>[43-45]</sup> for the three experimentally known amorphous ices – LDA (green), HDA (blue) and VHDA (red). Plot taken from reference 43 using data from references 44 and 45.

## 6.2. Atomistic Water Models

### 6.2.1. Introduction

An accurate model of water is desirable given the broad range of applications in a potential number of fields, including environmental science, biochemistry, planetary sciences, geology and materials sciences. However, the complexity of the hydrogen bonding and other inductive effects in water make its modelling an enormously complex task. Consider, for example, the liquid phase - no two water molecules are in the same chemical or electronic environment due to the effects of differing degrees of hydrogen bonding and polarisation. Thus, despite a great deal of research into the area, a universally accurate description of water is not currently available.<sup>[46-48]</sup>

Over the years, a huge number of water models have been developed<sup>[41,46,47,49-56]</sup> in an attempt to emulate the complex behaviour of water, although no single model accurately replicates all of the intrinsic properties of water. Indeed, most water models have been developed to accurately fit one particular physical property or parameter of water, such as density, melting point or distribution function. Such models are often excellent at reproducing this particular parameterised property, but are often then disastrous at predicting the values of other parameters. The ultimate goal in computational water studies would be to design a universal model which behaves correctly under a range of thermodynamic conditions, but sadly the best option currently is to choose a model which best fits the parameters under scrutiny.

The first realistic model for water was developed in 1933 by Desmond Bernal and Sir Ralph Howard Fowler,<sup>[31]</sup> long before the computer era. Bernal and Fowler's model consisted of a series of point charges combined with a rare-gas like repulsion-dispersion term centred on the oxygen atom. Such a model was used as the starting point for future work in the field, and it would be nearly half a century before Jorgensen developed the *TIPS* model,<sup>[57]</sup> the precursor to the ubiquitous *TIP3P* and *TIP4P* models.<sup>[49]</sup> Since then, a huge number of water

models have been developed, using both *empirical* (i.e. based on an experimental observation) and *ab initio* methods to define the models.<sup>[47,56,58]</sup>

Atomistic water models based on empirical parameterisation can be categorised in three ways:

1. The **number of sites**, atomic or virtual, used to describe the model. This usually ranges between three and six sites;
2. Whether or not the H-O-H framework is **rigid** (fixed bond lengths and angles) or **flexible**;
3. Whether or not the effects of **polarisation** are included within the model.

This work utilises the *TIP4P/Ice* rigid body water model,<sup>[41]</sup> and so only this model, its predecessors and related potentials will be discussed.

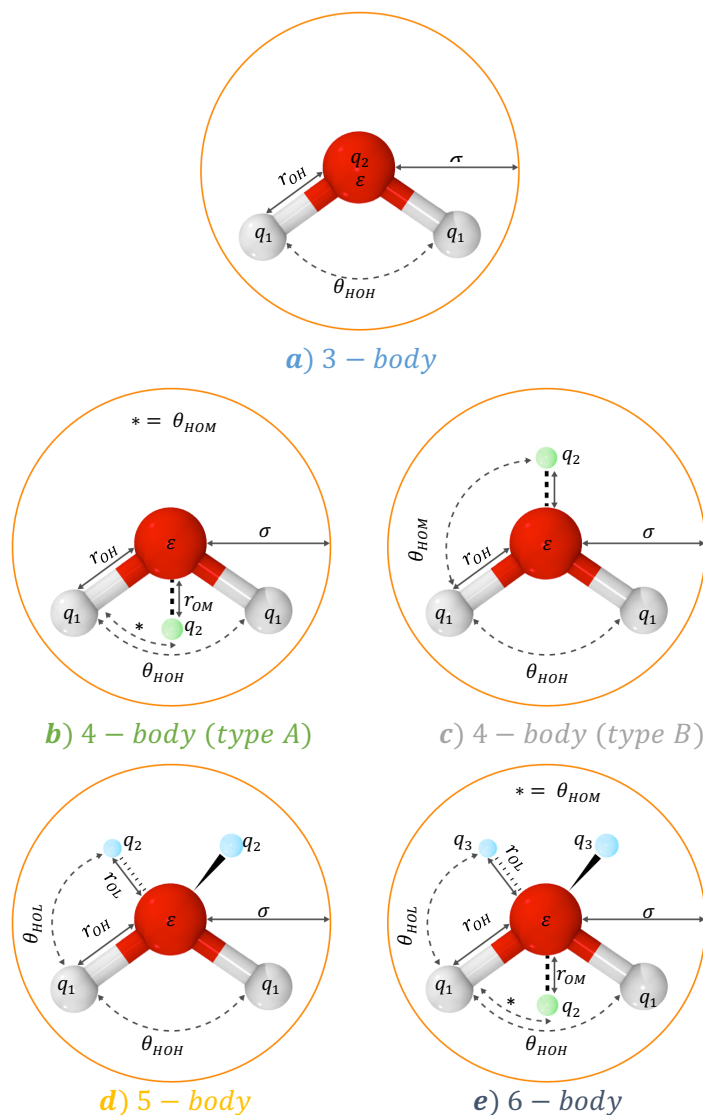


**Figure 6.viii:** Generalised schematics of the various types of models used to simulate water molecules, as well as all of their required parameters. In this nomenclature, single virtual sites (blue) have been denoted  $M$ , whereas pairs of virtual sites designed to emulate the lone pairs of oxygen (green) have been denoted  $L$ . In rigid body models, the distances  $r_{OH}$ ,  $r_{OM}$ ,  $r_{OL}$  and angles  $\theta_{HOH}$ ,  $\theta_{HOM}$ ,  $\theta_{HOL}$  are strictly defined, whereas these quantities are allowed to vary in flexible-body models. Additional advanced effects, such as polarisation, can also be incorporated to these models with further parameters. Three-body rigid models (top), such as *TIP3P*, are amongst the simplest and most utilised models in computational studies of water. The addition of extra parameters often (but not always!) increases the accuracy of the model, at the expense of longer computing times.

### 6.2.2. Transferrable Intermolecular Potential (*TIPnP*) Models

The *Transferrable Intermolecular Potential* (*TIPnP*) family of water models are amongst the most widely used computational descriptions of water and ice. In this generalisation,  $n$  corresponds to the number of ‘sites’ modelled by the potential; most *TIPnP* models have three, four or five modelled sites, which depict both *real* and *virtual* atoms within the model. These sites can be described in terms of Lennard-Jones parameters (to describe dispersion and repulsive effects) and Coulombic interactions (which describe the electrostatic effects). However, the van der Waals and Coulomb terms do not always occupy the same positions in space – Certain sites may be represented only by a Lennard-Jones type interaction, whereas another may be depicted by only a point charge. The distribution of these terms across the water molecule, as well as their total number, depends on the exact *TIPnP* model being utilised.

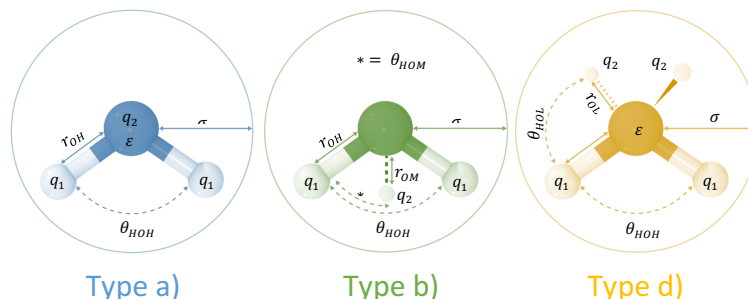
In addition, all of the bond lengths and angles in most *TIPnP* models are kept constant (meaning that they are *rigid-body* models), but again these values can vary significantly between the different depictions. Certain *TIPnP* models may also have additional terms to account for more advanced effects, such as polarisation. Altogether, this means that there are very many *TIPnP* type models available in the literature; usually each model has been tuned to fit one parameter of water particularly well, and so one must be careful when choosing which description of water to utilise in order to model the system of interest.

The simplest of the *TIPnP* models is the ubiquitous *TIP3P* description.<sup>[49]</sup> First developed in 1983 by William Jorgensen *et al*, this extremely basic model is essentially a modified version of Bernal and Fowler’s original description of water.<sup>[31]</sup> The *TIP3P* model consists simply of a Lennard-Jones centre at the oxygen site, and point charges at the atomic sites of both hydrogen and oxygen.

In the original model, no van der Waals interactions are computed for the hydrogen atoms; however, modifications to the original do exist where Lennard-Jones terms are also present at the two hydrogen sites – most notably in the CHARMM forcefield.<sup>[59]</sup> *TIP3P* has found



widespread use in computational studies of water as a result of its reasonable accuracy for the liquid phase and light computational demand.



	<i>TIP3P</i> <sup>[49]</sup>	<i>TIP4P</i> <sup>[49]</sup>	<i>TIP4P</i> – <i>Ew</i> <sup>[53]</sup>	<i>TIP4P</i> / <i>Ice</i> <sup>[41]</sup>	<i>TIP4P</i> / 2005 <sup>[51]</sup>	<i>TIP4P</i> / $\epsilon$ <sup>[52]</sup>	<i>TIP5P</i> <sup>[54]</sup>
$\sigma$ / Å	3.15061	3.15365	3.16435	3.1668	3.1589	3.165	3.120
$\epsilon$ / $\text{kJ mol}^{-1}$	0.6364	0.6480	0.680946	0.8822	0.7749	0.7732	0.6694
$r_{OH}$ / Å	0.9572	0.9572	0.9572	0.9572	0.9572	0.9572	0.9572
$r_{OM}$ / Å	-	0.15	0.125	0.1577	0.1546	0.1505	0.70
$\theta_{HOH}$ / °	104.52	104.52	104.52	104.52	104.52	104.52	104.52
$\theta_{HOM}$ / °	-	52.26	52.26	52.26	52.26	52.26	109.47
$q_1$	+0.417	+0.520	+0.52422	+0.5897	+0.5564	+0.5270	+0.2410
$q_2$	-0.834	-1.040	-1.04844	-1.1794	-1.1128	-1.054	-0.2410
<b>Published</b>	1983	1983	2004	2005	2005	2016	2000
<b>Type</b>	<b>a)</b>	<b>b)</b>	<b>b)</b>	<b>b)</b>	<b>b)</b>	<b>b)</b>	<b>d)</b>

**Table 6.ix:** Parameters for and schematics of a selection of *TIPnP* models with three, four and five sites. The model ‘type’ corresponds with the family to which the particular model is associated, as described in Figure 6.vii and summarised above. The charge  $q_2$  is located at different positions in the model depending on the type – at the centre of the oxygen *O* for type a), on the single virtual site *M* at the bisector of the HOH angle for type b), and split between two virtual sites *L* occupying ‘lone pair’ type positions for type d). Most of the work in this project has been carried out using the *TIP4P/Ice* model (highlighted), which belongs to type b) (centre)

However, it was well known (even at its publication) that the *TIP3P* model is very limited in its ability to predict the properties of water. For example, Ice  $I_h$  at the freezing point under 1 atmosphere of pressure is unstable when described by the *TIP3P* model – instead, the potential predicts that, at standard pressure, water freezes to form Ice II.<sup>[60]</sup> As such, it is immediately apparent that *TIP3P* cannot predict even simple phase behaviour of water in the solid phase. Despite this, it is possibly still the most commonly utilised model for water in research today, particularly in biochemical simulations where liquid water is only required as a solvent.

	<i>TIP3P</i>	<i>TIP4P</i>	<i>TIP4P</i> – <i>Ew</i>	<i>TIP4P</i> / <i>Ice</i>	<i>TIP4P</i> /2005	<i>TIP4P</i> / $\epsilon$	<i>TIP5P</i>	<b><i>Exp.</i></b>
Temperature of max. density / °C	-91	-25	+1	+ 22	+5	+4	+4	<b>+3.984</b>
Melting T of Ice $I_h$ /°C	146.0	232.0	245.5	272.2	252.0	240.0	273.9	<b>273.15</b>
Density of Ice $I_h$ at melting temperature	0.947	0.940	0.936	0.906	0.921	0.920	0.967	<b>0.917</b>
Density of liquid at melting temperature	1.017	1.002	0.992	0.986	0.993	0.986	0.987	<b>0.999</b>
$\Delta H_{melting}$ for Ice $I_h$ / kcal mol <sup>-1</sup> (298 K)	0.3	1.05	1.05	1.29	1.16	n/a	1.75	<b>1.44</b>
Dipole moment / D (298 K)	2.347	2.18	2.32	2.426	2.305	2.4345	2.29	<b>2.95</b>

**Table 6.x:** Various physical data as predicted by the *TIPnP* models discussed in this report.

Notice how the *TIP3P* model gives very poor results to most of the parameters listed, whereas the four-site models tend to give very good agreement to the properties for which they have been parameterised. None of the models are particularly good at reproducing all of the physical properties exhibited by the experimental substance.<sup>[41,46,49,51-54,60-62]</sup>

The desire for a more accurate of water that retained the simplicity of an  $n$  site rigid-body model led Jorgensen *et al* to simultaneously develop the *TIP4P* model. This is a four-body model, created by the addition of a *virtual* site positioned away from the centre of the oxygen atom at the bisector of the angle  $\theta_{HOH}$ . The original *TIP4P* model was published in the same paper by Jorgensen *et al* in 1983<sup>[49]</sup> and has proven to be a much more reliable model than its three-body counterpart<sup>[63]</sup> – but not without its limitations.<sup>[58]</sup>

At the turn of the millennium, a five-body model dubbed *TIP5P* was developed, in which the bisecting virtual site is substituted for two ‘lone-pair’ type charge sites situated around the central oxygen atom. The *TIP5P* model has been shown to be in excellent agreement with the temperature of maximum density, the melting temperature and the density of the liquid water. However, as is so often the case, many other properties are poorly emulated by the model (such as the actual values of density for the ice phases) and the additional computational time needed to model the additional virtual site has hindered the popularity of five-site rigid-body models.<sup>[54,58]</sup>

As a result, the four-site rigid-body models may appear to be the perfect compromise between quality and efficiency, as they emulate the features of water with reasonable accuracy whilst not being too computationally expensive. This has led to the desire to design more reliable four-body potentials, based on this original model but with the parameters tweaked in order to be more accurate for certain applications. Numerous re-parameterisations of the *TIP4P* potential have been carried out since the conception of the original potential, usually with consideration to accurately modelling one or two particular parameters. Some notable examples include:

- The *TIP4P – Ew* forcefield<sup>[53]</sup> was developed for use with Ewald techniques, which led to a significant improvement in the enthalpy of vaporisation;
- The *TIP4P/2005* model<sup>[51]</sup> is parameterised to successfully model the stability of crystalline phases and the temperature of maximum density;

- One of the latest examples from 2016, the *TIP4P/ε* model,<sup>[52]</sup> accurately describes various properties of water, but is still far from perfect. It shows that parameterisation of water models is not a finished project – in fact, new and more accurate parameterisations are still being developed today.

The re-parameterisation used in this work, *TIP4P/Ice*,<sup>[41]</sup> was too designed specifically with certain properties and features of water in mind.

### 6.2.3. *TIP4P/Ice* Model

The *TIP4P/Ice* model was developed by J. L. F. Abascal, E. Sanz, R. García Fernández and C. Vega in 2005. This re-parameterisation of the classic four-body model was designed specifically with phase-coexistence lines, density of phases and the melting temperature of Ice I<sub>h</sub> in mind. As such, the parameters of the *TIP4P/Ice* model give rise to a fairly accurate phase diagram for the solid phases of water, with all major phases described well and with only a small offset in temperature and pressure when compared to experimental values.<sup>[41]</sup>

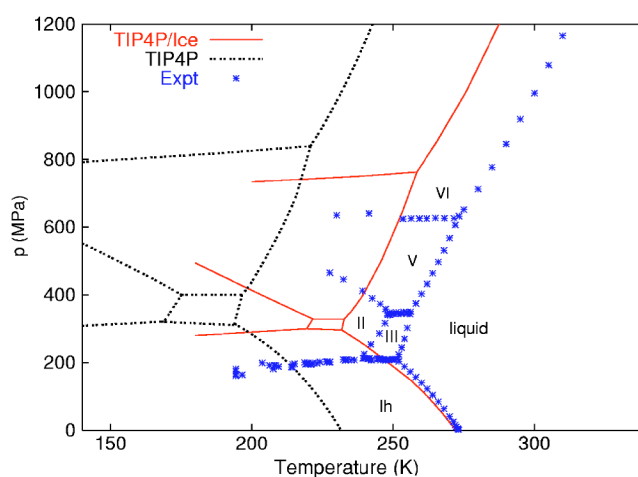


**Figure 6.xi:** The phase diagram for experimental, *TIP4P* and *TIP4P/Ice* water. Note the very close approximation of the coexistence line between Ice I<sub>h</sub> and the liquid phase, as well as the relatively correct distribution and prediction of crystalline phases<sup>[41]</sup>

The reasons for choosing this model over others were obvious. Firstly, this is the only rigid body model currently in the literature parameterised specifically for use with solid phases of water. As the overall aim of this project is to find a phase transition between two or more phases of ice, this seemed like the logical model to utilise. Secondly, as the model belongs to the 4-body family of rigid water models, it is intended that it will exhibit the advantages of a four-body model over the three- or five- body variants – that is, a good compromise between simulation time and computational fidelity.

### 6.3. Previous Simulations of Ice Phases

Attempts to simulate transformations between water and ice have been made for many decades. Despite this, there remains very few examples of successful simulations of the transitions between crystalline ice phases using atomistic models. The main reason for this is due to the vast configuration space of spatially unrestricted water, resultant from the many possible combinations of hydrogen bonding orientations within the solid and liquid phases of ice. This creates a vast configuration space littered with local minima.

Thus, a great deal of the work in the literature aims to attack the problem by using enhanced sampling techniques to accelerate sampling of the configuration space.

The majority of work in the literature relates to the crystallisation of Ice I<sub>h</sub> or Ice I<sub>c</sub> from liquid water. This clearly has considerable relevance in a number of fields, including in biology, astronomy, geology and medicine.

Matsumoto *et al* utilised molecular dynamics within the *NVT* ensemble (without the use of any acceleration techniques) to instigate the freezing of *supercooled* water to solid ice.<sup>[64]</sup> Matsumoto *et al* report the crystallisation of ‘perfect honeycomb’ structure of water ice (the exact phase was not identified). However, the authors do admit that their reported results were only one of many attempts, the rest which resulted in failure. In addition, the technique only works for supercooled, low-density variants of liquid water, and required over 250 ns of simulation time before any crystallisation processes were identified.

The work of Matsumoto *et al* is the only example of work known to the author of an ice crystallisation process occurring as a result of a ‘standard’ molecular dynamics calculation with no additional bias. Other examples, as the work of Svishchev and Kusalik in 1994,<sup>[65]</sup> impose external influences to promote the phase change – In this case, the application of a homogenous static electric field, which leads to the crystallisation of liquid water to the cubic ice  $I_c$  polymorph within 200 ps of simulation time.

In 2003, Radhakrishnan and Trout published work on the nucleation of Ice  $I_h$  using an umbrella sampling approach<sup>[66]</sup> with two order parameters. Radhakrishnan and Trout were able to crystallise their entire simulation system, as well as characterise a number of key transition states necessary to the transformation.

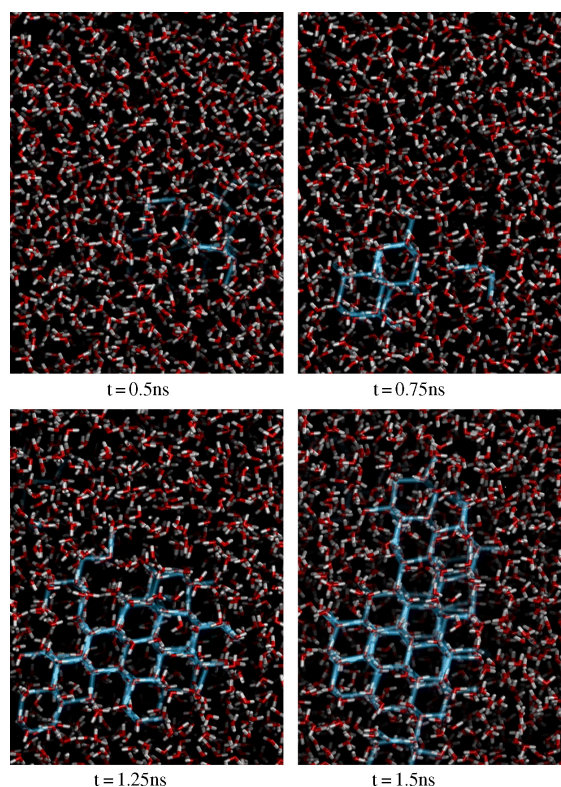


**Figure 6.xii:** Snapshots at 0.5, 0.75, 1.25 and 1.5 ns, showing the crystallisation of the unspecified ice structure from the work of Quigley and Roger. This was achieved by using a metadynamics scheme in which four collective variables were biased.<sup>[67]</sup>

More recently, metadynamics-based approaches have been extensively utilised. In 2008, Quigley and Rodger published two papers on a scheme to instigate crystallisation by applying a metadynamics scheme in the space of four collective variables – the Q4 and Q6 Steinhardt parameters,<sup>[68]</sup> a tetrahedral ordering parameter and the potential energy of the system. By applying this scheme to water, they were successfully able to nucleate ice from liquid water.<sup>[67,69]</sup>

In one publication, Quigley and Rodger report the growth of a critical nucleus which occurred within the first 500 ps and subsequent expansion over the next 1.5 ns of simulation time. The phase in this work was not formally identified, however it appears to be composed once again of Ice I<sub>c</sub>.<sup>[67]</sup> In another work, Quigley and Roger showed the successful growth of Ice I<sub>c</sub> using their metadynamics scheme.<sup>[69]</sup>

Work continues in an attempt to improve the metadynamics schemes already developed in an attempt to further the ability to sample the configuration space of ice. Just a few months before the publication of this thesis, Pipolo *et al* published a novel work in which they claim to be able to ‘navigate at will on the water phase diagram’,<sup>[70]</sup> visiting Ices I and VII, as well as the liquid phase, a number of amorphous phase and a hypothetical crystalline phase ‘Ice Y’. Pipolo *et al* defined the collective variables scheme in terms of permutation invariant vectors (PIVs),<sup>[71]</sup> constructed from inter-atomic Cartesian distances. A similar method has recently been employed by Pietrucci and Martonák, who were able to use the scheme to clearly differentiate between both crystalline and amorphous phases of ice.<sup>[72]</sup>

Outside of the crystalline phases, there exists a wealth of literature pertaining to the transformations between the different amorphous phases of ice. A notable example is the work of Martonák *et al*, who successfully navigated between the low, high, and very high density amorphous phases of ice using molecular dynamics simulations within the isothermal-isobaric ensemble.<sup>[73]</sup> Another example is the work of Tse *et al*, who examined the Ice I<sub>h</sub> to high-density amorphous ice transformation.<sup>[74]</sup>

#### 6.4. Summary

From the literature, it is clear that there are still many unanswered questions in the field of atomistic modelling of water ice. There exists a considerable number of structures to target, an even greater number of water models to represent their constituent molecules, and a number of advanced tools with which to enhance the rate of configuration space sampling. Yet despite this, accurate and efficient modelling of the condensed phases of water, and the phase transitions that link them, is still an extremely non-trivial endeavour. It remains the case that considerable research is to be done before the phase space of water, and the order parameters linking the metastable basins it supports, are fully characterised.

With this in mind, the work contained within this chapter represents an attempt to add to scientific knowledge to the field of condensed matter phase transitions within bulk systems of H<sub>2</sub>O. Both sections of this work make considerable use of *metadynamics*, however in the two sections the procedure is implemented in two very different ways.

The first results section of this chapter involves the use of the *Martonák et al* implementation<sup>[75,76]</sup> of metadynamics, in which modifications to the simulation cell are applied to the system in order to instigate structural change (see chapter 4 for further details). This is coupled to a technique developed in this work, coined *rotational shooting*, which is designed to perturb the hydrogen bonding network within the system and is described in detail in the next section.

The second component of the results discussion is dedicated to an investigation using metadynamics within the *plumed* plug-in.<sup>[77]</sup> Having taken inspiration from previous work,<sup>[69]</sup> the metadynamics scheme was applied in the space of three collective variables: the global Q4 and Q6 parameters, and a tetrahedral ordering parameter. These parameters and their implementations are discussed in detail prior to the reported results, which successfully show the occurrence of a phase transition between two crystalline states of water ice.



## 6.5. Metadynamics to the Cell with “Rotational Shooting”

### 6.5.1. Methodology

#### 6.5.1.1. The basis of “Rotational Shooting”

The *rotational shooter* is a technique developed and used in this work in an attempt to find a novel way to form a perturbed distribution of interactions between water molecules in a simulated system, with the ultimate desire being to instigate a phase transition between ice configurations.

In the original *shooter* algorithm used in transition path sampling calculations,<sup>[78,79]</sup> the velocities of the atomic centres within the system are redistributed under strict conservation of momentum, in order to simulate a novel regime of atomic movements. The *rotational shooter* instead modifies the angles between pairs of water molecules, whilst keeping the total angular momentum constant. The procedure for *rotational shooting* is as follows:

1. Choose a subset of the water molecule pairs in the system to be involved in the procedure. This can range from one pair (two molecules) to all molecules (for a system with an even number of water molecules) or every molecule minus one (for an odd numbered system).
2. Randomly choose two water molecules  $a$  and  $b$  within the system of interest, defining the position vectors of  $a$  and  $b$  as the centres of the oxygen site of each water molecule;
3. Define the vector  $v$  between the two water molecules  $a$  and  $b$ ;
4. Rotate the hydrogen atoms of water molecule  $a$  about vector  $v$  by an angle  $\theta$  degrees;

5. Similarly, rotate the hydrogen atoms of water molecule *b* about vector *v* by an angle  $-\theta$  (equivalent to  $360 - \theta$ ) degrees;
6. Repeat steps 1 – 5 until all water molecules have been paired and rotated by  $\pm \theta$ . Should the system contain an odd number of water molecules, leave the one remaining water molecule un-rotated by the procedure.

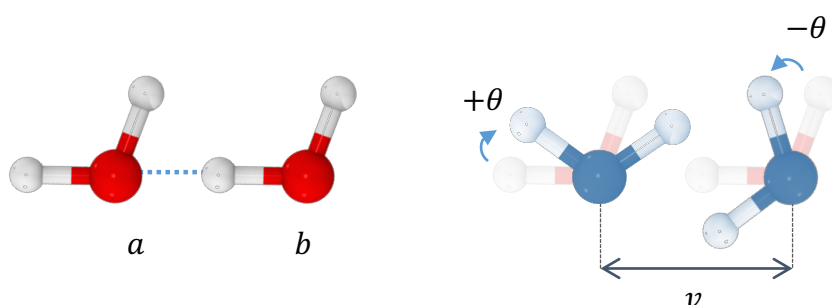


**Figure 6.xiii:** A hypothetical situation corresponding to two adjacent water molecules *a* and *b*, with O—H---O arrangement as allowed by the Ice rules (left). The two molecules are randomly assigned by the *rotational shooter* to be a rotation pair and are thus linked by the vector *v*. Remember that any two water molecules may be paired and they need not be adjacent, thus *v* can be long or short depending on the initial positions of the water molecules chosen to be *a* and *b*. The two molecules are rotated about vector *v* by an angle of  $\theta$  and  $360 - \theta$  degrees respectively, which causes a break the hydrogen bonding network and modifies the positions of the protons. This creates a new and possibly disfavoured configuration which may lead to a structural change.

All water polymorphs are four-coordinate and tetrahedrally coordinated, and thus the exotic polymorphism of water ice is caused solely by proton ordering and hydrogen bonding. The idea behind the rotational shooter, therefore, is to ‘break’ the hydrogen bonding network and locally redistribute the locations of protons within the ice structure, in order to instigate some change to the structure. In this way, it is analogous to the regular *shooter* – i.e., some

conserved quantity within the system is redistributed in order to generate a configuration that would not typically be accessible from molecular dynamics simulations alone.

#### 6.5.1.2. Computational Details

All work reported in this section were carried out using the *cp2k* package within the canonical ensemble (*NVT*). Molecular dynamics calculations were performed using the *velocity Verlet* scheme, with an integration time-step of between 0.5 and 1.0 fs (depending on the particular scheme) in order to ensure appropriate time reversibility. Periodic boundary conditions were implemented in the *x*, *y* and *z* directions for all of the systems tested in order to simulate a bulk sample of ice.

The *TIP4P/Ice* rigid-body model was used to describe interatomic interactions between the water molecules.<sup>[41]</sup> Long range electrostatic effects were accounted for using an Ewald summation.

The coupled *rotational shooting/metadynamics* procedure was initiated from two types of configurations, corresponding to a small 120 molecule Ice I<sub>h</sub> system and a larger 1200 molecule Ice III system. This allowed for the testing of how two different polymorphs of ice behaved during the scheme, as well as for an analysis of how system size and symmetry affects the procedure. All starting configurations were generated such that they strictly obeyed the Bernal-Fowler ice rules and exhibited no forbidden Bjerrum defects. The *RATTLE* algorithm was utilised within *cp2k* to impose the geometric constraints on the system.<sup>[80]</sup>

In all of the water work presented, the simulation temperature was controlled by using the *Canonical Sampling through Velocity Rescaling* (CSVR) thermostat, with an appropriate time constant chosen in order to facilitate a suitable temperature control scheme.<sup>[81]</sup>

The parameters used in the *rotational shooter* (the number of water molecule pairs to be rotated and the degree of rotation) varied between each simulation. Water pairs were chosen

at random for each rotation, meaning that a different sub-set of water molecules received changes to their orientations each time a *rotational shooting* move was implemented.

In addition, the *rotational shooter* scheme was coupled with the Martonák scheme of metadynamics, in order to induce changes to the simulation cell.<sup>[75,76]</sup> The motivation behind this was to introduce a ‘collective’ change alongside the ‘random’ change instigated by the *rotational shooting*, with the ultimate goal of maximising the chance of instigating a structural change within the simulated system. For example, whilst rotational shooting causes perturbations in the local hydrogen bonding arrangement, the metadynamics driver concurrently changes the shape, size and symmetry of the simulation cell (and hence the density), with the aim of facilitating a transformation event. Parameters for the metadynamics scheme were also system dependent, and are reported on a case-by-case basis.

### 6.5.2. Results and Discussion

#### 6.5.2.1. Overview

The *rotational shooting* technique, coupled with the metadynamics driver, produced a great number of interesting configurations within very short simulation time scales. Unfortunately, no direct crystalline solid-solid transformations were observed in this way. However, the combination of the two methods allowed for the generation of trajectories corresponding to melting events, phase transitions between crystalline and amorphous phases and the coexistence of liquid and solid phases, as well as the generation of exotic configurations, from crystalline Ice I<sub>h</sub> and Ice III phases. Each of these types of event is discussed below.

#### 6.5.2.2. Melting Events

A considerable number of metatrajectories with rotational shooting produced configurations that corresponded to melted, or partially melted structures. Liquid configurations could be generated from both Ice I<sub>h</sub> and Ice III configurations – this is expected, as the simulations were carried out at the triple point of these three phases for the *TIP4P/Ice* model. Such trajectories could find significant use in the modelling of the melting of Ice – for example, by using the model to generate an initial trajectory for use in a subsequent path sampling investigation of the transformation.

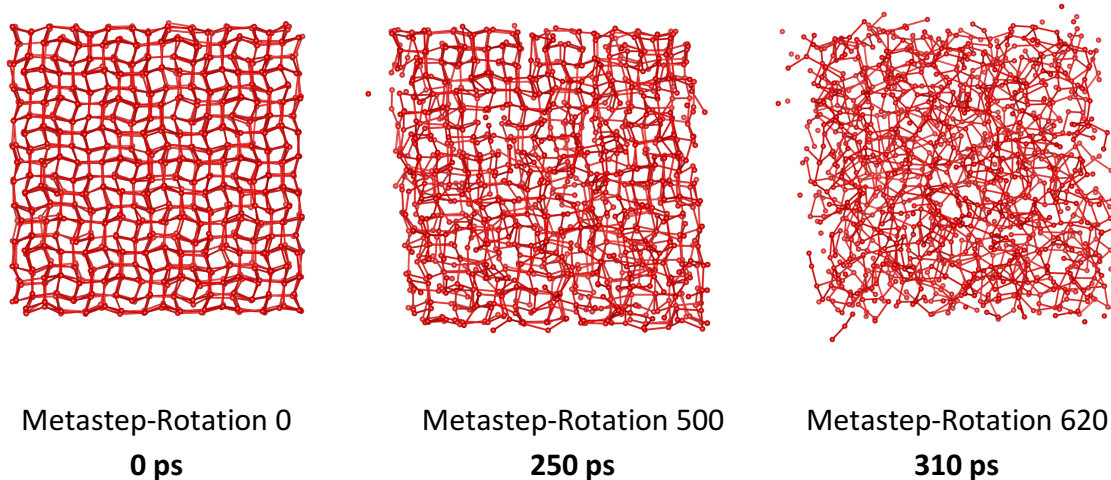


**Figure 6.xiv** (previous page): An example of a metatrayjectory showing a melting event. The initial ice III structure (left) undergoes partial melting (centre) before forming liquid water (right). The intermediate structure clearly shows regions that are still solid, as well as portions of the structure that have fully liquefied. Such observations are facilitated by joint use of the metadynamics and rotational shooting techniques. Only O-O contacts are shown for clarity.

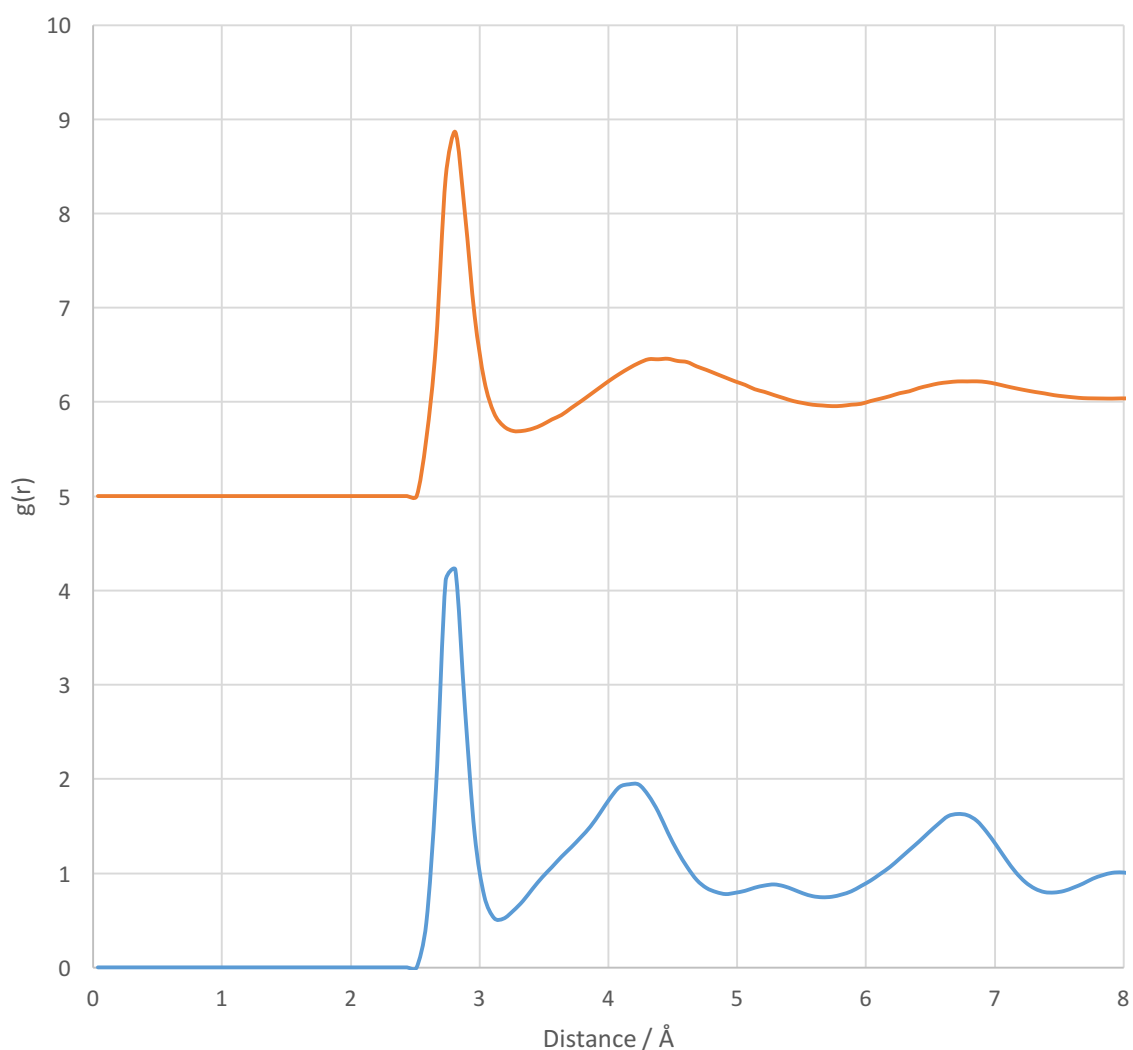


**Figure 6.xv:** Oxygen-oxygen radial distribution functions for the initial configurations (Ice III, blue) and the final configurations (orange) corresponding to the melted phase from the example exhibited in Figure 6.xiv. The orange plot clearly exhibits the distribution function of liquid water, and has been offset by 5.0 along the  $y$  axis for clarity.

Melting was observed in simulations where the metadynamics parameters were ‘strong’ and the rotational parameters ‘weak’ – for example, systems in which only 1-2% of the water molecules were rotated at each metastep. In the represented Ice III system (Figure 6.xiv), melting was achieved by rotation of 10 molecules by  $10^\circ$  each metastep, with an external pressure of 50 KPa. The Gaussian widths and heights were 2.0 and 4.0 respectively and deposited every 500 simulation steps. The system temperature was set at 219.4 K (the triple point of Ice I<sub>h</sub>, III and liquid water for the model), and the molecular dynamics integration time step was 1 fs.

The simulation of melting events in this way is undoubtedly facilitated by the combined use of both the *rotational shooting* procedure and the Martonák metadynamics driver. Configurations which were subjected to rotational shooting only, without a corresponding volume change, tended to produce amorphous phases (the exact type of which was dependent on the initial configuration). Trajectories that were subjected to metadynamics only transformed in a collective fashion after considerably longer periods of time, with resultant trajectories often not containing any ‘local’ deformation and hence nucleation and growth events. Whilst such events need not necessarily accurately model a physically meaningful growth or nucleation process, they were often present in trajectories in which *rotational shooting* was also used and may represent more plausible transformation pathways than those exhibited solely by metadynamics.

#### 6.5.2.3. Amorphous Phases

The combined technique was able to generate samples of all three of the experimentally known amorphous ice structures – LDA, HDA and VHDA. The nature of the generated amorphous structure was dependent on both the initial configuration and the *rotational shooting* / *metadynamics* parameters utilised. The identities of the amorphous ices were conclusively confirmed by plotting their radial distribution functions and densities, and comparing them with the plots displayed in Figure 6.vii.

Low density amorphous ice could be generated from samples of Ice I<sub>h</sub>, often forming mixtures with liquid water. Such configurations were generated when both the *rotational shooting* and metadynamics parameters were modest – for example, with 1-2% of the molecules in the sample undergoing rotation, with deposited Gaussians having very small widths and heights for the system size. It is believed that breaking the hydrogen bonding network in this way, whilst not affecting the density of the system too much, allowed for the formation of the low density amorphous ice phase from the starting hexagonal ice structure.

However, it is difficult to truly differentiate between the liquid and amorphous solid phases using radial distribution measurements. In addition, the density of most of these final configurations measured at around 0.97 g cm<sup>-3</sup> – halfway between the liquid and the amorphous phase. Such configurations could represent a mixture of solid and liquid components, or a transition state between the amorphous and the liquid phases. Alternatively, they could represent a variation of the low density ice structure, or be resultant simply from an overestimation of the density according to the *TIP4P/Ice* model.

Amorphous phases of higher density could also be generated, with the nature of the presented phase appearing to be highly dependent on the initial configuration. The high and very high density amorphous phases were generated only from initial samples of Ice I<sub>h</sub> and Ice III, respectively.

High density amorphous ice (HDA) could be generated from Ice I<sub>h</sub>, in simulations where reasonably ‘strong’ parameters for the *rotational shooter* and the metadynamics driver were utilised.

In the example presented, a 480 molecule system was utilised. HDA was produced by rotation of ~5% of the molecules at each metastep by 30° and with Gaussian widths and heights of 0.05 and 0.5 respectively being deposited every 500 simulation steps. A lower temperature of 100 K was used in this example, with an integration time step of 0.5 fs. The density of the final structure (1.20 g cm<sup>-3</sup>), as well as its O-O radial distribution plot, unambiguously confirms its identity as the high density amorphous structure.



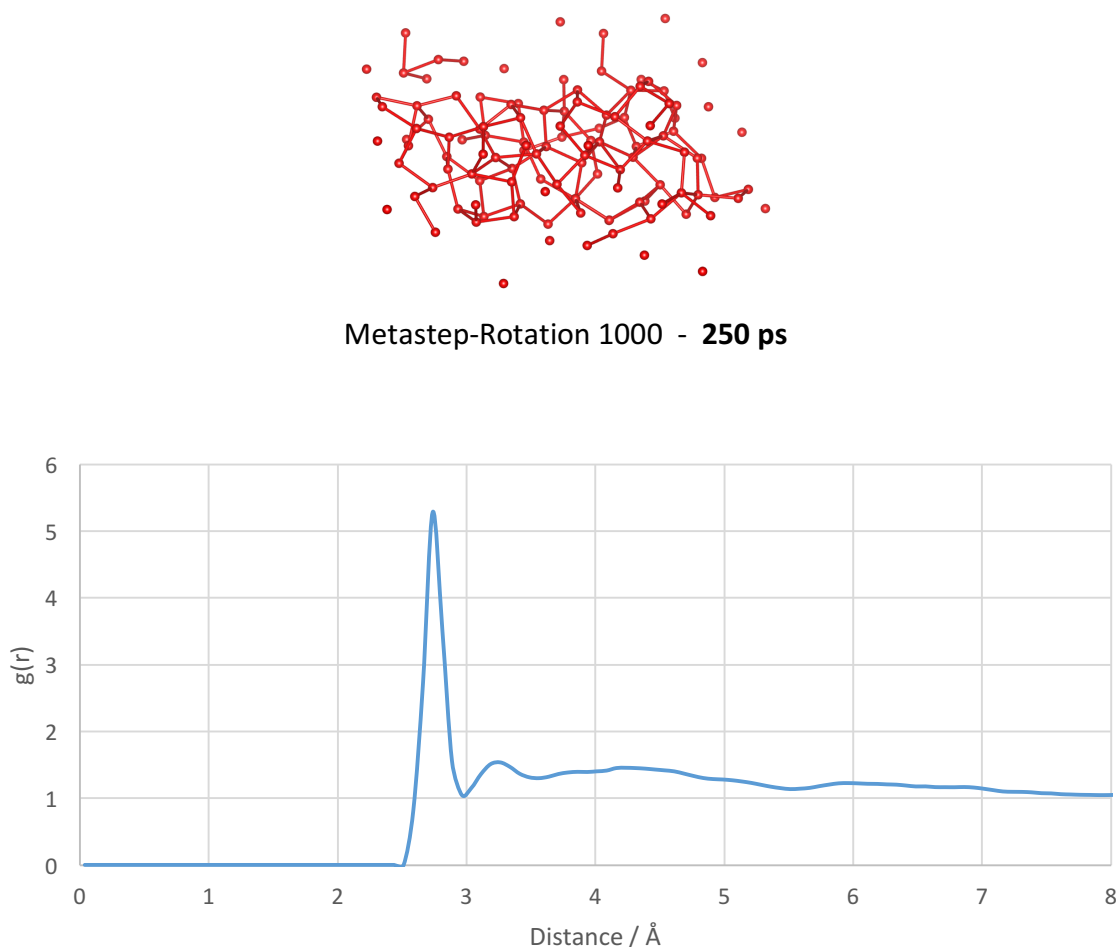
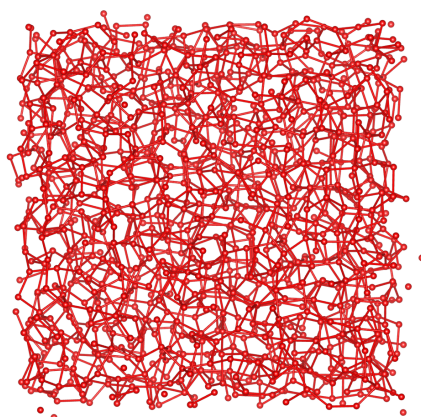


**Figure 6.xvi:** A high-density amorphous ice configuration, produced from an initial 120 molecule Ice I<sub>h</sub> structure (top) and its associated O-O radial distribution function (bottom).

With a density of  $1.20 \text{ g cm}^{-3}$  and the 'double peak' centred around  $4 \text{ Å}$  in the radial distribution function (similar to the literature data presented in Figure 6.vii) this configuration can be conclusively characterised as high density amorphous (HDA) ice.

Similarly, very high density amorphous ice (VHDA) could be generated from initial configurations of Ice III, in systems with relatively 'strong' *rotational shooting* and metadynamics parameters.

The example presented here was obtained from rotation of 600 molecules by  $10^\circ$  at each metastep, with an external pressure of 100 KPa with Gaussian widths and heights of 3.0 and 9.0 respectively. Gaussians were deposited every 500 simulation steps, each of which equated to 1 fs. Once again, the radial distribution plot and density ( $1.30 \text{ g cm}^{-3}$ ) conclusively confirms the formation of a very high density amorphous phase.



Metastep-Rotation 279 - **139.5 ps**

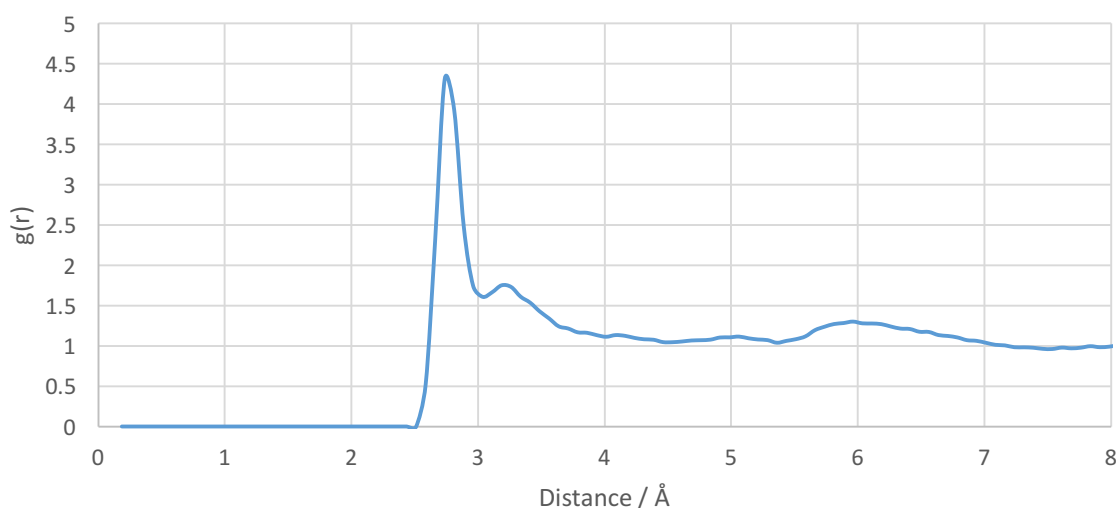


**Figure 6.xvii:** A very high-density amorphous ice structure, produced from the large Ice III structure (top). The O-O radial distribution function (bottom) shows similar peaks at approximately 3 Å and 6 Å as the literature data in Figure 6.vii, corresponding to the VHDA structure. A density of  $1.30 \text{ g cm}^{-3}$  also confirms this designation.

6.5.2.4. Non-typical Events

**Figure 6.xviii:** An example of an atypical ice configurations generated by the rotational shooting / metadynamics procedure - the formation of an internal surface by shearing caused by rapid lengthening of the  $c$  axis of the simulation cell. Such configurations could also be very useful in ice modelling.

The rotational shooter method also gave rise to some very unusual configurations of ice. Examples included systems with large pores, cavities and channels; the generation of shears and internal surfaces; and the formation of two-dimensional layers of water/ice with large inter-layer gaps. If such processes represent physically meaningful processes, they could find use in the modelling of catalysis, carbon dioxide/methane sequestration, and environmental sciences.

Unfortunately, there appears to be little correlation between the magnitude of the parameters used and the different events witnessed from the procedure. Despite this, the generation of such configurations remains interesting and potentially useful. Further investigation to determine how to accurately replicate these events, as well as assessing their physical viability, would be beneficial in the future.

## 6.6. Metadynamics using *plumed*

### 6.6.1. Methodology

#### 6.6.1.1. Introduction

The second part of this results chapter is dedicated to the investigation of the phase behaviour of ice using *metadynamics* without the *rotational shooting* implementation and with a different set of collective variables.

To ascertain the most effective order parameters to use for this work, a number of different collective variables were initially tested in order to determine which best captured the behaviour of the water molecules. The prescription ultimately used was a combination of three collective variables; the Q4 and Q6 Steinhardt Parameters, and a tetrahedral ordering Parameter. Both the Steinhardt parameters<sup>[82,83]</sup> and tetrahedral ordering<sup>[84]</sup> variables are implemented within the *plumed* metadynamics plugin, and both are briefly described in the following section.<sup>[77]</sup>

#### 6.6.1.2. Steinhardt Parameters (Q4 and Q6)

Occasionally the difference in densities between different solid phases (and even the solid and liquid phases) of a material are very similar to one another, thus differentiation between different phases and states of matter can often be difficult using coordination number alone. Steinhardt parameters<sup>[68]</sup> offer an intuitive way of calculating the degree of ordering within the first coordination sphere of a material by using a spherical harmonic function – a mathematical expression defined on the surface of a sphere. Within *plumed*,<sup>[82,83]</sup> Steinhardt parameters are calculated using the expression:

$$q_{lm}(i) = \frac{1}{\sum_j \sigma(r_{ij})} \sum_j \sigma(r_{ij}) Y_{lm}(\mathbf{r}_{ij}) \quad [Eq\ 6.1]$$

where  $\sigma$  corresponds to the switching function acting on the distance between sites  $i$  and  $j$ ,  $\mathbf{r}_{ij}$  corresponds to the vector linking the two aforementioned atoms and  $Y_{lm}$  corresponds to the spherical harmonic function. The degree of global ordering can be ascertained by taking the norm of the vector quantity produced by the below equation:

$$Q_l(i) = \sqrt{\sum_{m=-l}^l q_{lm}(i)^* q_{lm}(i)} \quad [Eq\ 6.2]$$

Using spherical harmonics in this way means that atoms coordinated to a central site will ‘point’ towards similarly valued regions of the spherical function, meaning that highly ordered phases will give a large positive (or negative) value of the collective variable. Conversely, highly disordered phases will produce values closer to zero according to the function, as such configurations where atoms are orientated towards differently valued regions of the spherical function will largely cancel out.

The value of  $l$  determines which order of spherical harmonics is to be utilised for the collective variable. The possible number of orthogonal functions for a particular order of spherical harmonics, given by value of  $m$ , is equal to  $\pm l$ . Thus, the total number of possibilities of  $m$  is equal to  $2l + 1$ , which accounts for all of the possible orthogonal ways that the spherical function can be orientated. For example, when using the sixth-order Steinhardt parameter  $q_6$ , thirteen different configurations of spherical harmonics are calculated in order to ensure that only the ordering, not the orientation, of the substituents bound to the central atom affect the final quantity calculated for the collective variable.

Whilst the Steinhardt parameters are generally used to distinguish between the solid and liquid phases of a material, they have been used to great effect in the modelling of solid-solid phase transitions. In particular, a considerable amount of literature uses such functions exactly for solid-solid phase transitions, including in water ice. Within *plumed*, they are referred to as the multi-collective variables  $Q4$  and  $Q6$  for the fourth-order and sixth-order Steinhardt parameters, respectively.

6.6.1.3. Tetrahedral Parameter (TET)

The tetrahedral ordering parameter incorporated into *plumed* is used to measure the degree to which the first coordination sphere around a central atom is tetrahedrally coordinated.<sup>[84]</sup>

This is given by the function:

$$s(i) = \frac{1}{\sum_j \sigma(\mathbf{r}_{ij})} \sum_j \sigma(r_{ij}) \left[ \frac{(x_{ij} + y_{ij} + z_{ij})^3}{r_{ij}^3} + \frac{(x_{ij} - y_{ij} - z_{ij})^3}{r_{ij}^3} + \frac{(-x_{ij} + y_{ij} - z_{ij})^3}{r_{ij}^3} + \frac{(-x_{ij} - y_{ij} + z_{ij})^3}{r_{ij}^3} \right] \quad [Eq\ 6.3]$$

where once again  $\sigma$  corresponds to the *plumed* switching function acting on the distance between atoms  $i$  and  $j$ ,  $\mathbf{r}_{ij}$  corresponds to the vector linking atoms  $i$  and  $j$ , and  $x_{ij}$ ,  $y_{ij}$  and  $z_{ij}$  correspond to the x, y and z components of vector  $\mathbf{r}_{ij}$  respectively.

Although all water molecules in all ice phases are arranged tetrahedrally, small variations in the degree of this ordering can be detected using this multi-collective variable. In addition, it can be used to easily classify the differences between solid, liquid and melt phases, as well as between crystalline and amorphous solid phases.

6.6.1.4. Computational Details

All calculations contained in this section were carried out using the *cp2k* package within the canonical ensemble (*NVT*). Molecular dynamics integration was performed using a *velocity Verlet* scheme, with a time-step of 2 fs. Periodic boundary conditions were implemented in the  $x$ ,  $y$  and  $z$  directions to emulate a bulk crystalline system.

As above, the *TIP4P/Ice* rigid-body model was utilised to describe interatomic interactions between the water molecules.<sup>[41]</sup> 1200 water molecules were simulated in each system, corresponding to 4800 atomic sites (two hydrogens, one oxygen and one virtual site per

molecule). All starting configurations were generated such that they strictly obeyed the Bernal-Fowler ice rules, exhibiting no Bjerrum defects. The *RATTLE* algorithm was utilised within *cp2k* to impose the geometric constraints on the system.<sup>[80]</sup> Long range electrostatics were accounted for using an Ewald summation.

The system temperature was controlled by using the *Canonical Sampling through Velocity Rescaling* (CSVR) thermostat,<sup>[81]</sup> with an appropriate time constant chosen such that the temperature was effectively regulated but not overdriven. The simulation temperature was set at 219.4 K, corresponding to the temperature at the triple point of Ices I, III and liquid water, as described by the *TIP4P/Ice* model.

Metadynamics was implemented using the *plumed* plug-in,<sup>[77]</sup> coupled to the *cp2k* MD integrator. The standard implementation of metadynamics was utilised in this work, i.e. without the well-tempered or multivariate-Gaussian modifications. The Q4, Q6 and TET collective variables were utilised, with Gaussian widths of 0.3, 0.3 and 0.2 for each parameter, respectively. The Gaussian heights were set at 16 kJ mol<sup>-1</sup>. Gaussians were deposited in the space of the collective variables every 500 time steps, corresponding to each picosecond of simulation time. This combination of Gaussian height and deposition rate allowed for the bias potential to be built up within an acceptable time-frame whilst giving the system enough time to evolve appropriately during the intervening molecular dynamics propagations.

### 6.6.2. Results and Discussion

#### 6.6.2.1. Evolution of the Metatrajectory

The metadynamics with *plumed* approach was able to induce a solid-solid phase transition between two configurations of water ice. A third polymorph appeared as a transient structure during this transformation, corresponding to a medium-density intermediate phase. Additionally, a number of amorphous regions were generated over the procedure, which appeared to play a crucial role in the transformation between Ice III and the cubic Ice  $I_c$  phase. This result could only be achieved by simultaneously applying the bias potential in the space of all three collective variables described above.

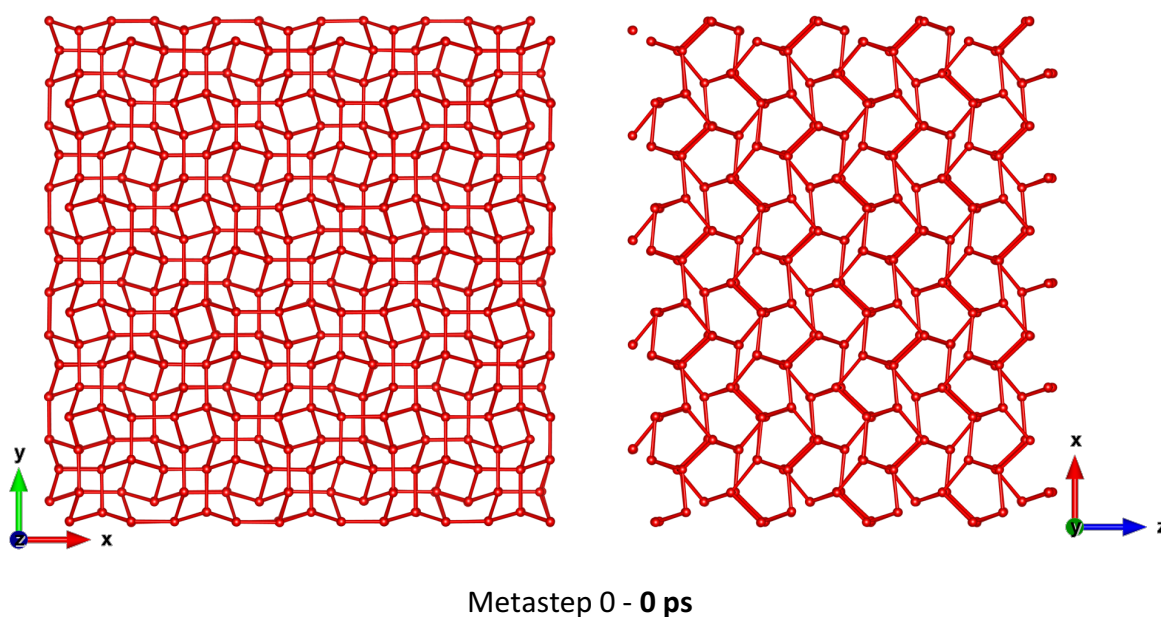


**Figure 6.xix:** Two representations of the starting Ice III structure. As previously, only oxygen-oxygen contacts have been drawn for clarity.

Initial Gaussian deposition simply caused the Ice III structure to fluctuate within its associated energy basin, causing local distortions and oscillations. However, after 360 ps of simulation, the system began to transform into a new configuration. Starting from a small seed of the



new material, the new configuration grew at the expense of the Ice III starting structure over the next 200 ps of simulation.

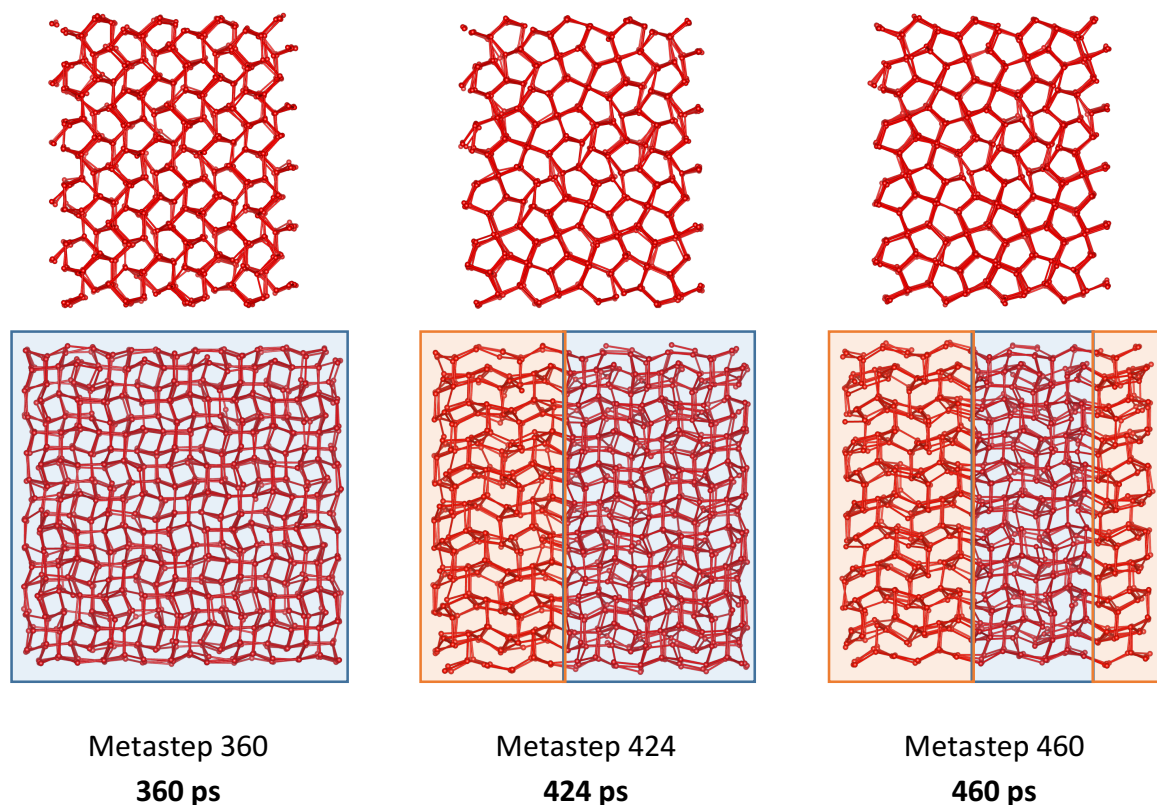


**Figure 6.xx:** Evolution of the meta-trajectory between metasteps 720 and 920. Ice III (highlighted in blue) is gradually replaced by an intermediate phase (highlighted in orange). The intermediate phase had a coordination number intermediate between that of Ice III and Ice  $I_c$

The growth of the new material continued to take place until all of the initial Ice III motifs had been transformed. By metastep 550, Ice III has been completely eliminated and replaced by the second crystalline phase.

This new configuration of ice appears to have a coordination sphere intermediate between that of Ice III and Ice  $I_c$ , and does not correspond to any of the eighteen-known phases, clathrate phases or the so-called ‘*computer ice*’ Ice 0. Its geometry is defined by puckered

sheets of pentagonal rings (similar to that of the *Cairo tiling*),<sup>[85]</sup> with every other water molecule hydrogen bonding to the layer above or below it in an alternating fashion. Inter-oxygen distances vary considerably during the simulation, ranging between 2.55 Å and 2.95 Å, with little correlation between same- and inter-layer O-O contacts.

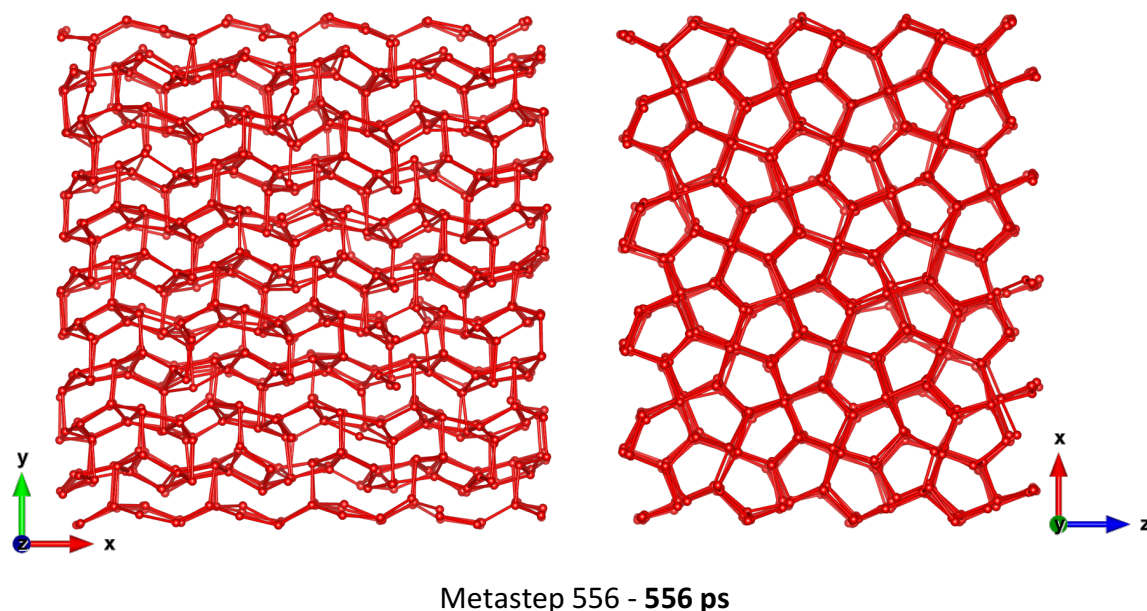


**Figure 6.xxi:** Representations of the intermediate polymorph of ice. The structure bears resemblance to that of the *Cairo tiling*, with alternating water molecules in each layer involved with same-layer and inter-layer interactions. The puckered layers are clearly seen in (a), whereas the characteristic pentagonal tiling is displayed in (b).

The intermediate species persisted within the simulation in its entirety for approximately 160 ps, corresponding to the same number of additional metasteps. However, at metastep 600 the system begins to undergo another change. At metastep 640 an abrupt modification occurs, with two-thirds of the system reverting back to Ice III, while the remainder of the system loses its crystallinity to form an amorphous phase. Over the following nanosecond of simulation, the reconstructed ice III is gradually consumed by the amorphous phase, which slowly spreads along the [010] direction until the ice III is once again completely consumed.

Simultaneously, isolated regions of the amorphous ice begin to crystallise into cubic Ice I<sub>c</sub>, which too spreads along the [010] direction. At this point in the simulation, pockets of Ice I<sub>c</sub> are very localised and largely insignificant to the overall structure. However, it can be seen that for large periods of the metatrajectory between metasteps 640 and 1200, there exists co-existing motifs of Ices I<sub>c</sub> and III, as well as the medium-density amorphous phase.

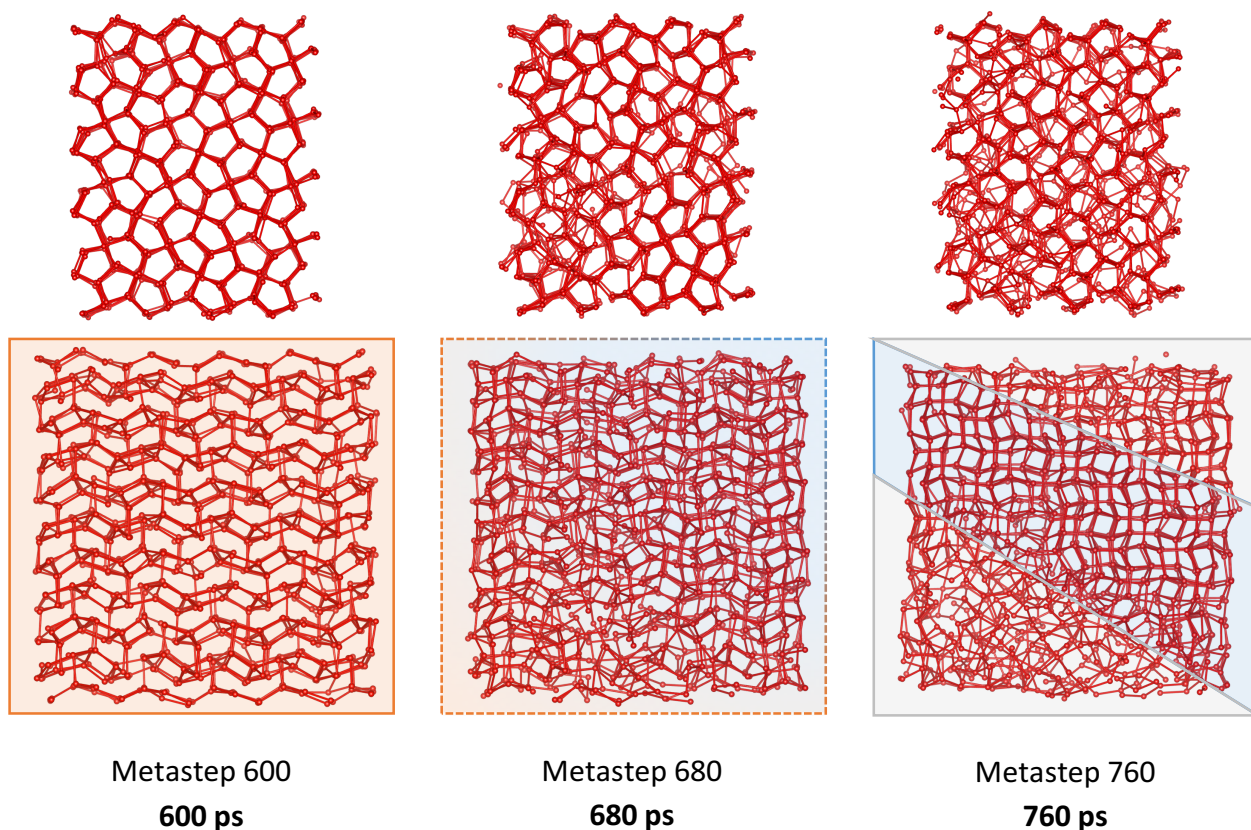


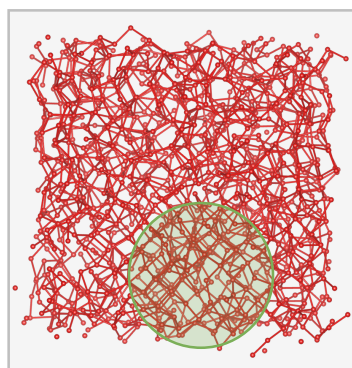
**Figure 6.xxii:** Illustrations showing the partial reconstruction of Ice III from the ice intermediate phase (shaded in orange). Approximately 2/3 of the structure regains an Ice III-like topology (blue), with the remainder dominated by an amorphous phase (grey). There are also trace amounts of Ice I<sub>c</sub> nestled within the amorphous phase.

Local motifs of Ice III persist for the following nanosecond of simulation time, however most of these structures are subject to local distortions caused by the surrounding oscillations in the amorphous phase. At this point, a large region of Ice I<sub>c</sub> slowly begins to crystallise within the amorphous structure, and gradually replaces it by once again spreading in the [010]

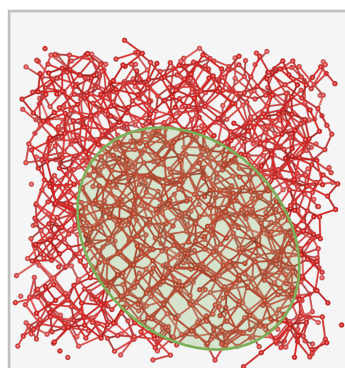


direction. By metastep 1200, there is no trace of Ice III remaining in the structure, and the system is dominated by amorphous ice, with small trace of cubic Ice  $I_c$  present.

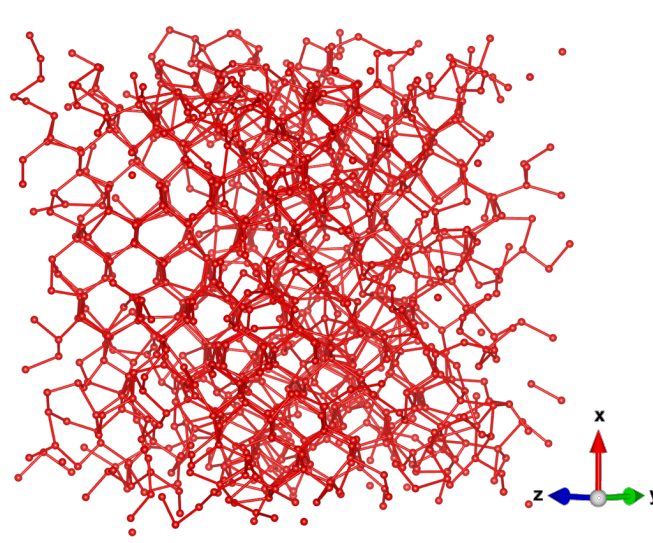
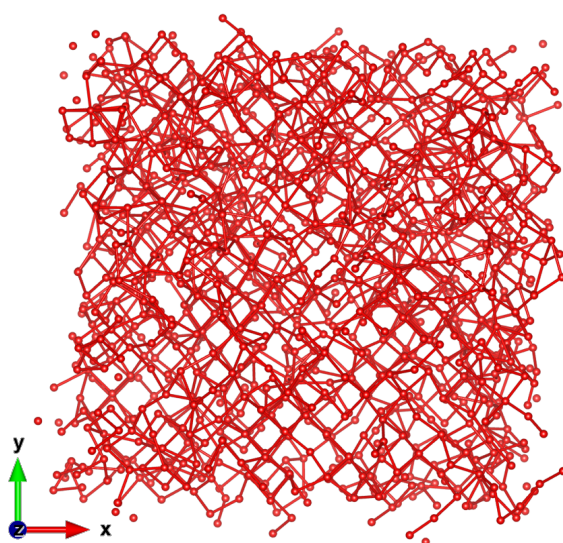
The simulation continues for another 4800 metasteps, corresponding to a further 4.8 nanoseconds. However, very few structural changes occur during this considerable time frame, with the exception being that some of the amorphous ice undergoes crystallisation to Ice  $I_c$ . The final structure in the metadynamics run is an almost entirely Ice  $I_c$  structure, albeit containing a substantial quantity of defects and some small regions corresponding to the amorphous ice. Further metasteps were unable to alter the structure reported here.



Metastep 1140  
1.14 ns



Metastep 2040  
2.04 ns



Metastep 6600 – 6.6 ns

**Figure 6.xxiii (previous page):** The evolution of the amorphous phase of ice. At metastep 1140, a clear region of Ice I<sub>c</sub> (labelled green) has begun to form, which spreads along (010) at the expense of the amorphous ice. This continues to grow for the next 5.46 ns of simulation time, with the final structure at metastep 6600 (after 6.6 ns of simulation) consisting predominantly of Ice I<sub>c</sub> but containing a considerable number of defects.

It is curious that the metadynamics procedure was able to find the Ice I<sub>c</sub> polymorph, however showed no trace of ambient hexagonal Ice I<sub>h</sub>. However, this is not entirely unexpected; previous theoretical work has suggested that cubic ice will be generated preferentially over the ambient hexagonal form in certain circumstances,<sup>[69]</sup> one of which is if the simulation cell corresponds with the symmetry of Ice I<sub>c</sub>. This is the case in this work, as the simulation cell did not exhibit a geometry commensurate with hexagonal symmetry.

Thus, the results of the metadynamics simulations presented here helps to corroborate both the experimental and theoretical work that has been published in the past. However, it presents a novel solid-solid mechanism between two experimentally known crystalline phases of ice, as well as an intermediate phase not experimentally known.

Analysis of the radial distribution plots during key moments of transformation gives some insight into the crystallinity and structure types present during the transformation. The  $g_{00}$  distribution function for Ice III and the intermediate structure show an ordered, crystalline behaviour within the first 10 Å. The Ice I<sub>c</sub>/amorphous distribution function, however, shows considerable long-term disorder, caused by the many defects present in the structure. The double-peak around 4 Å is similar to that seen in high-density amorphous ice.

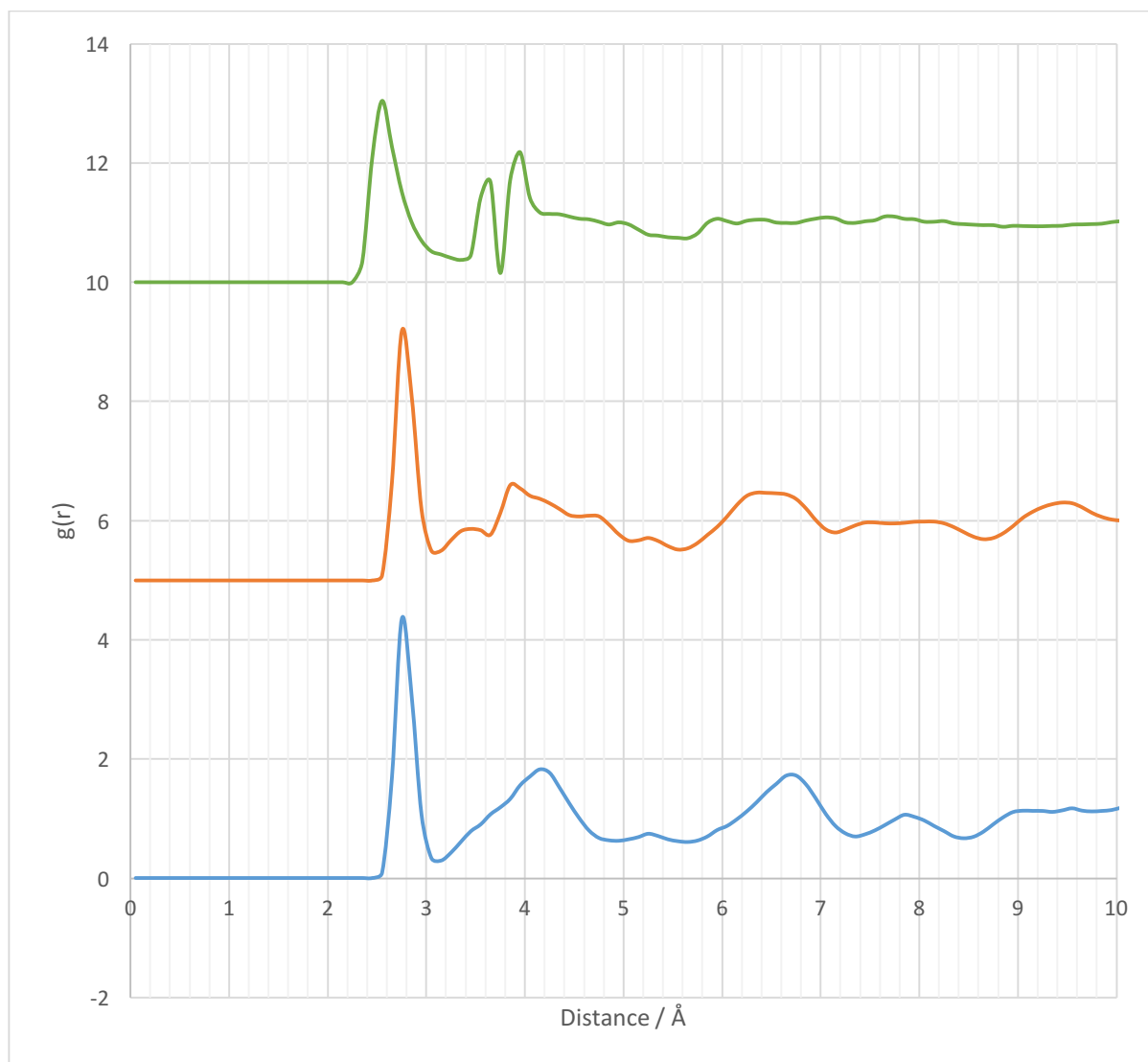


**Figure 6.xxiv:** Oxygen-oxygen radial distribution function for the pure Ice III polymorph (blue), the intermediate polymorph (orange) and the final product, which was a mixture of cubic Ice  $I_c$  and amorphous ice (green). The plots for Ice III and the intermediate phase demonstrated the ordered, periodic nature of these structures. The Ice  $I_c$  curve, however, exhibits some features corresponding to a crystalline phase, however at large values of distance clearly shows amorphous behaviour, with no ordered peaks after 6 Å. Both the Ice  $I_c$ /amorphous and intermediate distribution plots bear some resemblance to the radial distribution function of high density amorphous (HDA) ice, featuring the characteristic ‘double-peak’ at approximately 4 Å seen in Figure 6.vii. The orange and green plots have been offset along the y axis by 5 and 10 respectively, for clarity.

6.6.2.2. Evolution of the Collective Variables

It is clear that the beginning of the simulation, the system is very responsive to the application of the bias potential in the space of three chosen collective variables. The amplitude exhibited by the variation in each of the CVs increases steadily for the first 200 metasteps. A number of pronounced changes can be observed, which can be attributed directly to observed events over the course of the trajectory.

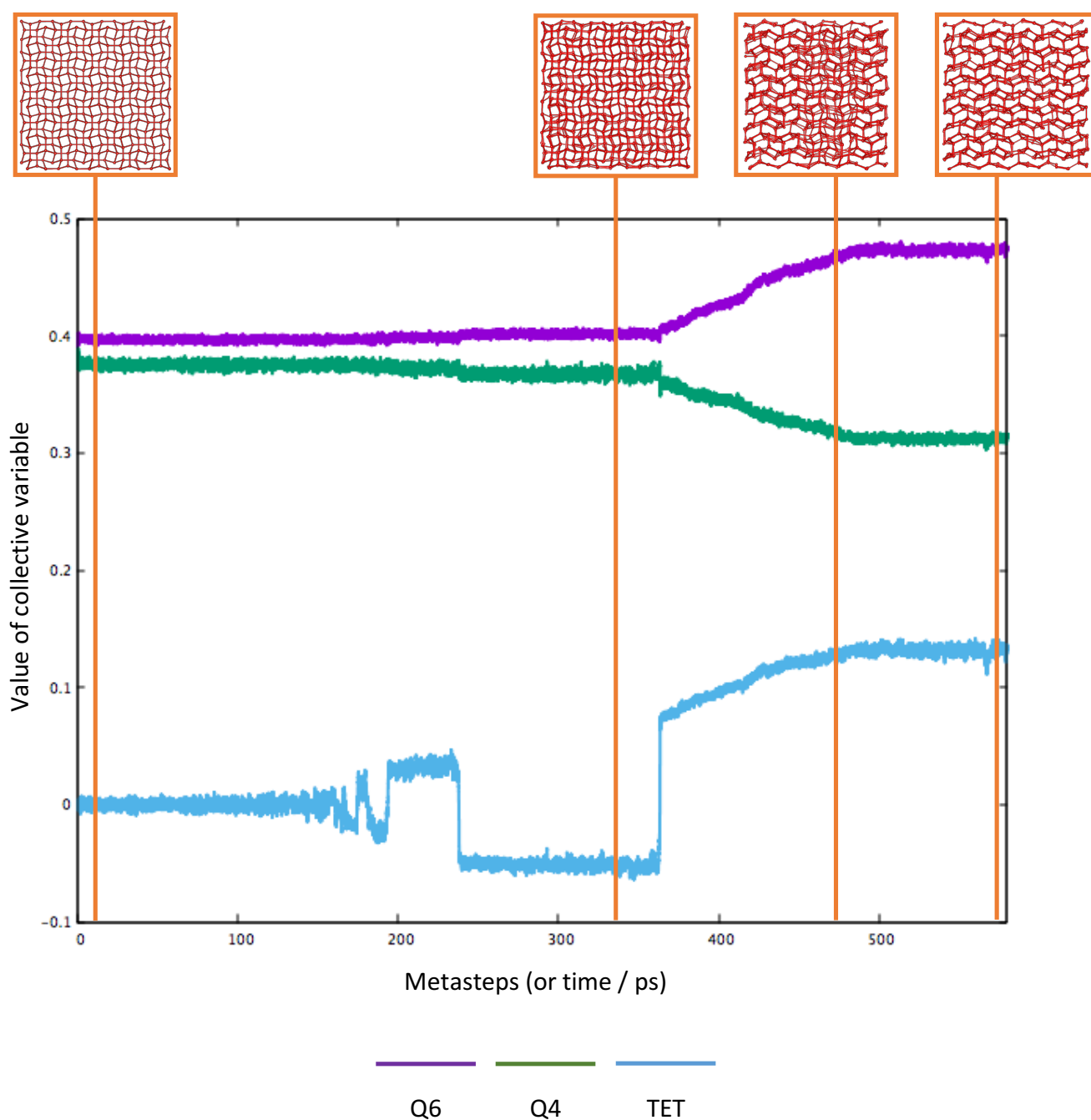


**Figure 6.xxv (previous page):** The variation in the three collective variables over the first 580 metasteps (580 ps) of the simulation. The *TET* parameter in particular is very responsive to the metadynamics procedure at this stage, being able to distinguish between small fluctuations in the initial Ice III phase, as well as between Ice III and the intermediate polymorph. The *Q4* and *Q6* parameters show little variation when the system resides in the Ice III basin, however shows a clear change after the transformation to the intermediate phase.

The system continues to respond to the collective variable bias for the next 400 metasteps, corresponding to the re-formation of the Ice III and subsequent replacement by the amorphous phase. However, following the formation of this phase, the system no longer reacts to the action of the metadynamics. Instead, after approximately 980 ps of simulation, the collective variables gradually relax into their final basin, corresponding to the mixed Ice I<sub>c</sub> / amorphous product.

There are numerous possible reasons for this. Firstly, as the resultant phase is largely amorphous in nature, it is possible that average coordination parameters are unlikely to have a significant global effect on the system. However, it is believed that the most likely explanation for this loss of effectiveness of the metadynamics procedure is that the Gaussian dimensions are no longer appropriate for the system in this configuration. To combat this, rescaling of the widths and heights of the Gaussian would be necessary at this point. This can be justified by looking at the variation in the collective variables. In particular, the *TET* parameter takes on a range of values over the last 5 ps of the simulation, despite ice configurations not appearing to alter significantly.

Thus, there is a clear sequence of events during this metatrajectory:

Ice III → *Cairo*-like Intermediate → Ice III/Amorphous → Amorphous → Ice I<sub>c</sub>/Amorphous

This raises the tantalising possibility that, whilst a direct phase transition between Ice III and the novel intermediate phase is possible, a transition to Ice I<sub>c</sub> may proceed via an amorphous



intermediate. A possible future investigation using path sampling techniques would be highly desirable to classify this transformation further.

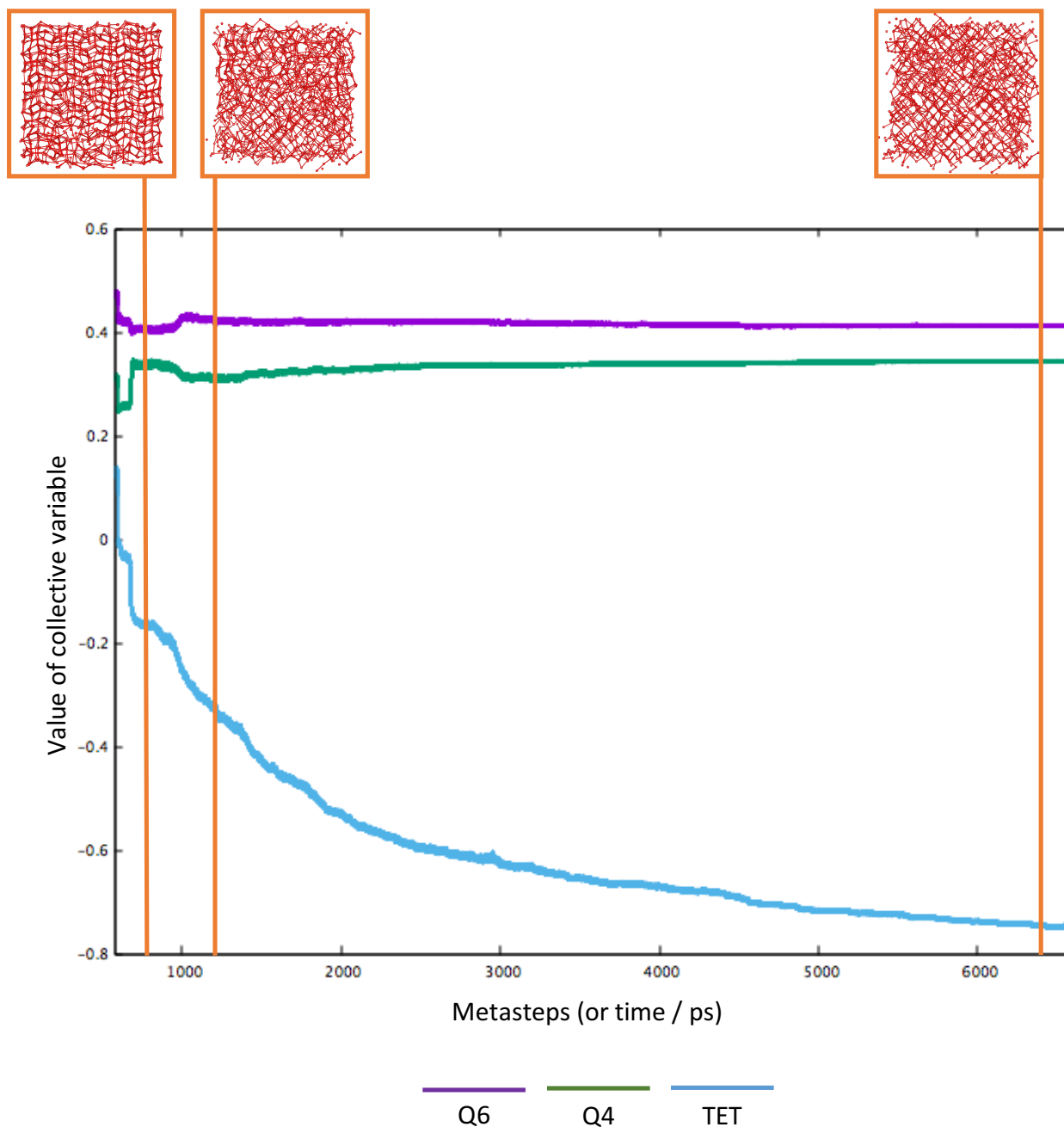


**Figure 6.xxvi:** Collective variable analysis during the remainder of the simulation. Abrupt changes are seen before 1 ns, corresponding to the reformation of Ice III and the formation of the amorphous phase. However, after this the CVs appear to be unresponsive to further metadynamics iterations, and the system simply ‘relaxes’ into the Ice I<sub>d</sub>/amorphous basin.

### 6.7. Conclusions and Future Work

Within this work, two distinct methods have been utilised in an attempt to disrupt the hydrogen bonding network between molecules in simulated systems of water ice, and hence endeavour to facilitate a phase transition. The first method, the *rotational shooting technique*, was developed in this work and is used to directly break the hydrogen bonding network by enforcing a change to the orientation of a sub-set of the water molecules within the system. The second method, *metadynamics*, biases the entire system within the space of a defined set of collective variables, in order to induce geometric change within the structure.

The *rotational shooter* has demonstrated that, when coupled with Martonák-style metadynamics, it offers a powerful tool for generating atypical configurations of water ice. The rotational shooter was successfully able to generate configurations of the three experimentally known amorphous phases, as well as ‘melting’ events leading to the formation of liquid water. The densities and radial distribution plots of these phases bears remarkable resemblance to those seen in previous theoretical and experimental studies. In addition, fissures and cavities within structures of ice, as well as the generation of internal surfaces which could have interesting implications for gas adsorption or catalysis. However, the method can be unpredictable. Whilst the method certainly facilitates the generation of novel and surprising effects, greater control over the rotation process would be highly desirable. One possible way to achieve this would be to implement the rotation as a true collective variable within the metadynamics framework (rather than as an external perturbation) to allow for a more systematic approach to its variation.

Unfortunately, no direct solid-solid phase transition was observed using the rotational shooter method with Martonák-style metadynamics. The reason for this is likely due to the low probability of a regional re-orientation of hydrogen bonding forming an ordered, crystalline phase – let alone the propagation and subsequent growth of that phase. It is speculated that inducing a phase transition in this way is possible, albeit unlikely without a systematic screening of sub-set sizes, angle ranges and metadynamics parameters.

Nevertheless, it presents a useful tool for generating amorphous phases of ice, as well as simulating rare configurations which feature internal surfaces and structural defects.

Using metadynamics with *plumed* to bias the system in the space of three collective variables – the Steinhardt Q4 and Q6 parameters, and a tetrahedral ordering parameter – was an extremely successful approach to modelling a phase transition between two ice phases. Not only was able to model a solid-solid phase transition between Ice III and (predominantly) Ice I<sub>c</sub>, it also forced the system to visit an intermediate configuration, which did not correspond to any of the eighteen phases of water-ice present on the phase diagram. However, this approach is not without considerable potential for improvement.

Firstly, whilst the metadynamics scheme presented has been an excellent tool for finding a number of ice configurations, it does not give any definitive evidence of how these phases transform between each other. The results reported seem to suggest a pathway between Ice III and Ice I<sub>c</sub> via a series of crystalline and amorphous intermediates; however, such a conclusion cannot be drawn without further analysis into the transformation mechanism. As alluded to previously, utilising transition path sampling methods (and potentially the *metashooting* implementation, as described in chapter 4) to fully classify this transformation would be a very interesting and worthwhile future project.

Secondly, there remains a great deal of scope to improve the collective variables utilised in the metadynamics scheme. Whilst the combination of the Q4, Q6 and TET collective variables proved to be effective at instigating a phase transition, there is little doubt that they did not behave optimally in this situation. Firstly, in the case of the two Steinhardt parameters, their values varied very little over the course of the whole simulation, returning the same values for Ice III as for the mixed Ice I<sub>c</sub>/amorphous phase. It has been well documented that the global Steinhardt parameters have their shortcomings and are unable to fully classify transformation processes between the polymorphs of ice. Despite this, it has been previously reported that they work reasonably well with additional parameters (such as the tetrahedral order parameter) – a statement which is fully corroborated by the results presented here. All three of the variables clearly played a role in the metadynamics, as such a trajectory was not achievable without all three collective variables working in conjunction. Nevertheless, it is

believed that there is considerable scope here to improve the collective variables, possibly with the scope of being able to survey much more of the water-ice phase diagram by using a more ‘collective’ order parameter.

Related to the previous point, there also exists the problem of the collective variables losing responsiveness after the formation of the amorphous phase. This effectively halted the metadynamics component of the simulation, meaning that the system remained in the mixed Ice I<sub>c</sub> / amorphous state. Finding a collective variable set up which would continue to work in such an amorphous system would be highly desirable, and once again would likely increase the viability for surveying larger regions of the configuration space. Alternatively, using a well-tempered<sup>[86]</sup> or an adaptive-Gaussian scheme<sup>[87]</sup> may help here, as perhaps it is not the reaction coordinates that are at fault, but the values corresponding to the widths and heights of the Gaussians deposited within their respective spaces.

It is clear from the literature, and from this work, that accurate and efficient modelling of water and ice still poses a significant challenge to the materials science community. The ultimate aim for water simulation (and, indeed, for the simulation of all materials), would be to find a *global collective variable* which is able to differentiate between all phases and allow navigation across the configuration space of a material at the will of the user. It is obvious that no such order parameter has yet been found or defined, although the recent works using PIVs seems promising.<sup>[70-72]</sup> Another possibility is that high-order coordination sequences and more sophisticated nearest neighbour methods, such as the three discussed in this work, represent a step in the right direction. However, it is clear that the prescription defined here is not a perfect one, and that there remains work to be done before computational materials scientists are able to use advanced techniques to fully survey the configurations space of water ice.

Nevertheless, the work presented here represents a novel contribution to the field, and demonstrates that such investigations are far from impossible. Indeed, by using both novel and existing techniques, it is possible to visit numerous crystalline and amorphous structures of ice - including ones that are not yet defined on the ice phase diagram!

References – Chapter 6

1. <https://water.usgs.gov/edu/earthhowmuch.html> "How much water is there on, in, and above the Earth?" - Last Accessed 28/09/2017
2. C. J. Hansen, L. Esposito, A. I. F. Stewart, J. Colwell, A. Hendrix, W. Pryor, D. Shemansky and R. West, *Science*, 2006, **311**, 1422-1425
3. <http://www.jpl.nasa.gov/news/news.php?feature=3983> "Hubble sees evidence of water vapour at Jupiter Moon" - Last Accessed 28/09/2017
4. A. C. Lockwood, J. A. Johnson, C. F. Bender, J. S. Carr, T. Barman, A. J. W. Richert and G. A. Blake, *Astrophys. J.*, 2014, **783**, L29
5. A. Hanslmeier, *Water in the Universe*, Springer Science & Business Media, 2010
6. <https://water.usgs.gov/edu/solvent.html> "Water, the universal solvent" - Last Accessed 28/09/2017
7. N. N. Greenwood and A. Earnshaw, *Chemistry of the Elements*, Elsevier, 2<sup>nd</sup> Edition, 2012
8. C. L. Braun and S. N. Smirnov, *J. Chem. Educ.*, 1993, **70**, 612
9. S. L. Shostak, W. L. Ebenstein and J. S. Muenter, *J. Chem. Phys.*, 1991, **94**, 5875-5882
10. A. D. Fortes, I. G. Wood, D. Grigoriev, M. Alfredsson, S. Kipfstuhl, K. S. Knight and R. I. Smith, *J. Chem. Phys.*, 2004, **120**, 11376-11379
11. L. G. Dowell and A. P. Rinfret, *Nature*, 1960, **188**, 1144-1148
12. B. Kamb, *Acta Crystallogr.*, 1964, **17**, 1437-1449
13. R. L. McFarlan, *J. Chem. Phys.*, 1936, **4**, 253-259
14. H. Engelhardt and B. Kamb, *J. Chem. Phys.*, 1981, **75**, 5887-5899
15. B. Kamb, A. Prakash and C. Knobler, *Acta Crystallogr.*, 1967, **22**, 706-715
16. B. Kamb, *Science*, 1965, **150**, 205-209
17. B. Kamb and B. L. Davis, *Proc. Natl. Acad. Sci. U.S.A.*, 1964, **52**, 1433-1439
18. J. M. Besson, P. Pruzan, S. Klotz, G. Hame, B. Silvi, R. J. Nemes, J. S. Loveday, R. M. Wilson and S. Hull, *Phys. Rev. B. Condens. Matter*, 1994, **49**, 12540-12550
19. S. J. La Placa, W. C. Hamilton, B. Kamb and A. Prakash, *J. Chem. Phys.*, 1973, **58**, 567-580
20. R. J. Hemley, A. P. Jephcoat, H. K. Mao, C. S. Zha, L. W. Finger and D. E. Cox, *Nature*, 1987, **330**, 737-740

21. A. J. Leadbetter, R. C. Ward, J. W. Clark, P. A. Tucker, T. Matsuo and H. Suga, *J. Chem. Phys.*, 1985, **82**, 424-428
22. C. Lobban, J. L. Finney and W. F. Kuhs, *Nature*, 1998, **391**, 268-270
23. C. G. Salzmann, P. G. Radaelli, A. Hallbrucker, E. Mayer and J. L. Finney, *Science*, 2006, **311**, 1758-1761
24. C. G. Salzmann, P. G. Radaelli, E. Mayer and J. L. Finney, *Phys. Rev. Lett.*, 2009, **103**, 105701
25. A. Falenty, T. C. Hansen and W. F. Kuhs, *Nature*, 2014, **516**, 231-233
26. L. del Rosso, F. Grazzi, M. Celli, D. Colognesi, V. Garcia-Sakai and L. Ulivi, *J. Phys. Chem. C.*, 2016, **120**, 26955-26959
27. P. Demontis, R. LeSar and M. L. Klein, *Phys. Rev. Lett.*, 1988, **60**, 2284-2287
28. J. Russo, F. Romano and H. Tanaka, *Nat. Mater.*, 2014, **13**, 733-739
29. M. Ji, K. Umemoto, C. Z. Wang, K. M. Ho and R. M. Wentzcovitch, *Phys. Rev. B.*, 2011, **84**, 220105
30. [https://upload.wikimedia.org/wikipedia/commons/0/08/Phase\\_diagram\\_of\\_water.svg](https://upload.wikimedia.org/wikipedia/commons/0/08/Phase_diagram_of_water.svg) “Phase Diagram of Water” - Last Accessed 28/09/2017
31. J. D. Bernal and R. H. Fowler, *J. Chem. Phys.*, 1933, **1**, 515-548
32. M. Cogoni, B. D’Aguanno, L. N. Kuleshova and D. W. M. Hofmann, *J. Chem. Phys.*, 2011, **134**, 204506
33. [http://www1.lsbu.ac.uk/water/ice\\_phases.html](http://www1.lsbu.ac.uk/water/ice_phases.html) “Ice phases” - Last Accessed 28/09/2017
34. N. Bjerrum, *Science*, 1952, **115**, 385-390
35. K. Röttger, A. Endriss, J. Ihringer, S. Doyle and W. F. Kuhs, *Acta Crystallogr. B.*, 2012, **68**, 91
36. A. K. Soper, *Chem. Phys.*, 2000, **258**, 121-137
37. B. J. Murray, D. A. Knopf and A. K. Bertram, *Nature*, 2005, **434**, 202-205
38. F. W. Starr, C. A. Angell and H. E. Stanley, *Phys. Stat. Mech. Its Appl.*, 2003, **323**, 51-66
39. J. D. Londono, W. F. Kuhs and J. L. Finney, *J. Chem. Phys.*, 1993, **98**, 4878-4888
40. M. Bauer, M. S. Elsaesser, K. Winkel, E. Mayer and T. Loerting, *Phys. Rev. B.*, 2008, **77**, 220105
41. J. L. F. Abascal, E. Sanz, R. García Fernández and C. Vega, *J. Chem. Phys.*, 2005, **122**, 234511

42. T. Loerting, K. Winkel, M. Seidl, M. Bauer, C. Mitterdorfer, P.H. Handle, C. G. Salzmann, E. Mayer, J. L. Finney and D. T. Bowron, *Phys. Chem. Chem. Phys.*, 2011, **13**, 8783-8794
43. [http://www1.lsbu.ac.uk/water/amorphous\\_ice.html](http://www1.lsbu.ac.uk/water/amorphous_ice.html) "Amorphous Ice" Last Accessed 28/09/2017
44. J. L. Finney, A. Hallbrucker, I. Kohl, A. K. Soper and D. T. Bowron, *Phys. Rev. Lett.*, 2002, **88**, 225503
45. J. L. Finney, D. T. Bowron, A. K. Soper, T. Loerting, E. Mayer and A. Hallbrucker, *Phys. Rev. Lett.*, 2002, **89**, 205503
46. [http://www1.lsbu.ac.uk/water/water\\_models.html](http://www1.lsbu.ac.uk/water/water_models.html) "Water models" - Last Accessed 28/09/2017
47. J. F. Ouyang and R. P. A. Bettens, *Chimia*, 2015, **69**, 104-111
48. M. P. Allen and D. J. Tildesley, *Computer Simulation of Liquids*, Clarendon Press, 1989
49. W. L. Jorgensen, J. Chandrasekhar, J. D. Madura, R. W. Impey and M. L. Klein, *J. Chem. Phys.*, 1983, **79**, 926-935
50. H. J. C. Berendsen, J. R. Grigera and T. P. Straatsma, *J. Phys. Chem.*, 1987, **91**, 6269-6271
51. J. L. F. Abascal and C. Vega, *J. Chem. Phys.*, 2005, **123**, 234505
52. R. Fuentes-Azcatl and J. Alejandre, *J. Phys. Chem. B.*, 2014, **118**, 1263-1272
53. H. W. Horn, W. C. Swope, J. W. Pitera, J. D. Madura, T. J. Dick, G. L. Hura and T. Head-Gordon, *J. Chem. Phys.*, 2004, **120**, 9665-9678
54. M. W. Mahoney and W. L. Jorgensen, *J. Chem. Phys.*, 2000, **112**, 8910-8922
55. H. Nada and J. P. J. M. van der Eerden, *J. Chem. Phys.*, 2003, **118**, 7401-7413
56. G. A. Cisneros, K. T. Wikfeldt, L. Ojamäe, J. Lu, Y. Xu, H. Torabifard, A. P. Bartók, G. Csányi, V. Molinero and F. Paesani, *Chem. Rev.*, 2016, **116**, 7501-7528
57. W. L. Jorgensen, *J. Am. Chem. Soc.*, 1981, **103**, 335-340
58. B. Guillot, *J. Mol. Liq.*, 2002, **101**, 219-260
59. A. D. MacKerell, D. Bashford, M. Bellott, R. L. Dunbrack, J. D. Evanseck, M. J. Field, S. Fischer, J. Gao, H. Guo, S. Ha, D. Joseph-McCarthy, L. Kuchnir, K. Kuczera, F. T. Lau, C. Mattos, S. Michnick, T. Ngo, D. T. Nguyen, B. Prodhom, W. E. Reiher, B. Roux, M. Schlenkrich, J. C. Smith, R. Stote, J. Straub, M. Wantanabe, J. Wiórkiewicz-Kuczera, D. Yin and M. Karplus, *J. Phys. Chem. B*, 1998, **102**, 3586-3616
60. C. Vega, E. Sanz and J. L. F. Abascal, *J. Chem. Phys.*, 2005, **122**, 114507

61. C. Vega and J. L. F. Abascal, *J. Chem. Phys.*, 2005, **123**, 144504
62. R. Fuentes-Azcatl and M. C. Barbosa, *Phys. Stat. Mech. Its Appl.*, 2016, **444**, 86-94
63. E. Sanz, C. Vega, J. L. F. Abascal and L. G. MacDowell, *Phys. Rev. Lett.*, 2004, **92**, 255701
64. M. Matsumoto, S. Saito and I. Ohmine, *Nature*, 2002, **416**, 409-413
65. I. Svishchev and P. Kusalik, *Phys. Rev. Lett.*, 1994, **73**, 975-978
66. R. Radhakrishnan and B. L. Trout, *J. Am. Chem. Soc.*, 2003, **125**, 7743-7747
67. D. Quigley and P. M. Rodger, *Mol. Simul.*, 2009, **35**, 613-623
68. P. J. Steinhardt, D. R. Nelson and M. Ronchetti, *Phys. Rev. B.*, 1983, **28**, 784-805
69. D. Quigley and P. M. Rodger, *J. Chem. Phys.*, 2008, **128**, 154518
70. S. Pipolo, M. Salanne, G. Ferlat, S. Klotz, A. M. Saitta and F. Pietrucci, *Cond. Mat. Mtrl. Sci.*, 2017
71. G. A. Gallet and F. Pietrucci, *J. Chem. Phys.*, 2013, **139**, 74101
72. F. Pietrucci and R. Martonák, *J. Chem. Phys.*, 2015, **142**, 104704
73. R. Martonák, D. Donadio and M. Parrinello, *J. Chem. Phys.*, 2005, **122**, 134501
74. J. S. Tse and M. L. Klein, *J. Chem. Phys.*, 1990, **92**, 3992-3994
75. R. Martonák, A. Laio, M. Bernasconi, C. Ceriani, P. Raiteri and M. Parrinello, *Crystalline Materials*, 2005, **220**, 489-498
76. R. Martonák, A. Laio and M. Parrinello, *Phys. Rev. Lett.*, 2003, **90**, 75503
77. G. A. Tribello, M. Bonomi, D. Branduardi, C. Camilloni and G. Bussi, *Comput. Phys. Commun.*, 2014, **185**, 604-613
78. P. G. Bolhuis, D. Chandler, C. Dellago and P. L. Geissler, *Annu. Rev. Phys. Chem.*, 2002, **53**, 291-318
79. C. Dellago, P. G. Bolhuis and P. L. Geissler, *Advances in Chemical Physics*, edited by I. Prigogine and S. A. Rice, John Wiley & Sons, 2002, 1-78
80. H. C. Andersen, *J. Comput. Phys.*, 1983, **52**, 24-34
81. G. Bussi, D. Donadio and M. Parrinello, *J. Chem. Phys.*, 2007, **126**, 14101
82. [https://plumed.github.io/doc-v2.3/user-doc/html/\\_q6.html](https://plumed.github.io/doc-v2.3/user-doc/html/_q6.html) “plumed Q6” - Last Accessed 28/09/2017
83. [https://plumed.github.io/doc-v2.3/user-doc/html/\\_q4.html](https://plumed.github.io/doc-v2.3/user-doc/html/_q4.html) “plumed Q4” - Last Accessed 28/09/2017



84. [https://plumed.github.io/doc-v2.3/user-doc/html/\\_t\\_e\\_t\\_r\\_a\\_h\\_e\\_d\\_r\\_a\\_l.html](https://plumed.github.io/doc-v2.3/user-doc/html/_t_e_t_r_a_h_e_d_r_a_l.html)  
*“plumed TET”* - Last Accessed 28/09/2017
85. G. E. Martin, *Transformation Geometry: An Introduction to Symmetry*, Springer Science and Business Media, 1996
86. A. Barducci, G. Bussi and M. Parrinello, *Phys. Rev. Lett.*, 2008, **100**, 020603
87. D. Branduardi, G. Bussi and M. Parrinello, *J. Chem. Theory Comput.*, 2012, **8**, 2247-2254

Chapter 7Crystal Structure Prediction

***“The whole is greater than the sum of its parts”***

– Aristotle (384-322 BC), paraphrased from *Metaphysics*

7.1. Introduction

In computational materials science, *crystal structure prediction* corresponds to the elucidation of novel structures of crystalline solids by calculation. It can involve both the deduction of the crystal structure and chemical bonding between atoms within a system, and how this relates to the macroscopic properties of the material. As many of the properties exhibited by a material are determined by its crystal structure, knowledge of the arrangement of its atoms allows for computation of many aspects of its behaviour, even before it is synthesised in the laboratory.<sup>[1,2]</sup>

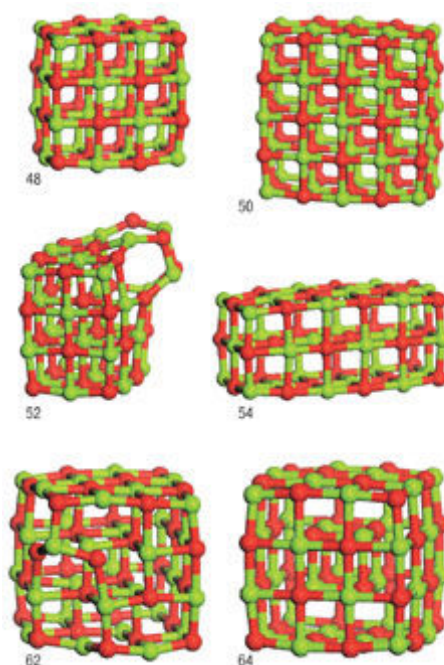


**Figure 7.i:** Hypothetical MgO structures published by Christopher Roberts and Roy L. Johnson, predicted using a genetic algorithm.<sup>[3]</sup> The number underneath corresponds to the number of Mg-O units in the simulation cell.

However, despite this well-known structure-property relationship, the direct connection between certain structural motifs and the specific behaviour of a material is often not obvious. In addition, the properties of a material can be drastically altered simply as a function of the position of the atomic coordinates. For example, the allotropes of carbon exhibit an incredible range of properties, just as a result of varying the arrangement of the same atoms by changing the external conditions such as temperature and pressure.

Crystal structure prediction is an extremely new field of materials science, having only really taken off in the opening years of the twenty-first century.<sup>[4]</sup> Until very recently, it was widely believed by the scientific community that the structure of crystalline substances was completely unpredictable, and that it was not possible to determine the configuration of atoms in a material just from knowledge of its composition:

*“One of the continuing scandals in the physical sciences is that it remains impossible to predict the structure of even the simplest crystalline solids from knowledge of their chemical composition”* – John Maddox, 1988<sup>[5]</sup>

Fortunately, a great deal of progress has been achieved since the publication of this controversial statement. However, it still remains a significant challenge to predict the structure of solid state systems. This is a result of the high-dimensionality of the problem, as well as the many (possibly infinite) energy minima present on the vast configuration space of a chemical system, which becomes exponentially more complex with increasing system size.

The ultimate aim of crystal structure prediction techniques would be the ability to predict the global minimum (and associated local minima) of any system, given its composition, its stoichiometry and the thermodynamic conditions in which it resides. Unfortunately, no such method currently exists to fully classify the configuration space of a system. However, numerous methods have been developed to search for minima on an energy surface. Such methods include random sampling techniques,<sup>[6,7]</sup> simulated annealing,<sup>[8]</sup> topological techniques,<sup>[9]</sup> accelerated molecular dynamics methods (e.g. metadynamics),<sup>[10,11]</sup> and evolutionary algorithms.<sup>[12,13]</sup> It is worth discussing these techniques in turn, and highlighting the contribution they have made to this exciting field of materials science.

## 7.2. Crystal Structure Prediction Methodologies

This introduction section is based largely on the comprehensive review at the following references.<sup>[1,2]</sup>

### 7.2.1. Random Sampling Techniques

Perhaps the simplest way to predict crystal structures is to use random sampling methods.<sup>[14]</sup> As (meta)stable states coincide with configurations corresponding to energy minima, structure prediction in this way is simply equivalent to minimising the energy function of a random system with respect to the parameters that control it – namely the atomic positions. Hence, this is achieved by geometry optimisation algorithms such as the *conjugate gradient* technique, which find the local minimum associated with a particular configuration.

One possible scheme to achieve random configuration searching follows the general procedure set out below:

- i. Generate a configuration of atomic positions and cell vectors;
- ii. Apply a scheme of local optimisation, to minimise the energy of the structure;
- iii. Repeat until the system has converged upon an associated energy minimum.

Such a scheme for crystal structure prediction is advantageous as it is fast and inexpensive to implement. In addition, it has been shown that random sampling schemes can be more efficient at sampling the configuration space than ‘grid’ based searching methods<sup>[15]</sup> and are particularly effective at distinguishing between close energy configurations, which may be very different in terms of geometry. This results from the fact that random search methods can survey the entire underlying energy landscape of a system, and are often not limited to sampling small regions of the configuration space.

However, it is quite clear that such a method is unlikely to be the most efficient, particularly for increasingly large systems. In addition, there is no way to determine how many runs it will

take to survey the whole landscape – in practice, this is impossible for all but the smallest systems. In addition, only crystal structures whose unit cell contains the same number (or a factor of the number) of atoms used in the original random configuration can possibly be found. However, despite these disadvantages, it remains a powerful tool in the search for novel crystal structures using computational techniques.

One of the more recent implementations of such a scheme is the *ab initio random structure searching* (AIRSS) technique developed by Chris Pickard and Richard Needs.<sup>[7]</sup> Using their technique, Pickard and Needs have successfully utilised AIRSS to study the structures of solids, surfaces and clusters in materials as diverse as high pressure aluminium,<sup>[16]</sup> silane,<sup>[17]</sup> nitrogen<sup>[18]</sup> and iron,<sup>[19]</sup> amongst others.

### 7.2.2. Simulated Annealing Techniques

Analogous to the physical annealing used in industrial processes such as steel making, *simulated annealing* involves the modelling of a cooling process in order to encourage molten atoms to crystallise.<sup>[20]</sup> If started from a very high temperature (i.e. the atoms have enough kinetic energy for the system to overcome local energy barriers with a high probability), the molten system under scrutiny can be gradually cooled to form an ordered, crystalline structure. Alternatively, if the procedure is initiated at a low temperature or is cooled rapidly, a glassy structure with defects and dislocations will be generated.

At each temperature simulated during an annealing process, the resident atoms are propagated with molecular dynamics or Monte Carlo iterations. This allows the system to relax into its associated local minimum at each iteration of the procedure.

However, the advantage of this iterative technique is that if carried out slowly enough, the system will ultimately relax into the global minimum. This is achievable if the temperature is rescaled very slowly at each step, allowing for the system to populate the associated local minimum during each run. Clearly, the procedure will eventually culminate in the system

residing in the deepest basin on the underlying energy landscape, corresponding to the global minimum.

There are many examples of structure prediction using simulated annealing, including using the technique on binary systems such as boron nitrides,<sup>[21]</sup> as well as much more complicated systems such as proteins.<sup>[22,23]</sup>

### 7.2.3. Metadynamics for Structure Prediction

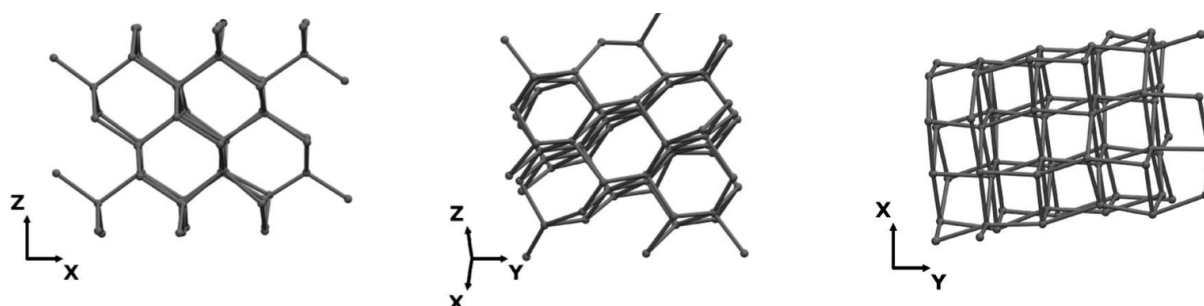


**Figure 7.ii:** Three different allotropes of germanium, found using the Martonák metadynamics technique of structure prediction in the work of Selli *et al.*<sup>[24]</sup>

Metadynamics can be an excellent tool for use in structure prediction. By applying a bias potential in the space of a set of collective variables, one can force the system to explore its associated configuration space, whilst at the same time preventing it from returning to any previously adopted configurations. In particular, the Martonák method of metadynamics<sup>[25]</sup> which uses the cell parameters as collective variables, is very efficient at predicting novel allotropes and polymorphs of systems at varying pressures. The intricacies of both standard metadynamics and the Martonák scheme have already been discussed in chapter 4, and so only a general scheme is presented here.

To initiate structure prediction, one must first take a random or a known configuration, and relax by steepest descent or conjugate gradient optimisation such that the system enters a

local minimum. At this point, the metadynamics driver may be initiated. By alternatively applying changes to the shape and size of the simulation box and propagating the system with molecular dynamics as described in chapter 4, one can explore the underlying energy landscape and hence visit new configurations corresponding to different local energy minima. However, similarly to the random structure prediction methods, only structures whose number of atoms are the same as (or a factor of) the number of atoms in the metadynamics simulation cell can be found in this manner.

The Martonák scheme of metadynamics has been used to great success in structure prediction work in both organic and inorganic systems. One notable example is the work of Selli *et al* on the prediction of novel germanium allotropes.<sup>[24]</sup>

#### 7.2.4. Topological Techniques

Topological techniques to predict novel structures have found great success in the prediction of large framework structures. Instead of using a geometric model, which represents the crystal structure as points in space corresponding to the coordinates of the atomic sites, *topological* methods focus on the system of chemical interactions holding the atoms in place. By considering a crystal structure as an infinitely large molecule, one can consider that the chemical bonds linking the atomic sites form an infinite *graph*. The graph is a topological space containing a set of points on which the topology is formed by pairing the points together. Such an infinite graph is called a *net* and deduction and enumeration of these nets (and how they may be tiled with polyhedra) can be used to determine novel crystal structures.<sup>[9]</sup> The pioneering work on topological techniques for determining crystal structures was carried out by Wells,<sup>[26]</sup> however many have since added significant contributions to the field. Of particular relevance to this work, there has been a recent advancement provided by Winkler *et al*, who have developed an approach based on graph theory and quantum mechanics in order to predict novel carbon allotropes.<sup>[27]</sup> There also exists a number of algorithms and codes for determining structures by their topologies – a notable example is *ToposPro*, developed by Blatov, Proserpio *et al*.<sup>[28]</sup>

### 7.2.5. Evolutionary Techniques

Genetic algorithms work using the same principle as Darwinian evolution. By setting up an initial population of structures, which can then ‘reproduce’ and produce ‘offspring’. New structures are generated which contain features from both parent structures, passed down by a ‘crossover’ operator, in which features from the two parents are combined within a new structure. In addition, a ‘mutation’ operator (usually in the form of a Monte Carlo move to displace a few atomic positions) instigates random change to offspring structures. Competition between structures is simulated by taking into account their energies and stabilities within the virtual conditions set, and allowing ‘successful’ structures to survive and propagate to pass on their characteristics. Ultimately, similarly to nature, the algorithm will eliminate poorly suited structures, and select for configurations which are best adapted to the simulated environment.

There are numerous ways such schemes can be implemented. Some simulated competition using a ‘roulette-wheel’ type system or instigating random ‘tournaments’ between different structures, in order to determine the best candidates in a given population.<sup>[29]</sup> Another method involves keeping only offspring structures and the ‘strongest’ structure from the previous generation.<sup>[30]</sup>

It is easy to see why such a technique for structure prediction is very powerful indeed, as the analogous biological process has taken place on Earth for some four billion years, and has produced an extraordinary wealth of lifeforms each best suited to their local environment and ecological niche. The motivation, therefore, is a well-designed structure prediction genetic algorithms could be as successful at producing systems with chemical structures finely tuned for the simulated thermodynamic conditions.

Genetic algorithm methods have been used to great effect in the prediction of structures of many materials, from peptides<sup>[31]</sup> to nanoclusters of metal oxides.<sup>[3]</sup>



### 7.3. This Work: Random Structure Searching using *Random Atomic Placement (RAP)*

The aim of this work was to generate novel crystal structures which had not yet been discovered or synthesised for the system under scrutiny. It was desired that structures be sought at any value of pressure and at any point in configuration space, i.e. no strict thermodynamic or boundary conditions (except composition and stoichiometry) be imposed. In addition, it was desired that the method be able to find structures that do not represent the global minimum of the system, but represent higher-energy metastable configurations that have not yet been found for the element or compound of interest. However, the ability to obtain the global minimum (and known local minima) during a proportion of the runs is desirable, as it validates the parameters being used to describe the system, as well as the method of structure prediction being utilised. As such, it was decided that a random structure prediction method was best suited to the work.

The principle tactic used for structure prediction is a random sampling technique coined *Random Atomic Placement (RAP)*. RAP is analogous to other random prediction methods, in that a set of box vectors are generated, followed by subsequent population of the cell with randomly positioned atoms from which the system of interest is composed. After this, the disordered system is optimised by conjugate gradient relaxation of both the atomic positions and the simulation cell.

There are numerous facilities within the RAP scheme which allow for customisation of the initial configuration. Firstly, any number of atoms and atom types may be generated per configuration, such that stoichiometry and composition can be finely controlled. This means that exotic configurations, which feature non-typical stoichiometries for a particular chemical composition, can be generated with ease. Secondly, box vectors are designed according to the van der Waals radii of the atoms, and the number of such atoms included in the system, to emulate an appropriate simulation cell size. This density parameter, as well as the minimum distance between atomic positions, can be specified by the user. This allows for densely or sparsely populated initial cells to be created at will. This level of customisation of the box parameters and the inter-atomic spacing means that a great variety of initial *pseudo*-random configurations may be generated.

Prior to the relaxation step, the generated configuration may be altered by multiplying the lattice constants by some value between 0.5 and 1.5. This can be applied isotropically or anisotropically, in order to simulate hydrostatic pressure or directional strain on the system, be it positive or negative. This configuration is then passed to an external molecular dynamics integrator, where it undergoes an initial cell and geometry optimisation by conjugated gradient. Following this, the systems are reviewed and promising structures selected, whilst very high energy configurations, or those with unphysical features (such as unfeasible coordination sequences, bond lengths or angles), are reviewed or abandoned.

Selected configurations at this point are subjected to a gamma-point analysis, where the Hessian matrix is calculated as a preliminary indicator of mechanical stability. Should all of the eigenvalues of the Hessian matrix (the matrix form of the second derivative of the energy) be returned as positive, the preliminary structure proceeds onwards in the procedure. Viable structures are then relaxed once again within the external molecular dynamics engine, this time more rigorously with a larger basis set and stricter criteria for the forces acting on the atomic sites. Subsequently, the optimised structures are analysed for their electronic and mechanical properties by means of band and phonon calculations respectively. Thus, random structure prediction by the *RAP* method incorporates a complete method composed of discrete steps, from *pseudo*-random structure generation through to highly optimised and characterised potential crystal structures. A flow-chart demonstrating the entire procedure is shown overleaf.

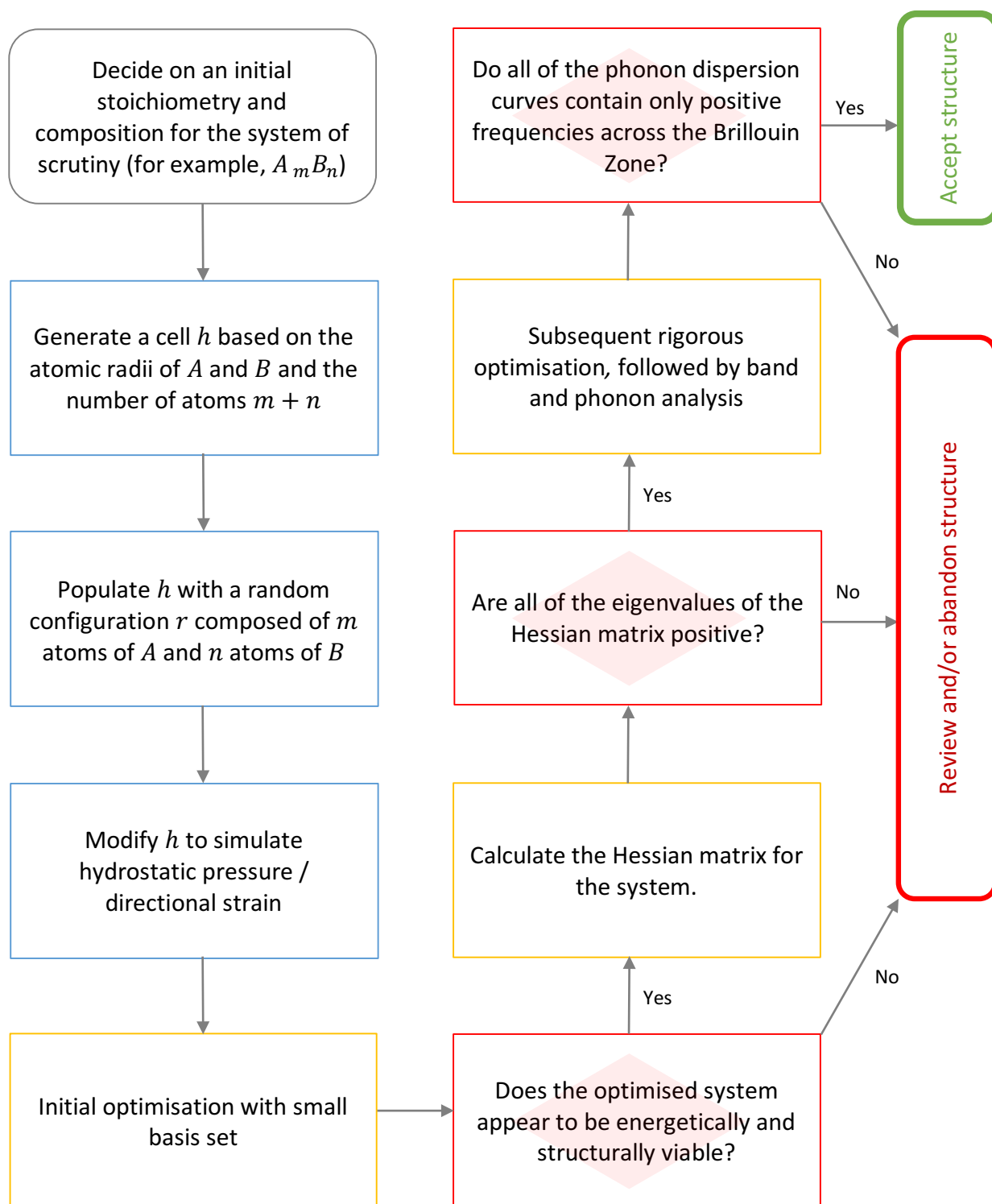


**Figure 7.iii:** Flow chart of the structure prediction and analysis procedure using the *Random Atomic Placement* method. The initial step is coloured grey, preparatory steps are coloured blue, optimisation and analysis steps are coloured orange. The entire *RAP* procedure can be used, coupled with a molecular dynamics integrator, to produce fully characterised structures from initial *pseudo*-random configurations

## 7.4. Carbon Structure Prediction at Ambient Pressure

### 7.4.1. Introduction

Carbon is without doubt one of the most fascinating and incredible elements in nature. Despite being the fourth most abundant element in the Universe, it is only the tenth most common element on planet Earth, found in only 180ppm in the Earth's crust.<sup>[32]</sup> Despite this relative terrestrial lack of carbon, it is the fundamental element of all life on Earth (an argument some use to illustrate the assumed ubiquity of carbon as the basis for any hypothetical extra-terrestrial life). This is likely a result of the unique ability of carbon to form four strong covalent bonds with most other elements (including itself) at ambient conditions, leading to the huge catalogue of diverse organic compounds we know today. Millions of organic compounds have catalogued, and this is but a tiny proportion of the number of possible carbon-based molecules that can exist under ambient conditions.<sup>[33]</sup>

In its bulk elemental form, carbon exhibits an extraordinary wealth of structural allotropes. Over 280 predicted forms of carbon are known,<sup>[34]</sup> only a few of which have been realised in the laboratory. The most familiar of the allotropes of carbon – graphite and diamond – are well known and have been utilised by mankind for millennia. Graphene, consisting of a single layer of graphite, has also received a great deal of public and scientific scrutiny in recent years. In addition, many more unusual allotropes of carbon, such as the fullerenes (including Buckyballs) and nanotubes are increasingly commonly identifiable to the general public and are finding uses in both commercial and industrial settings. Many other more exotic forms of the element have also been predicted to exist by theoretical materials scientists. New allotropes of carbon are still regularly being found, as a result of its peculiar ability to form  $sp^2$ ,  $sp^3$  and mixed  $sp^2$ - $sp^3$  structures with itself so readily at ambient conditions.

The first half of this results chapter is dedicated to an investigation into the polymorphism of elemental carbon using the *Random Atomic Placement* method. A brief outline of the existing knowledge of the structural variety of carbon will be presented, followed by work exhibiting

an attempt to discover and hence classify novel and existing allotropes of carbon using density functional methods.

### 7.4.2. Carbon Allotropes

#### 7.4.2.1. The Structures of Graphite and Graphene

The word *graphite* was coined by Abraham Gottlob Werner in 1789, derived from the Greek for 'writing stone'.<sup>[35]</sup> Prior to this, it had been known as *black lead* or *plumba* due to its inherent physical similarity to lead(II) sulphide. Indeed, the misnomer 'lead' is still used today, to refer to the graphite within pencils. In addition to the manufacture of these familiar drawing and writing implements, graphite has found extensive use in industry as a refractory material within furnaces, reactors and incinerators; as an anode material within batteries; in steelmaking processes; and as an industrial lubricant.<sup>[36]</sup>

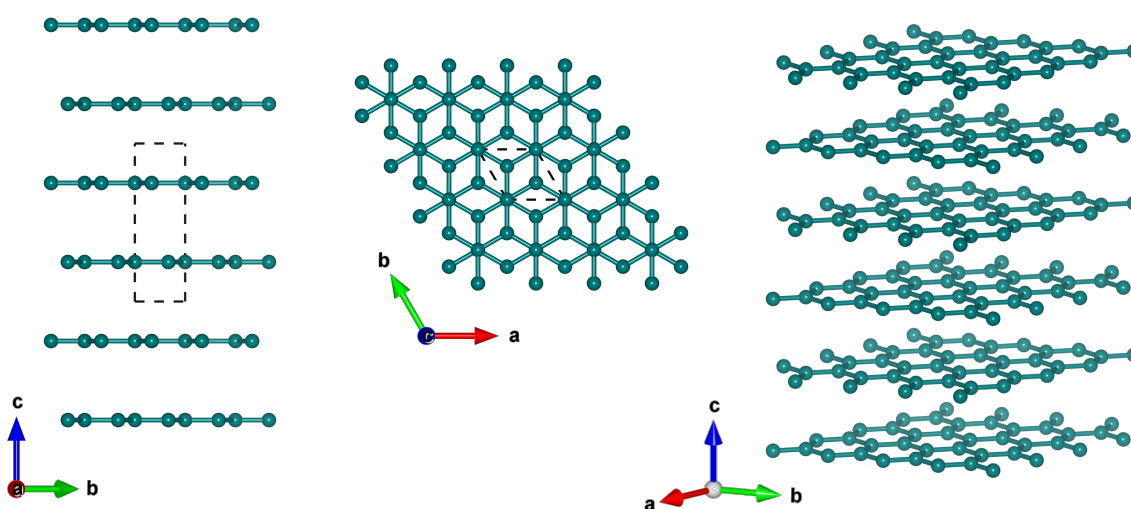


**Figure 7.iv (previous page):** Three different representations of a 3x3 graphite super-cell. Looking down the  $a$ -axis along the layers (left) and  $c$ -axis down the layers (centre), the ABAB stacking of graphite is evident. The unit cell of graphene is labelled in the first two images but is omitted from the right-hand image, which is present to clearly show the honeycomb geometry of the layers.<sup>[37]</sup>

Graphite is a layered and planar structure stacked in an ABAB configuration, held together by van der Waals forces. These interlayer interactions are relatively weak and can easily be sheared to separate the layers – indeed, this is the method of action in a pencil ‘lead’. In each graphite layer, the atoms are exclusively  $sp^2$  hybridised and arranged in the well-known ‘honeycomb’ shaped formation, with average interatomic distances equal to 1.42 Å and interlayer distances approximately 3.35 Å. This intriguing structure has hexagonal symmetry and has the Hermann-Mauguin space group classification  $P6_3/mmc$ .<sup>[38]</sup>

The anisotropic electronic, thermal and acoustic properties of graphite can be readily explained as a result of its layered geometry. Electrons and phonons within the material can readily move along the graphitic layers in the  $ab$  plane, but are much slower to move between the different layers along the  $c$ -axis.<sup>[39]</sup> Thus, many of the properties of graphite exhibit two-dimensional character. For example, graphite is an excellent conductor of electricity along the  $ab$  plane, due to the delocalisation of  $\pi$ -electrons along the honeycomb layers. Conversely, some forms of graphite can actually be used as thermal insulators, although graphite too shows excellent thermal conductivity along the plane of the honeycomb layers.

*Graphene* is composed of a single honeycomb layer of graphite, and can be thought of as an infinitely large aromatic molecule formed of six-membered carbon rings.<sup>[40]</sup> This two-dimensional allotrope has been the subject of intense scientific and public attention due to its vast array of unusual properties.

Graphene is over 200 times stronger than steel, with a tensile strength of over 130 GPa.<sup>[41]</sup> It is also virtually transparent in appearance and is an incredibly effective transporter of thermal energy. Graphene is also an exceptional conductor of electricity – it is actually a ‘zero-gap’

semiconductor, as the valence and conduction bands meet at *Dirac points* at six different points near the edges of the Brillouin zone.<sup>[42]</sup> At ambient conditions, graphene has an electron mobility of over  $15\,000\text{ cm}^2\text{ V}^{-1}\text{ s}^{-1}$  and resistivity of  $10^{-6}\text{ }\Omega\text{ cm}$ .<sup>[43]</sup> Intriguingly, lithium-coated graphene has also been shown to be superconducting, as has the single-layer material when in the presence of other superconducting compounds such as PCCO. The combination of these properties means that graphene has profound potential for use in future electronic devices, and much work still remains to be done to fully characterise this simple yet immensely peculiar material.<sup>[44]</sup>

#### 7.4.2.2. The Structure of Diamond

The word *diamond* originates again from a Greek word – this time for ‘unalterable’ or ‘unbreakable’,<sup>[45]</sup> which gives an insight into the intrigue of diamond for thousands of years. Unlike its thermodynamically more stable counterpart graphite, diamond is composed entirely of  $sp^3$  tetrahedrally-arranged carbon atoms forming a three-dimensional covalent network. The interatomic distance in diamond is  $1.54\text{ }\text{\AA}$  – the largest known for regular, single covalent C-C bonds.

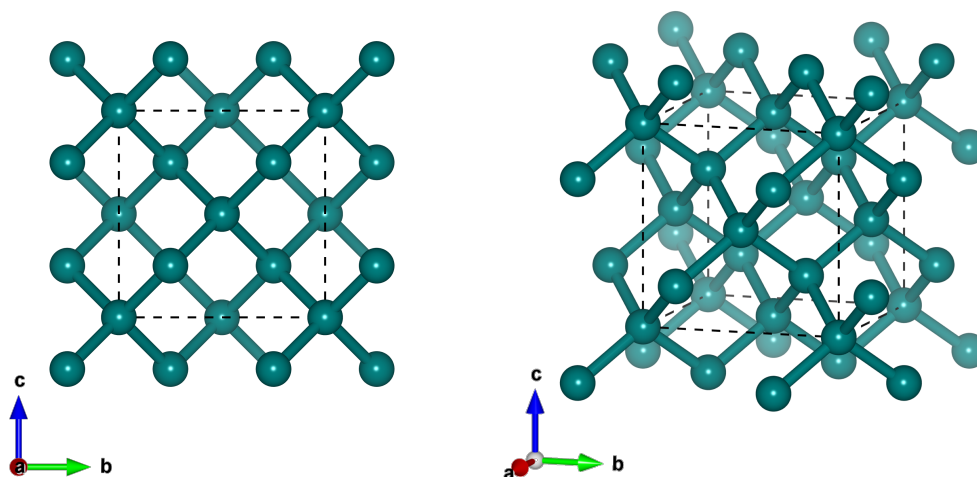


**Figure 7.v:** Two different representations of the diamond structure, featuring one unit cell and adjoining atoms. When seen down the  $a$ ,  $b$  and  $c$  axes, the perspective shows ‘squares’ of carbons (left). However, when tilted one can see the true  $sp^3$ -hybridised, tetrahedral covalent nature of the carbon atoms (right).<sup>[37]</sup>

The strong covalent bonding seen in diamond results in it being the hardest naturally occurring substance known, with a Mohs scale value of 10 and a Vickers scale value of 10000HV, or around 100 GPa. Actual recorded values for the hardness of pure diamond vary considerably, and the absolute value of hardness for a sample of diamond depends greatly on its purity and crystal orientation.

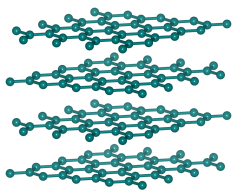
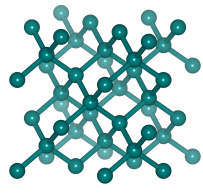
With a relatively wide band gap of 5.5 eV,<sup>[46]</sup> well into the ultraviolet region of the electromagnetic spectrum, pure diamond is an electronic insulator and appears colourless and transparent. Impurities within the diamond structure can impart colour to the crystal, and certain dopant species can significantly alter the electronic structure – so called *blue* diamonds, which contain boron and are semiconducting, are an example of this.<sup>[47,48]</sup> Diamond also has a very high refractive index and optical dispersion, affording the material with its characteristic lustre. It is also worth noting that, despite the large band gap in the pure material, diamond is the best thermal conductor of any natural bulk material, with thermal conductivity measurements of around 2200 W m<sup>-1</sup> K<sup>-1</sup>.<sup>[49]</sup>

Diamond naturally crystallises in the eponymous *diamond cubic* crystal structure the Hermann-Mauguin space group  $Fd\bar{3}m$ . However, a less stable, hexagonal variant of diamond known as *Lonsdaleite* is also known.<sup>[50]</sup> Named in honour of the British crystallographer Kathleen Lonsdale, hexagonal diamond was first synthesised in 1966 and is thought to occur within the interior of astronomical bodies such as asteroids. Some data suggests that Lonsdaleite is even harder than diamond (up to 58% harder),<sup>[51]</sup> however the little experimental data that is available does not yet corroborate nor disprove this, likely as a result of impurities and defects present within the synthesised hexagonal crystal structure.

The mechanical and optical properties of diamond have made it a most coveted material for use in jewellery since time immemorial. It is an extremely sought-after commodity, and has played a significant role in the cultural and economic history of humankind. More recently, its exceptional hardness has also seen it find use in a number of industrial applications, particularly in tools used for cutting, engraving and exerting high pressure.



7.4.2.3. Comparison of Graphite and Diamond

<b>Graphite</b> $(P6_3/mmc)$ 	<b>Diamond</b> $(Fd\bar{3}m)$ 
Hexagonal crystal system	Cubic crystal system
Completely $sp^2$ -hybridised	Completely $sp^3$ -hybridised
Excellent conductor of electricity *	Poor conductor of electricity
Poor conductor of thermal energy *	Excellent conductor of thermal energy
Very soft material (Mohs Scale = 2)	Very hard material (Mohs scale = 10)
Opaque and black	Transparent and colourless
Used as a lubricant	Used as an abrasive

\* Along certain crystallographic directions

**Table 7.vi:** Table summarising the differences in structure and property between graphite and diamond, symbolising the stark variety exhibited by carbon allotropes.

The above figure exemplifies the stark differences in property that are exhibited by different atomic configurations of the same element. Graphite and diamond have very little in common, with the exception that they are composed solely of carbon. The huge variety displayed here is likely but a drop in the ocean, considering that there are so many predicted allotropes of carbon.

There also exists a large number of other forms of elemental carbon, some of which will be discussed in the following section.

7.4.2.4. Fullerenes and Glassy Carbon

*Fullerenes* is the broad name given to any molecule or allotrope of carbon that forms a hollow geometric shape. IUPAC define fullerenes as “compounds composed solely of an even number of carbon atoms, which form a cage-like fused ring polycyclic system”.<sup>[52]</sup> The most common geometries of fullerenes are spherical or elliptical, however more exotic forms have been predicted to exist.

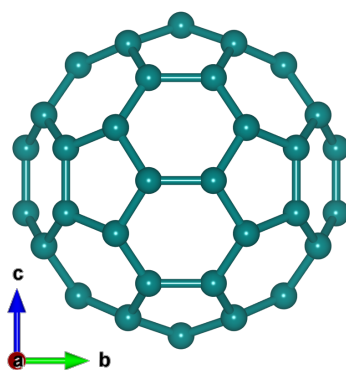


**Figure 7.vii:** A single molecule of Buckminster fullerene ( $C_{60}$ ), the first known, and most widely studied, of the Bucky-ball type fullerenes.

The best known examples of fullerenes are the so-called *Bucky-balls*. The first and most famous example, *Buckminster fullerene*, is composed of sixty carbon atoms arranged to form a sphere. The sphere is formed by alternating five- and six- membered carbon rings, analogous to the geometry of a soccer ball. First synthesised in 1985 at Rice University in Houston, the molecule is named after the American architect Buckminster Fuller, who was famous for the construction of geodesic domes.<sup>[53]</sup> Members of the group at Rice University ultimately went on to win the Nobel Prize for their work on the discovery of Buckminster fullerene, as well as other members of the fullerene family.

Other commonly encountered Bucky-ball fullerenes include  $C_{20}$  (the smallest possible fullerene),  $C_{70}$  and  $C_{84}$ . Theoretically, fullerenes can take on any formula according to the expression:

$$C_{2n} \quad n = 10, 12, 13, 14 \dots$$

Additionally, the number of geometric possibilities for a given number of atoms is vast and exponentially increases with  $n$ . To exemplify this, for  $C_{60}$  there are 1812 possible unique configurations for the Bucky-ball, however the Buckminster fullerene (a *truncated icosahedron*) configuration is the only possibility that exists where no five-membered rings are adjacent to one another. Coincidentally, this is also the smallest such fullerene for which this geometric curiosity is possible.

Interestingly, Bucky-ball type fullerenes have found extensive use in medical applications, including as contrast agents for magnetic resonance imaging (MRI) and x-ray imaging, and as vehicles for drugs and gene delivery.<sup>[54]</sup>

So called ‘glassy-carbon’ has properties intermediate between that of graphite and ceramic, with a relatively high hardness (7 on the Mohs scale), low density, low electrical resistance and significant resistance to temperature and chemical reaction. Much like graphite, it finds significant use in high temperature industrial applications, as well as in electronic devices.<sup>[55]</sup>

Unrelated to the fullerenes, another type of carbon materials is the family of amorphous carbon materials. These materials are a mixture of  $sp^2$  and  $sp^3$  hybridised and again correspond to a huge family of varied materials. Their properties can be tuned to essentially fill the vast continuum of possible properties between the insulating, hard diamond and the soft, conducting graphite.

7.4.2.5. Carbon Nanotubes

Another broad range of carbon allotropes are the *carbon nanotubes*. These are composed of a single sheet of graphene, folded at a specific angle. Many of the general properties of graphene (high electrical and thermal conductivity and significant mechanical strength) are conferred to the nanotubes, but these properties can be greatly tuned by the size of the ‘rolling’ angle, and the diameter of the aperture that the fold creates. The nature of the folding can be determined by using the integers  $m$  and  $n$ , which correspond to the number of unit cell vectors in two different crystallographic directions of the graphene lattice.<sup>[56]</sup> This gives rise to three possibilities:

- If  $m = n$ , the nanotubes are known as *armchair* nanotubes. Armchair nanotubes tend to be metallic, whereas others tend to be semiconducting.
- If  $m = 0$  and  $n \neq 0$ , the nanotubes are referred to as *zigzag* nanotubes.
- For any other combination of  $m$  and  $n$ , the nanotubes are referred to as *chiral*.

As a result of their highly tuneable properties, extreme mechanical strength and relative lack of expense to produce, carbon nanotubes have found extensive use in commercial applications and industry. In particular, carbon nanotubes are currently used in the construction of high-strength, high-performance materials, such as in vehicles and sports equipment.

However, a greater number of unutilised potential for carbon nanotubes still exist, and the structures could find possible uses in electronic devices, as optical (fluorescent) agents, as a gas storage and filtration material (in particular  $H_2$  and  $CO_2$ ), as a solar panel material due to its high UV-absorption, as a battery anode material, as a filtration material and in textiles and lubricants, amongst many others. Once again, this firmly reiterates the wondrous variety of properties conferred by small changes to the structure of an elemental material.<sup>[57]</sup>

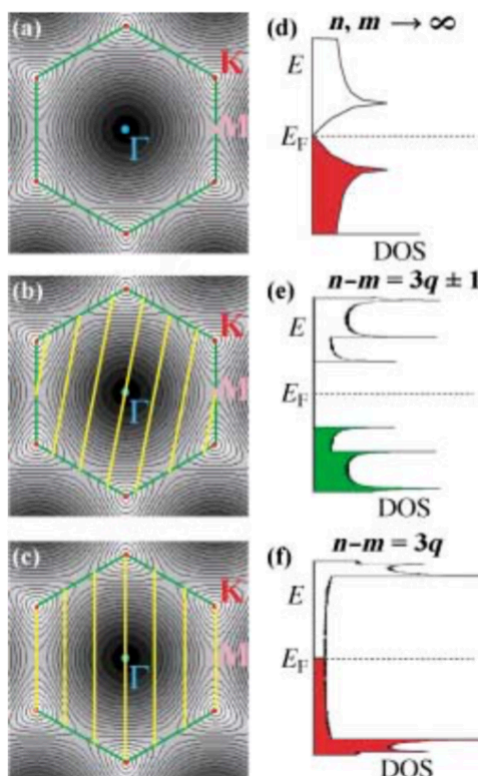


**Figure 7.viii:** 2-dimensional band plots (left) and density of states (right) of (a)/(d) a sheet of graphene, (b)/(e) a semi-conducting *chiral* nanotube and (c)/(f) a metallic *armchair* nanotube.

Notice the presence of the Dirac cones at the edges of the Brillouin zone. Darker colours correspond to energies further away from the Fermi level in the  $k_x, k_y$  plane. Yellow lines correspond to the permitted wave-vectors allowed in the folded-up graphene sheets.<sup>[57]</sup>

#### 7.4.2.6. Even More Exotic Allotropes...

In addition to the vast number of carbon allotropes already synthesised, there exists a huge array of theoretical structures that are yet to be conclusively experimentally validated, or which have only been created once or twice in the laboratory under extremely harsh conditions. There also exist a large number of polymorphs which await experimental validation. Some of these allotropes are described below:

*Bcc-carbon* – In 1989, Roy Johnson and Roald Hoffman predicted that at very high pressures (i.e. above 1000 GPa), diamond transforms into a body-centred cubic structure.<sup>[58]</sup> Consisting of a cube of eight carbon atoms in the unit cell, this geometry is already known to be a constituent of a high-pressure metastable allotrope of silicon. This allotrope is believed to have been synthesised in 2008 using pulsed laser induced liquid-solid interface reaction (PLIIR) techniques;

*Bct-carbon* – Another super-hard and super-dense form, body-centred tetragonal carbon was first predicted in 2010.<sup>[59]</sup>

*M-carbon* – This monoclinic form of carbon features alternating odd-numbered rings consisting of pentagons and heptagons and was discovered using *ab initio* methods in 2006 by Oganov *et al.*<sup>[60]</sup> In 2009, it was then shown that this phase corresponded to a previously synthesised structure from forty-six years prior.<sup>[61]</sup> Subsequent research has shown that M-Carbon is formed by compression of graphite, and that it is the most kinetically likely structure to form as a result of this process;<sup>[62]</sup>

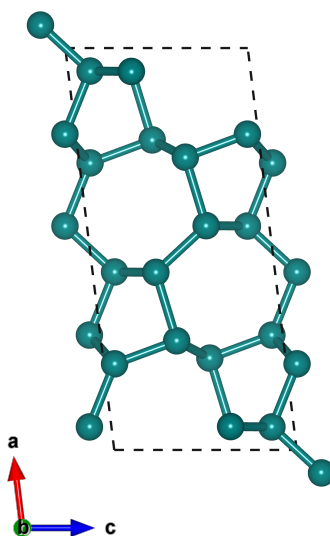


**Figure 7.ix:** Cartoon representation of a unit cell of *M-Carbon*, a hypothetical super-hard and super-dense carbon allotrope predicted by Oganov *et al* (space group  $C2/m$ ).<sup>[60]</sup>

*Q-carbon* – Discovered very recently in 2015, Q-carbon is an allotrope composed of a mixture of  $sp^2$  and  $sp^3$  hybridised carbon. Despite its amorphous structure, it is purported to be harder than diamond by 10-20%, due to dense packing resulting from its ‘melted’ structure. Q-carbon is also reported to be ferromagnetic, with a Curie temperature of approximately 500 K;<sup>[63]</sup>

*T-carbon* – Another recently reported form from 2011, T-carbon is formed by replacing the carbon atoms in a diamond structure with four atoms forming a tetrahedron. With a much lesser density and a hardness one third-less that of diamond, this semiconducting phase could have interesting uses in gas storage and aerospace applications;<sup>[64]</sup>

*Metallic carbon* – The work of Correa *et al* in 2005 demonstrated using *ab initio* methods that carbon at very high pressures exhibits metallic behaviour. Their work predicts that carbon at extreme conditions exists as a low-coordinated metallic melt, retaining a degree of covalent bonding even under such extreme conditions.<sup>[65]</sup>

Previous work by Selli *et al* predicted a number of novel carbon phases.<sup>[66]</sup> Selli *et al* discovered four possible new allotropes of carbon by the simulation of the cold compression of graphite using Martonák-type metadynamics.<sup>[11]</sup> This work established the possibility of coexisting even- and odd- numbered ring motifs, a previously unknown geometric variation in carbon allotropes. The work of Selli *et al* also found a number of previously known phases, such as *M*- and *W*- carbons, showing that metadynamics could be used to visit both existing and novel allotropes.

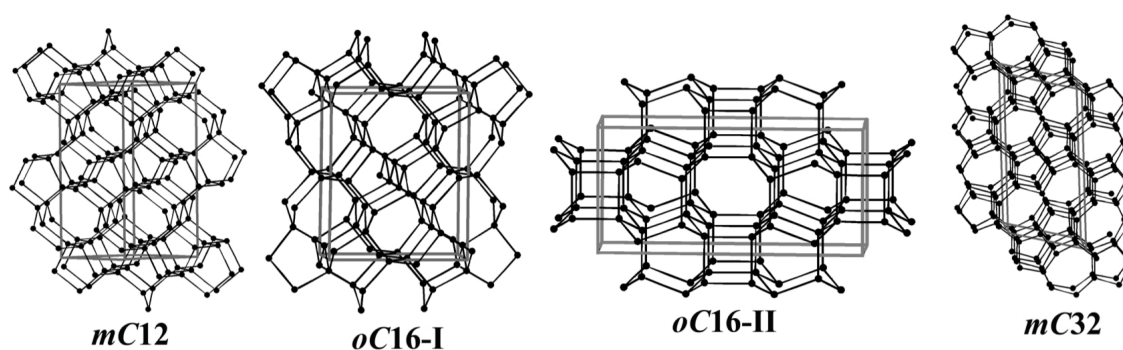


**Figure 7.x:** The four novel phases of carbon discovered by Selli *et al* by simulating the cold compression of graphite using the Martonák metadynamics method.<sup>[66]</sup>

#### 7.4.2.7. Summary

The examples presented within the above discussion are but a small subset of the vast array of carbon allotropes predicted, displaying the vast wealth of configurations that this fascinating element can exhibit.

With such a huge configuration space and wide range of possible structure types and properties, novel carbon allotropes could find a considerable number of potential applications. For example, one could attempt to find a novel super-hard, transparent phase analogous to diamond, with potential uses in industrial, optical or catalytic processes. Alternatively, one could search for a novel, electrically-conducting two dimensional phase analogous to graphene, which could find use in high performance electronic devices. Indeed, there exists a continuum of structures and properties in between these two extremes, as demonstrated by some of the phases described above, each with its own potential commercial or industrial application. Thus, the motivation behind the quest to search for additional carbon allotropes with novel structures and useful properties is evident.

#### 7.4.3. Methodology

As described previously, this work used a random structure prediction technique described as *Random Atomic Placement* to search the configuration space of carbon. Atomic configurations were generated with varying numbers of sites, randomly distributed within cubic unit cells whose dimensions were proportional to the number of atomic sites. Subsequently, these randomly generated systems were optimised at 0 GPa using the conjugate gradient method of optimisation. Promising structures were then tested for mechanical stability by calculating the Hessian matrix at the gamma point  $\Gamma$  of the Brillouin zone. Structures which featured positive eigenvalues for the Hessian matrix were subjected to further analysis, including more rigorous optimisation and subsequent analysis of electronic and mechanical properties.



All calculations, including the optimisations and calculations of bands and phonon structures, were completed within the *SIESTA* package.<sup>[67]</sup> Density functional theory (DFT) within the generalised gradient approximation (GGA) with the Perdew-Burke-Ernzerhof (PBE) exchange-correlation functional<sup>[68]</sup> were utilised for the optimisations and subsequent analyses. A norm-conserving Troullier-Martins pseudopotential<sup>[69]</sup> was utilised to describe the core states. For the initial relaxation of the randomly generated configurations, electronic states were expanded in a single-zeta basis set. Follow-up calculations saw the electronic states expanded in a double-zeta basis set with additional polarization functions for the  $2p$  orbitals. Charge densities were represented by a finite 3-D grid in real-space with a cut-off of 250 Ry. For electronic structure and phonon spectrum calculations, the systems were rigorously relaxed such that the forces acting on each atom were less than 0.01 eV. Phonons were calculated using the *supercell* method as implemented within *SIESTA*. The number of  $k$ -points was carefully chosen, depending on system size and the nature of the calculation being undertaken, to ensure accurate sampling.

7.4.4. Results and Discussion7.4.4.1. Overview and Efficacy of the *Random Atomic Placement* Method

Over two-hundreds simulation boxes were set up, containing three, four, six, eight and twelve carbons atomic units. Many of the relaxation runs produced known structures, including graphite and diamond. A significant number also produced highly implausible structures, with unusual bond lengths, angles and coordination sequences.

However, twenty-five plausible structures, including graphite and diamond, were obtained from the random structure search. Many of these predicted structures already correspond to known structural types of carbon, however eight of the presented structures are novel for carbon. Of the twenty-three structures, excluding diamond and graphite:

- Four of the structures consist entirely of  $sp^2$  hybridised carbons, forming planar layers with large distances separating the sheets;
- An additional four of the possible configurations are 3-D carbons formed entirely from  $sp^2$  hybridised atomic sites, each bonded to only three other atomic neighbours;
- Two of the potential allotropes consist of layers of  $sp^2$  and  $sp^3$  carbons, forming puckered sheets that are non-planar but still feature large separations between the layers;
- A further six structures are formed of a mixture of  $sp^2$  and  $sp^3$ -hybridised carbons, forming 3-D molecular 'sponge-like' networks;
- The final seven of the found structures are 'diamond-like', formed by covalent 3-D networks formed exclusively by four-coordinated carbon atoms.

Index	Crystal ( <i>space group</i> )	Dimensionality	3-letter code	Notes
C1	Tetragonal ( $I4/mmm$ )	3D	crb	
C2	Orthorhombic ( $Imma$ )	3D	sra	
C3	Tetragonal ( $P4mm$ )	2D	fes	
C4	Orthorhombic ( $Cmmm$ )	3D	moc	
C6	Tetragonal ( $P4_122$ )	3D	unc	
C9	Cubic ( $Fd\bar{3}m$ )	3D	dia	Diamond
C10	Hexagonal ( $P6_3/mmc$ )	2D	gra	Graphite
C11	Monoclinic ( $I1m1$ )	3D		New Structure
C12	Orthorhombic ( $Pmmm$ )	2D		New Structure
C14	Orthorhombic ( $F222$ )	3D		New Structure
C15	Hexagonal ( $P6_422$ )	3D	eta	
C17	Monoclinic ( $I12/m1$ )	3D		New Structure
C18	Orthorhombic ( $Pmma$ )	3D	jbw	
C19	Orthorhombic ( $P2mm$ )	2D		
C20	Monoclinic ( $C12/m1$ )	3D	dme	
C21	Orthorhombic ( $C2mm$ )	2D		
C22	Monoclinic ( $C121$ )	3D		
C23	Hexagonal ( $P6_522$ )	3D	unj	
C24	Trigonal ( $R\bar{3}m$ )	3D	pcu-h	
C25	Tetragonal ( $P4mm$ )	2D	mcm	“Cairo Tiling”
C30	Monoclinic ( $C12/m1$ )	3D		New Structure
C33	Tetragonal ( $P\bar{4}2m$ )	3D		New Structure
C35	Monoclinic ( $C12/m1$ )	3D	cbs	
C36	Monoclinic ( $P12/m1$ )	2D		New Structure
C38	Monoclinic ( $C12/m1$ )	3D		New Structure

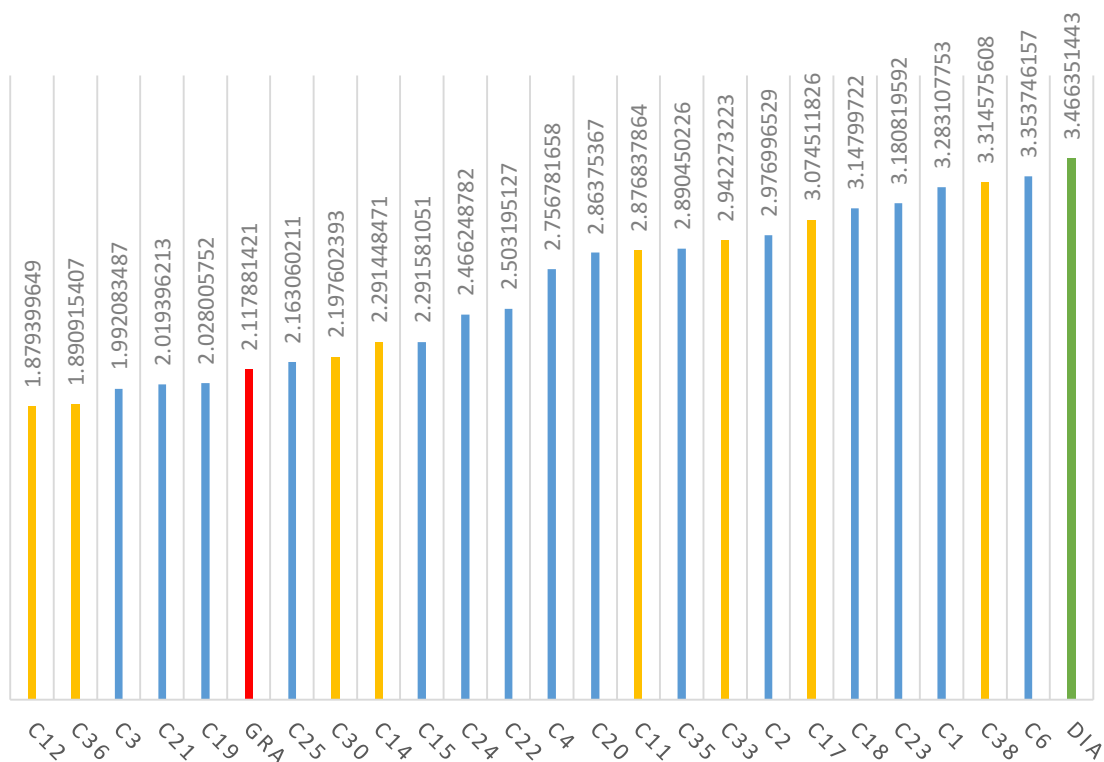
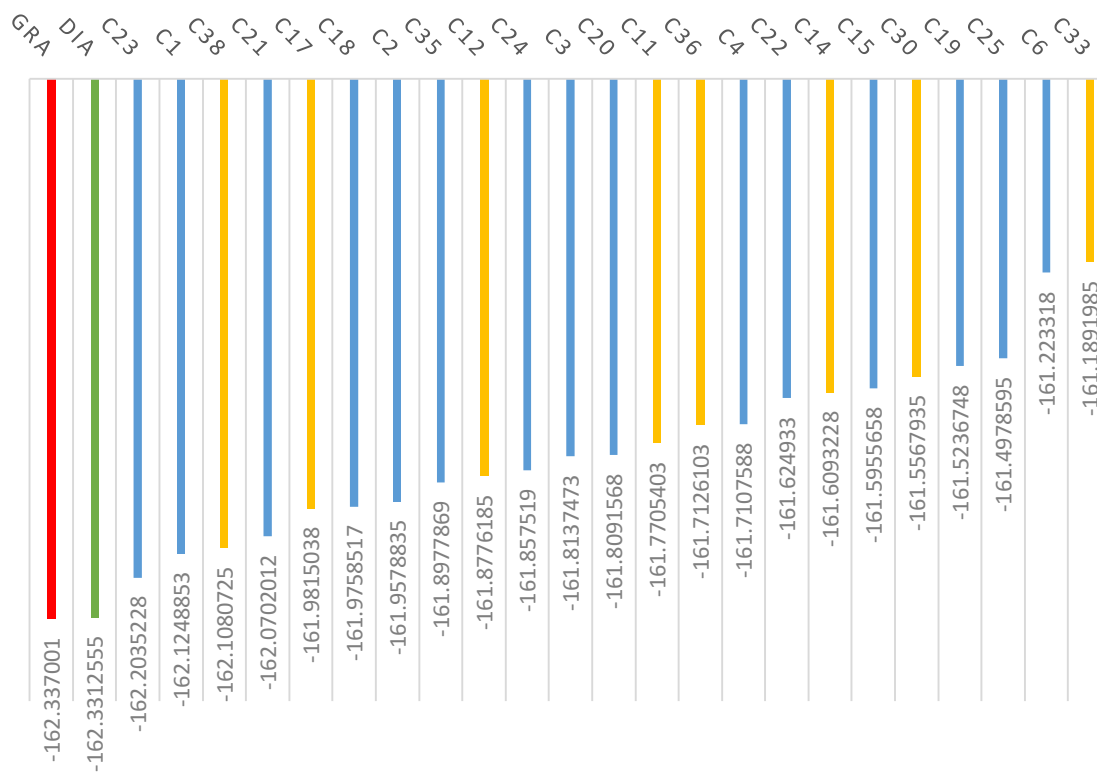
**Table 7.xi (previous page):** Data summarising the twenty-five carbon phases found in this work. The ‘index’ number corresponds to order of which the structures were first found using the prediction method. Missing integers correspond to structures that were later determined to be equivalent to already included structures by symmetry. Diamond and graphite, the two most familiar forms of carbon, are highlighted in green and red respectively. Allotropes that have not yet been reported for carbon are highlighted in gold.

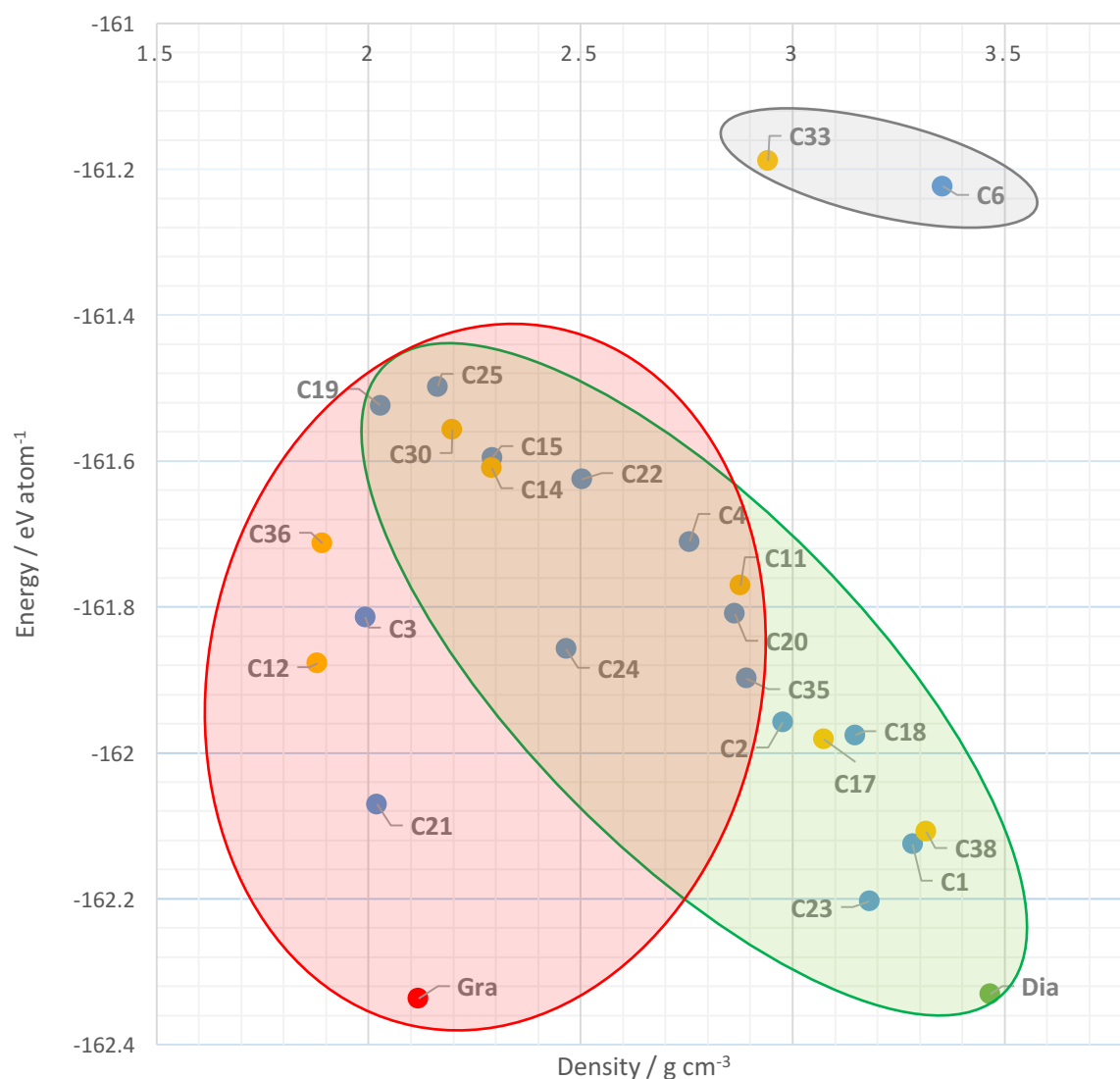
The following data shows that the twenty-five allotropes, including the eight novel structures found, feature a huge variety of values for density and energy. This demonstrates that the *Random Atomic Placement* method is able to find carbon phases with a very wide range of physical characteristics, from the planar and conducting graphite-like allotropes, to the covalent, electrically insulating diamond-like structures. In addition, all but two of the twenty-three phases discovered by the method were within 1.0 eV of the diamond and graphite structures. This kind of structure searching technique, which is able to resolve energetically similar but structurally different motifs over a large area of the configuration space, is exactly what was desired when designing the structure prediction procedure.

Of particular interest is the density vs. energy plot, which appears to show three distinct regions – a favourable- $sp^3$  region (referred to here as the *Main Sequence*), an  $sp^2$  region, and a prohibitive- $sp^3$  region. Overlaps between these regions correspond to mixed structures containing both motifs characteristic of those regions of the graph.

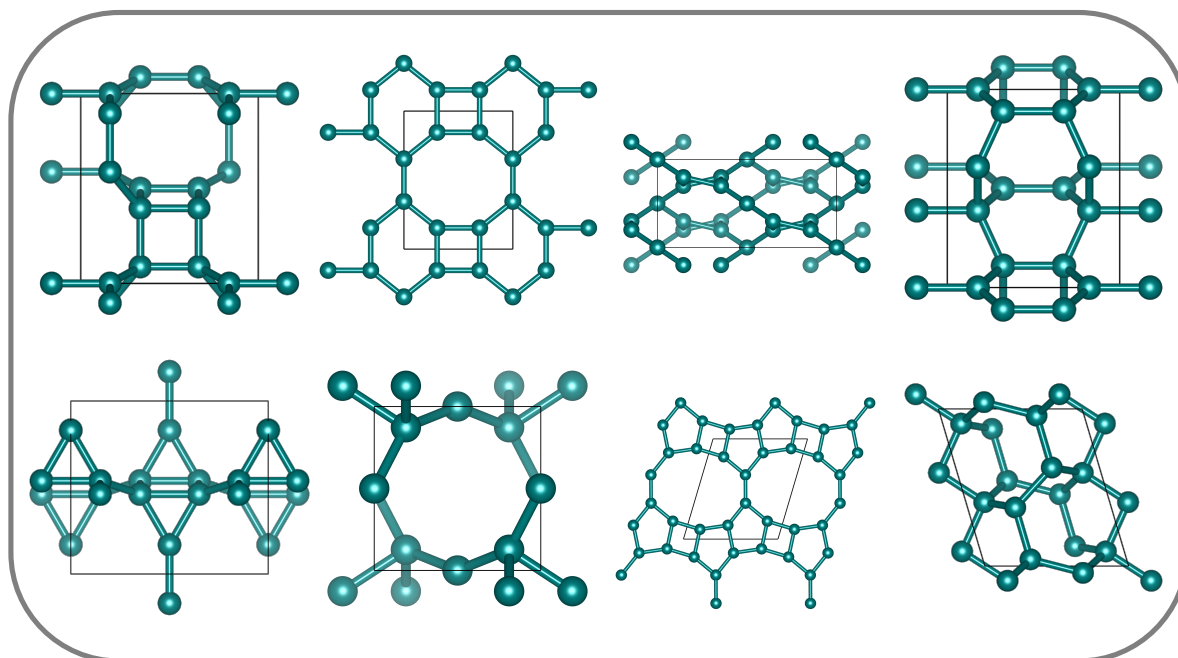
Following this, the remainder of the discussion will focus exclusively on the eight novel allotropes. All of the data presented about these eight carbon structures, unless otherwise indicated, is taken from simulations with the pressure set at 0 GPa.

**Figure 7.xii (overleaf):** Plots of the densities (top) and energies (bottom) of the predicted carbon phases at 0 GPa. Diamond and graphite are labelled green and red respectively. Previously known or predicted phases are labelled in blue, whereas novel phases from this work are depicted in gold. Note the wide range of densities exhibited by the new allotropes, and that all but one of the novel predicted phases are within 1 eV of graphite.

Densities of predicted carbon phases /  $\text{g cm}^{-3}$ Energies of predicted carbon phases /  $\text{eV atom}^{-1}$ 



**Figure 7.xiii:** Plots of density vs. energy for the twenty-five carbon phases predicted in this work. Many of the structures are centred along the diagonal of the plot (the ‘Main Sequence’, indicated by the green-edged region), which appears to show a linear relationship between increasing density and decreasing energy for the structures observed. The exceptions are those centred around density = 2 g mol<sup>-1</sup> which correspond to low-energy aromatic or graphitic-like phases (red-edged region), and high-energy phases at high density corresponding to disfavoured bonding configurations (grey region). In general, configurations found exclusively in the red and green regions are entirely  $sp^2$  and  $sp^3$  respectively, whereas those in both the green-red overlap region are a mixture of  $sp^2$  and  $sp^3$ , either forming sponges or puckered layers. All data is recorded at 0 GPa, and the points are coloured according to the scheme discussed previously.

7.4.4.2. The Eight Novel Carbon Structures7.4.4.2.1. Overview

**Figure 7.xiv:** The eight previously unpredicted structures of carbon discovered in this work.

From top left to bottom right: C11, C12, C14, C17, C30, C33, C36 and C38.

The eight novel allotropes found in this work account for many of the different classes of carbon structures. Three of the structures correspond to diamond-like covalent networks formed exclusively by  $sp^3$  bonding. Two of the structures are graphite or graphene-like forming layers of exclusively  $sp^2$  hybridised carbon atoms, whilst another is an entirely  $sp^2$  hybridised molecular network. The remaining two structures are composed of a mixture of  $sp^2$  and  $sp^3$  bonding. All eight of the structures could be relaxed at 0 GPa, strongly indicating that they are valid metastable configurations. The symmetries and some structural data pertaining to each of the structures is summarised in Table 7.xv, and volume vs. energy plots for all structures (except for the graphenic structures) are given in Figure 7.xvi.

	Crystal ( <i>space group</i> )	Pearson Symbol	Volume at 0 GPa / Å <sup>3</sup> atom <sup>-1</sup>	Density at 0 GPa / g cm <sup>-3</sup>	Energy at 0 GPa ( <i>Diff. w/ Gra</i> ) / eV atom <sup>-1</sup>	Coord. Sphere
<b>C11</b>	Monoclinic ( <i>I1m1</i> )	<i>mS12</i>	6.927	2.877	-161.771 (+ 0.566)	3.67, 8.67, 19.00, 34.67, 53.00
<b>C12</b>	Orthorhombic ( <i>Pmmm</i> )	<i>oP6</i>	10.603	1.879	-161.878 (+ 0.459)	3.00, 5.33, 8.33, 11.33, 14.33
<b>C14</b>	Orthorhombic ( <i>F222</i> )	<i>oF24</i>	8.696	2.291	-161.609 (+ 0.728)	3.00, 5.33, 9.33, 16.67, 29.33
<b>C17</b>	Monoclinic ( <i>I12/m1</i> )	<i>mS12</i>	6.481	3.075	-161.982 (+ 0.355)	3.67, 9.33, 20.33, 36.00, 56.33
<b>C30</b>	Monoclinic ( <i>C12/m1</i> )	<i>mS12</i>	9.068	2.198	-161.557 (+ 0.780)	3.67, 7.33, 14.33, 26.67, 42.67
<b>C33</b>	Tetragonal ( <i>P4̄2m</i> )	<i>tP6</i>	6.773	2.942	-161.189 (+ 1.148)	4.00, 9.33, 19.67, 40.00, 62.33
<b>C36</b>	Monoclinic ( <i>P12/m1</i> )	<i>mP8</i>	10.538	1.891	-161.713 (+ 0.624)	3.00, 5.50, 7.50, 10.75, 14.5
<b>C38</b>	Monoclinic ( <i>C12/m1</i> )	<i>mS16</i>	6.012	3.315	-162.108 (+ 0.229)	4.00, 12.00, 26.5, 46.75, 71.5
<b>Gra</b>	Hexagonal ( <i>P6<sub>3</sub>/mmc</i> )	<i>hP4</i>	9.409	2.118	-162.337 (± 0.00)	3.00, 6.00, 9.00, 12.00, 15.00
<b>Dia</b>	Cubic ( <i>Fd3̄m</i> )	<i>cF8</i>	5.749	3.466	-162.331 (+ 0.006)	4.0, 12.0, 24.0, 42.0, 64.0

**Table 7.xv:** Crystallographic and structural data relating to the eight novel polymorphs of carbon. Note the wide variety of predicted structures, ranging from low density sponges to high-density three dimensional structures. Densities for C12 and C36 are reported in their *graphitic* configuration using the original unit cell after optimisation, not the larger cell used in subsequent analysis.



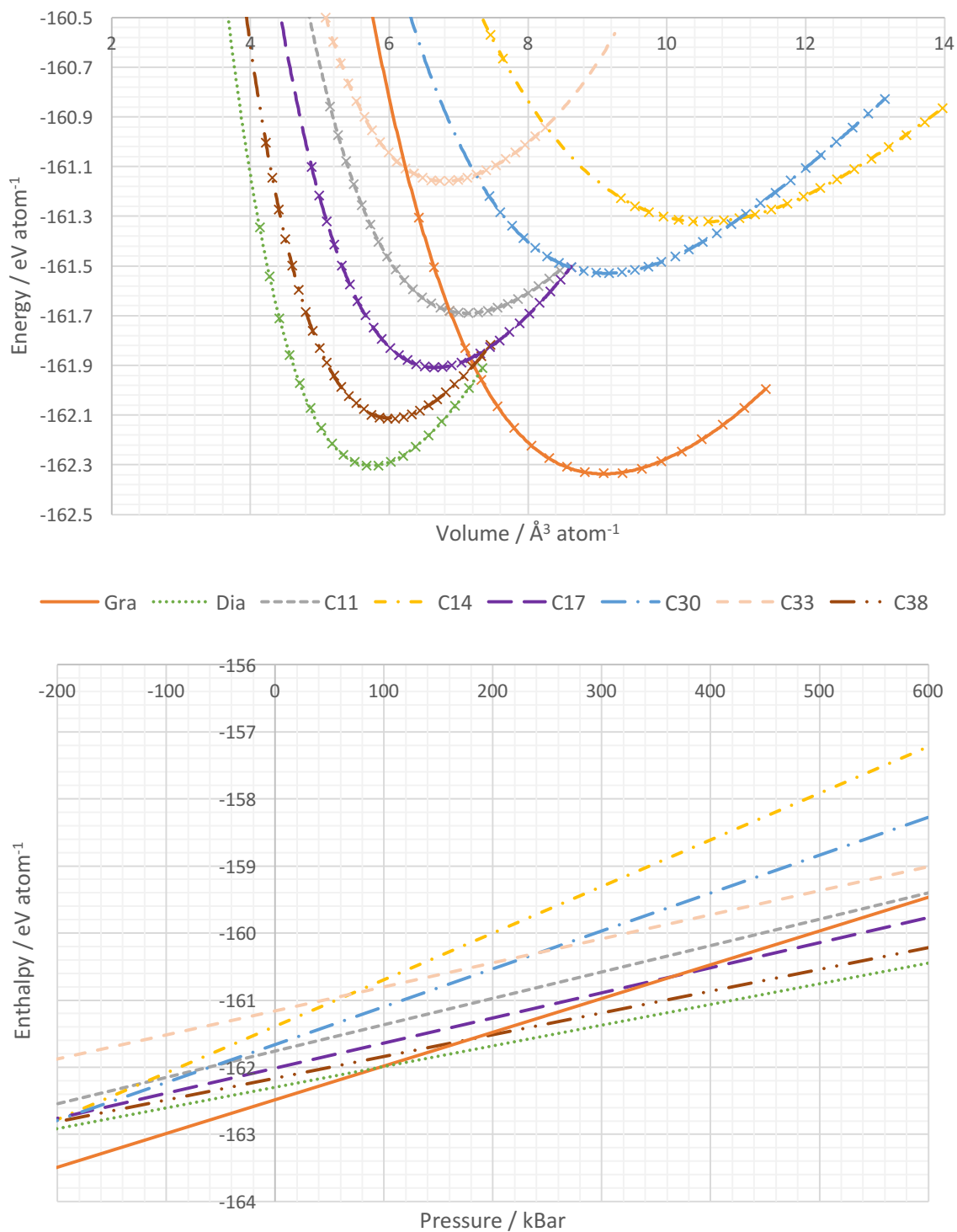


**Figure 7.xvi:** Volume vs. energy (top) and pressure vs. enthalpy (bottom) profiles for all of the non-planar carbon allotropes. The plots for graphite and diamond have also been included for reference. All of the structures could be stabilised at 0 GPa by conjugate gradient geometry optimisation. Computed points have been indicated and the curves extrapolated with polynomial and linear trend lines for the top and bottom plots, respectively.

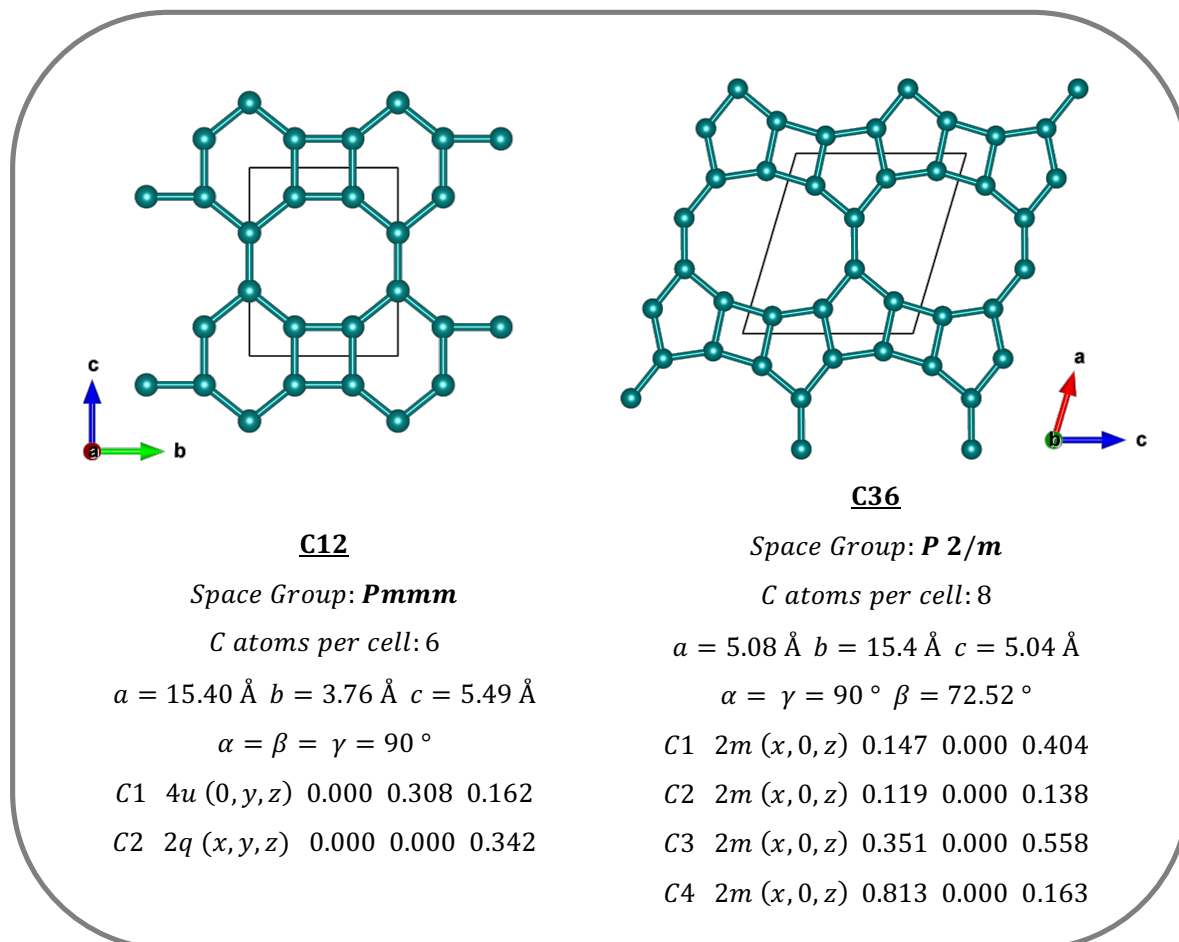
7.4.4.2.2.  $sp^2$ -layer Carbons: C12 and C36

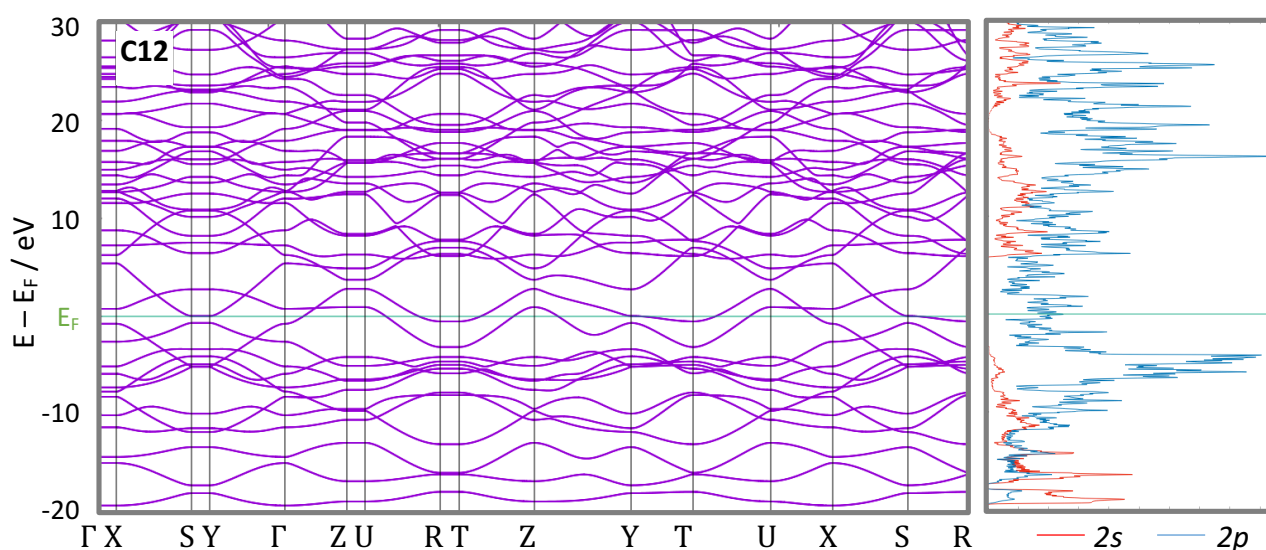
Figure 7.xvii: Structures of the two  $sp^2$ -layer structures found, C12 (left) and C36 (right), as well as crystallographic data including the conventional unit cell space group, lattice parameters and crystallographic coordinates with Wyckoff positions.

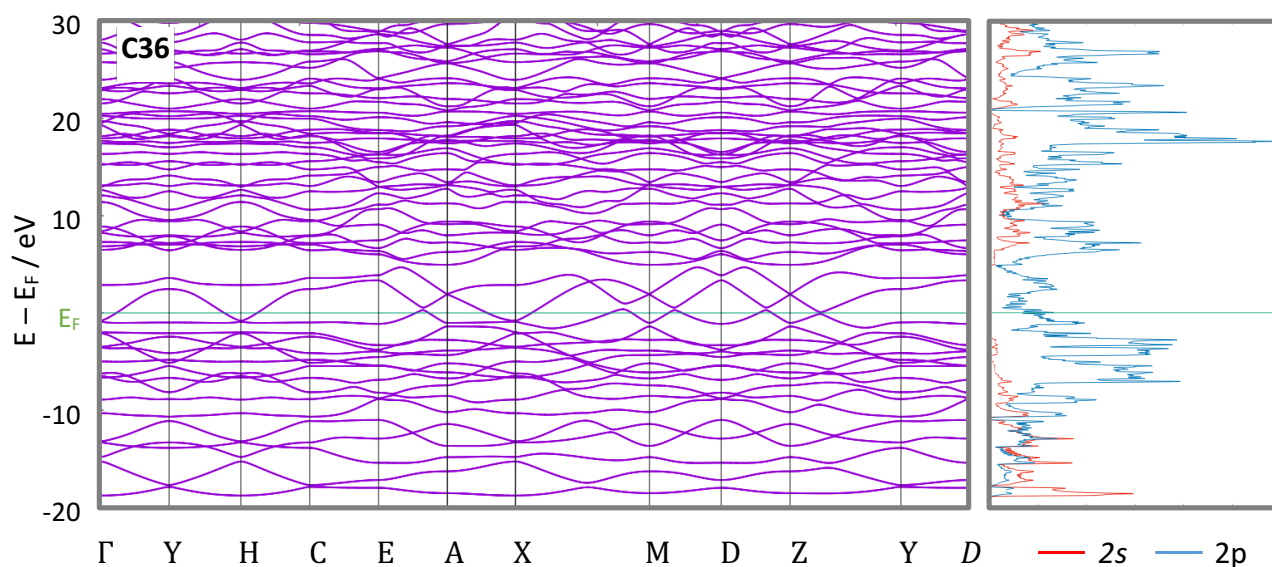
C12 and C36 are both two-dimensional carbons, consisting of planar sheets of  $sp^2$ -hybridised atoms. The structures generated were initially treated as layered materials, forming an infinite crystal in every direction with an inter-layer distance analogous to graphite. However, from inspection of the initial data it was clear that each planar layer could be considered *graphenic* in nature. In order to ensure that there is no inter-layer interaction for the band and phonon analysis, the distance between layers was increased to  $15.4 \text{ \AA}$  in both structures.

The C12 structure consists of four, six and eight sided rings, none of which form perfect polygons as a result of a number of different bond lengths within the structure. The shortest contact, at 1.42 Å, corresponds to the C-C bond defining the edge between hexagonal and octagonal motifs, while the longest at 1.49 Å defines the C-C bond forming the edges between the rectangles and hexagons. This imparts a rather distorted geometry to the rings, with a multitude of different angles away from the values expected of perfect four, six and eight sided polygons. Of the twenty-five allotropes found, this structure was intermediate in energy, at +0.46 eV atom<sup>-1</sup> higher in energy than graphite at 0 GPa.

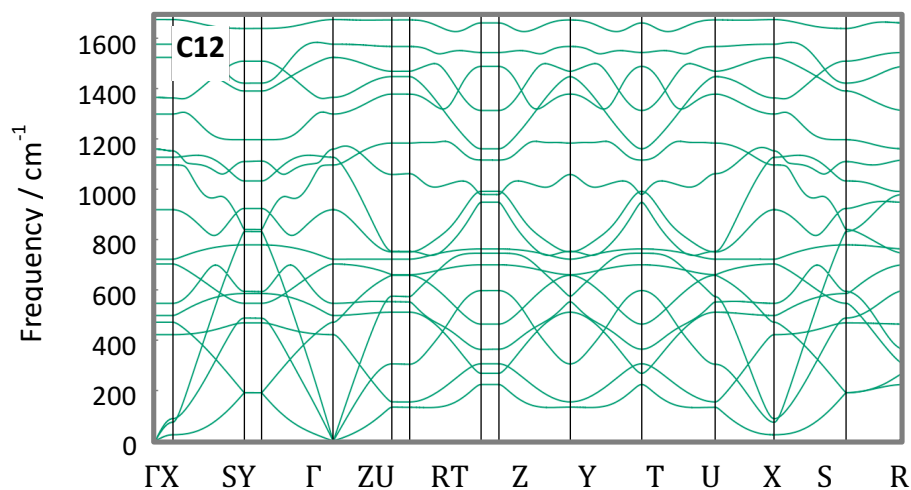
The C36 structure is formed by four, five and ten membered rings, forcing the bond lengths to vary even more than in C12. The longest bonds at 1.51 Å are C-C interactions forming the vertex between the four and five membered rings, whereas the shortest defining the edge between the pentagon and the decagon is a mere 1.40 Å. With a slightly higher energy than the C12 structure, this allotrope is less favourable than graphite by some +0.62 eV atom<sup>-1</sup>.

The band structures of C12 and C36 indicate that both of the structures are expected to be metallic in nature. The projected density of states (PDOS) for both materials also shows significant population of electronic states around the Fermi level, confirming the metallic character of the allotropes. The mechanical stability of C12 was confirmed by the lack of imaginary frequencies in its phonon dispersion plot. However, a negative frequency was present in the phonon spectrum of C36, indicating that this structure is unstable.



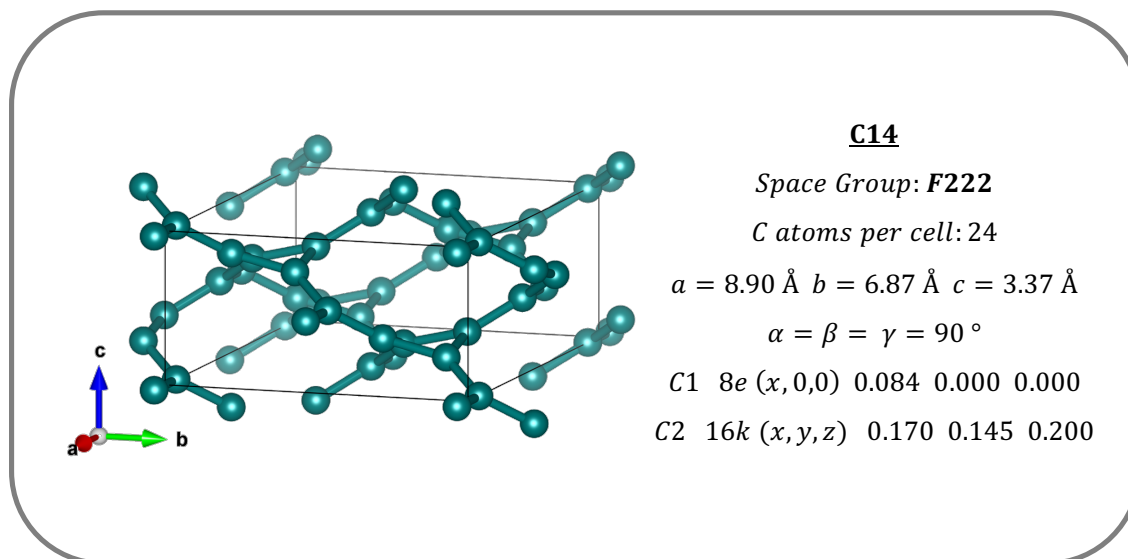


**Figure 7.xviii:** Electronic band structures (left) and projected density of states (PDOS, right) of C12 (previous page) and C36 (above). The green line denotes the Fermi level, and red and blue plots in the PDOS represent the carbon 2s and 2p contributions respectively. Note the bands crossing the Fermi level and presence of states around  $E_F$  in both plots, confirming their metallic character.



**Figure 7.xix (left):** Phonon dispersion curves for C12 showing no negative frequencies at any points in their respective Brillouin zones. The lack of any values below zero in the phonon spectra indicates that the materials of interest is dynamically stable at 0 GPa.

Despite C36 not returning a phonon spectrum with all positive values, it is believed that it may still represent a novel, plausible structure type for carbon, which may be mechanically stable with some small changes to the geometry. For example, initial indications show that the three-dimensional analogue of this topology may represent a stable configuration. However, further investigation is necessary to confirm this.

7.4.4.2.3.  $sp^2$ -3D molecular carbons: C14

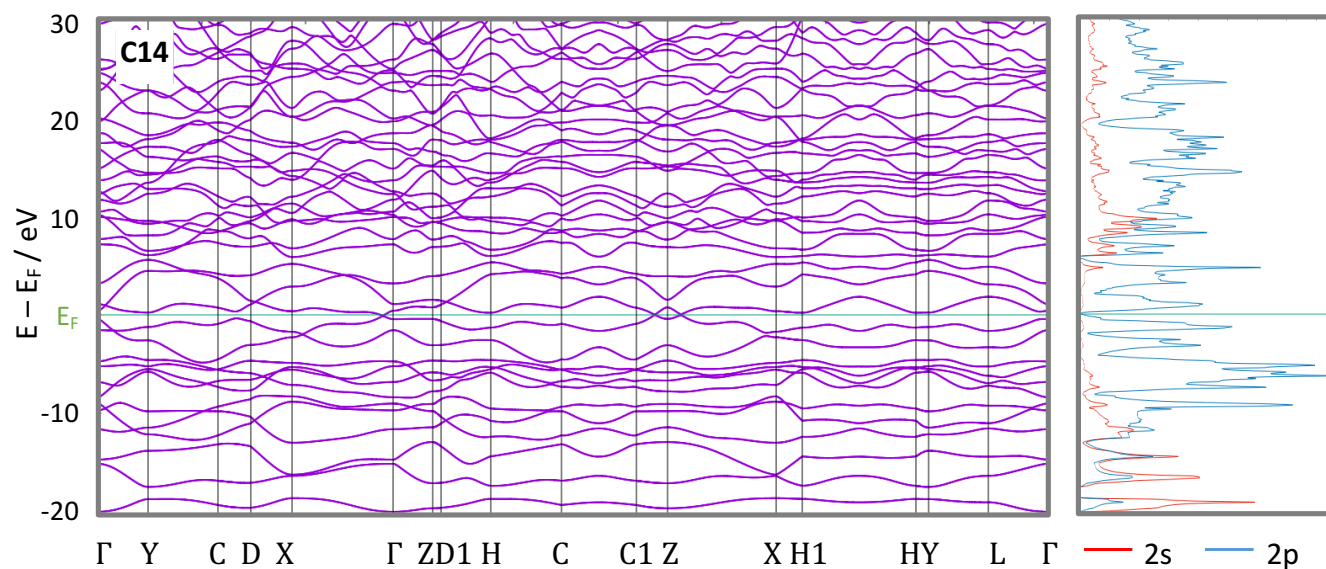
**Figure 7.xx:** Structure and crystallographic data relating to C14, the only structure found to be conclusively formed by a three dimensional lattice of exclusively  $sp^2$  hybridised carbon atoms.

C14 forms a complex three dimensional structure featuring both four- and twelve- membered rings of carbon centres. When viewed down the  $b$  and  $c$  axes, the structure exhibits striking spiralling motifs, with the two sets of orthogonal helices meeting each other at the four-membered rings. C-C distances within the relaxed structure range from  $1.42 \text{ \AA}$  to  $1.50 \text{ \AA}$ , giving it a similar bond distance variation to the layered  $sp^2$  structures discussed previously.

The electronic properties of this allotrope are most intriguing. The band plot shows three instances of band crossing at the Fermi level, and the projected density of states shows that there is a very small (but non-zero) amount of  $2p$  states populated at  $E_F$ . The collected phonon dispersion curve (which is not reported here) had a very small imaginary component around the  $\Gamma$  point. However, it is fully believed that this is due to the size of the simulation super-cell, and that the structure should be mechanically stable.

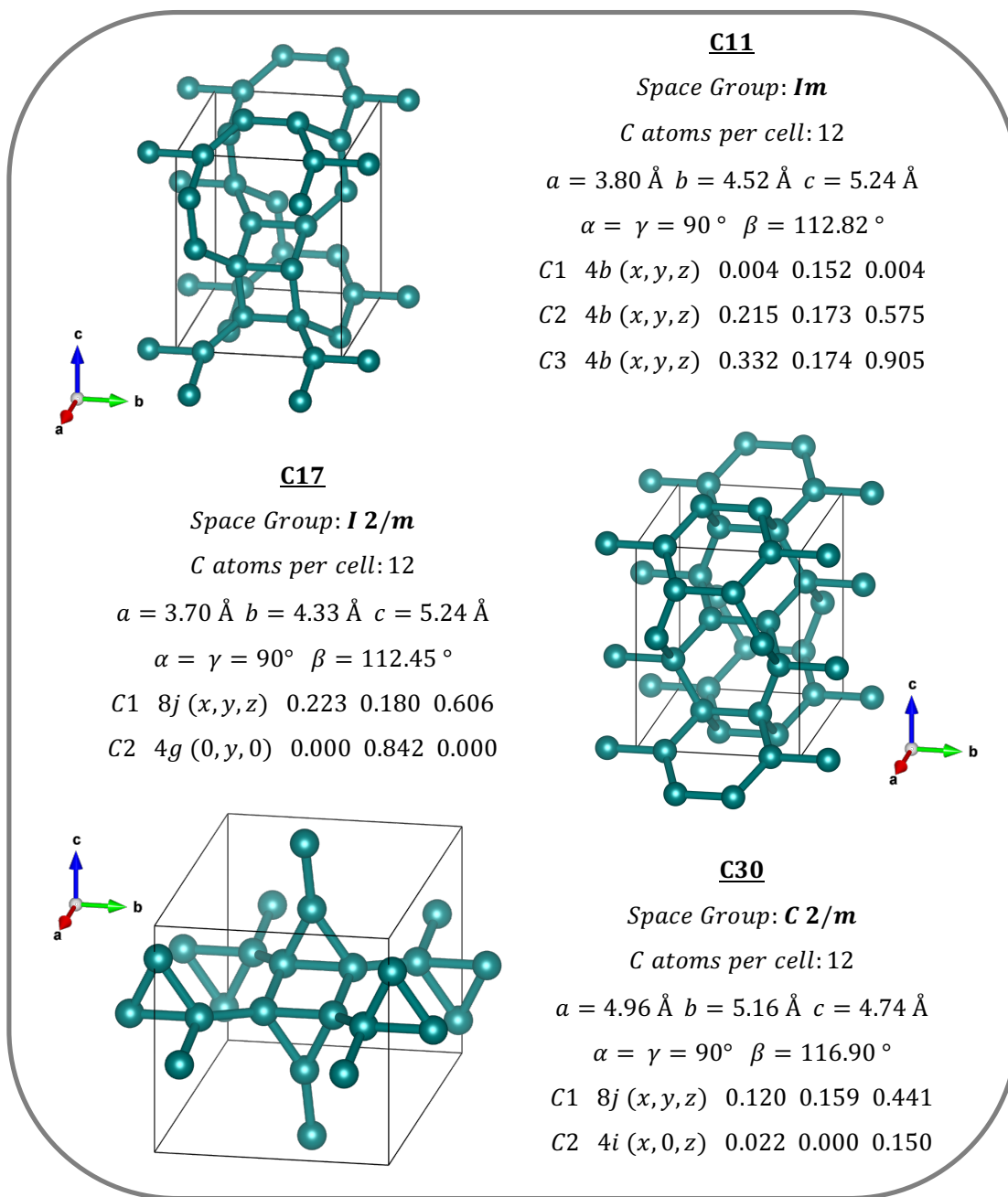
With a density of only  $2.291 \text{ g cm}^{-3}$ , the material is not much denser than graphite, despite forming a three dimensional molecular structure. The helical carbon structure exhibited down

the  $b$  and  $c$  axes creates large pores through the material parallel to the direction of the spiralling, explaining its low density. It would be interesting to investigate the adsorption properties of this material, with the possibility of utilising the pores to host guest gas molecules for storage or catalysis. A future study using a method such as Grand Canonical Monte Carlo could be extremely worthwhile on this material.



**Figure 7.xxi:** Electronic band structures and projected density of states (PDOS) for the 2s and 2p functions of C14 (above), a three dimensional  $sp^2$  allotrope.

The phonon dispersions for C14 are not reported here, as there was a negative frequency centred around the  $\Gamma$  point in the obtained spectrum. Sadly, any efforts to eliminate this discrepancy have so far been unsuccessful. Nevertheless, the anomaly is believed to be a numerical issue, and not an inherent problem with the structure – thus, it is *speculated* that C14 represents a mechanically stable configuration, but sadly this cannot be verified at this time.

7.4.4.2.4.  $sp^2$ - $sp^3$  mixed carbons: C11, C17 and C30

**Figure 7.xxii:** Illustrations of and crystallographic data for C11 (top), C17 (centre) and C30 (bottom). All three of these structures are formed of a mixture of  $sp^2$  and  $sp^3$  carbons.

The three mixed  $sp^2$ - $sp^3$  carbons are quite varied in character, although there are notable similarities between them. Firstly, they all crystallise within a *monoclinic* space group.



Secondly, they all contain a 2:1 ratio of four-coordinate and three-coordinate carbons, leading to a first coordination number of 3.667 for all three of the structures. Thirdly, all three materials are semiconducting in nature, although their band structures are quite dissimilar.

C11 and C17 are both fairly dense structures and are both intermediate in terms of the energy ranking of the twenty-five found polymorphs. Both also exhibit significant variation in C-C bond lengths, with both C11 and C17 exhibiting interatomic distances between 1.37 Å and 1.62 Å. However, C11 has a much more 'open' structure than C17, containing spiralling carbon atoms along the *a*-axis. On the contrary, C17 does not feature spiralling, but instead forms internal four, six, eight and ten membered rings, making it the denser of the two structures. C17 is also the more energetically favoured of the two structures.

C30 is the least dense of the three structures, with large cavities and channels running along three crystallographic directions of the structure. Once again, the structure is characterised by extreme variations in bond lengths, of the same order as C11 and C17. The peculiar geometry of the carbon atoms within the structure leads to a fascinating topology, containing three-, four-, eight-, ten- and twelve-membered rings. The large pores and channels in this structure also make it an interesting putative target for gas storage calculations. However, the unusual topology of this material means that it ranks second in terms of the highest energy of the eight novel structures found.

The considerable bond lengths observed in all three of these allotropes do raise the question of whether or not these longest interactions are 'true' bonds, or whether or not these structures would be better categorised as  $sp^2$  molecular structures. However, unlike C14, all three allotropes exhibit atomic sites that adopt an  $sp^3$ -like geometry and a fourth 'bonding' interaction within 10% of a standard carbon-carbon bond. A detailed analysis of the bonding in these structures would be an interesting future project to undertake.



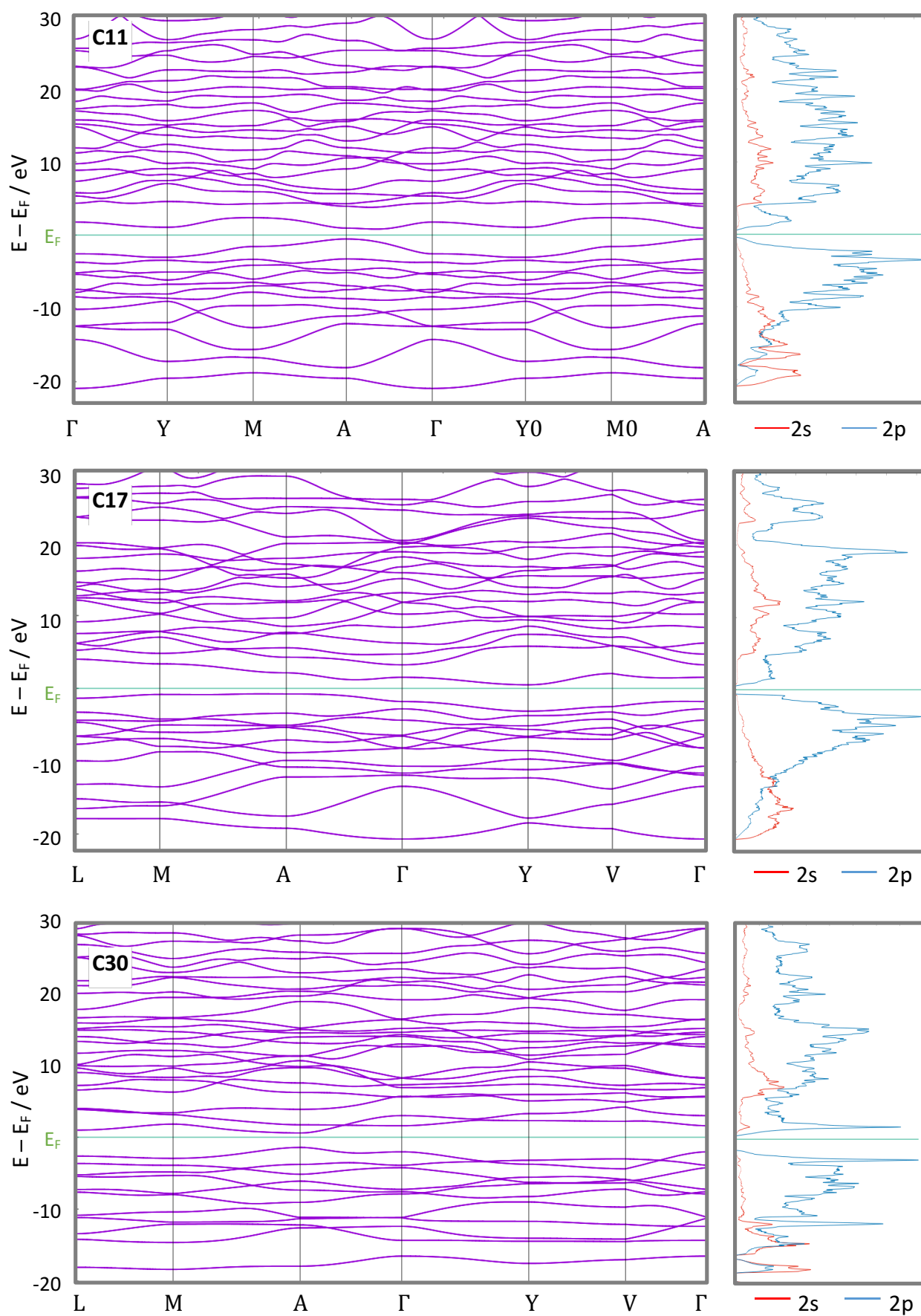


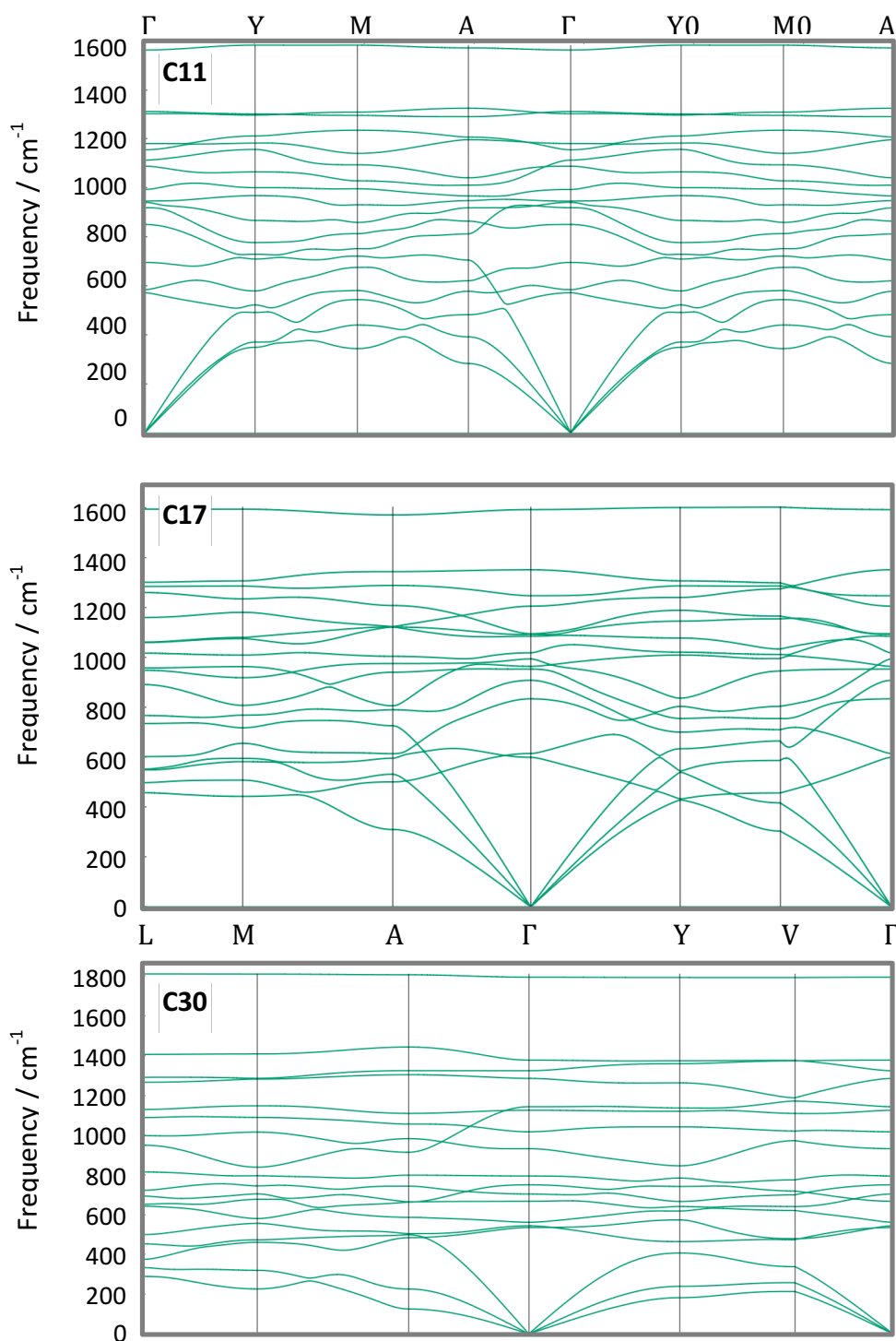
**Figure 7.xxiii (previous page):** Electronic band structures and projected density of states (PDOS) for the 2s and 2p orbitals of C11 (top), C17 (centre) and C30 (bottom). The C11 and C17 materials are both indirect narrow gap semiconductors: C11 has a band gap of 1.60 eV from *A* to *Y0*, whereas C17 has a smaller gap of 1.25 eV between *A* to *Y*. C33 has a much larger, direct band gap of 2.00 eV, also at the *A* high symmetry point. The projected density of states also corroborates this, starkly showing the lack of populated electronic states at  $E_F$ .

**Figure 7.xxiv**

(right):

Phonon dispersion  
curves of C11  
(top), C17 (centre)  
and C30 (bottom).

All three of the  
allotropes are  
dynamically stable  
at 0 GPa



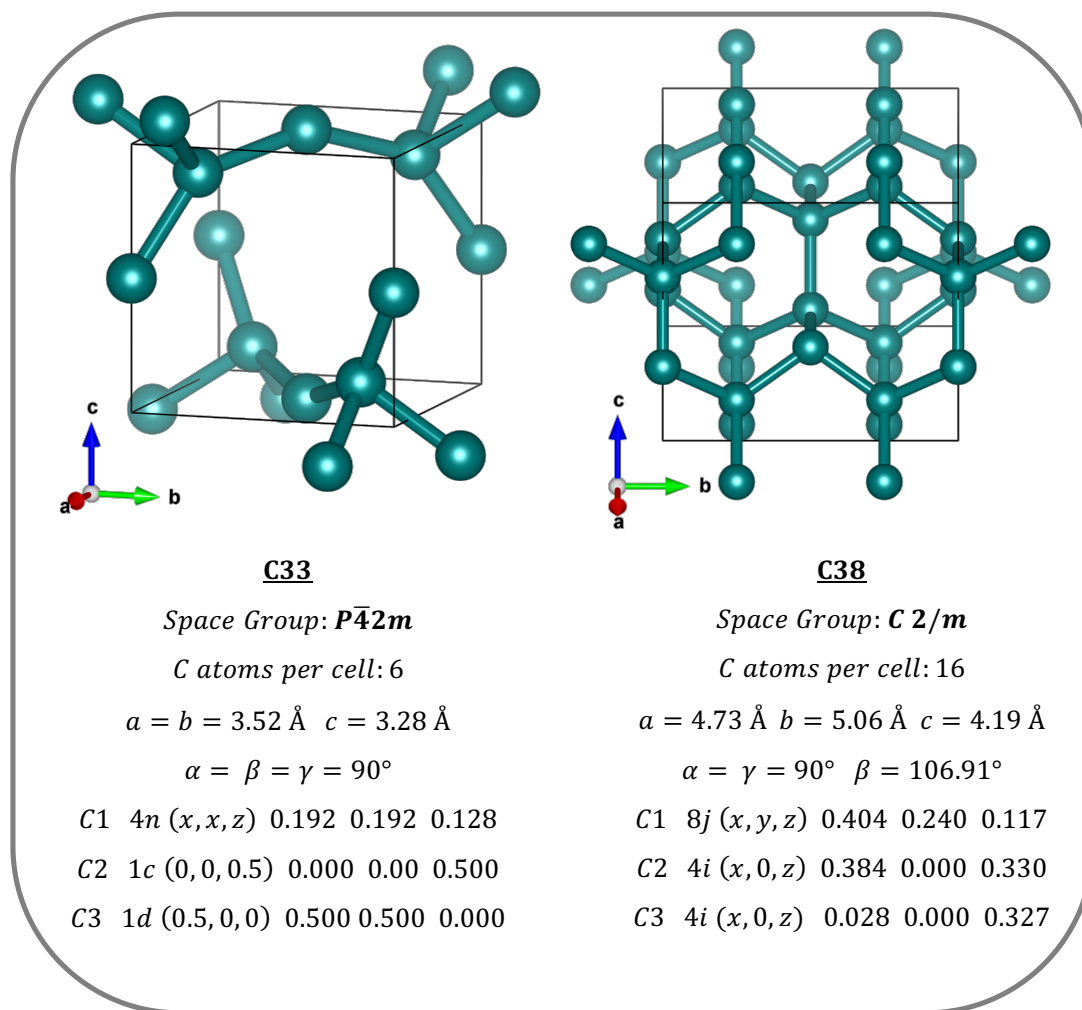
7.4.4.2.5.  $sp^3$ -3D molecular carbons: C33 and C38

Figure 7.xxv: Structures and crystallographic information relating to the two structures composed entirely of  $sp^3$  hybridised carbons – C33 and C36.

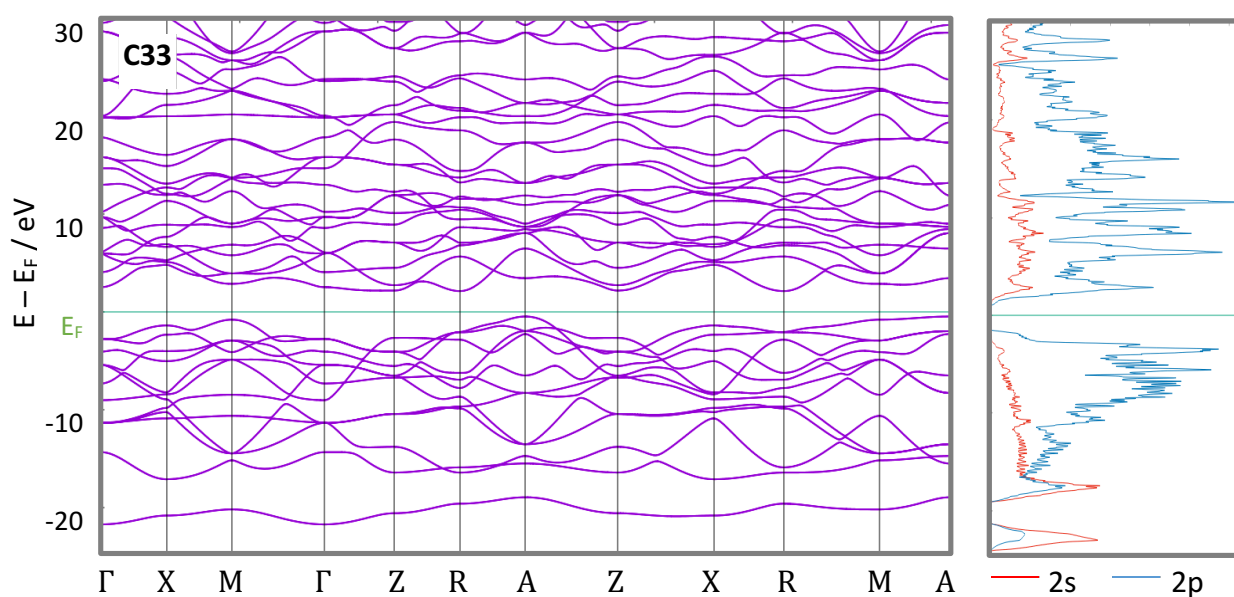
Despite the fact that the final two structures are dense, four-coordinated and exclusively  $sp^3$  hybridised allotropes of carbon, C33 and C38 are not at all alike and constitute the two 'extremes' in terms of energy of the eight novel structures elucidated.

With very little variation in bond lengths, which come in at a healthy range of between 1.55 Å and 1.59 Å, the four-coordinate C-C interactions of the C33 structure at first seem quite reasonable. However, it is immediately evident from inspection of the topology that C33 is a highly unfavourable configuration. The carbon atoms in C33 are arranged to form highly

distorted six-membered rings, which form two bonds across the hexagonal face to atoms on opposing sides of the polygon. Each of the atoms in these hexagons is joint to another six-sided fragment via a four-coordinate carbon with a heavily distorted see-saw geometry. Even with the relatively dense packing of the atoms and completely four-coordinate nature of this allotrope, it is still a significant  $+1.15 \text{ eV atom}^{-1}$  higher in energy than graphite.

On the contrary, the C38 structure is the lowest in energy of the eight structures found, at only  $+0.23 \text{ eV}$  higher in energy than graphite. The carbon atoms are arranged to form five-, six-, seven- and nine- membered rings within the structure, with most of the C-C bond lengths corresponding to that of a reasonable single covalent interaction. However, one of the ‘bonds’ forming the pentagonal rings in the structure measures a significant  $1.68 \text{ \AA}$ . The carbon atoms associated with this bond are most certainly  $sp^3$  hybridised, forming almost perfect tetrahedra. Thus, a more detailed investigation into the bonding exhibited by this allotrope would be very interesting to consider in the future, particularly into the nature of this elongated bond.

Both of these feature much larger band gaps of  $2.60 \text{ eV}$  and  $5.06 \text{ eV}$  for C33 and C38 respectively. Additionally, both structures exhibit no imaginary frequencies in their phonon dispersion curves.



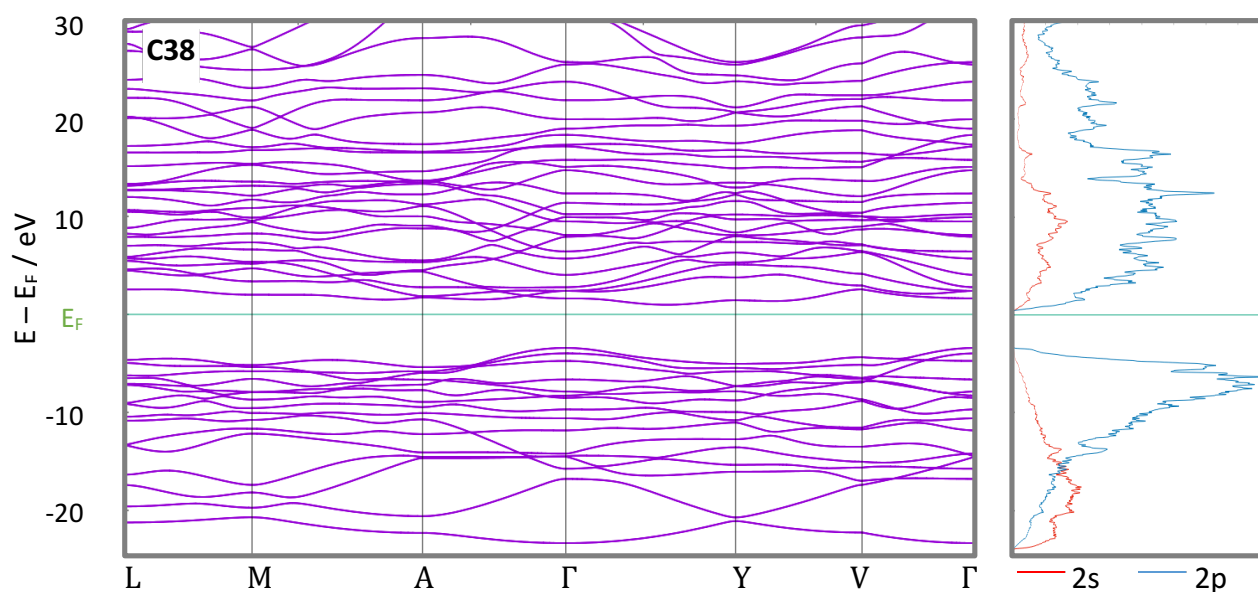


**Figure 7.xxvi:** Band structure and projected density of states for C33 and C38, indicating their insulating nature.

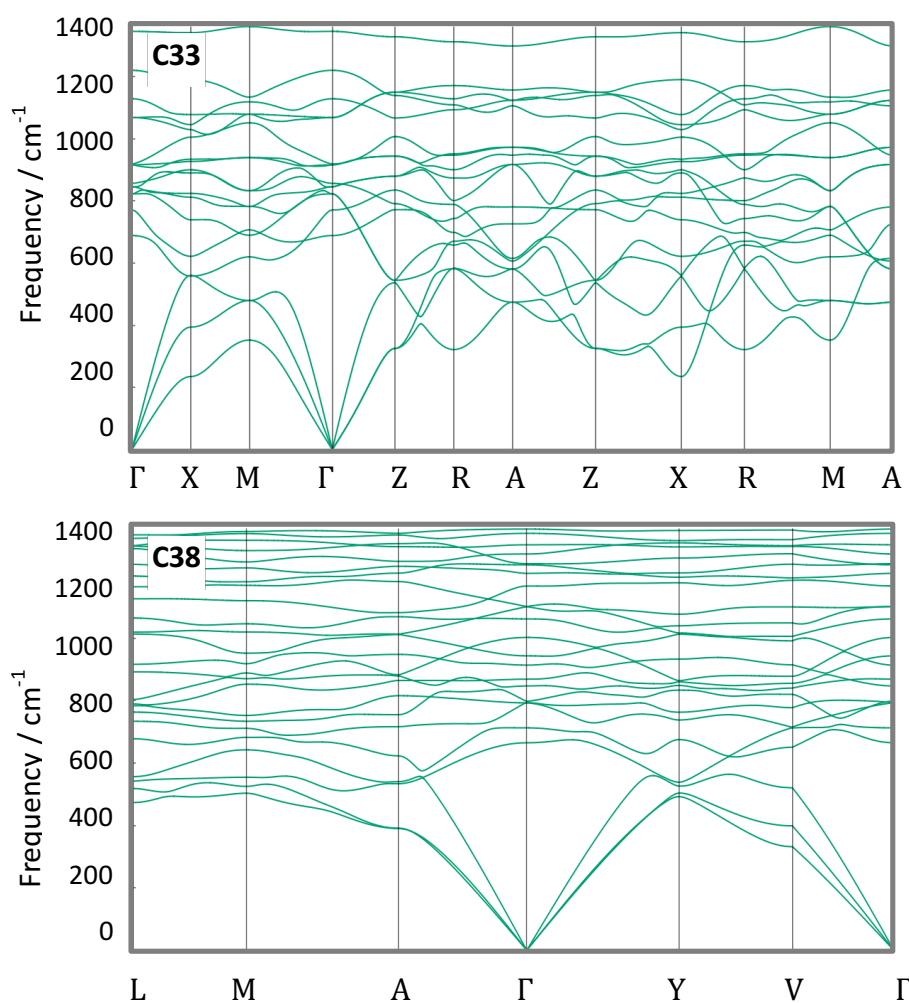


**Figure 7.xxvii:** Phonon dispersion curves for the two  $sp^3$  hybridised structures. Both plots show no negative frequencies, once again indicating the stability of the allotropes.

7.4.5. Conclusions and Future Work

To summarise, twenty-five allotropes of carbon have been discovered using a random structure searching technique; eight of which were deemed to be previously unreported for carbon. All eight of the novel structures can be stabilised at 0 GPa. Six of the eight returned phonon spectra with no imaginary frequencies, indicating that they could be metastable at ambient conditions. The physical properties exhibited by the eight new allotropes are extremely varied in nature, spanning the broad continuum between three-coordinate, conducting graphite and four-coordinate, insulating diamond. Of the eight structures described in this work:

- Two are four-coordinated, three are three-coordinated, and three are a mixture of three- and four- coordinated;
- Two are insulating, two are metallic and four are semiconducting;
- Two are layered in nature, whereas the other five form molecular structures;
- All but one falls within 1.0 eV atom<sup>-1</sup> of graphite.

With such varied properties, should any of these allotropes be synthesised, they could easily find a potential industrial or commercial use.

There is considerable scope for further investigations into these materials. Perhaps the most obvious would be an investigation into how the phases reported in this work could be produced from known structures of carbon, as well as into the external conditions that would be most optimal for the eight allotropes. For example, one could investigate, using transition path sampling methods, the transformation mechanisms between the novel polymorphs and existing phases of carbon.

Each allotrope also raises its own questions, as already alluded to in the analysis of each material. For example, a comprehensive bonding analysis into the  $sp^2$ - $sp^3$  mixed structures would be useful for determining the nature of the very long C-C contacts, whereas a much more detailed investigation into the electronic properties of C14 would be desirable as a

result of the three crossing bands at the Fermi level. Some of the materials are also very porous, containing large cavities and channels through their crystal structures. As such, an investigation into their gas storage properties using Grand Canonical Monte Carlo could be very beneficial, particularly with emphasis on  $\text{H}_2$ ,  $\text{CO}_2$  and  $\text{CH}_4$  selective storage and release.

With respect to finding additional allotropes, further iterations of the *Random Atomic Placement* procedure would undoubtedly lead to the discovery of more structure types for carbon. In addition, full automation of the procedure, or coupling with other structure prediction methods such as *simulated annealing*, may further increase the efficacy of the method.

It is clear from the literature, and the work presented, that the field of carbon crystal structure prediction is still an incredibly interesting and open area of research. To date, approximately 500 allotropes of carbon have been synthesised or predicted, however it is plausible that many more remain to be discovered, each with its own set of unique properties and potential applications. It seems likely, with the arsenal of crystal structure prediction tools now available to computational materials scientists, that the field of carbon structure prediction will continue to be fruitful for many years to come.



7.5. Zinc Oxide Structure Prediction at High Pressure7.5.1. Introduction

As discussed in Chapter 5, zinc oxide is a truly fascinating and versatile compound with a great number of existing and potential uses. Existing uses include in the manufacture of rubber, plastics, ceramics and lubricants, but novel and functionalised forms of the material have great potential for use in future electronics and optical devices. A detailed introduction to the structure, formation and uses of zinc oxide was presented in Chapter 5.

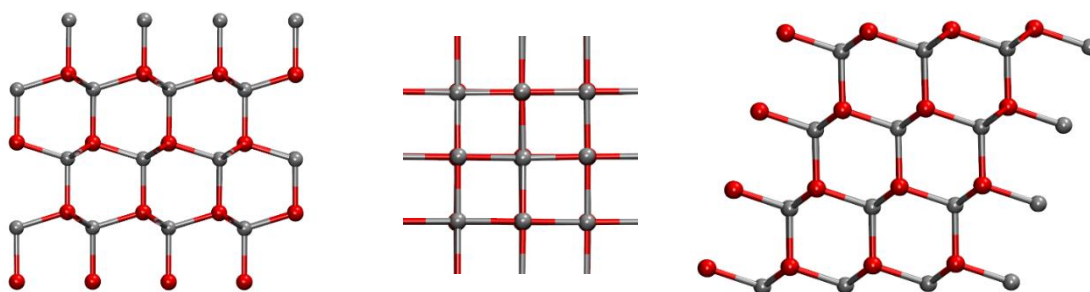


**Figure 7.xxviii:** A brief reminder of the three experimentally observed polymorphs of ZnO – wurtzite (left), rocksalt (centre) and zincblende (right)

Zinc oxides is an excellent contender to be explored with the *Random Atomic Placement* procedure. This is because zinc oxide both already exhibits a number of experimentally known polymorphs (wurtzite, zincblende, and rocksalt) which are very close in energy, and is also likely to display additional structures in the high pressure regime. Other crystal prediction work has proven that exotic stoichiometries and configurations are possible at extreme pressure, even in the most familiar AB compounds. Thus, it can be expected that ZnO should behave no differently. To consider this, a literature review of hypothetical zinc oxide polymorphism follows.



7.5.2. Previous Work on Bulk ZnO Crystal Structure Prediction

Limited attention has been paid to the polymorphism of bulk zinc oxide. Rather, most academic effort has concentrated on the structure and properties of zinc oxide nanoclusters and nanofilms, as well as into the functionalisation of ambient zinc oxide (and, of course, the wurtzite-rocksalt phase transition, which is reviewed extensively in Chapter 5).

For example, Al-Sunaidi *et al* used genetic algorithms to predict possible geometries of zinc oxide clusters containing between 1 and 32 Zn-O units.<sup>[70]</sup> Similarly, Trushin *et al* used density functional theory to assess the stability of the geometries of zinc oxide nanoclusters consisting of between 2 and 9 Zn-O units.<sup>[71]</sup>

Very little is currently known about the true extent of *bulk* zinc oxide polymorphism, especially how it behaves under extreme conditions. Recent literature has shown that even familiar compounds like sodium chloride can exhibit incredibly exotic structures and bonding properties at high pressures. It is thus likely that zinc oxide too will present some intriguing characteristics under extreme conditions.

Only the three above polymorphs of bulk zinc oxide (wurtzite, zincblende and rocksalt) have so far been realised experimentally. A fourth high-pressure polymorph with caesium chloride (CsCl)-type topology has been postulated, but not yet experimentally verified. There is great deal of ambiguity regarding the pressure range at which this CsCl-type polymorph is expected to exist or be directly competitive with the rocksalt phase. Density functional theory seems to suggest that the rocksalt polymorph is favoured up to 260 GPa<sup>[72]</sup>, however others have suggested very different values for the transition pressure.

Analogous to experimental work, very few theoretical studies have been carried out to search the configuration space of bulk zinc oxide outside of these four known polymorphs. One notable exception is a recent set of papers on the polymorphism of zinc oxide published Jansen *et al*. The most comprehensive of these (Zagorac *et al*)<sup>[73]</sup> employ structural annealing to search for minima on the underlying energy landscape. Zagorac *et al* showed that their technique found a great number of potential minima, including topologies shared with

germanium telluride ( $\alpha$ -GeTe), germanium phosphide (GeP), nickel arsenide (NiAs), tungsten carbide ( $\alpha$ -WC) and beryllium oxide ( $\beta$ -BeO), as well as a number of distorted rocksalt configurations corresponding to previously uncharacterised structure types.

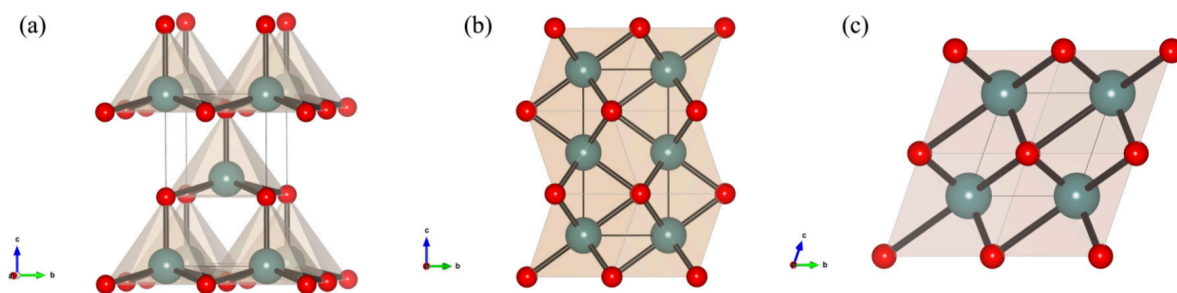


**Figure 7.xxix:** Three of the hypothetical phases of zinc oxide discovered by Zagorac *et al*, including the germanium phosphide (GeP)-type structure (a, left), the nickel arsenide (NiAs)-type geometry (b, centre) and the germanium telluride ( $\alpha$ -GeTe) structure (c, right).

In addition to this work on the polymorphism of zinc oxide, Zagorac *et al* have also investigated polytypism in zinc oxide, and have shown that varying the stacking order in wurtzite and wurtzite-like ZnO can have a profound effect on the electronic properties of the material without invoking the need for dopant atoms. This goes some way to explain the curious properties exhibited by certain zincite-containing minerals.<sup>[74]</sup>

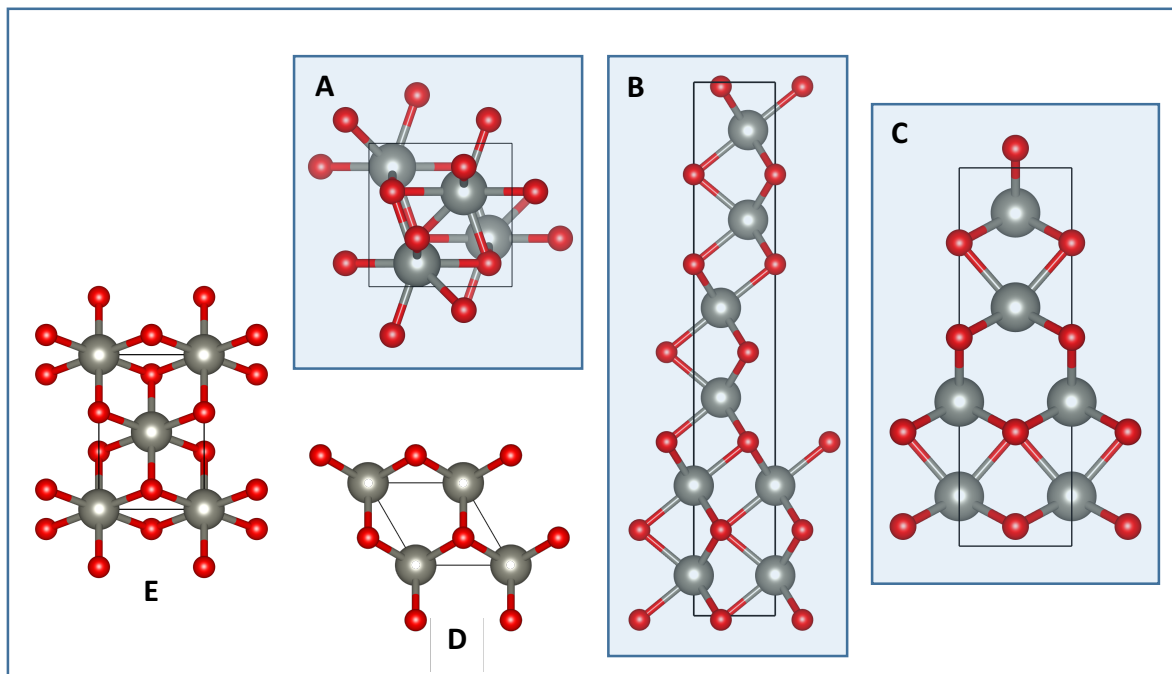
Aside from the above work, there appears to be almost no literature on theoretical studies of the polymorphism of *bulk* zinc oxide at high pressure. As a result of this (and taken in context with the phase transition work between zincblende and rocksalt ZnO already discussed in Chapter 5), it was deemed a prime target for random structure searching techniques at high pressure.

7.5.3. Methodology

Analogous to the carbon structure prediction work, this work too utilised the *Random Atomic Placement* method to search for high-pressure polymorphs of zinc oxide. Firstly, atomic configurations were generated with two, four and six sets of zinc oxide pairs (all of the work presented here was carried out using a 1:1 stoichiometry of zinc and oxygen). The randomly generated systems were then relaxed under pressure using the conjugate gradient method of geometry optimisation. High pressure was induced by multiplying the lattice vectors of the generated cell by a factor of between 0.5 and 0.8 prior to the optimisation, in order to significantly constrict the system from its ambient size but without specifying a particular value of pressure to be exerted.

Promising structures were then further optimised at the pressure obtained due to the volume contraction, such that the total forces acting on each atom were less than 0.01 eV. An initial test for stability was carried out by calculating the vibrational spectrum at the gamma point  $\Gamma$  of the Brillouin zone. Prospective zinc oxide structures which featured positive eigenvalues for the Hessian matrix were subjected to further analysis, including the full calculation of band structures and phonon dispersion curves to elucidate electronic and structural information.

All of the below calculations, including the optimisations and calculations of bands and phonons, were completed within the SIESTA package,<sup>[67]</sup> coupled with the *Random Atomic Placement* scripts. Density functional theory (DFT) within the local density approximation (LDA) with the Ceperley-Alder (CA)<sup>[75]</sup> parameterisation was utilised for the optimisations and analysis. A norm-conserving Troullier-Martins pseudopotential<sup>[69]</sup> was utilised to describe the core states of the zinc and oxygen atoms. Phonons were calculated in *SIESTA* using the *supercell* approach. The number of  $k$  points was suitably chosen for each task depending on system size and the nature of the calculation being undertaken. For the initial relaxation of the randomly generated binary configurations, electronic states were expanded in a single-zeta basis set. Follow-up calculations saw the electronic states expanded in a more rigorous double-zeta basis set with additional polarization functions for the O 2*p* and Zn 4*s* orbitals. Charge densities were represented by a finite 3-D grid in real-space with a cut-off of between 200 and 300 Ry, depending on the system.

7.5.4. Results and Discussion7.5.4.1. Overview

**Figure 7.xxx:** The five hypothetical polymorphs of zinc oxide predicted using the *Random Atomic Placement* method at high pressure. Polymorphs that have not been reported previously for zinc oxide by Zagorac *et al* are highlighted in blue.

From the random crystal structure prediction technique, nine zinc oxide structures were obtained – the three experimentally known structures, the high-pressure caesium chloride form, and an additional five promising high-pressure configurations. Two of the structures have been previously predicted for zinc oxide in the work of Zagorac *et al*, whereas the other three, to the knowledge of the author, have so far not been reported as *possible* structure types for zinc oxide.

Three of the five polymorphs generated could be subsequently optimised at 0 GPa. Four had phonon dispersions with no imaginary frequencies at their respective high pressures. All five of the predicted structures correspond to known structural types. However, some of the

predicted topologies are very rare indeed, being found in only a handful of compounds. The five predicted structures of zinc oxide found in this work are:

- **Structure A** – a cubic, seven-coordinated structure analogous to RS with an FeSi-like distortion (space group  $P2_13$ ). Can be stabilised only at very high pressures and previously unreported as a possible structure type for zinc oxide;
- **Structure B** – a trigonal system (space group  $R3m$ ), with alternating structural motifs corresponding to the geometries of rocksalt and nickeline (NiAs). Of the polymorphs found, this had the lowest energy. Also previously unreported for ZnO;
- **Structure C** – a body-centred tetragonal crystalline structure (space group  $I4_1md$ ), with an atomic arrangement analogous to that of niobium arsenide (NbAs). The third and final novel polymorph found in this work;
- **Structure D** – a hexagonal structure (space group  $P\bar{6}m2$ ), akin to the structure of alpha tungsten carbide ( $\alpha$ -WC). Previously predicted by Zagorac *et al* in 2014, this work fully corroborates their findings for this polymorph;
- **Structure E** – a completely nickel arsenide (NiAs)-type system within an orthorhombic crystal setting (space group  $Cmcm$ ). Also previously predicted by Zagorac *et al* in their papers.<sup>[73]</sup> However in this work this configuration could not be stabilised at ambient or high pressure, readily transforming to the 50:50 rocksalt-nickeline structure B.

Some of the data summarising the five predicted phases, as well as the three experimentally known phases of zinc oxide, are presented in Table 7.xxxii. Following this, a description of all five of the predicted structures in terms of their geometry and band/phonon curves is presented. Predictions about possible uses and routes of synthesis are discussed, where appropriate. Data for each polymorph refers to the pressure of discovery, as indicated for each system.

	Crystal ( <i>space group</i> )	Pressure found /GPa	Can be relaxed at 0 GPa?	Volume at 0 GPa / Å <sup>3</sup> pair <sup>-1</sup>	Density at 0 GPa /g cm <sup>-3</sup>	Energy at 0 GPa (Diff. w/ WZ) /eV pair <sup>-1</sup>	Coord. Sphere
<b>A</b>	Cubic ( $P2_13$ )	909	No	N/A – structure reverts to RS at 0 GPa			7, 24, 55, 98, 151
<b>B</b>	Trigonal ( $R3m$ )	177	Yes	20.1101	6.71984	-1933.18 (+ 0.21)	6, 19, 41, 72, 111
<b>C</b>	Tetragonal ( $I4_1md$ )	232	Yes	19.9671	6.76799	-1932.99 (+ 0.40)	6, 20, 43, 76, 117
<b>D</b>	Hexagonal ( $P\bar{6}m2$ )	174	Yes	20.1823	6.69580	-1933.03 (+ 0.36)	6, 20, 42, 74, 114
<b>E</b>	Orthorhombic ( $Cmcm$ )	168*	No	N/A – structure reverts to B at 0 GPa			6, 19, 42, 74, 114
<b>WZ</b>	Hexagonal ( $P6_3mc$ )	N/A	Yes	24.6630	5.47934	-1933.39 (± 0.00)	4, 12, 25, 44, 67
<b>ZB</b>	Cubic ( $F\bar{4}3m$ )	N/A	Yes	24.6594	5.48014	-1933.35 (+ 0.04)	4, 12, 24, 42, 64
<b>RS</b>	Cubic ( $Fm\bar{3}m$ )	N/A	Yes	19.9267	6.78170	-1933.38 (+ 0.01)	6, 18, 38, 66, 102

\* Despite polymorph E being found in the search and included in the data, it could not be stabilised even at high pressure, returning two imaginary phonon frequencies along multiple  $k$ -vectors in the Brillouin zone. However, its analysis has been included as this structure is reported to be metastable by Zagorac *et al.*

**Table 7.xxi:** Table summarising some data pertaining to the five discovered configurations of zinc oxide, compared to the three experimentally known phases. Phase labels highlighted in blue correspond to previously unreported structure types for ZnO, postulated in this work as possible metastable forms of zinc oxide at very high pressures.

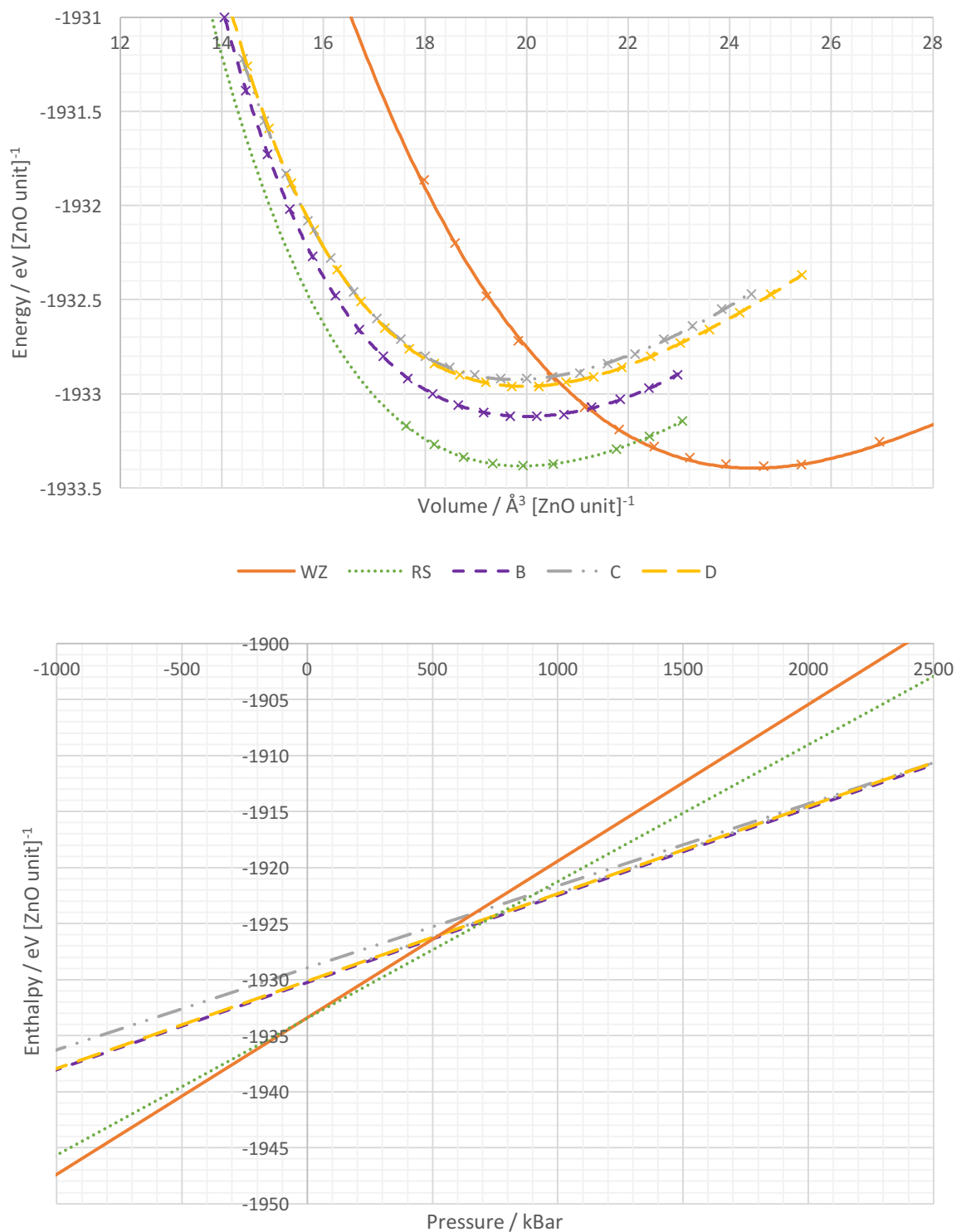


**Figure 7.xxxii:** Volume vs. energy (top) and pressure vs. enthalpy (bottom) plots for the three predicted zinc oxide polymorphs that could be stabilised at a range of pressures, compared to those of wurtzite (WZ) and rocksalt (RS). The plots of materials A and E are not included, since these transform into rocksalt and B respectively when relaxed using conjugate gradient methods at the lower pressures required to generate the above plot.

7.5.4.2. The Five Predicted Phases of ZnO7.5.4.2.1. Structure A – NaCl-like with FeSi distortion

The first of the five structures discovered using the *Random Atomic Placement* technique is a cubic polymorph with space group  $P2_13$ , designated structure A.

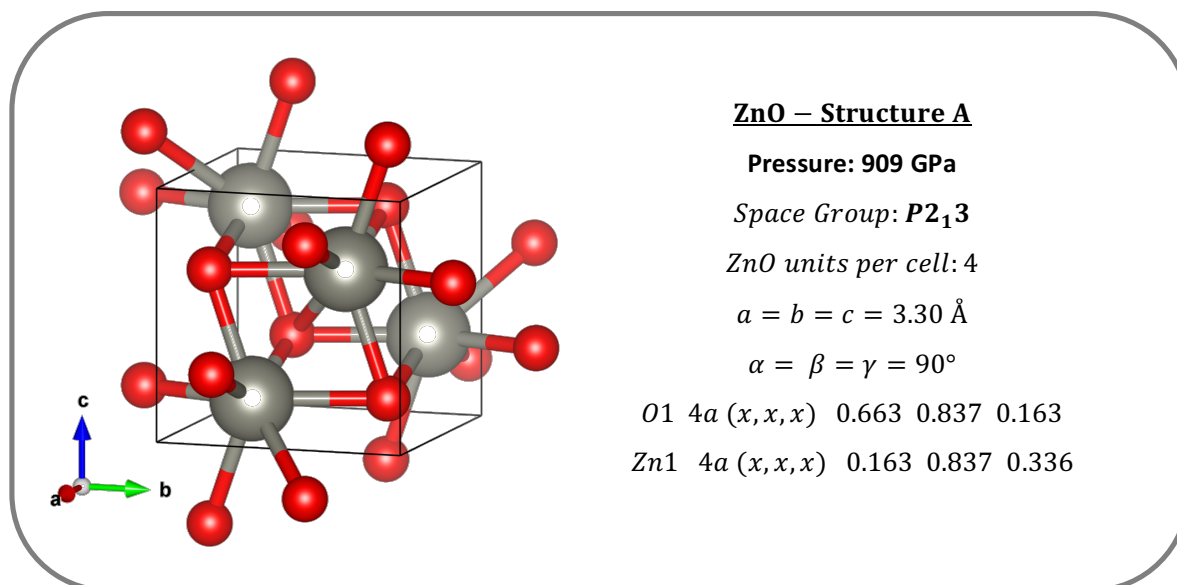


**Figure 7.xxxiii:** Structure A, showing the seven-fold coordination and highly symmetric cubic configuration, as well as crystallographic data relating to the unit cell of the novel polymorph.

This highly symmetrical phase was found initially at the very high pressure of 909 GPa, well above the pressure at which the rocksalt to caesium chloride transition is expected. As a result of this extreme pressure, this form of ZnO has a number of fascinating geometric properties. Strikingly, each zinc is bound to seven oxygens, and vice versa, giving a local distorted pentagonal bipyramidal molecular environment. At 909 GPa, six of these bonds are approximately  $1.75 \text{ \AA}$  in length, with the seventh slightly longer at  $1.87 \text{ \AA}$ . The structure can be thought of as a distorted rocksalt structure, with a geometry intermediate between that of the structures of rocksalt and iron silicide (FeSi). This seven-coordinate form of zinc oxide has not yet been reported, and nor observed in any collected experimental evidence.



Releasing the high pressure and running a conjugate gradient relaxation at 0 GPa causes the structure to promptly revert back to rocksalt zinc oxide, indicating it is highly unstable at ambient pressure. However, this material persisted when propagated at much lower pressures than 909 GPa – The system was also able to be relaxed at 500, 400 and 300 GPa.

The electronic band structure at 909 GPa shows an indirect band gap of approximately 4.40 eV, meaning that the material has a larger band gap than the known zinc oxide polymorphs. In addition, all of the phonon frequencies across the Brillouin zone are positive, indicating that the structure is mechanically stable at 909 GPa.

Although such pressures are presently far too high for any immediate application of this material, it is not inconceivable to imagine scenarios where such a polymorph of zinc oxide could exist, particularly in the context of planetary sciences. For example, the core of the planet Jupiter experiences pressures of up to 4,500 GPa. Thus, it is quite plausible to imagine that this polymorph could be present within exoplanets which both feature high levels of zinc and oxygen and are of a comparable size to the gas giants in our Solar System.

Alternatively, this material could exist as an intermediate or transition state during the phase transition between six-coordinate (RS) and eight-coordinate (CsCl) type zinc oxide. It would be very interesting to apply the transition path sampling and *metashooting* procedures (refer to Chapter 5) on such a transition in order to determine whether or not this could be a viable intermediate for this transformation. However, its independent existence at 909 GPa indicates that it is a *bona fide* phase itself, and not just a transient state linking two more ‘conventional’ polymorphs.

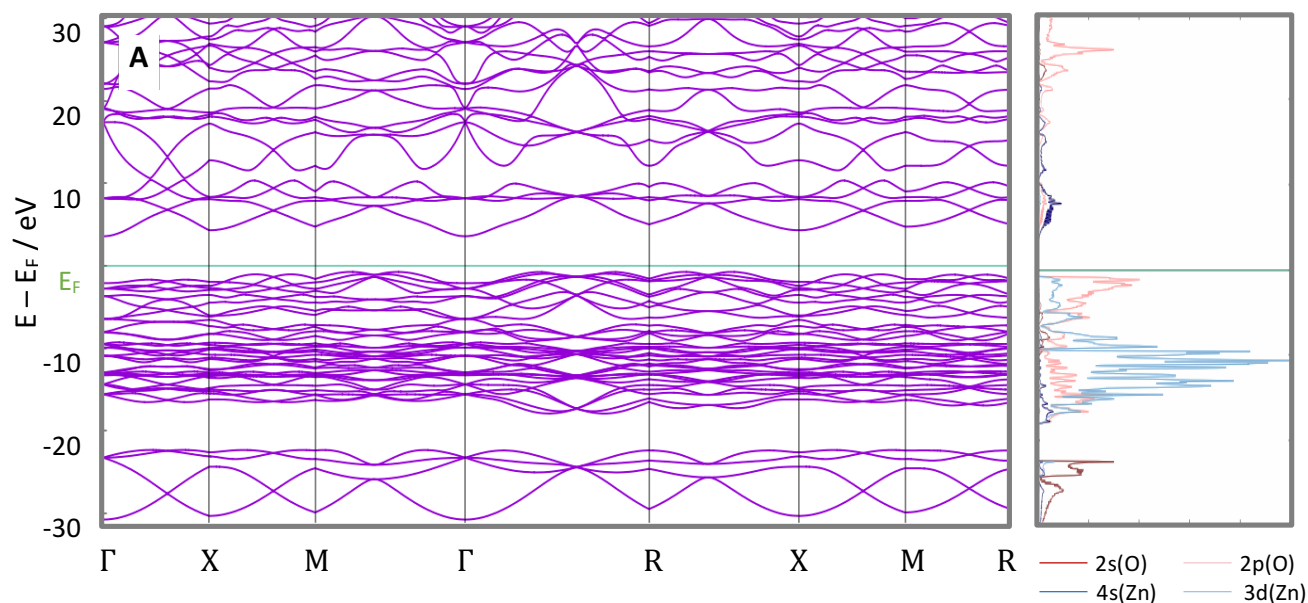


**Figure 7.xxxiv** Electronic band structure and projected density of states showing contributions from zinc and oxygen atoms for the hypothetical  $P2_13$  structure at 909 GPa. Oxygen 2s and 2p states are given in dark red and pink respectively, whereas zinc 4s and 4d states are denoted in dark and light blue. The band plot shows an indirect band gap of approximately 4.40 eV between  $R$  and  $\Gamma$ .

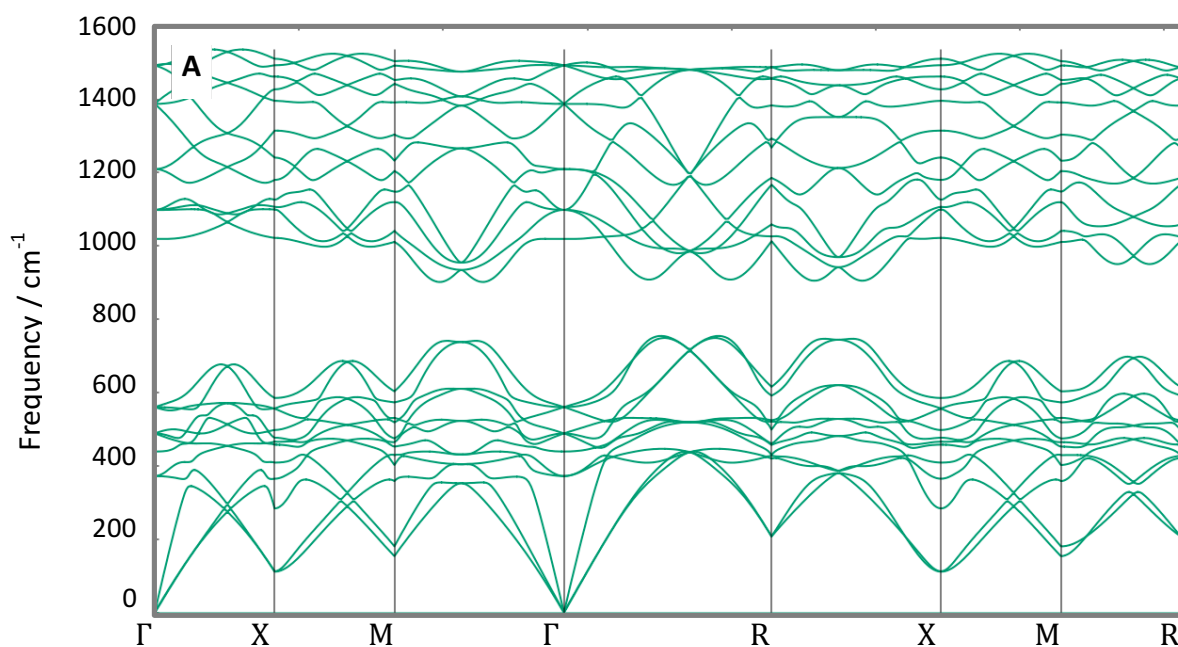


**Figure 7.xxxv:** Phonon dispersion curves of the hypothetical  $P2_13$  structure at 909 GPa showing no imaginary frequencies across the Brillouin Zone, confirming the mechanical stability of the seven-coordinate polymorph at this pressure

7.5.4.2.2. Structure B – NaCl-NiAs intergrowth

The second high-pressure zinc oxide structure discovered in this work crystallises within the trigonal space group  $R\bar{3}m$ . Present at the much lower (but still very high!) pressure of 177 GPa, its six-coordinate geometry is an intergrowth of RS and NiAs-type topologies, with alternating motifs of each structure type present throughout the system. It is believed that this polymorph is also novel for zinc oxide.

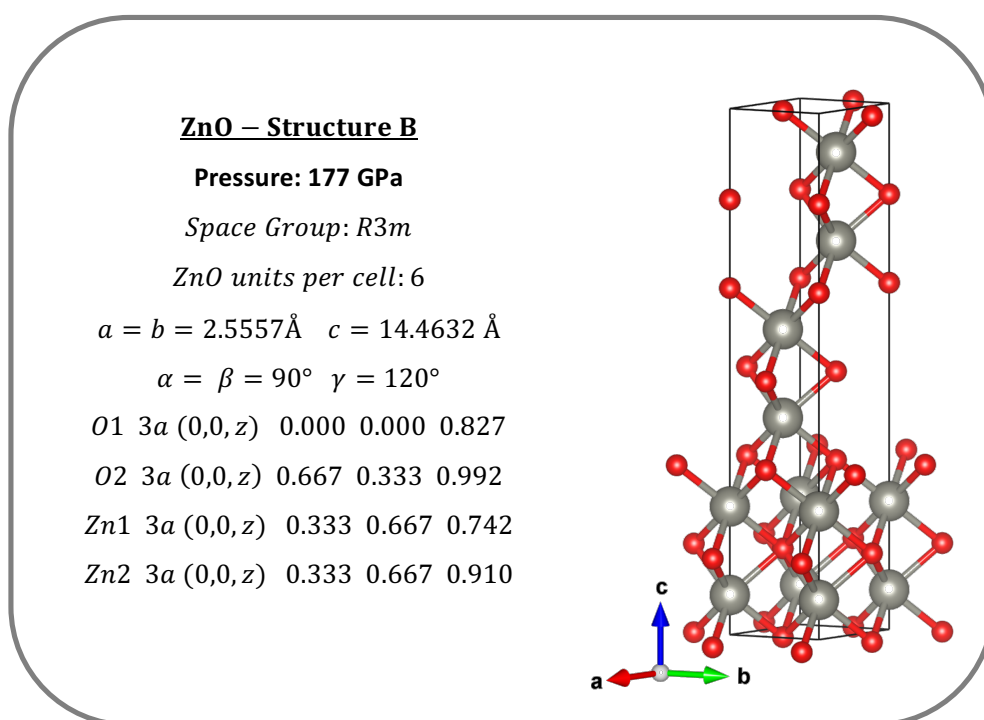


Figure 7.xxxvi: A depiction of structure B, showing the mixed rocksalt-nickeline topology.

Crystallographic data is also presented.

Mixed topology materials such as this have recently gathered significant interest because of their potential uses in electronic devices. Most notably, layered materials are being increasingly considered for use in thermoelectric materials, with the idea being that alternating layers of a material can conduct electricity but scatter phonons at their interfaces, leading to poor thermal conductivity. This increases the figure of merit (ZT) of the material and hence its capability as a thermoelectric material.

The mixed nature of the material means that there are three distinct Zn-O bond lengths. At the initial pressure of 177 GPa, Zn-O contacts within rocksalt motifs have lengths of 1.89 Å, whereas in nickel arsenide environments they are longer at 1.92 Å. Zn-O contacts connecting the two different topologies are intermediate in length, at around 1.9 Å long.

The electronic structure of this material at 177 GPa shows that this material has a direct band gap of 3.18 eV, making it a fairly wide band-gap semiconductor with a gap similar to that of ambient zinc oxide. The phonon spectrum shows no imaginary frequencies, confirming the high pressure stability of the material at the simulated pressure.

Unlike the previous structure, the structural integrity of this polymorph is retained when relaxed at zero-pressure. Energy calculations at 0 GPa showed that this structure was the most favourable of the three structures that could be relaxed at zero pressure, with a Zn-O unit volume and density very similar to that of rocksalt and an energy only 0.2 eV atom<sup>-1</sup> above the NaCl-type configuration. However, phonon dispersions at 0 GPa featured several imaginary frequencies, indicating its instability at lower pressures.

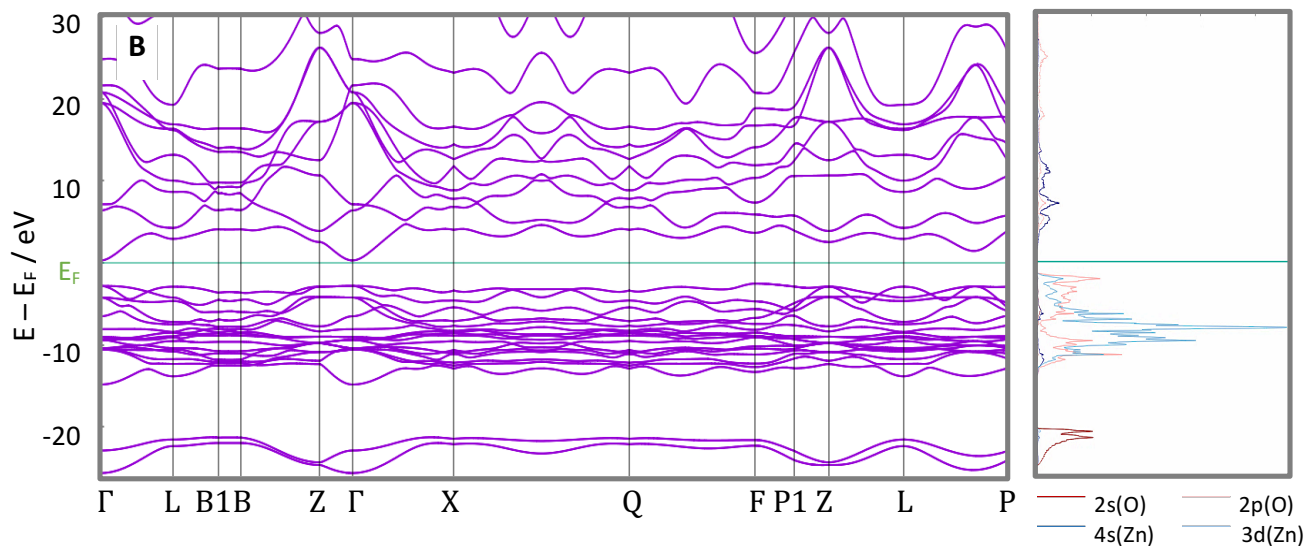


**Figure 7.xxxvii:** Electronic band structure and projected density of states for polymorph B at 177 GPa, showing a large gap centred at the Fermi level.

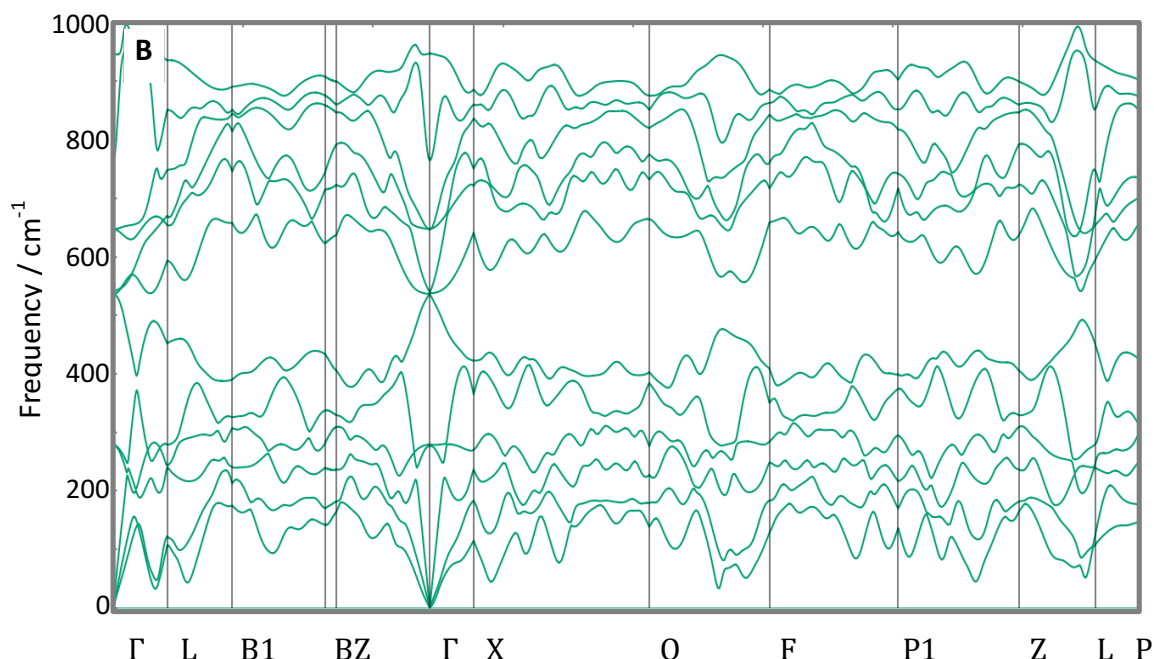


**Figure 7.xxxviii:** Phonon spectrum for structure B at 177 GPa, showing no negative frequencies. The undulations seen in the phonon dispersions are almost certainly non-physical, resulting from insufficient  $k$ -grid sampling. Nonetheless, the lack of imaginary frequencies confirms the mechanical stability of the polymorph at 177 GPa.

#### 7.5.4.2.3. Structure C – NbAs-like

The third structure determined by the random crystal structure search is another rare configuration (and as yet unknown for zinc oxide), crystallising in the body-centred tetragonal space group  $I4_1md$ . This structure, which was stabilised at 232 GPa, is analogous to the structure of niobium arsenide (NbAs).

Structurally, the system can be described in terms of layers that are shifted along either the  $a$  or the  $b$  direction with respect to neighbouring layers, leading to an overall ‘screw’ pattern along the  $c$ -axis. Additionally, the structure contains no centre of inversion. At the reported pressure of discovery, there exists a slight asymmetry in the Zn-O bonds, with half of the Zn-O interactions equal to 1.875 Å and the second half slightly longer at 1.884 Å.

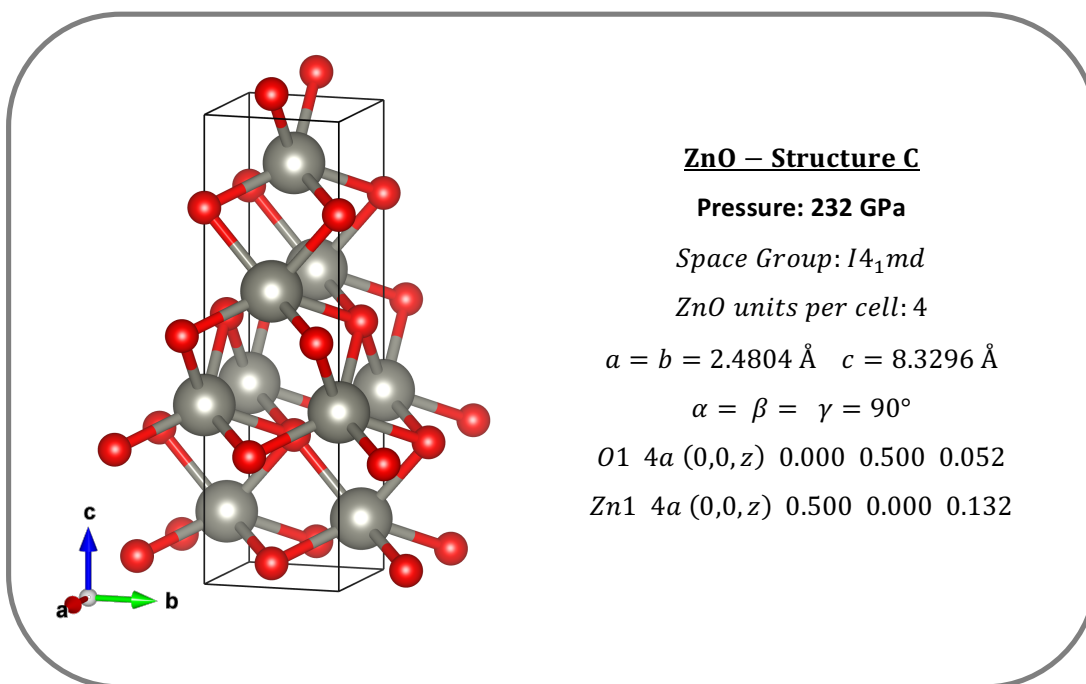
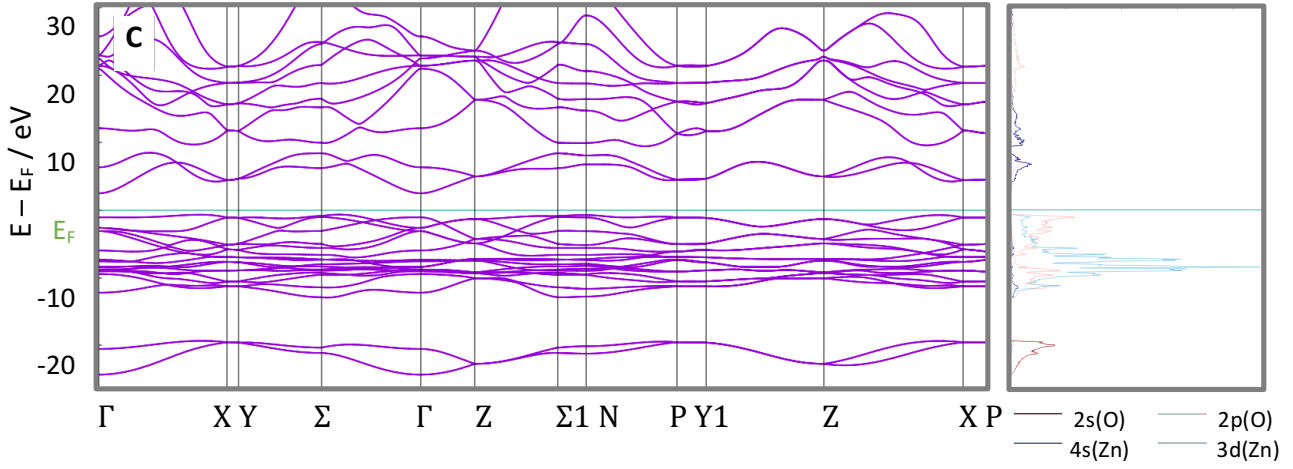


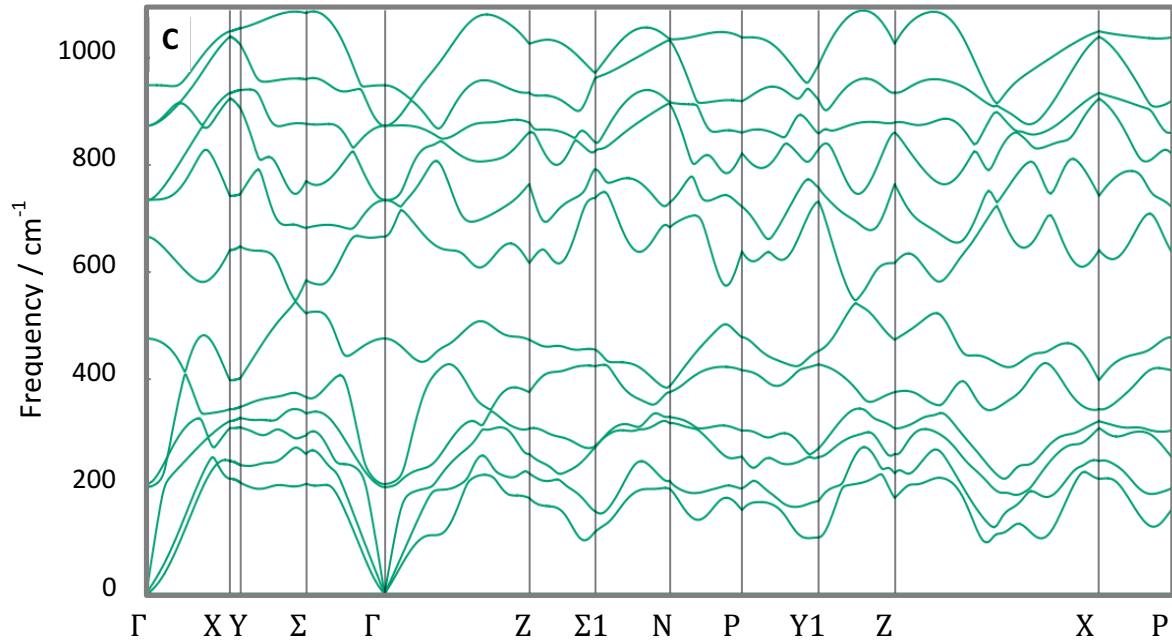
Figure 7.xxxix: An illustration of the niobium arsenide-like structure C, with some associated crystallographic data.

Unlike the true niobium arsenide compound (which is metallic), the Fermi level in this material is once again found in the gap between the highly dispersed conduction bands and the localised *d*-electron band, making this polymorph a semiconductor. This form of zinc oxide has an *indirect* band gap of around 3.25 eV (very similar to the gap exhibited by wurtzite ZnO), from the  $\Sigma$  point in the valence band to the  $\Gamma$  point in the conduction band. Phonon dispersions at the pressure of discovery confirmed the mechanical stability of the NbAs structure at 232 GPa.

At 0 GPa, the volume and density of this material are almost identical to rocksalt; however, it was the highest in energy of the three zero-pressure metastable phases reported, with an energy just shy of  $0.4 \text{ eV atom}^{-1}$  greater than ambient zinc oxide at 0 GPa. However, the phonon dispersion curves at 0 GPa featured numerous negative frequencies, indicating that the structure is only stable at high pressure.

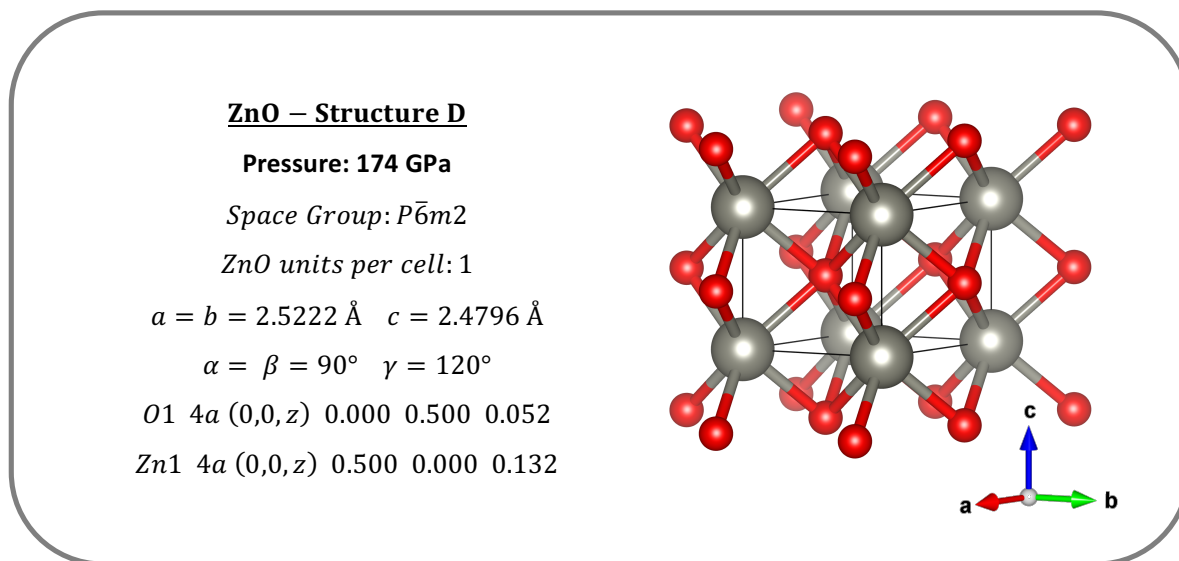


**Figure 7.xl:** Electronic band structure and projected density of states for structure C at 232 GPa, showing that it behaves as a semiconductor with an indirect band gap of 3.25 eV.



**Figure 7.xli:** Phonon dispersion curves for structure C, confirming the mechanical stability of the material at 232 GPa.



7.5.4.2.4. Structure D –  $\alpha$ -WC-like

**Figure 7.xlii:** A depiction of structure D, as well as associate crystallographic data for the unit cell at the pressure of discovery.

The fourth predicted high-pressure zinc oxide polymorph crystallises in a hexagonal configuration, analogous to the structure of alpha-tungsten carbide ( $\alpha$ -WC). Found at a pressure of 174 GPa, the structure can be considered as a simple hexagonal lattice of zinc atoms forming layers which stack directly on top of each other, with oxygen atoms filling exactly one half of the interstitial sites. This leads to a six-coordinate structure with local trigonal prismatic geometry. At the pressure reported, all of the Zn-O bonds are equivalent in length at 1.91 Å. The distance between zinc atoms in each hexagonal layer is equal to 2.52 Å, whereas the distances between the zinc layers themselves are slightly shorter at 2.47 Å.

The phonon dispersion curves for this material at 174 GPa confirm its dynamical stability, and electronic structure calculations indicate that the material is semiconducting, with an indirect band gap of approximately 3.5 eV from  $M$  in the valence band to  $\Gamma$  in the conducting band. As with structures B and C, this form of ZnO could also be relaxed at 0 GPa, however its phonon spectrum once again featured several imaginary frequencies at zero pressure.



This form of zinc oxide has been found previously in the work of Zagorac *et al*, who also predicted that the  $\alpha$ -WC structure of zinc oxide is possible at very high pressure, and could be an important intermediate in the transition between rocksalt and caesium chloride type ZnO. This would be a fascinating future project to undertake with the transition path sampling and *metashooting* methodologies.

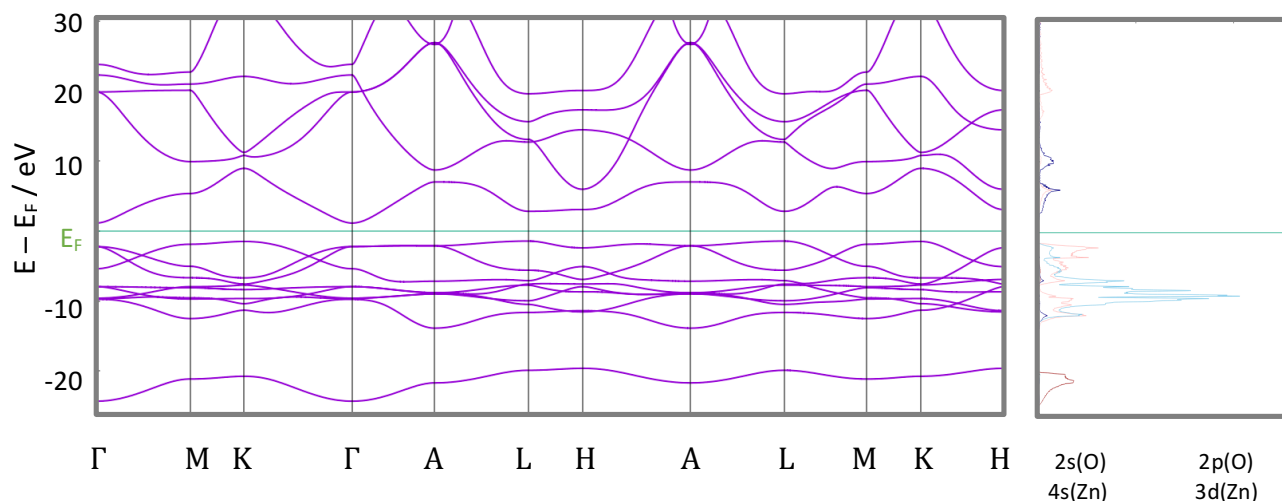


**Figure 7.xliii:** Electronic band structure and projected density of states at 174 GPa for structure D, the  $\alpha$ -WC-like phase of ZnO, showing an indirect band gap of 3.5 eV.

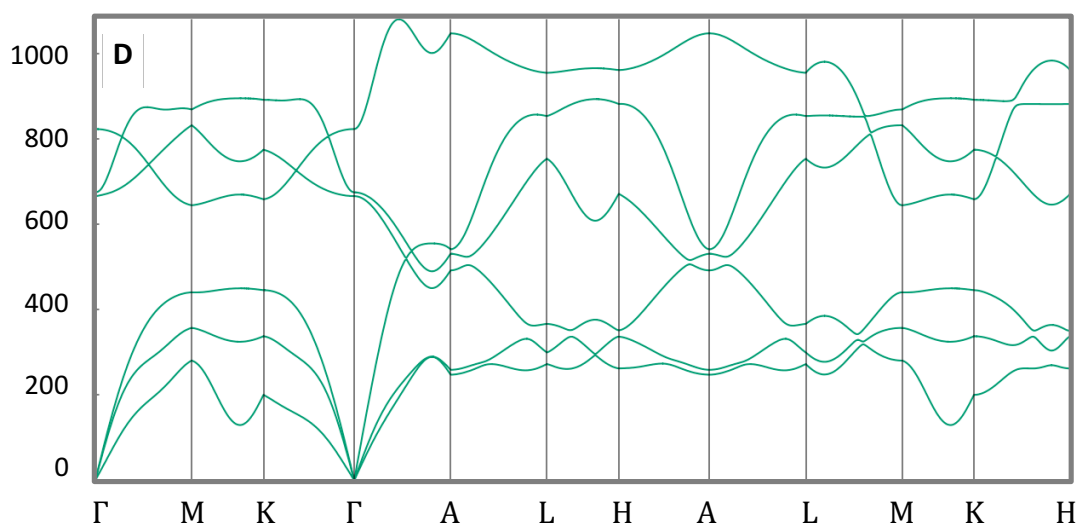


**Figure 7.xliv:** Phonon dispersion curves for structure D at the pressure of discovery, confirming its dynamical stability at 174 GPa.

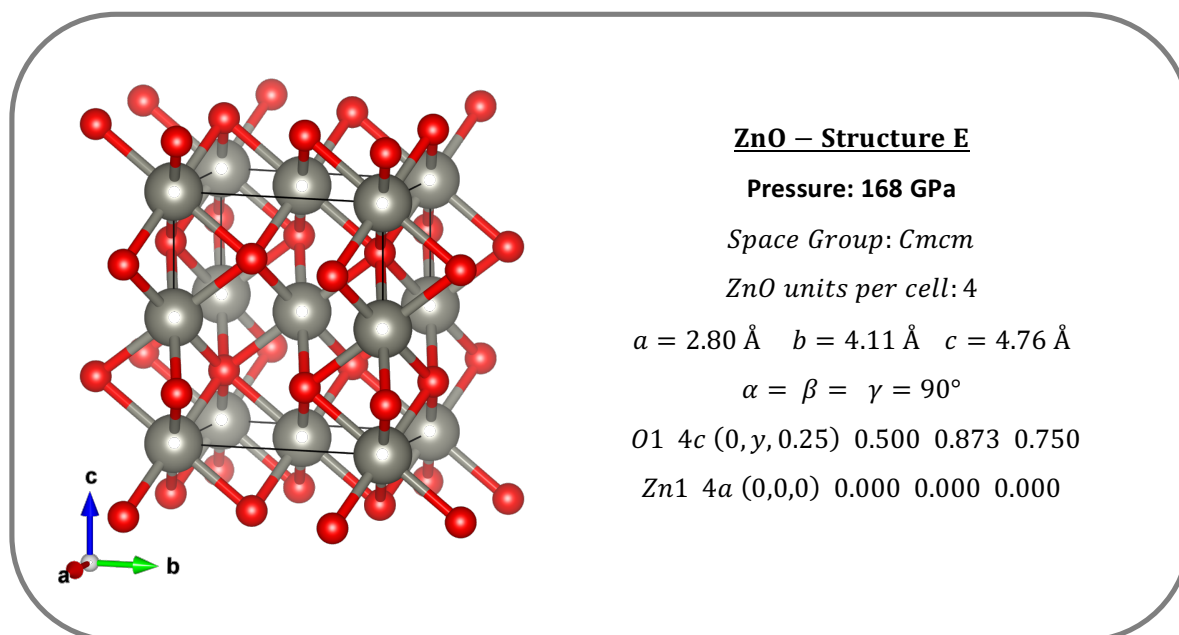
7.5.4.2.5. Structure E – NiAs-like

Figure 7.xlv: Illustration and crystallographic data of structure E, the NiAs analogue.

The fifth and final of the five polymorphs discovered is analogous to the nickel arsenide (NiAs) structure, crystallising in the orthorhombic space group  $Cmcm$ . This atomic configuration is common for many transition metal sulphides with a 1:1 stoichiometry, but has not yet been experimentally realised for zinc oxide.

Structurally, it can be seen that the arrangement consists of a hexagonal close-packed arrangement of zinc atoms, with oxygens then filling all of the available octahedral holes. Once again, the coordination number of the atomic sites is 6. The layers of zinc and oxygen order in an ACBCA fashion, meaning that unlike in the rocksalt configuration, the cationic and anionic sites are not interchangeable. Nickeline arrangements tend to occur in compounds with a significant degree of covalent nature to their bonding. In addition, the metal ions in nickeline systems often tend to be slightly closer to each other than expected, due to stronger metal-metal interactions.

This structure was found at the initial pressure of 168 GPa. However, two bands within the calculated phonon dispersion curves were imaginary along certain  $k$ -vectors of the Brillouin

zone at this pressure, indicating that the structure is not mechanically stable. In addition, any attempts to relax or propagate this structure at 0 GPa saw it revert back to structure B (the intergrowth structure), indicating that this configuration appears not to be stable at neither ambient nor high pressures. This is likely a result of the significant ionicity exhibited by ZnO, and hence its unwillingness to adopt configurations more usually associated with covalent structures.

Recall that the intergrowth RS-NiAs structure was dynamically stable in this pressure regime, and could also be relaxed to 0 GPa without issue. It is theorised that perhaps a 50:50 ratio of RS (the ultimate ionic configuration) and NiAs is sufficient to stabilise the structure, but that a pure NiAs is not possible for the highly ionic zinc oxide.

Zagorac *et al* also found the NiAs topology in their structure prediction work.<sup>[73]</sup> However, they reported that the NiAs phase was metastable at both ambient and very high pressures, which directly conflicts with the findings presented here. The work described here appears to directly contradict this result, which may explain why NiAs-type ZnO has never been found experimentally. However, given that the structure was found in this work by random structure prediction, as well as by others, it is postulated that this zinc oxide topology may be possible, albeit very energetically demanding, under certain conditions.

### 7.5.5. Conclusions and Future Work

Five potential high-pressure phases of zinc oxide have been discovered in this work using the *random atomic placement* method, followed by geometry optimisations under high pressure. Four of the structures discovered are dynamically stable at high pressure, and three of these structures can be geometry optimised at 0 GPa. Three of the structures appear to be novel for zinc oxide and have not been previously reported. The structures have thus been analysed for their structural, electronic and vibrational properties, giving insight into the conditions under which these materials could exist, as well as their possible uses. Despite LDA not being a standard method of choice for ZnO DFT, it appeared to work very well in this work, producing reasonable structures and properties at all of the pressures tested.

It is extremely unlikely this study has exhausted the potential high-pressure structures of zinc oxide. Indeed, given the wealth of exotic structures exhibited by other diatomic compounds at high pressure, it seems likely that this work has merely scratched the surface of the high-pressure phase behaviour of zinc oxide. Nevertheless, it presents novel work in the form of a random structure prediction technique utilised at high pressure to find and categorise a number of novel structural types for zinc oxide.

An appropriate follow-up to this work would be to study the plausibility of transforming from ambient zinc oxide (or the rocksalt phase) to one or more of the predicted high pressure phases. This could certainly be achieved using the transition path sampling and *metashooting* methodologies discussed previously, as the initial and final configurations are well defined, as are the order parameters differentiating them. However, it is suggested that it would be advisable to use higher order values of the coordination sphere to better distinguish between the different phases. As all but one of the newly discovered phases had the same first coordination shell (CN=6, the same as rocksalt) and this could prove to be a problem when trying to discriminate between different states in the path sampling procedure. Using higher values of coordination, such as the 3<sup>rd</sup> and the 5<sup>th</sup>, enables much greater resolution of the configuration space and could allow for mechanisms to be determined for the transition.

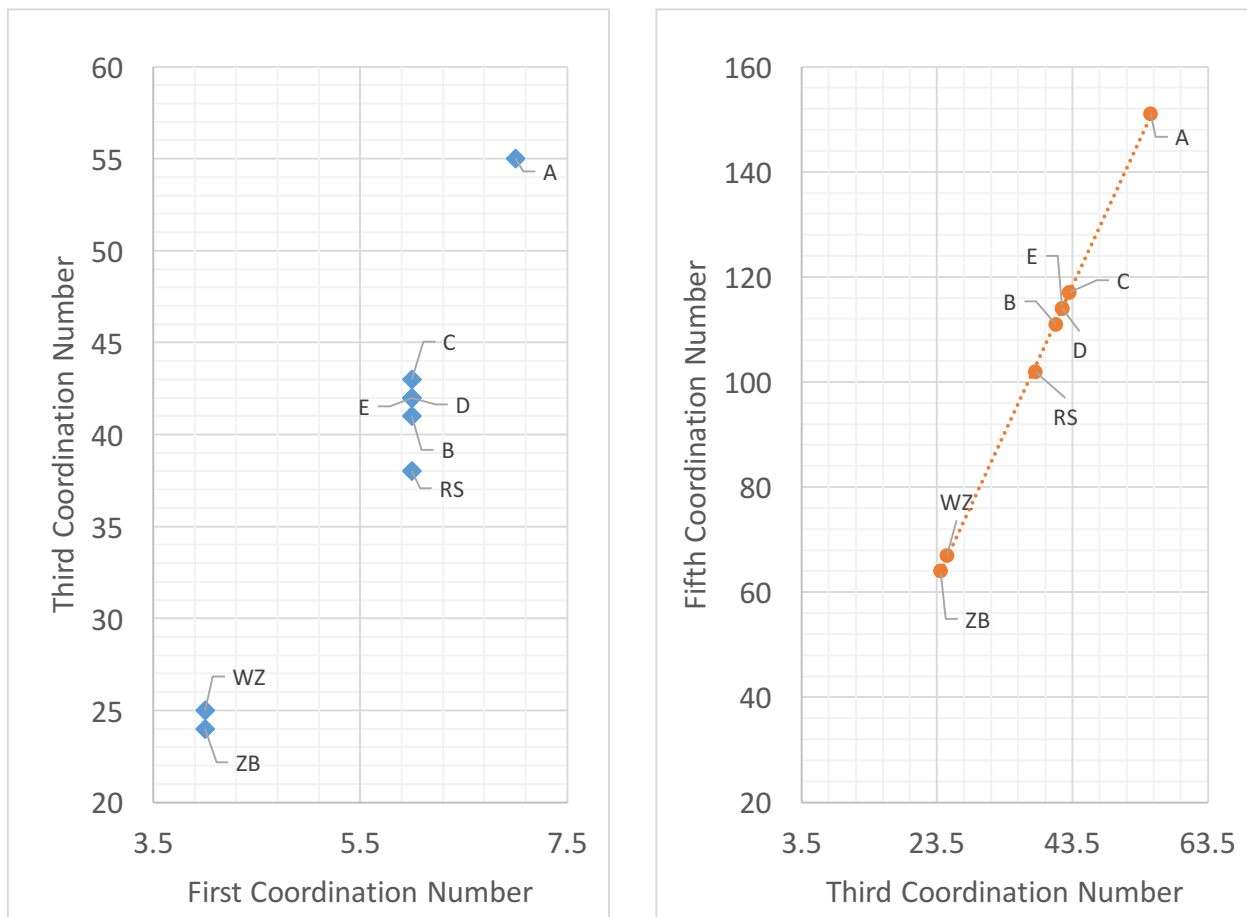


**Figure 7.xlvi:** Coordination number plots of the discovered and known phases. The diagram on the left shows a plot of 1<sup>st</sup> vs. 3<sup>rd</sup> coordination sphere (the same collective variable set up as used for the zinc oxide path sampling and *metashooting* procedure in chapter 5) Most of the discovered phases are found at 1<sup>st</sup> CN=6. However, when plotting higher coordination numbers, such as 3<sup>rd</sup> vs. 5<sup>th</sup> (right), the structures show a clear linear relationship.

Given that compound B is both the closest in energy to the rocksalt configuration of zinc oxide, and is the least dissimilar in terms of coordination sphere ( $RS = \{6, 8, 18\}$ ,  $B = \{6, 19, 41\}$ ), it is believed that this would be the best target to search for both experimentally and theoretically.

The formation of the  $\alpha$ -WC phase in this work corroborates the previous findings of Zagorac *et al*<sup>[73]</sup>, and an investigation into the role of this polymorph in the rocksalt to caesium chloride transition using the path sampling/*metashooting* techniques would too be fascinating.

Additionally, it would be fascinating to investigate whether or not the seven-coordinate structure A play any role in the transition from the six-coordinate rocksalt to the eight-coordinate caesium chloride.

However, crucially different to the work of Zagorac *et al*, the nickeline (NiAs) phases could not be stabilised at ambient or high pressures. Instead, this work suggests that a 50:50 mixture of nickeline and rocksalt topology produces a much more favourable configuration for zinc oxide. Further investigations into the stability of the nickeline and intergrowth structures would be a useful future project, in order to address the inconsistencies seen between this data and previous work.

Finally, a very exciting prospect to extend this work would be to design a more intelligent algorithm to search for high pressure zinc oxide structures, incorporating the random structure searching technique presented here with other prediction methods. For example, as there is a clear relationship between the 3<sup>rd</sup> and 5<sup>th</sup> coordination spheres of the ZnO materials, one could perform a configuration space search within the constraints of this linear relationship, in order to accelerate the search for novel polymorphs. Indeed, this scheme could foreseeably be extended for any system, assuming that such a relationship exists for higher coordination sphere, or some other 'global' collective variable. Such a procedure could be used to efficiently survey a constrained configuration space for a range of systems, in order to find novel allotropes and polymorphs of interest.

References – Chapter 7

1. A. R. Oganov, *Modern Methods of Crystal Structure Prediction*, John Wiley & Sons, 2011
2. S. M. Woodley and C. R. A. Catlow, *Nat. Mater.*, 2008, **7**, 937-946
3. C. Roberts and R. L. Johnston, *Phys. Chem. Chem. Phys.*, 2001, **3**, 5024-5034
4. G. R. Desiraju, *Nat. Mater.*, 2002, **1**, 77-79
5. J. Maddox, *Nature*, 1988, **335**, 201
6. Y. Wang, J. Lv, L. Zhu and Y. Ma, *Comput. Phys. Commun.*, 2012, **183**, 2063-2070
7. C. J. Pickard and R. J. Needs, *J. Phys. Condens. Matter*, 2011, **23**, 53201
8. S. Kirkpatrick, C. D. Gelatt and M. P. Vecchi, *Science*, 1983, **220**, 671-680
9. V. A. Blatov and D. M. Proserpio, in *Modern Methods of Crystal Structure Prediction*, ed. A. R. Oganov, John Wiley & Sons, 2010
10. R. Martonák, A. Laio and M. Parrinello, *Phys. Rev. Lett.*, 2003, **90**, 75503
11. R. Martonák, A. Laio, M. Bernasconi, C. Ceriani, P. Raiteri and M. Parrinello, *Crystalline Materials*, 2005, **220**, 489-498
12. A. R. Oganov and C. W. Glass, *J. Phys. Condens. Matter*, 2008, **20**, 64210
13. A. R. Oganov, A. O. Lyakhov and M. Valle, *Acc. Chem. Res.*, 2011, **44**, 227-237
14. W. W. Tipton and R. G. Hennig in *Modern Methods of Crystal Structure Prediction*, ed. A. R. Oganov, John Wiley & Sons, 2010
15. R. S. Anderssen and P. Bloomfield, *J. Optim. Theory Appl.*, 1975, **16**, 383-398
16. C. J. Pickard and R. J. Needs, *Nat. Mater.*, 2010, **9**, 624-627
17. C. J. Pickard and R. J. Needs, *Phys. Rev. Lett.*, 2006, **97**, 045504
18. C. J. Pickard and R. J. Needs, *Phys. Rev. Lett.*, 2009, **102**, 125702
19. C. J. Pickard and R. J. Needs, *J. Phys. Condens. Matter. Inst. Phys. J.*, 2009, **21**, 452205
20. J. C. Schön and M. Jansen, in *Modern Methods of Crystal Structure Prediction*, ed. A. R. Oganov, John Wiley & Sons, 2010
21. K. Doll, J. C. Schön and M. Jansen, *Phys. Rev. B*, 2008, **78**, 144110
22. Y. Okamoto in *Encyclopedia of Optimization*, eds. C. A. Floudas and P. M. Pardalos, Springer US, 2008
23. Y. Sakae, T. Hiroyasu, M. Miki and Y. Okamoto, *J. Comput. Chem.*, 2011, **32**, 1353-1360
24. D. Selli, I. A. Baburin, R. Martonák and S. Leoni, *Sci. Rep.*, 2013, **3**, 1466

25. R. Martonák, A. R. Oganov and C. W. Glass, *Phase Transit.*, 2007, **80**, 277-298
26. A. F. Wells, *Acta Crystallogr.*, 1954, **7**, 535-544
27. B. Winkler, C. J. Pickard, V. Milman and G. Thimm, *Chem. Phys. Lett.*, 2001, **337**, 36-42
28. V. A. Blatov, A. P. Shevchenko and D. M. Proserpio, *Cryst. Growth Des.*, 2014, **14**, 3576-3586
29. R. L. Johnston, *Dalton Trans.*, 2003, **0**, 4193-4207
30. N. L. Abraham and M. I. J. Probert, *Phys. Rev. B.*, 2006, **73**, 224104
31. J. T. Pedersen and J. Moulton, *Curr. Opin. Struct. Bio.*, 1996, **6**, 227-231
32. <http://periodictable.com/Properties/A/CrustAbundance.v.html> "Abundance in Earth's Crust of the Elements" - Last Accessed 28/09/2017
33. N. N. Greenwood and A. Earnshaw, *Chemistry of the Elements*, Elsevier, 2<sup>nd</sup> Edition, 2012
34. R. Hoffmann, A. A. Kabanov, A. A. Golov and D. M. Proserpio, *Angew. Chem. Int. Ed.*, 2016, **55**, 10962-10976
35. <http://etymonline.com/index.php?term=graphite> "Etymology of Graphite" - Last Accessed 28/09/2017
36. <https://minerals.usgs.gov/minerals/pubs/commodity/graphite/> "Graphite: Statistics and Information"- Last Accessed 28/09/2017
37. R. W. G. Wyckoff, *Crystal Structures*, 1963, **1**, 7-83
38. P. Delhaes, *Graphite and Precursors*, CRC Press, 2000
39. K. S. Krishnan and N. Ganguli, *Nature*, 1939, **144**, 667
40. K. S. Novoselov, A. K. Geim, S. V. Morozov, D. Jiang, Y. Zhang, S. V. Dubonos, I. V. Grigorieva and A. A. Firsov, *Science*, 2004, **306**, 666-669
41. C. Lee, X Wei, J. W. Kysar and J. Hone, *Science*, 2008, **321**, 385-388
42. D. R. Cooper, B. D'Anjou, N. Ghattamaneni, B. Harack, M. Hilke, A. Horth, N. Majlis, M. Massicotte, L. Vandsburger, E. Whiteway and V. Yu, *ISRN Cond. Matt. Phys.*, 2012, **2012**, 501686
43. J. H. Chen. C. Jang, S. Xiao, M. Ishigami and M. S. Fuhrer, *Nat. Nanotechnol.*, 2008, **3**, 206-209
44. A. K. N Geim and K. S. Novoselov, *Nat. Mater*, 2007, **6**, 183-91
45. <http://en.wiktionary.org/wiki/diamond> "Etymology of Diamond" - Last Accessed 28/09/2017



46. F. Occelli, P. Loubeyre and R. LeToullec, *Nat. Mater.* 2003, **2**, 151-154
47. K. Iakoubovskii, and G. J. Adriaenssens, *Diam. Relat. Mater.*, 2002, **11**, 125-131
48. A. T. Collins, *Phil. Trans. R. Soc. Lond. A.*, 1993, **342**, 233-244
49. J. R. Olson, R. O. Pohl, J. W. Vandersande, A. Zoltan, T. R. Anthony and W. F. Banholzer, *Phys. Rev. B. Condens. Matter.*, 1993, **47**, 14850-14856
50. C. Frondel and U. B. Marvin, *Nature*, 1967, **214**, 587-589
51. Z. Pan, H. Sun, Y. Zhang and C. Chen, *Phys. Rev. Lett.*, 2009, **102**, 55503
52. <https://goldbook.iupac.org/html/F/F02547.html> "Fullerenes" - Last Accessed 28/09/2017
53. H. W. Kroto, J. R. Heath, S. C. O'Brien, R. F. Curl and R. E. Smalley, *Nature*, 1985, **318**, 162
54. G. Lalwani and B. Sitharaman, *Nano LIFE*, 2013, **3**, 1342003
55. J. C. Lewis, B. Redfern and F. C. Cowland, *Solid-State Electron*, 1963, **6**, 251-254
56. E. A. Laird, F. Kuemmeth, G. A. Steele, K. Grove-Rasmussen, J. Nygård, K. Flensberg and L.P. Kouwenhoven, *Rev. Mod. Phys.*, 2015, **87**, 703-764
57. E. Joselevich, *ChemPhysChem*, 2004, **5**, 619-624
58. R. L. Johnston and R. Hoffmann, *J. Am. Chem. Soc.*, 1989, **111**, 810-819
59. K. Umemoto, R. M. Wentzcovitch, S. Saito and T. Miyake, *Phys. Rev. Lett.*, 2010, **104**, 125504
60. A. R. Oganov and C. W. Glass, *J. Chem. Phys.*, 2006, **124**, 244704
61. Q. Li, Y. Ma, A. R. Oganov, H. Wang, H. Wang, Y. Xu, T. Cui, H. K. Mao and G. Zou, *Phys. Rev. Lett.*, 2009, **102**, 175506
62. S. E. Boulfelfel, A. R. Oganov and S. Leoni, *Sci. Rep.*, 2012, **2**, 471
63. J. Narayan and A. Bhaumik, *J. Appl. Phys.*, 2015, **118**, 215303
64. X. L. Sheng, Q. B. Yan, F. Ye, Q. R. Zheng and G. Su, *Phys. Rev. Lett.*, 2011, **106**, 155703
65. A. A. Correa, S. A. Bonev and G. Galli, *Proc. Natl. Acad. Sci.*, 2006, **103**, 1204-1208
66. D. Selli, I. A. Baburin, R. Martonák and S. Leoni, *Phys. Rev. B*, 2011, **84**, 161411
67. J. M. Soler, E. Artacho, J. D. Gale, A. García, J. Junquera, P. Ordejón and D. Sánchez-Portal, *J. Phys. Condens. Matter*, 2002, **14**, 2745
68. J. P. Perdew, K. Burke and M. Ernzerhof, *Phys. Rev. Lett.*, 1996, **77**, 3865-3868
69. N. Troullier and J. L. Martins, *Phys. Rev. B*, 1991, **43**, 1993-2006

70. A. A. Al-Sunaidi, A. A. Sokol, C. R. A. Catlow and S. M. Woodley, *J. Phys. Chem. C.*, 2008, **112**, 18860-18875
71. E. V. Trushin, I. L. Zilberberg and A. V. Bulgakov, *Phys. Solid. State*, 2012, **54**, 859-865
72. J. E. Jaffe, J. A. Snyder, Z. Lin and A. C. Hess, *Phys. Rev. B.*, 2000, **62**, 1660-1665
73. D. Zagorac, J. C. Schön, J. Zagorac and M. Jansen, *Phys. Rev. B*, 2014, **89**, 075201
74. D. Zagorac, J. C. Schön, J. Zagorac and M. Jansen, *RSC Adv.*, 2015, **5**, 25929-25935
75. D. M. Ceperley and B. J. Alder, *Phys. Rev. Lett.*, 1980, **45**, 566-569

## Chapter 8

### General Conclusions and Closing Statements

**“Chemistry means the difference between poverty and starvation, and the abundant life”**

- Robert Brent, *The Golden Book of Chemistry Experiments* (1960)

Within this thesis, three distinctive pieces of work have been presented which, despite the significant and obvious differences between them, are all related by a single underlying theme: the use of advanced computational techniques to investigate the properties and behaviour of metastable systems. Such detailed atomistic analyses, using both classical and density-functional based techniques, give an unprecedented view into the underlying microscopic structures and processes ultimately responsible for the macroscopic properties of materials. This is one of the true benefits of materials study and innovation using computational techniques - without simulation, such intrinsic, thorough and vibrant insight would be all but impossible to achieve.

A detailed conclusions and future work section was presented at the end of each results chapter. Thus, this final section of the thesis will give a more general overview of the work carried out, and how it relates to the ‘wider picture’ in both a materials science and simulation context.

Firstly, a detailed analysis of the pressure-induced phase transition between a mixed wurtzite-zincblende system and the high pressure rocksalt phase was presented. With the motivation of using metastable zinc oxide as a material for use in electronic and optics devices, it was thought to be extremely beneficial to understand the mechanisms of phase transitions between the different forms of the material. Using transition path sampling methodology, several different pathways linking the two structures were elucidated with a number of opposing intermediates documented, including the well-established competition between the *iT* and *iH* structures. Additionally, using a combination of metadynamics and path sampling techniques known as *metashooting*, the underlying free energy landscape for the

transformation was generated. Upon this coarse-grained surface, trajectories could be mapped, energy barriers could be quantitatively ascertained, and the nature of important intermediate and transition state configurations easily extrapolated. It is believed that the *metashooting* procedure has significant potential to become a routine tool in the computational study of condensed matter, and that this investigation could establish an innovative paradigm for future studies into the elucidation of solid-solid phase transitions.

Following this, an extensive investigation into the phase behaviour of ice was discussed. Water and ice are extremely important to our everyday lives, and an accurate understanding of their natures is fundamental to a huge range of disciplines, ranging from biological to planetary sciences. The transformations between the eighteen experimentally known structures of water ice are currently very poorly understood. Two separate investigations were carried out; the first utilising metadynamics coupled with a new technique known as *rotational shooting*; the second, using metadynamics without *rotational shooting* in the space of three collective variables known to be effective in the simulation of water and ice. The first investigation produced transformations from crystalline phases to all three of the experimentally defined amorphous phases of ice and the liquid state, as well as a number of more unusual events such as the formation of internal surfaces and cavities. The second investigation demonstrated a possible phase transition between Ice III and cubic Ice I<sub>c</sub> via both an amorphous polymorph and an as-yet unidentified structure, somewhat reminiscent of the Cairo tiling structure. These fascinating insights will hopefully go some way to classifying the vast configuration space of condensed-matter water... whilst simultaneously they demonstrate how much we still *do not* know about this ubiquitous and essential compound!

Finally, a comprehensive crystal structure search for novel allotropes of carbon and new high pressure polymorphs of zinc oxide was conducted using *density functional theory*. The field of carbon structure prediction is continually growing, with hundreds of allotropes currently known or predicted. Zinc oxide presents a different story: literature pertaining to bulk structure prediction of the compound is scarce, with the broader scientific community focusing more on the functionalisation of wurtzite and synthesis of nanoparticles. Using a random structure prediction technique referred to as *random atomic placement*, eight carbon and five zinc oxide novel structures were elucidated, each of which had unique structural and

electronic properties and thus potential applications. The rapid expansion of the field of crystal structure prediction, coupled with the desire to find new high-performance materials to address the problems of the modern world, means that the discovery of novel structure types for such common materials is more pertinent now than ever before.

With the widespread availability of both powerful hardware and efficient software, working together within a rigorous mathematical and scientific framework, the scientific community is now able to utilise simulation techniques as a primary means of materials discovery and innovation. With such a broad range of methods and tools available, essentially any structure can be investigated, any transformation elucidated, or any property calculated within a *numerical laboratory*, without the need for prior experimental knowledge.

The work presented in this thesis hopes to demonstrate not only the conclusions drawn within each individual chapter, but the broader perspective that simulation techniques are invaluable to future investigations in materials science. No other range of techniques can give such an intrinsically detailed and beautiful view into the atomistic domain that largely dictates the properties of the world around us. With ever-increasing computing power, the continual improvement of algorithms and techniques, and the inexorable expansion of scientific knowledge, it seems almost certain that the role of simulation will only continue to strengthen in the years to come. It is hoped that the presented work helps to corroborate these viewpoints by both demonstrating the worth of simulation techniques, and by promoting further investigations, in this fascinating field of scientific discovery.